PRODUCTION-INDUCED RESERVOIR COMPACTION, PERMEABILITY LOSS AND LAND SURFACE SUBSIDENCE

A DISSERTATION

SUBMITTED TO THE DEPARTMENT OF GEOPHYSICS

AND THE COMMITTEE ON GRADUATE STUDIES

OF STANFORD UNIVERSITY

IN PARTIAL FULFILLMENT OF THE REQUIREMENTS

FOR THE DEGREE OF

DOCTOR OF PHILOSOPHY

Alvin Wing-Ka Chan

December 2004

I certify that I have read this dissertation and that, in my opinion, it is fully adequate in scope and quality as a dissertation for the degree of Doctor of Philosophy.

Mark D. Zoback (Principal Adviser)

I certify that I have read this dissertation and that, in my opinion, it is fully adequate in scope and quality as a dissertation for the degree of Doctor of Philosophy.

Gary Mavko

I certify that I have read this dissertation and that, in my opinion, it is fully adequate in scope and quality as a dissertation for the degree of Doctor of Philosophy.

Margot Gerritsen

I certify that I have read this dissertation and that, in my opinion, it is fully adequate in scope and quality as a dissertation for the degree of Doctor of Philosophy.

Amos Nur

Approved for the University Committee on Graduate Studies

Abstract

Deformation associated with hydrocarbon production in unconsolidated or poorly consolidated reservoirs can lead to reservoir compaction, permeability loss, land surface subsidence and, potentially, fault reactivation. These production-induced deformations can have significant impacts on both the exploitation scheme and the surface environments in the vicinity of the hydrocarbon reservoir. To understand the severity of the deformation, it is important to understand the physical and mechanical properties of the producing formations in response to depletion. There are three main goals in this thesis: 1) To understand the mechanism of production-induced porosity loss and reservoir compaction in weak sand reservoirs, 2) To investigate how the change in porosity will affect permeability and reservoir productivity, and 3) To examine the impact of oil and gas production on land surface subsidence as a result of reservoir compaction and fault reactivation, with particular interest in the Louisiana Coastal Zone.

To examine the impact of pressure reduction on porosity, I introduce a formalism termed Deformation Analysis in Reservoir Space (DARS) that combines simple laboratory rock mechanics experiments with *in situ* stress measurements. Production and laboratory data can be evaluated simultaneously by utilizing DARS to study the potential of induced faulting and reservoir compaction. I use Valhall field, a chalk reservoir located in the North Sea, and Field X, a turbidite sand reservoir located in the Gulf of Mexico, to demonstrate how this simple formalism can be applied to reservoirs in different geological settings given appropriate laboratory experiments and stress measurements.

The influence of porosity reduction can have a significant impact on the permeability of a producing formation. Using available laboratory experiments and published data, I establish an empirical relationship between porosity loss and permeability loss. The empirical relationship provides a range of the potential permeability loss resulting from compaction. If not considered, these drastic changes in permeability experienced in some of the samples may affect the estimated productivity of a compacting reservoir from

simulations. I therefore investigate the impact of production-induced changes in porosity and permeability on reservoir productivities through a simple flow simulator.

Time-dependent inelastic deformation can be observed in weakly consolidated to unconsolidated sands. To capture these time-dependent deformations, I incorporate the Perzyna viscoplastic theory into the modified Cam-Clay cap model such that volumetric strain can be determined as a function of both stress and rate. With viscoplasticity, I expand the pressure-dependent, but time-independent, static DARS formalism to a pressure-and time-dependent dynamic DARS formalism. Re-examining the production history at Field X, I demonstrate how the dynamic DARS can be used for forecasting porosity reduction as a function of production rate.

In Louisiana, it has been documented that hydrocarbon production might have some impacts on surface subsidence that lead to massive wetland loss in the coastal area. Utilizing both the static and dynamic DARS formalisms, I examine the impact of reservoir compaction on surface subsidence and its potential to trigger slip on nearby faults. Applying both analytical and numerical modeling, I demonstrate how production in the Lapeyrouse field in southern coastal Louisiana may have induced some of the observed local subsidence. I also investigate the potential influence of reservoir compaction on reactivation of the nearby Golden Meadow Fault.

Finally, stress estimation is extremely important to geomechanical modeling. While hydrofractures, minifractures and leak-off tests can provide accurate estimates of *in situ* stress, these tests can result in significant damage to the formation. An alternative stress estimation method has been proposed by Schlumberger based on acoustic velocity dispersion data gathered from Dipole Sonic Imager logs. I construct a forward model based on the Kirsch equation to examine the sensitivity and applicability of this method for stress estimation around a vertical borehole.

Acknowledgements

It has been slightly more than five years since I stepped foot on the Stanford Campus as a prospective student. Good times fly by like lightening and now I am ready to begin a new chapter in my life. Looking back down memory lane, there are a few people I need to thank who have helped me through this stressful but exciting time.

I would like to thank my advisor, Mark Zoback, who has been very patient with me throughout all these years. His enthusiasm, cheerfulness and excitement towards some of my tiniest accomplishments always amused me. His thoughtful advice has saved me from stepping onto the wrong path. Due to his guidance, I have learned the essentials of how to be a successful researcher and speaker. Although demanding at times, Mark has been great in reminding me to enjoy life outside my little cubicle. He has made my time here at Stanford both challenging and rewarding. My committee, Margot Gerritsen, Gary Mavko and Amos Nur, have also been extremely helpful in reviewing my work throughout the past few years. Their criticisms have lead to countless extensions for all my work, ensuring I have considered all alternatives.

I would also like to thank Bob Morton from the USGS who introduced the hypothesis of the potential linkage of hydrocarbon production and Louisiana wetland loss to me. He opened my eyes to investigating a complicated problem through different perspectives. He also provided financial support for this project and has constantly given me suggestions on my modeling and interpretation.

To successfully complete this project, I also want to acknowledge all the help and support from Stephen Willson, Frank Mitchum and George Fenati from BP who provided their production data, rock samples and other background information that enabled me to explore and perfect the techniques I developed throughout my research.

Special thanks to Richard Sears, Alan Cohen, Matthias Hartung, Peter Schutjens, Andrey Bakulin, Matt Hauser and Gustavo Ugueto from Shell who have given me support, advice and encouragement during my three months as an intern in New Orleans. Thanks to Nona and Phyllis who constantly gave me their helping hands and treated me like their own kid, ensuring I have a wonderful time in the Big Easy.

The encouragement and support from Paul Hagin cannot be forgotten either. He has been a great friend and mentor for me. His vast knowledge in viscoplasticity and laboratory skills has guided me through all the chaotic times I experienced when dealing with soft sediments. He has spent countless hours helping me run experiments, and I really appreciate all the fruitful discussions we had on the applicability of our studies. I would also like to express gratitude to Aitokhuehi who helped me set up a flow simulator in short notice and Tricia Fiore who taught me how to use Poly3D and GoCAD. Daniel Ashford from the Louisiana Department of Natural Resources helped me tremendously by pointing me to the right place for all the information I needed for the Lapeyrouse field. And of course, many thanks to Naomi Boness and Ellen Mallman who painstakingly read through all my manuscripts from the very first draft to the final product. Also would like to thank Jeannette, Susan, Margaret, Laruen, Dianne, Kimberley, Lourdes, Felicia and all the staff from the Department and the Dean's office, all the help you have given me made the last few years less stressful for me.

Aside from my research, I have met many great friends here at Stanford who made my stay enjoyable. Especially Lourdes and Naomi who not only are great office mates, but you two have been my best audience through good and bad times. Thanks to Stephen, Daniel, James, Justin, Kamini, Hannah, John, Amie, Amy, and many more who have the special power to keep me from going back to my desk and work! I am also blessed with special friends from volleyball: Dan, Matt, Rich, Balta, Ansel, Denise, Will, Ray, Edwin, Guille, Tom, Dawn, Greg, Bryan, Johnny, Jet, and many more. You all have helped me rediscover my volleyball touch and sure have given me excuses not to go to work in the evenings and/or the weekends. Also would like to thank all my friends and mentors in Hong Kong and Toronto, especially Junny and Bill Morris, you two have put in some big investment in me even before I considered applying to Stanford.

I would like to give special thanks to Michael who has been supportive throughout the last few years. Especially thank you for reminding me to eat, to sleep and to smile regardless of how stressed I am. Your encouragement has helped me ease through some of the toughest times I have faced.

Last but not least, all the courage and love from my parents, my brother and my god family have made me believe in achieving my childhood dream.

Table of Contents

List of Illustrations

CHAPTER 1

Production-Induced Reservoir Compaction, Permeability Loss and Land Surface Subsidence: An Introduction

1.1 INTRODUCTION

In unconsolidated or poorly consolidated reservoirs, deformation associated with hydrocarbon production can lead to reservoir compaction, land surface subsidence and potentially fault reactivation. In the United States, surface subsidence has been reported in at least 37 out of 50 states affecting an area of more than 80,000km^2 (Johnson, 1998). With 40% of the United States coastal wetland located in Louisiana, the Louisiana Coastal Wetlands Conservation and Restoration Task Force and the Wetlands Conservation and Restoration Authority reported in 1998 that land loss in the Louisiana Coastal Zone since the 1930's has account for 80% of the total coastal land loss in the United States. It is anticipated this can cost up to $37B in the next 50years if the wetland loss remains at the current rate. Wetland loss is a complex interaction between human activities and natural processes; a slight change in elevation can affect a much larger area of wetland. Several mechanisms have been proposed for the submergence of coastal wetland such as deltaic sediment compaction; however, most of these mechanisms cannot explain the sudden increase and localization in wetland loss between the 1960s and 1970s. Morton *et al*. (2002) suggest that some of these land loss hotspots in the Louisiana Coastal Zone are related to oil and gas production due to their proximity to the fields and that the peak land loss rate coincides with the peak production rate. Therefore, it is essential to understand how production-induced reservoir deformation at depth may translate to land surface subsidence and fault reactivation.

For a depleting hydrocarbon reservoir, the decrease in pore pressure as a result of production can have a significant impact on the physical properties of the formation. Deformations commonly observed in producing reservoirs include compaction, fault reactivations and surface subsidence. Understanding the deformation mechanisms associated with these changes will have important implications for many aspects of oilfield development from exploitation schemes to environmental management.

While it is well known that fluid injection can induce faulting in oil and gas reservoirs, several studies have reported that both fluid withdrawal and fluid injection appear to have induced active faulting (see review by Grasso, 1992). When a reservoir is depleting, the reduction in pore pressure within the formation will result in an

instantaneous change in the horizontal stresses acting on the reservoir. These changes in stresses will affect the producing formation in terms of compaction and potentially induce faulting (Zoback *et al*., 2001). Slip on active faults appears to be the cause of sheared casings within production wells in some fields (Maury *et al*., 1992) and, in others, shear slip on pre-existing faults and bedding planes appears to be a serious source of wellbore instability during drilling (e.g., Willson *et al*., 1998). Critically stressed faults in many low permeability reservoirs (i.e., faults that are active in the present stress field) contribute significantly to the overall reservoir permeability (Finkbeiner *et al*., 1998; Dohlakia *et al*., 1998). Meanwhile, re-activation of reservoir bounding faults can cause a loss of seal capacity and leakage to occur (e.g., Wiprut & Zoback, 1999). Slip on active faults may also control the vertical extent of the hydrocarbon column that a fault-bounded reservoir can contain (e.g., Finkbeiner *et al*., 2001). As a result, a better knowledge of the physical properties of the formation and how they will be affected by the exploitation scheme is needed to minimize the damages associated with production.

There are three main goals in this thesis: 1) to understand the mechanism of production induced porosity loss and reservoir compaction in weak sand reservoirs; 2) to investigate how the change in porosity will affect permeability and reservoir productivity; and 3) to examine the impact of oil and gas production on land surface subsidence as a result of reservoir compaction and fault reactivation with particular interest in the Louisiana Coastal Zone.

1.2 STRUCTURE OF THIS THESIS

To address the problems associated with oil and gas production, I have divided this thesis into six chapters. This first chapter is a general overview of deformation associated with hydrocarbon production. Chapters 2, 3 and 4 will introduce a formalism that combines laboratory experiments with *in situ* stress measurements in order to efficiently estimate the potential of production-induced normal faulting, the degree of reservoir compaction and their implications for the permeability and productivity of the reservoir. Chapter 5 will address the impacts of oil and gas production in the Louisiana Coastal Zone on wetland loss. The final chapter is part of a project conducted during my

internship at Shell International Exploration and Production (SIEP) in Fall 2003. The following sections are general outlines of the issues discussed in Chapter 2 to Chapter 6.

1.2.1 Deformation Analysis in Reservoir Space (DARS): Predicting Reservoir Compaction and Induced-Normal Faulting in Hydrocarbon Reservoirs (Chapter 2)

A formalism known as Deformation Analysis in Reservoir Space (DARS) is introduced in this chapter, which combines simple laboratory rock mechanics experiments and *in situ* stress measurements in a depleting reservoir. Production and laboratory data can be evaluated simultaneously using DARS to study the potential of production-induced faulting and reservoir compaction. For a depleting reservoir initially in a normal faulting stress state (where the vertical stress, S_V, is larger than the two horizontal stresses), the potential of induced normal faulting depends on the empirical depletion stress path, $\boldsymbol{A}$, which defines the change of minimum horizontal stress, ΔS_h, as a function of depletion, ΔP_p. If the depletion stress path exceeds 0.68 (equivalent to the Mohr-Coulomb criterion for normal faulting with coefficient of friction, μ, of 0.6), production-induced normal faulting is prone to occur. Utilizing relatively simple laboratory experiments, end caps associated with shear-enhanced compaction are transformed from laboratory space into reservoir space such that production data can be evaluated directly to study the evolution of the deforming reservoir due to production. In this chapter, I will demonstrate how this formalism can be applied to reservoirs in different geological settings given appropriate laboratory experiments and stress measurements.

1.2.2 Estimating Permeability Changes Associated with Depletion in Weak Sand Reservoirs (Chapter 3)

In this chapter, I will extend the reservoir compaction predicted from DARS to examine its impact on permeability change and reservoir productivity performance. Based on laboratory studies on sands from the Gulf of Mexico, empirical upper and lower bounds of permeability reductions corresponding to porosity reductions are derived. These two empirical relationships constrain 95% of the laboratory results. The lower bound of permeability change agrees with the Kozeny-Carman relationship for extremely

permeable sands. These empirical relations are then used in conjuncture with DARS to examine the effects of production-induced deformation on permeability reduction in a Gulf of Mexico reservoir, Field Z. DARS predicts a 0.7% change in porosity in Field Z and the corresponding permeability changes derived using the empirical relationships are in good agreement with the measured permeability changes in three different wells. While most reservoir simulations assume constant rock properties during depletion, I will demonstrate that applying both production-induced porosity and permeability changes to a simple simulation model can result in significant variations in the predicted reservoir productivity.

1.2.3 Time-Dependent Elastic-Viscoplasticity and the Dynamic DARS (Chapter 4)

Inelastic deformation associated with hydrocarbon production can lead to irrecoverable porosity and permeability loss as discussed in the two previous chapters. In this chapter, I will expand the pressure-dependent but time-independent static DARS introduced in Chapter 2 to a pressure- and time-dependent dynamic DARS to capture the viscous behavior demonstrated by some soft sediment. I extend the elastic-viscoplastic model used by Hagin (2003) for laboratory conditions to incorporate some successive loading history such that the cumulative elastic-viscoplastic strain at any given time can be estimated. Following Hagin's experimental procedure, two new samples from the Gulf of Mexico Field X are examined to determine their elastic-viscoplastic behavior and the necessary Perzyna viscoplastic parameters. I then apply the elastic-viscoplastic rheological model to expand the capability of the static DARS formalism to a dynamic DARS formalism and re-visit the porosity and permeability loss in the Gulf of Mexico Field X. The sensitivity of the laboratory derived constants on the total strain estimation based on the dynamic DARS formalism is also examined.

1.2.4 Louisiana Coastal Wetland Loss: The Role of Hydrocarbon Production (Chapter 5)

In this chapter, I will examine the impact of on-shore oil and gas production on land subsidence in the Louisiana Coastal Zone. There are a lot of factors contributing to the loss of wetland in coastal Louisiana, I will focus on production-induced reservoir

compaction and fault reactivation as they are proposed by several authors as the possible causes of the creation of the land loss hotspots in this region. With limited data available from on-shore oil fields, I will apply the experience developed through offshore fields in the previous chapter to demonstrate how they could apply to an on-shore field. I will use the DARS formalism to estimate the magnitude of reservoir compaction using constitutive law developed in previous chapters. Applying both analytical (the Geertsma Method) and numerical methods (Poly3D), I will demonstrate how the estimated compaction translates into land surface subsidence. I will also examine how compaction might have cause stress changes on a fault in close proximity to the reservoirs. Comparing the predicted elevation change with leveling data, I demonstrate the effects hydrocarbon production will have on land surface subsidence locally.

1.2.5 Variation of Velocity and Anisotropy around a Vertical Borehole and its Potential Application for Stress Estimation from Sonic Logs (Chapter 6)

Stress changes associated with production-induced reservoir compaction affect modeling (and decision-making) in terms of: fracture gradient development; borehole stability and sand production; 4-D seismic; compaction drive and reservoir performance; and induced seismicity. To estimate the change in stresses as a result of depletion (or stress path, $\boldsymbol{A}=\Delta S/\Delta Pp$), analytical models based on poroelasticity have been routinely used. However, Zoback *et al.* (2001) show that while poroelastic theory can be used in some reservoirs, the range of reported stress paths is so wide that they recommended mapping the stress evolution empirically throughout the time scale of production is essential (Chapter 2). While most of the stress measurements are collected empirically through leak-off tests, hydrofractures, minifractures or borehole imagers, these tests are not always readily available or conducted routinely once the wells are put into production. Schlumberger recently proposed a new approach using acoustic shear wave anisotropy from the Dipole Sonic Imaging (DSI) tool to determine both the orientation and magnitude of stress (e.g., Brie *et al*., 1998; Plona *et. al*., 2002; Sinha *et. al*., 2002). Given a set of elastic moduli from the literatures, this chapter will focus on determining the sensitivity and applicability of this new Schlumberger method on acoustic wave velocity and reservoir stress estimation.

1.3 REFERENCE

Brie, A.,Takeshi, E., Hoyle, D., Codazzi, D., Esmersoy, C., Hsu, K., Denoo, S., Mueller, M., Plona, T., Shenoy, R., & Sinha, B., 1998. New directions in sonic logging. *Oilfield Review*, **Spring 1998**, 40-55.

Dholakia, S. K., Aydin, A., Pollard, D., & Zoback, M.D. 1998. Development of fault-controlled hydrocarbon migration pathways in the Monterey formation, California. *AAPG Bulletin*, **82**, 1551-1574.

Finkbeiner, T., Barton, C.A. & Zoback, M.D. 1998. Relationship between in-situ stress, fractures and faults, and fluid flow in the Monterey formation, Santa Maria Basin, California, *AAPG Bull*, **81,** 1975-1999.

Finkbeiner, T., Zoback, M.D., Stump, B. & Flemings, P. 2001. Stress, pore pressure and dynamically-constrained hydrocarbon column heights in the South Eugene Island 330 field, Gulf of Mexico, *AAPG Bulletin*, **85**, 1007-1031.

Grasso, J. R. 1992. Mechanics of seismic instabilities induced by the recovery of hydrocarbons, *Pure and Applied Geophysics*, **139**, 507-533.

Hagin, P.N., 2003. *Application of Viscoelastic, Viscoplastic, and Rate-and-State Friction Constitutive Laws to the Deformation of Unconsolidated Sands*. Unpublished Ph.D. Thesis, Stanford University, 126pp.

Johnson, A.I., 1998. Land subsidence due to fluid withdrawal in the United States – an overview. In: *Borchers, J.W. (eds.), Land Subsidence: Case Studies and Current Research. AEG Special Publication No. 8*, 51-57.

Maury, V. M. R., Grasso, J. R. & Wittlinger, G. 1992. Monitoring of subsidence and induced seismicity in the Larq gas field (France): the consequences on gas production and field operation. *Engineering Geology*, **32**, 123.

Morton, R.A., Buster, N.A., & Krohn, M.D., 2002. Subsurface controls on historical subsidence rates and associated wetland loss in Southcentral Louisiana. *Gulf Coast Association of Geological Societies Transactions*, **52**, 767-778.

Plona, T.J., Kane, M.R., Sinha, B., & Walsh, J., 2002. Evaluating stress-induced anisotropy and mechanical damage from cross-dipole sonic data using dispersion analysis. SPE/ISRM 78233. SPE/ISRM Rock Mechanics conference, Irving, Texas, 20-23 October 2002.

Sinha, B.K., Kane, M.R., & Borland, W.H., 2002. Analyses of sonic data in an Indonesian well for formation damage, stresses and bedding. SPE/ISRM 78232. SPE/ISRM Rock Mechanics conference, Irving, Texas, 20-23 October 2002.

Willson, S., Last, N. C., Zoback, M. D. & Moos, D. 1998. Drilling in South America: A wellbore stability approach for complex geologic conditions. *SPE 53940, 1999 SPE*

Latin American and Caribbean Petroleum Engineering Conference, Caracas, Venezuela 21-23 April, 1999.

Wiprut, D. & Zoback, M. D. 1999. Fault reactivation and fluid flow along a previously dormant normal fault in the Norwegian North Sea. *Geology*, **28**, 595-598.

Zoback, M.D., Chan, A.W. & Zinke, J., Production-induced normal faulting. Proceedings of the 38th US Rock Mechanics Symposium, DC Rocks 2001, Washington D.C., 7-10 July 2001, 157-163

CHAPTER 2

Deformation Analysis In Reservoir Space (DARS): Predicting Reservoir Compaction and Induced-Normal Faulting In Hydrocarbon Reservoirs

2.1 ABSTRACT

A formalism known as Deformation Analysis in Reservoir Space (DARS) is introduced, which combines simple laboratory rock mechanics experiments and *in situ* stress measurements in a depleting reservoir. Production and laboratory data can be evaluated simultaneously using DARS to study the potential of production-induced faulting and reservoir compaction. For a depleting reservoir initially in a normal faulting stress state (where the vertical stress, S_V, is larger than the two horizontal stresses), the potential of induced normal faulting depends on the empirical depletion stress path, $\boldsymbol{A}$, which defines the change of minimum horizontal stress, ΔS_h, as a function of depletion, ΔP_p. If the depletion stress path exceeds 0.68 (equivalent to the Mohr-Coulomb criterion for normal faulting with coefficient of friction, μ, of 0.6), production-induced normal faulting is prone to occur. Utilizing relatively simple laboratory experiments, end caps associated with shear enhanced compaction are transformed from laboratory space into reservoir space such that production data can be evaluated directly to study the evolution of the deforming reservoir due to production. Two case studies (Valhall field in the North Sea and Field X in the Gulf of Mexico) are presented to illustrate the impact of production on reservoir deformation using the DARS formalism. In the Valhall fields where $\boldsymbol{A}$ for the flank is greater than 0.68, production–induced normal faulting will be an important mode of deformation accompanied by some degree of compaction (a reduction from 41% to 40%). In contrast, the depletion stress path from Field X is less than 0.68 implying that production-induced normal faulting is not likely to occur and deformation is dominated by compaction (from 30.8% to 29.4%).

2.2 INTRODUCTION

The deformation of a reservoir in response to hydrocarbon production is important to understand for a variety of reasons. Slip on faults, as a result of a change in the *in situ* stress state, can pose serious problems in the field since it may cause casing failure (Maury *et al*., 1992) or a loss of sealing capacity of the reservoir bounding faults (e.g., Wiprut & Zoback, 1999). Compaction associated with production will affect the rock

properties of the formation, such as compressibility and permeability, and can significantly affect the results of reservoir simulation if neglected (Chapter 3). Subsurface fluid withdrawal can also result in significant land surface subsidence (e.g., Poland *et al*., 1975; Pratt & Johnson, 1926). Therefore, it is desirable to predict quantitatively the degree of compaction that accompanies depletion as well as the degree of permeability loss and, in some cases, the possibility of induced faulting or fault reactivation. While most existing models describing deformation associated with depletion are based on poroelastic theory, the heterogeneity of the reservoir and the inelastic nature of the formation are often ignored. The inelastic properties of the reservoir are especially important for poorly consolidated rock since such formations behave differently than their well-cemented counterpart. To fully understand the nature of deformation associated with production, a detailed study that includes both laboratory rock mechanic experiments and *in situ* reservoir conditions are required.

A formalism referred to as Deformation Analysis in Reservoir Space (DARS) is introduced to integrate simple laboratory tests with the physical state of a reservoir and its evolution through time. One of the advantages of using DARS is its versatility and applicability to different reservoirs. This is achieved because the formalism quantitatively "maps", through time, the nature of the deformation observed during laboratory experiments into the parametric space that defines the mechanical state of a reservoir (the *in situ* principal stresses and pore pressure), hence allowing a direct estimation of the degree of compaction and the potential of fault reactivation through depletion. Because depletion can cause substantial increases in the effective compressive stresses acting on the reservoir, it can induce marked reductions in porosity and permeability. For weak sand reservoirs, the reduction of porosity may be caused by both elastic and inelastic deformations. The amount of compaction can be estimated by DARS if appropriate laboratory experiments are used.

In the sections below, I will present the theoretical framework and the construction of this DARS formalism. Two case studies, Valhall Field in the North Sea and Field X in the Gulf of Mexico, are then presented to illustrate quantitatively how depletion may have caused induced faulting and compaction in these fields.

2.3 DEPLETION STRESS PATH

Depletion stress path, ***A***, is defined as the change in horizontal stress, ΔS_h, in response to the change in pore pressure, ΔP_P, due to depletion. The depletion stress path any given the producing reservoir will follow is extremely important because it dictates the nature of reservoir deformation, from the degree of compaction to the potential of fault slip. Stress paths can be determined theoretically by poroelasticity or quantitatively by empirical measurements of *in situ* stresses throughout production time.

Based on poroelastic theory, for an isotropic, porous and elastic reservoir that is laterally extensive with respect to its thickness (i.e., length to height ratio of at least 20:1), Segall & Fitzgerald (1996) show that the theoretical stress path is:

$$\left(\frac{\Delta S_h}{\Delta P_p}\right) = \alpha \frac{(1-2\nu)}{(1-\nu)} \quad \text{and} \quad \Delta S_V = 0 \qquad (2.1)$$

where ν is Poisson's ratio and α is the Biot coefficient, $\alpha = 1 - K_b/K_g$, where K_b is the bulk modulus of the bulk rock and K_g is the bulk modulus of the mineral grains. The vertical stress, S_V, is unchanged for this laterally extensive reservoir because the weight of the overburden is assumed to be constant during depletion. Figure 2.1 demonstrates the theoretical value of depletion stress paths, based on Equation (2.1), as a function of Biot coefficient and Poisson's ratio. Published data on minimum horizontal stress changes with depletion are very limited; the field names on the right hand side of Figure 2.1 are some published stress paths. Note that some of these reported values are not directly related to depletion, but rather a combination of all stress-pressure measurements in the field (indicated with *italics*). Among the selected fields listed in Figure 2.1, the range of depletion stress path is quite large (from 0.48 to 1).

In order to explain the high stress path for some reservoirs, e.g., Valhall flank, an unusually low ν and high α are required. In other words, poroelastic theory may not be suitable to explain or predict reservoir depletion behavior universally. One possible reason for the shortcoming of poroelastic theory is that some depleting reservoirs undergo both elastic and inelastic deformation. As shown in the following sections, the depletion stress path is an important factor in understanding the potential of production-induced

faulting. As a result, the theoretical assumption explained above for determining a reservoir's depletion stress path is not recommended.

Alternatively, it is possible to measure the evolution of the minimum horizontal stress, S_{hmin} or S_3, through depletion. The magnitude of S_{hmin} can be determined from leak-off tests (LOTs), hydrofractures or minifractures. Measuring S_{hmin} as depletion occurs is preferred because it documents the evolution of stress empirically and defines a more accurate depletion stress path that can be used for assessing the potential of production-induced fault reactivations and the magnitude of compaction.

2.4 PRODUCTION-INDUCED NORMAL FAULTING

In a normal faulting stress environment where the vertical stress is larger than the maximum and minimum horizontal stresses, S_{Hmax} and S_{hmin}, the reduction of S_{hmin} and P_P can induce normal faulting within a reservoir if the depletion stress path exceeds a critical value (Zoback & Zinke, 2002). This critical value can be calculated based on the Coulomb failure condition for normal faulting (after Jaeger & Cook, 1971):

$$\frac{\left(S_V - P_p\right)}{\left(S_{h\min} - P_p\right)} = \left(\sqrt{\mu^2 + 1} + \mu^2\right)^2 = f(\mu) \quad \text{.....(2.2)}$$

Modifying Equation (2.2) for depletion yields:

$$\frac{\left[S_V - \left(P_P - \Delta P_P\right)\right]}{\left[\left(S_{h\min} - \Delta S_{h\min}\right) - \left(P_P - \Delta P_p\right)\right]} = f(\mu) \quad \text{.....(2.3)}$$

Simplifying Equation (2.3) results in:

$$S_V - P_P = \left[\left(S_{h\min} - P_P\right) - \left(\Delta S_{h\min} - \Delta P_P\right)\right] f(\mu) - \Delta P_P$$

$$\frac{S_V - P_P}{S_{h\min} - P_P} = \left[1 - \frac{\Delta S_{h\min} - \Delta P_P}{S_{h\min} - P_P}\right] f(\mu) - \frac{\Delta P_P}{S_{h\min} - P_P} \quad \text{.....(2.3.a)}$$

Notice the left hand side of Equation (2.3.a) is equivalent to $f(\mu)$, therefore,

$$f(\mu) = f(\mu) - \frac{\Delta S_{h\min} - \Delta P_P}{S_{h\min} - P_P} f(\mu) - \frac{\Delta P_P}{S_{h\min} - P_P}$$

$$\frac{\Delta S_{h\min} - \Delta P_P}{S_{h\min} - P_P} f(\mu) = -\frac{\Delta P_P}{S_{h\min} - P_P}$$

$$\frac{\Delta S_{h\min} - \Delta P_P}{\Delta P_P} = -\frac{1}{f(\mu)} \quad \text{.....(2.3.b)}$$

Substituting $A = \Delta S_{h\min} / \Delta P_P$ to Equation (2.3.b) yields

$$A = 1 - \frac{1}{\left(\sqrt{\mu^2 + 1} + \mu\right)^2} \quad \text{.....(2.4)}$$

For μ = 0.6, the theoretical stress path corresponding to normal faulting will be roughly equal to 0.68. I use a coefficient of friction of μ = 0.6, which is frequently measured in the laboratory for a wide variety of rocks (Byerlee, 1978) and confirmed by *in situ* stress measurements (c.f. Zoback & Healy, 1984; Townend & Zoback, 2000).

Following Zoback & Zinke, the evolution of stress and pore pressure for a depleting reservoir with a steep stress path (from I to 2 in Fig. 2.2) can induce normal faulting. The initial stress state in the formation is not close to shear failure. However, as pore pressure and stress decrease with production, the changes in the effective stress are such that a stress state with normal faulting could potentially be reached. In fact, anytime ***A*** is larger than the slope of the normal faulting line (~ 0.68), the stress path will eventually intersect the normal faulting failure line (such depletion stress paths are defined as 'unstable stress paths'). With subsequent decreases in pore pressure, the least principal stress must decrease along this line because it cannot decrease more rapidly without exceeding the frictional strength of the reservoir rocks. In contrast, if ***A*** is smaller than 0.68 (Fig. 2.2), the potential of production-induced normal faulting decreases with production (such depletion stress paths are defined as 'stable stress paths'). As a result, determining the empirical value of ***A*** relative to the theoretical normal faulting line (***A*** = 0.67) can be used as a tool to evaluate the potential of production-induced normal faulting even if significant inelastic deformations occur during depletion. The gray area in Figure 2.1 indicates the theoretical combination of α and ν required for the occurrence of production-induced normal faulting. However, if *in situ* stress measurements are

available through depletion, it is possible to assess the risk of induced faulting without prior knowledge on poroelastic constants measured in the laboratory.

I only considered reservoirs from normal faulting stress environments due to its simplicity. For reservoirs in the strike-slip stress environment (i.e., $S_{Hmax} > S_V > S_{hmin}$), depletion might potentially lead the reservoir into the normal faulting stress environment (or in some extreme cases, induced-normal faulting) because both S_{Hmax} and S_{hmin} will decrease during production while S_V remains constant. Prediction for production-induced faulting is impractical for reservoirs in the reverse faulting stress environment (i.e., $S_{Hmax} > S_{hmin} > S_V$) because the magnitude of the horizontal stresses are not readily measurable (fracture tests can only measured the magnitude of the minimum stress, i.e., S_V in the reverse faulting stress environment).

2.5 SHEAR-ENHANCED COMPACTION AND "END CAP" FAILURE

When reservoir rock is subjected to compressive loading, the formation materials will pass through progressive states of deformation once the *in situ* stress is increased beyond the material's failure limit. This limit is a quantitative parameter that can be obtained from laboratory experiments. For example, in hydrostatic compression tests, it is straightforward to measure porosity loss with confining pressure or in triaxial tests, the compressive or frictional strength of a given sample. However, in actual reservoirs (i.e., in 'reservoir space'), the *in situ* stress state is anisotropic and it is not always clear how to translate laboratory-derived deformation tests into a prediction of a mechanical response of the formation.

As reservoir depletion occurs, decreases in pore pressure, as a result of production, will increase the effective stresses within the reservoir. Once these increasing effective stresses reach the mechanical failure limit (or the preconsolidation pressure), plastic deformation such as compaction and grain rearrangement (and eventually grain crushing and pore collapse) occur resulting in an irrecoverable loss in porosity. To represent this ductile yielding behavior of rocks, yield caps (or end caps) are used. End caps are determined by laboratory experiments and are commonly represented in the p:q space (referred to as laboratory space in this thesis) where p is the mean stress and q is the

deviatoric stress. End caps represent the locus of points with the same volumetric plastic strain (Desai & Siriwardane, 1984) and their shape depends on the material properties and the failure criterion model chosen. During laboratory experiments, the changes in the hardening behavior of the rock sample results in a change in size of the end cap. As the rock hardens, the size of the end cap increases. The end caps in Figure 2.3a mark the boundary between the elastic and plastic deformation domains. These end caps represent the limit at which no inelastic compaction will occur if stress applied to the sample is within the end cap. However, if the sample is stressed beyond the end cap, inelastic deformation will occur and the sample will compact and become stronger. The "hardening" of the sample leads to an expansion of the end cap associated with the decrease in porosity. Mathematically, the three principal stresses and the p-q space are related as follows:

$$p = \frac{1}{3} J_1 = \frac{1}{3}(\sigma_1 + \sigma_2 + \sigma_3) = \frac{1}{3}(S_V + S_{H\max} + S_{h\min}) - P_P \quad \text{.....(2.3)}$$

$$q = \sqrt{3J_{2D}} \Rightarrow q^2 = \frac{1}{2}\left[(S_V - S_{H\max})^2 + (S_{H\max} - S_{h\min})^2 + (S_V - S_{h\min})^2\right] \text{....(2.4)}$$

where P_P is the pore pressure and $\sigma = S - P_P$ is the effective stress. J_1 and J_{2D} are the first and second invariants of the stress deviation tensors respectively. The equation of the yield loci shown in Figure 2.3a is derived based on the simple Cam Clay model as given by Desai & Siriwardane (1984):

$$M^2 p^2 - M^2 p^* p + q^2 = 0 \quad \text{.....(2.5)}$$

where M is known as the critical state line and can be expressed as $M=q/p$. The critical state line is also known in cap models as the fixed end cap surface that mark the critical state of stress at which shear failure will occur (Fig. 2.3a).

The intersection of the yielding locus and the p-axis is defined as p*, or the preconsolidation pressure, and each end cap has its own unique p* that defines the hardening behavior of the rock sample. The value of p* and the associated rock properties, e.g., porosity, can easily be determined from a uniaxial laboratory experiment. The Cam-Clay model is then used for transforming the uniaxial experiment to the p:q space.

2.6 DEFORMATION ANALYSIS IN RESERVOIR SPACE (DARS)

The principle idea of DARS is to bridge simple laboratory compaction measurements with *in situ* stress measurements to predict reservoir deformation associated with depletion. While the end caps model described in the previous section is widely used in engineering and laboratory experiments, it is obvious that the changes in p and q through time may not be readily applicable to a producing reservoir or during day-to-day operations. *In situ* stress measurements conducted in reservoirs involve the three principal stresses and pore pressure instead of p and q. As a result, transforming the end caps from the laboratory p:q space into the principle stresses-pore pressure space is needed. Combining and rearranging Equation (2.3) to (2.5) as a function of the three principle stresses and pore pressure (i.e., S_{Hmax}, S_{hmin}, S_V, P_P, p* and *M*) results in:

$$9P_P^{\,2}+\left(1+\frac{9}{M^2}\right)\left(S_V^{\,2}+S_{H\max}^{\,2}+S_{h\min}^{\,2}\right)+\left(2-\frac{9}{M^2}\right)\left(S_V S_{H\max}+S_V S_{h\min}+S_{H\max}S_{h\min}\right)$$

$$+9P_P p^*-3\left(2P_P+p^*\right)\left(S_V+S_{H\max}+S_{h\min}\right)=0 \quad \text{.....(2.6)}$$

Based on the Mohr-Coulomb failure criterion, the variable *M* can be expressed as a function of the coefficient of friction, μ. The failure criterion relates μ, the shear stress, τ, and normal stress, σ_n, acting on a pre-existing faults such that:

$$|\tau| = C_0 + \mu\sigma_n \quad \text{..... (2.7)}$$

where C_0 is the cohesion. The magnitude of shear and normal stress acting on the fault plane are related to the far field maximum and minimum compressive stresses such that:

$$\begin{cases} \sigma_n = \frac{1}{2}(\sigma_1+\sigma_3)+\frac{1}{2}(\sigma_1-\sigma_3)\cos 2\beta \\ |\tau| = \frac{1}{2}(\sigma_1-\sigma_3)\sin 2\beta \end{cases} \quad \text{.....(2.8)}$$

where β is the angle between the maximum compressive stress, σ_1, and the fault plane. sin2β and cos2β can be expressed in terms of μ (Jaeger and Cook, 1971) as

$$\sin 2\beta = \left(\mu^2+1\right)^{-½} \quad \text{and} \quad \cos 2\beta = -\mu\left(\mu^2+1\right)^{-½} \quad \text{.....(2.9)}$$

By combining Equations (2.7-2.9) and assuming the cohesion C_0 is negligible, *M* can be defined in terms of μ as:

$$M = \frac{6\mu}{3\sqrt{\mu^2 + 1} - \mu} \quad \text{.....(2.10)}$$

For μ=0.6, *M* is roughly equal to 1.24.

The three principal stresses and pressure are measured under *in situ* conditions in wellbores penetrating the reservoir of interest. Rearranging Equation (2.6) yields a relationship between the *in situ* reservoir stress measurements and the preconsolidation pressure used in the laboratory:

$$p^* = \frac{1}{3(S_V + S_H + S_h) - 9P_P}\left\{9P_P{}^2 + \left(1 + \frac{9}{M^2}\right)\left(S_V{}^2 + S_H{}^2 + S_h{}^2\right) + \left(2 - \frac{9}{M^2}\right)\left(S_V S_H + S_V S_h + S_H S_h\right) - 6P_P\left(S_V + S_H + S_h\right)\right\} \quad \text{.....(2.11)}$$

Rock properties measured in the laboratory associated with any p* (e.g., porosity) can then be transformed into the reservoir domain of *in situ* stress and pore pressure. S_V remains constant with depletion for a laterally extensive reservoir so the two dimensional end caps in p:q space may be transformed into three dimensional end cap ellipsoids in the reservoir domain ($S_{Hmax,}$ S_{hmin} and P_P).

Thus, by combining the shear (Coulomb) failure envelope with the transformed end-cap ellipsoids and projecting the ellipsoids onto the S_{hmin}:P_P domain, a new composite diagram is created for analyzing the degree of shear and compaction deformations that are associated with reservoir depletion (Fig. 2.3b). The evolution of the end caps of any given reservoir rock at different porosities can now be used as an indicator of the deformation induced by the increase of the effective stresses due to the decrease in pore pressure during production.

For a producing reservoir, the value of the vertical stress can be easily derived from density logs while *M* and p* can be determined from relatively simple laboratory experiments. For simplicity, we will limit ourselves to normal faulting regions where S_{hmin} is the least principal stress, which can be obtained from LOTs and minifractures,

and the initial S_{Hmax} is somewhere between S_{hmin} and S_V. The impact of the selection of μ and S_{Hmax} will be discussed later in this chapter.

The three depletion stress paths on Fig. 2.3b represent hypothetical paths a reservoir may experience during depletion. Stress path 1 represents a relatively low $\Delta S_{hmin}/\Delta P_P$ ratio. If the reservoir is depleted along this path, shear faulting is unlikely to occur, but shear-enhanced compaction will take place and be the dominant mechanism of reservoir deformation with a change in porosity from 40% to 34%. However, if the stress path of the reservoir is much steeper (stress path 2), the stress state in the reservoir will eventually hit the shear failure line and both compaction and normal faulting will be initiated (see discussions below). If depletion continues, the stress state in the reservoir will be controlled by the frictional strength resulting in stress path 3 on Figure 2.3b.

In summary, there are three essential steps to construct the DARS formalism:

1) The initial stress state and pore pressure in the reservoir must be measured.
2) The reservoir depletion stress path must be estimated, either using poroelastic theory or empirical observations.
3) Laboratory measurements of porosity reduction (or other physical properties) as a function of pressures are needed. If only hydrostatic experiments are available, the theoretical plasticity model can be utilized to extrapolate these data into p:q space and then into reservoir space. A Cam-Clay model is used in this study because of its simplicity. These laboratory end caps are then transformed into the reservoir space (i.e., S_{hmin} : P_P domain).

2.7 CASE STUDIES

A chalk reservoir in the North Sea, Valhall Field, along with a turbudite sand reservoir in the Gulf of Mexico, Field X, are presented to illustrate the construction of DARS for predicting porosity change and the potential of induced normal faulting as a result of hydrocarbon production.

2.7.1 Valhall

Located in the North Sea, the reservoir of the Valhall field consists of two late Cretaceous oil-bearing formations: the Tor formation and the underlying Hod formation that are overlain by Paleocene and Eocene age shale cap rock. Both formations are soft chalk facies with a primary porosity that varies between 36% and 50%. The preservation of such high porosity is primarily due to formation overpressure inhibiting mechanical compaction of the chalk. Data is available from October 1982 when the field went into production.

The data available from Valhall to constrain the magnitude of the least principal stress include conventional well logs, LOTs and minifractures. Drill-stem tests (DSTs) and remote formation tests (RFTs) are available to constrain pore pressure.

A very detailed evolution of S_{hmin} and P_P during depletion in Valhall is reported in Zoback *et al*. (2001) and Zoback & Zinke (2002); these measurements provide an excellent opportunity to observe the changes in deformation mode during depletion of this reservoir.

Detailed laboratory experiments based on rock samples from the Valhall field are not available for this study. However, published data from the nearby Ekofisk field is used in this DARS analysis of Valhall since the two fields are remarkably similar.

Figure 2.4 demonstrates how DARS transforms the laboratory measurements of porosity reduction into reservoir spaces. Figure 2.4a is semi-log plot of porosity versus confining pressure in the laboratory, along with the best-fit curves assuming an exponential porosity decrease with increasing confining pressure. The best-fit curves in Figure 2.4a are then mapped into reservoir space using the method discussed above to generate the composite diagram in Figure 2.4b that represents the predicted porosity based on initial reservoir conditions. Since the magnitude of S_{Hmax} is not known, it is assumed to be equal to the average of S_V and S_{hmin} in this normal faulting stress environment where S_{Hmax} is the intermediate principal stress.

As discussed by Zoback *et al.* (2001) and Zoback & Zinke (2002), the crest of the reservoir anticline was in a normal faulting stress state under initial, undepleted conditions. As depletion occurred, the crest remained in a normal faulting stress state even though pore pressure was decreasing with time. Thus, in the crest of the anticlinal

structure, active normal faulting was the natural state and as production occurred, the stress path was such that normal faulting continued. It is expected that both horizontal stresses were affected more or less equally by depletion. While we have no direct estimates of S_{Hmax} magnitudes at Valhall, a variety of techniques indicate little difference between the two horizontal stresses (Kristiansen, 1998). *In situ* measurements on Figure 2.4b also demonstrate that stress magnitudes on the flanks of the Valhall structure were initially appreciably higher than on the crest. However, despite the nearly isotropic initial stress state at the flank, the high stress path ($\boldsymbol{A} \approx 0.92$) accompanying production on the flanks of the reservoir is such that once depletion had reduced pore pressure to about 30 MPa, a normal faulting stress state is encountered. Thus, depletion appears to have induced normal faulting on the flanks of the reservoir. As normal faulting had already been occurring on the crest, it appears that normal faulting has spread outward from the crest of the structure onto the flanks as production and depletion have taken place.

Based on the initial reservoir conditions and the limited laboratory studies, DARS predicts that the porosity of the Tor formation at the crest was reduced from approximately 41% to 35%. While in the flank, the porosity reduction is from 41% to 40%.

2.7.2 Gulf Of Mexico Field X

Gulf of Mexico Field X is located on the continental shelf of the Gulf Coast basin off the Texas coast. It is one of the several fields along the Lower Miocene normal growth fault trend. The reservoir is bounded by major growth faults, and the reservoir is a rolled-over anticline with sand expansion as a result of the growth fault and thinning from the crest to the anticline. The sand is deltaic and has a porosity ranging from 18% to 33%. The discovery well was drilled in 1980 and the field went into production in 1985 with an initial gas column of over 220 m and an initial pressure of about 78 MPa.

As in the case of Valhall, minifractures and LOT data were provided to constrain the magnitude of S_{hmin} while DSTs and RFTs are available to constrain pore pressure.

I compiled and corrected the pore pressure and minimum horizontal stress measurements from most wells in the regions to a datum and a continuous decrease in P_P with time is observed (Fig. 2.5). This continuous trend suggests that sub-compartments

are unlikely to exist in Field X between these wells. The evolution of S_{hmin} and P_P is presented in Figure 2.6. No information about the initial stress condition is available; I therefore project the empirical stress path back to the original pore pressure and estimate the approximate magnitude of S_{hmin} at initial pore pressure. Notice that the empirical stress path in Field X ($\boldsymbol{A_{Field\ X}}$ = 0.55) is smaller than the normal faulting line (i.e., a stable stress path indicating that production seems to stabilize the reservoir from production-induced normal faulting.

Two laboratory reports from experiments on core from Field X on porosity changes as a result of increasing confining pressure are available. The results of the seven samples tested in these two studies are presented in Figure 2.7a. Initial porosities of these samples varied from 22% to 32%. Note that the 3 samples marked 'low-porosity samples' in Figure 2.7a are not loaded beyond 50MPa. This is because of the first set of tests, marked 'high porosity samples' in Figure 2.7a, which the samples experienced an abrupt loss in porosity when loaded beyond 50MPa. When examining the depth at which these samples were collected, the pressure where the abrupt porosity lost occurs is very close to the preconsolidation pressure the samples might have experienced. The preconsolidation pressure is the maximum theoretical pressure a sample could have experienced and is estimated assuming the sediments are buried under hydrostatic pressure (i.e., for the seven samples tested, the preconsolidation pressure is about 48MPa). Therefore, I assume the drastic change in porosity might be related to the preconsolidation pressure. In other words, the samples are compacting along the reloading path until they reach the preconsolidation pressure where they will compact following the virgin compaction curve.

Although there is a large variation in the initial porosities of these samples, their compaction behaviors are comparable. Figure 2.7b normalized the change in porosity of these samples with confining pressures. It appears that the compaction trends of the seven samples are quite similar regardless of their initial porosity. The solid green line represents the best-fit curve based on these laboratory test results from 0 to 48 MPa. The red line is generated based on a study by Hagin (*personal communications*) using the method described in Hagin (2003) and Hagin & Zoback (2004a, b). Using two new

samples from Field X, Hagin suggested that the instantaneous elastic strain for these two samples could be summarized by a power law such that:

$$\varepsilon_e = 0.01 p^{0.51} \quad \text{.....(2.12)}$$

where ε_e is the instantaneous elastic strain and p is the pressure. Equation 2.12 will be referred as the empirical Field X elastic rheology (or the Hagin's elastic curve). Hagin also investigated the inelastic deformation of these samples and other soft sediments and his results and findings will be discussed in greater detail in Chapter 4.

The blue curve on Figure 2.7b is the generalized compaction curve defined by Yale *et al.* (1993) for Gulf of Mexico sands (or the Yale's curve):

$$C_f = A\left(\sigma_{lab} - B\right)^C + D \quad \text{.....(2.13)}$$

where C_f is the formation compressibility and σ_{lab} is the laboratory stress. A, B, C and D are constants derived from laboratory experiments and, in the case of poorly sorted unconsolidated, they have the values of –2.805e-5, 300, 0.1395 and 1.183e-4 respectively. Re-arranging Equation (2.13) given that $C_f = \Delta\phi/\Delta p$, the corresponding change in porosity as a result of increasing confining pressure is plotted. Note that the curve seems to over-estimate the amount of compaction for the samples.

Assuming the preconsolidation pressure of 48 MPa, I used Hagin's elastic compaction curve to characterize the compaction behavior of the samples before they are loaded beyond the preconsolidation pressure. Using initial porosity of 31% as an example, the red curve on Figure 2.8 represents the theoretical compaction for this sample. The red dotted line is the compaction projection beyond the preconsolidation pressure and cannot fully describe the abrupt loss in porosity. Yale's compaction curve for unconsolidated sand is calibrated to Hagin's compaction curve assuming Yale's curve is adequate for virgin compaction once the loading exceeds the preconsolidation pressure. However, Figure 2.8 shows that Yale's curve cannot capture the abrupt decrease in porosity either. As a result, I use the empirical compaction curve to describe porosity reduction for pressures exceeding 48 MPa and couple it with Hagin's compaction curve to describe the porosity change due to pressure change.

Figure 2.9 illustrate the composite DARS diagram for Field X using only Hagin's compaction curve. Based on the initial reservoir conditions, the composite diagram shows that porosity from Field X is likely to reduce from about 30% to 28.3%. Comparing this with the combined compaction curve mentioned above, Figure 2.10 shows that the porosity reduction based on the combined curve will be slightly higher.

Under *in situ* reservoir conditions, as pore pressure decreases as a result of depletion, the effective vertical stress, S_V-P_P, increases. The amount of depletion that can occur within the reservoir without loading the formation beyond the preconsolidation pressure (or the critical depletion, $P_{critical}$) can then be defined as:

$$P_{critical} = P_{Pinitial} - \left(S_V - P_{preconsolidation}\right) \quad (2.14)$$

For Field X where the initial pore pressure, $P_{Pinitial}$, is about 78 MPa and S_V of 90 MPa, the critical depletion pressure is approximately 36 MPa. However, it is important to note that as depletion occurs, the magnitude of both S_{Hmax} and S_{hmin} will change. As a result, the change in vertical effective stress due to depletion may not provide enough information to evaluate if reservoir depletion has loaded the formation beyond the preconsolidation pressure. Moreover, precaution is required to interpret the critical depletion stress and predicted compaction from the composite diagram since the diagram is a projection of the end cap ellipsoids onto the S_{hmin}:P_P plane based on the initial stress condition without considering the change in S_{Hmax}. The composite diagram may therefore over-estimate the amount of porosity change. Incorporating ΔS_{Hmax} to the DARS transformation assuming $\Delta S_{Hmax} = \Delta S_{hmin}$, Figure 2.11 shows that the equivalent preconsolidation pressure (or the critical depletion pressure) for Field X is about 63 MPa (compare to 36 MPa calculated based only on pressure change). The higher critical depletion pressure suggests that a significant porosity change will not occur for another 15 MPa of depletion in Field X.

Unlike Valhall, the relatively low stress path implies that shear-enhanced compaction will be the dominating deformation mode in the GOM Field X as depletion continues and production-induce normal faulting is unlikely to occur. Based on these analyses with the inclusion of ΔS_{Hmax}, I predict that the porosity in the Field X has been reduced from about 30.8% to 29.4% (Figure 2.11).

2.8 EFFECTS OF S_{HMAX} AND μ ON DARS

The accuracy of the DARS formalism on porosity prediction depends on the accuracy of both the laboratory studies and the *in situ* measurements. Improvements on the quality of laboratory tests and estimation of S_V, S_{hmin} and P_P can be achieved be careful experimentation, while the uncertainties associated with μ and the magnitude of the initial S_{Hmax} are more difficult to eliminate. Using Field X as an example, Figure 2.12 demonstrates that the impact of the uncertainties associated with the initial S_{Hmax} and μ is minimal. When the initial S_{Hmax} ranges between the initial S_{hmin} and S_V, varying the precise value of S_{Hmax} has a negligible effect on the predicted porosity change due to depletion. Although the difference caused by the uncertainty of μ is slightly larger than that of the initial S_{Hmax}, the error for predicted porosity change is still within 1% of the estimated value. As a result, minimizing the errors in determining the initial S_{Hmax} and μ is not as important as an accurate laboratory test or the determination of S_V, S_{hmin} and P_P.

2.9 CONCLUSIONS

Modeling reservoir deformation during production is a complicated subject since it must combine what is known about rock deformation from laboratory studies with the reservoir stress path. The DARS formalism provides a straightforward method to explain how a reservoir may deform and considers both compaction and faulting deformations. To perform DARS, a detailed and accurate laboratory study is essential and can reduce the uncertainties of the prediction of porosity reduction as a result of depletion. Continuous measurements of the changes in the horizontal stresses and pore pressure within the vicinity of the reservoir are also required. The two examples given in this chapter show that if *in situ* stress measurements are available, it is possible to predict the likelihood of induced normal faulting during the production lifetime of the reservoir. The advantage of using an empirical stress path is that it is not necessary to make assumptions about the elastic moduli of the formation. The Cam-Clay model is used in this study to bridge the laboratory and reservoir space, however, other models could also be used. The

choice of model will only affect the ellipticity and the shape of the yield surfaces. The values of S_{Hmax} and μ used in the analysis have a relatively small effect on the prediction of porosity reduction.

The case studies demonstrate that individual reservoirs behave very differently. For Valhall, production has resulted in the spreading of normal faulting from the crest to the flank in the vicinity of the reservoir. While in GOM Field X, the formation becomes stiffer and more stable as compaction occurs. These different deformation responses are the direct result of the stress path followed by the formation during depletion.

2.10 REFERENCE

Addis, M.A. 1997. Reservoir depletion and its effect on wellbore stability evaluation: International Journal of Rock Mechanics and Mining Sciences, 34, 3-4, Paper 4.

Byerlee, J.D. 1978. Friction of Rock, *Pure and Applied Geophysics,* **116,** 615-626.

Desai, C.S. & Siriwardane, H.J. 1984. *Constitutive Laws for Engineering Materials, with Emphasis on Geologic Materials*. Prentice-Hall: Englewood Cliffs, N.J., 468p.

Finkbeiner, T., 1998. In-situ stress, pore pressure and hydrocarbon migration and accumulation in sedimentary basins. *PhD thesis, Department of Geophysics, Stanford University, CA*. 193pp.

Hagin, P.N., 2003. *Application of Viscoelastic, Viscoplastic, and Rate-and-State Friction Constitutive Laws to the Deformation of Unconsolidated Sands*. Unpublished Ph.D. Thesis, Stanford University, 126pp.

Hagin, P.N. & Zoback, M.D., 2004a. Viscous deformation of unconsolidated reservoir sands (Part 1): Time-dependent deformation, frequency dispersion and attenuation, *Geophysics*, **69**, 731-741.

Hagin, P.N. & Zoback, M.D., 2004b.Viscous deformation of unconsolidated reservoir sands (Part 2): Linear viscoelastic models, *Geophysics*, **69**, 742-751.

Jaeger, J.C. & Cook, N.G.W. 1969, *Fundamentals of Rock Mechanics*. Methuen and Co. Ltd.: London, 515p.

Kristiansen, G. 1998. Geomechanical characterization of the overburden above the compacting chalk reservoir at Valhall, *Eurock '98, SPE/ISRM Rock Mechanics in Petroleum Engineering, The Norwegian University of Science and Technology*. Trondheim, Norway: 193-202.

Maury, V. M. R., Grasso, J. R. & Wittlinger, G. 1992. Monitoring of subsidence and induced seismicity in the Larq gas field (France): the consequences on gas production and field operation. *Engineering Geology*, **32**, 123.

Poland, J.F., Lofgren, B.E., Ireland, R.L. and Pugh, R.G., 1975. *Land Subsidence in the San Joaquin Valley, California, as of 1972*. USGS Professional Paper 437-H, 78p.

Pratt, W.E. and Johnson, D.W., 1926. Local subsidence of the Goose Creek oil field. *Journal of Geology*, **34**, 577-590.

Salz, L.B. 1977. Relationship between fracture propagation pressure and pore pressure. *SPE 6870, 52nd Annual Conf., Denver, Colorado, 9-12 October 1977.*

Segall, P. & Fitzgerald, S. D. 1996. A note on induced stress changes in hydrocarbon and geothermal reservoirs. *Tectonophysics,* **289**, 117-128.

Teufel, L. W., Rhett, D. W. & Farrell, H. P. 1991. Effect of reservoir depletion and pore pressure drawdown on in situ stress and deformation in the Ekofisk field, North Sea, In: Roegiers, J. C. (EDS), *Rock mechanics as a multidisciplinary science:* 63-72. Rotterdam: Balkena.

Townend, J. & Zoback, M.D. 2000. How faulting keeps the crust strong. *Geology*, **28**, 399-402.

Warpinski, N.R. & Teufel, L.W. 1992. Determination of the effective stress law for permeability and deformation in low-permeability rocks. *SPE Formation Evaluation*, **June 1992**, 123-131.

Whitehead, W.S., Hunt, E.R. and Holditch, S.A. 1987. The effects of lithology and reservoir pressure on the in-situ stresses in the Waskom (Travis Peak) Field. *Society of Petroleum Engineering*, Paper 16403

Wiprut, D. & Zoback, M. D. 1999. Fault reactivation and fluid flow along a previously dormant normal fault in the Norwegian North Sea. *Geology*, **28**, 595-598.

Yale, D.P., Nabor, G.W., Russell, J.A., Pham, H.D., & Yousef, Mohamed, 1993. Application of variable formation compressibility for improved reservoir analysis. SPE 26647.

Zoback, M.D., Chan, A.W. & Zinke, J., Production-induced normal faulting. *Proceedings of the 38th US Rock Mechanics Symposium, DC Rocks 2001*, Washington D.C., 7-10 July 2001, 157-163

Zoback, M.D. & Healy, J.H., 1984. Friction, faulting and "*in situ*" stress. *Annales Geophsicae*, **2**, 689-698.

Zoback, M.D. & Zinke, J.C., 2002. Production-induced normal faulting in the Valhall and Ekofisk oil fields. *Pure and Applied Geophysics*, **159**, 403-420.

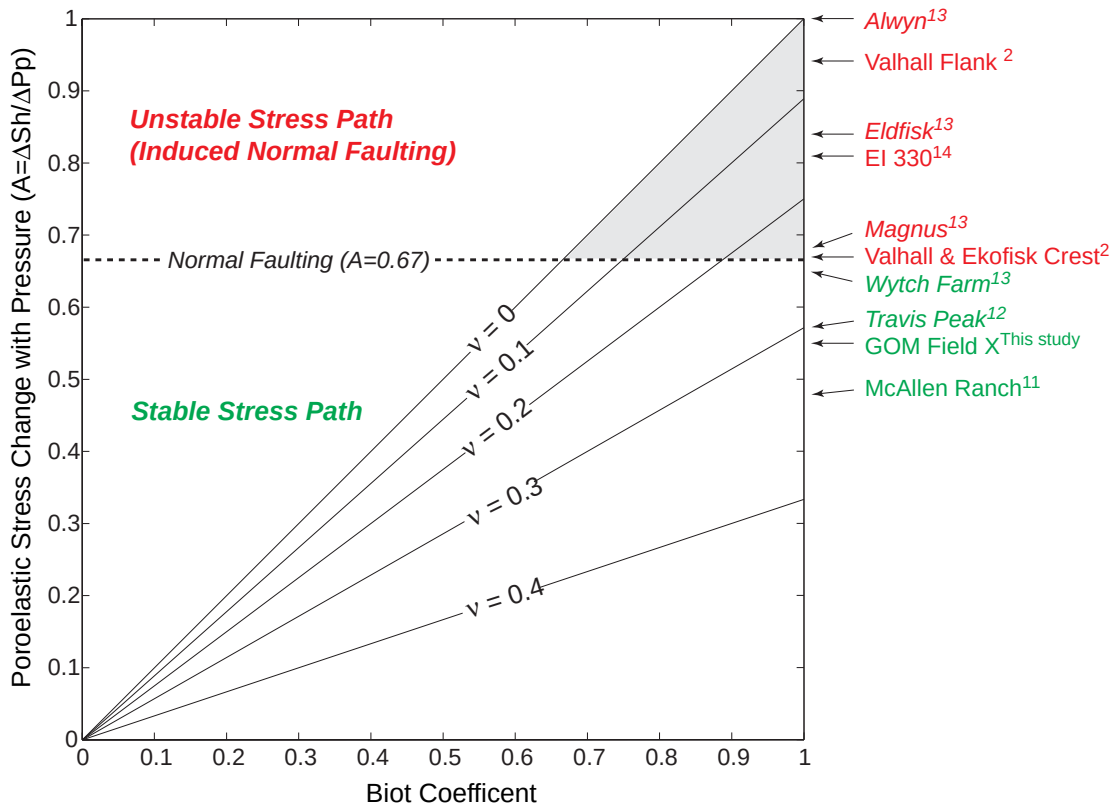

Figure 2.1: Variation of stress change with pressure as a function of Biot coefficient, α, and Poisson's ratio, ν. The normal faulting line represents A = 0.68. The gray area represents the possible combination of α and ν to create an unstable stress path based on poroelastic theory. Published stress paths of different reservoirs are marked on the right hand side of the diagram. Stress paths measured as a result of depletion are marked with filled circles; stress paths measured with unknown reservoir condition are marked with open circles with the italic field names. (1) Zoback & Zinke, 2002; (2) Salz, 1977; (3) Whitehead *et al*., 1987; (4) Addis, 1997; (5) Finkbeiner, 1998; (6) This study.

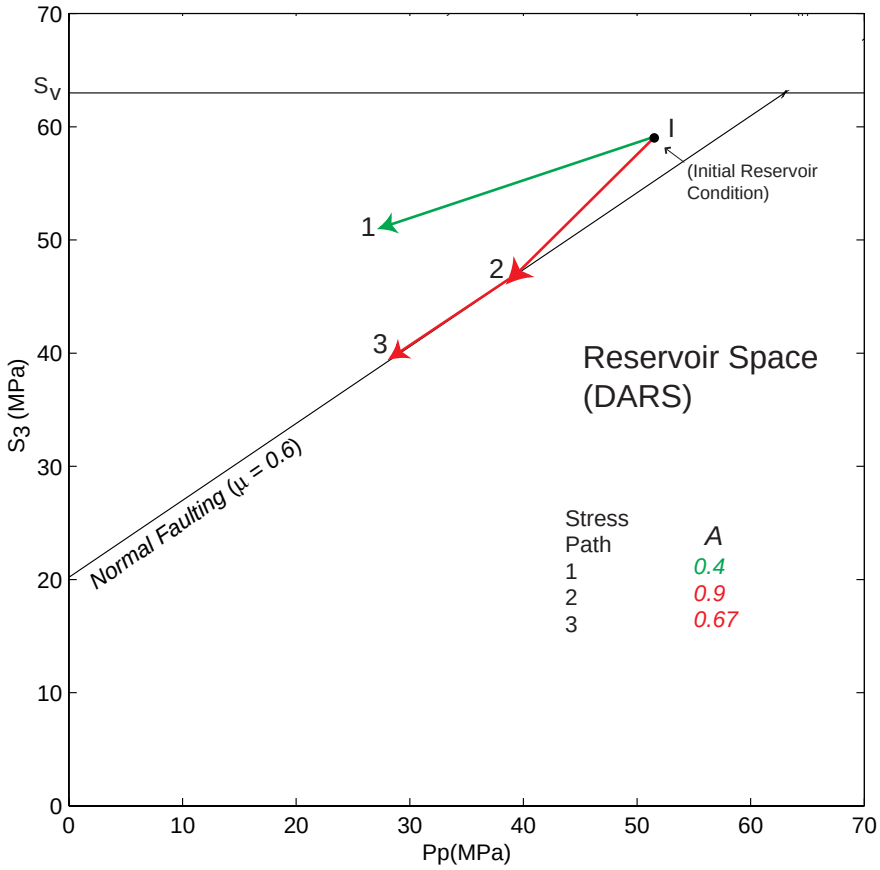

Figure 2.2: The schematic presentation of how stress path will control the potential of production-induced faulting in a reservoir. Stress paths 1, 2 and 3 are possible stress path that a depleting reservoir may follow. If the stress path is steeper than the critical value of 0.68, the producing reservoir will eventually reaches the normal faulting stress states as in stress path 2. If depletion continues to occur, the reservoir will deform following stress path 3 and induced normal faulting will continue. However, when ***A*** is smaller than 0.68, normal faulting is unlikely to occur. Indeed, the reservoir will become more stable from faulting. Stress path 1 shows such scenario.

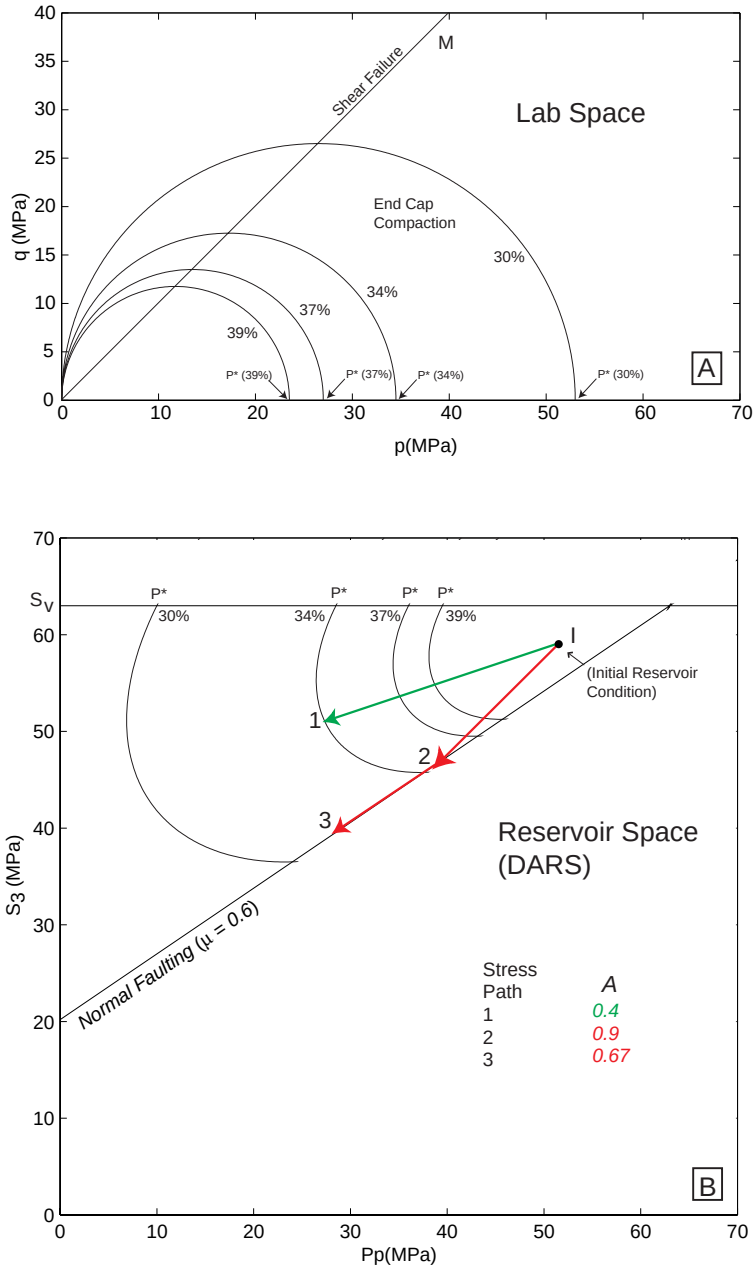

Figure 2.3: The transformation of yield caps from laboratory space (p:q) into reservoir space (S_{hmin}:P_P) based on the Cam Clay model. (a) Schematic diagram in laboratory space showing the changes in porosity of a rock sample as a result of changes in pressure where p is the mean stress and q is the deviatoric stress. As pressure increases, the porosity of the rock sample decreases. This behavior is reflected by the increase of the size of the yield cap. The yield cap represents the limit at which inelastic compaction will occur while M marks the critical state line. The critical state line is also known as the fixed yield cap in some contexts. Curves above the shear failure line only presented as a completeness of the yielding loci. (b) The transformed end caps in reservoir space.

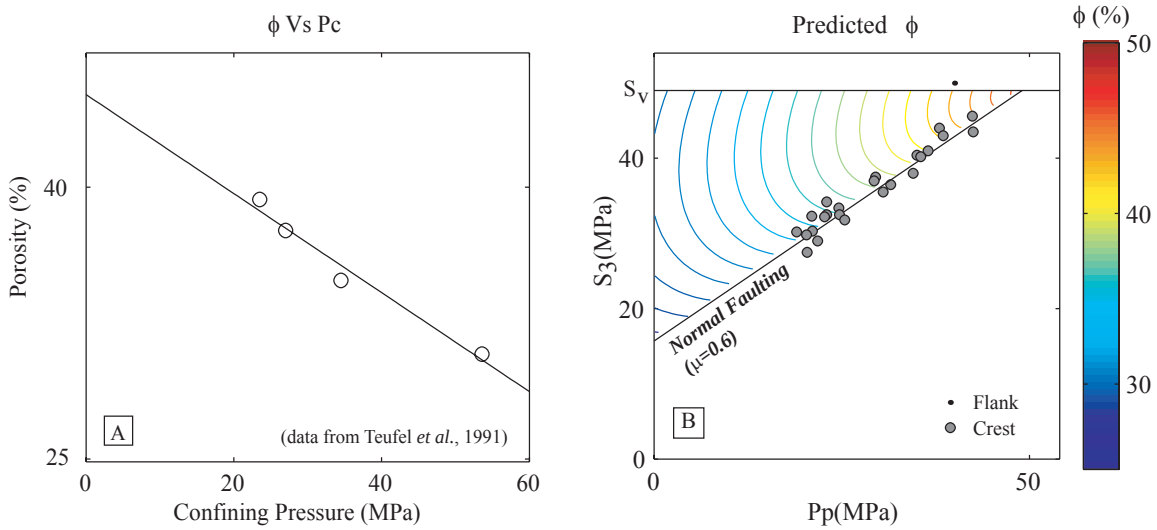

Figure 2.4: DARS analysis for the Valhall Field in North Sea. Laboratory experiments using Valhall chalk are unavailable; results based on Ekofisk chalks are used instead due to the proximity of the two formations (data from Tuefel *et al*., 1991; Warpinsky & Teufel, 1992). (a): Laboratory measurements of the porosity reduction of Ekofisk chalk as confining pressure increases. Conventional exponential fits are used to model the porosity response of increasing confining pressure. The best-fit curves are then transformed into reservoir space and the DARS plot is created. (b): DARS plots for predicted porosity for Valhall. The two symbols represent stress measurements from the flank and the crest of the field (Zoback & Zinke, 2002).

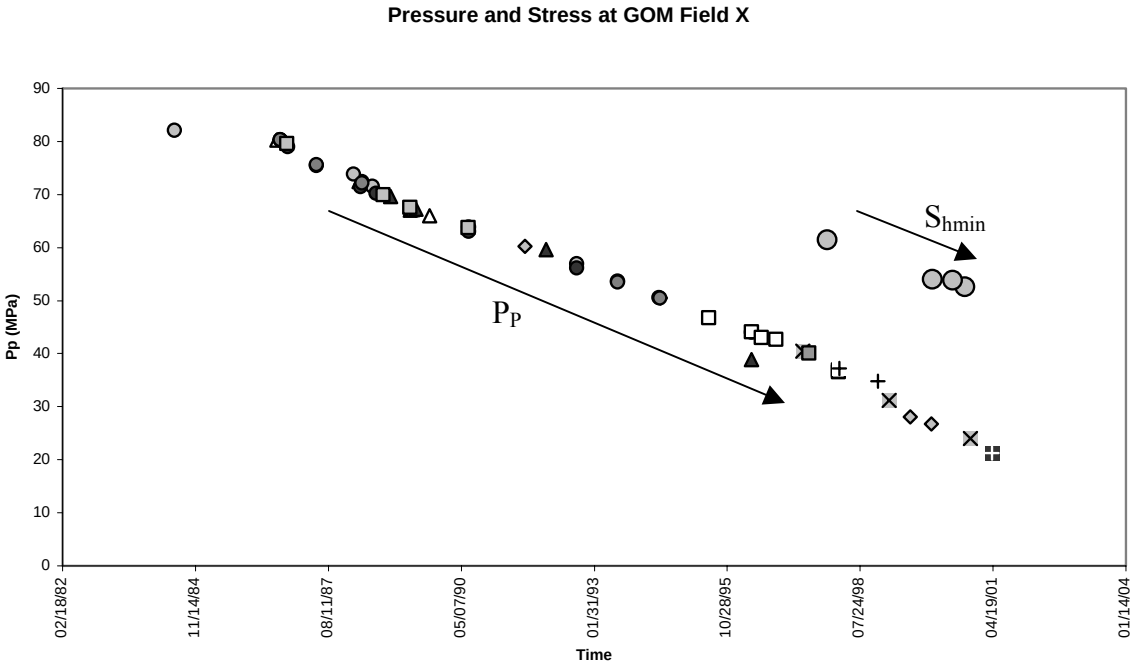

Figure 2.5: Pore pressure and minimum horizontal stress history of the GOM Field X. Different symbols represent measurements made in different wells. The magnitude of the pore pressure is then adjusted to the datum. Notice that the continuous decline of pore pressure measurement from different well implies that there is no sub-compartmentization within the reservoir.

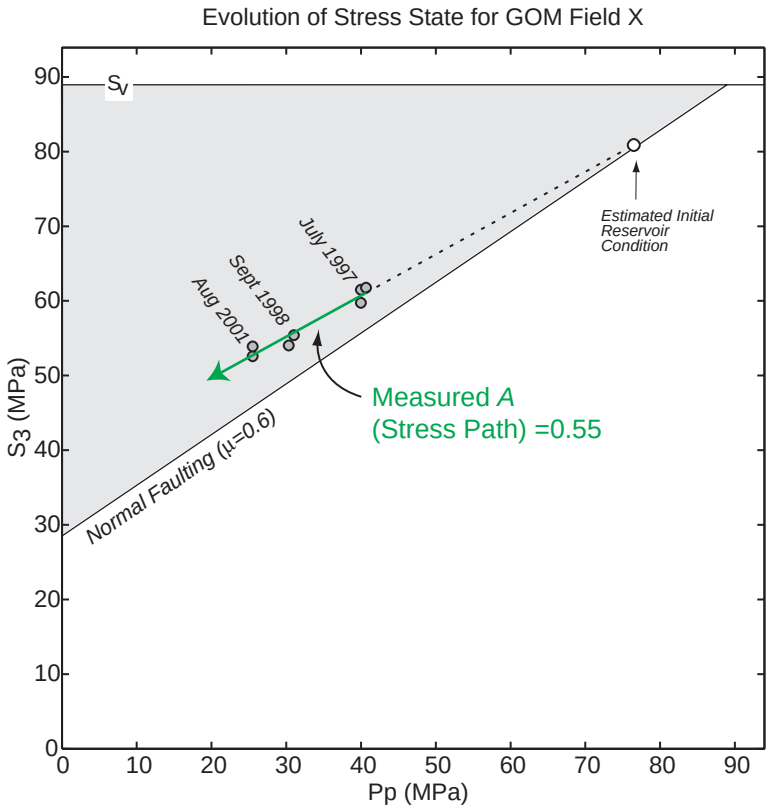

Figure 2.6: Stress measurements throughout the lifetime of the reservoir. Most measurements are recorded in the 1990s while none is made during the early stage of the production. Stress path is estimated based on the limited data points obtained. The initial reservoir condition is estimated based on the stress path presented. It is obvious that the reservoir initially is in a state of faulting equilibrium and moved away from failure as production continues. Production, in this case, is not likely to induce normal faulting within the reservoir sand.

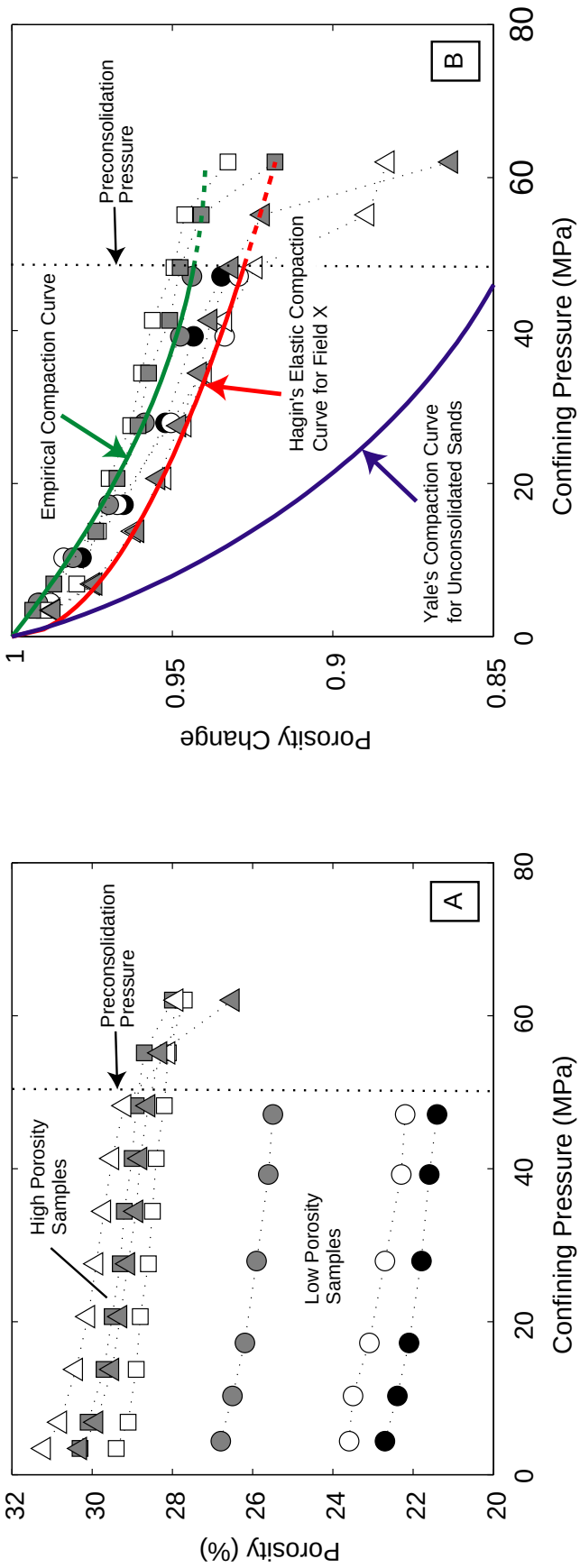

Figure 2.7: Laboratory experiments on porosity reduction for Field X. (a): Seven samples from two different reports are presented. The high porosity samples experienced an abrupt change in porosity when they are loaded beyond the preconsolidation pressure. While the lower porosity samples have not been loaded beyond that point. (b): Normalized porosity loss as a function of increasing confining pressure. Note that compaction behaviors of the seven samples are quite similar even though the initial porosity varies from 22 to 32%. Green line represents the empirical compaction curve estimated directly from the experimental data. The red line is based on the laboratory result conducted by Hagin using two new samples. The Hagin compaction curve is a power law compaction curve. The blue line is the compaction curve for unconsolidated sand based on Yale *et al.* (1993) and seems to over-estimated the amount of compaction for the Field X samples.

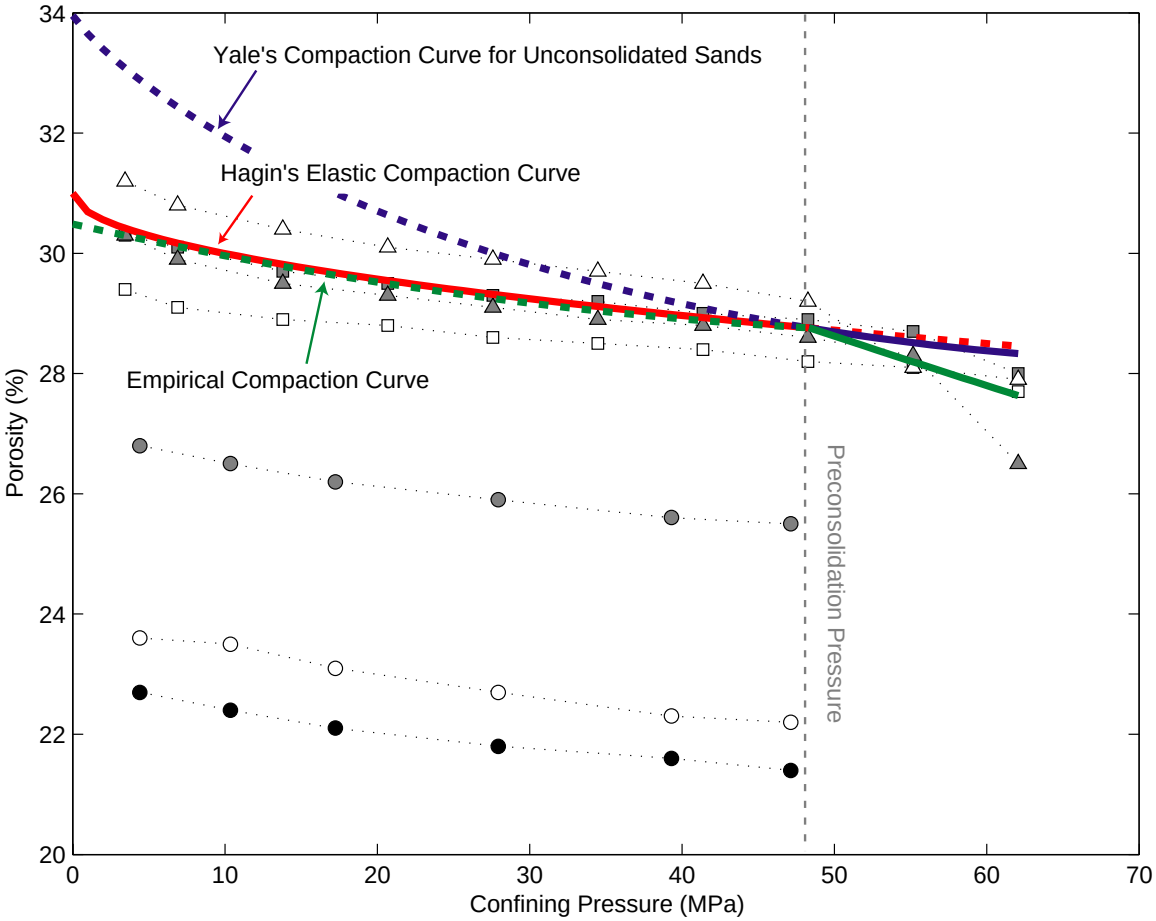

Figure 2.8:A combined Hagin's elastic compaction curve and the empirical compaction curve will be used to characterize the porosity response in Field X.

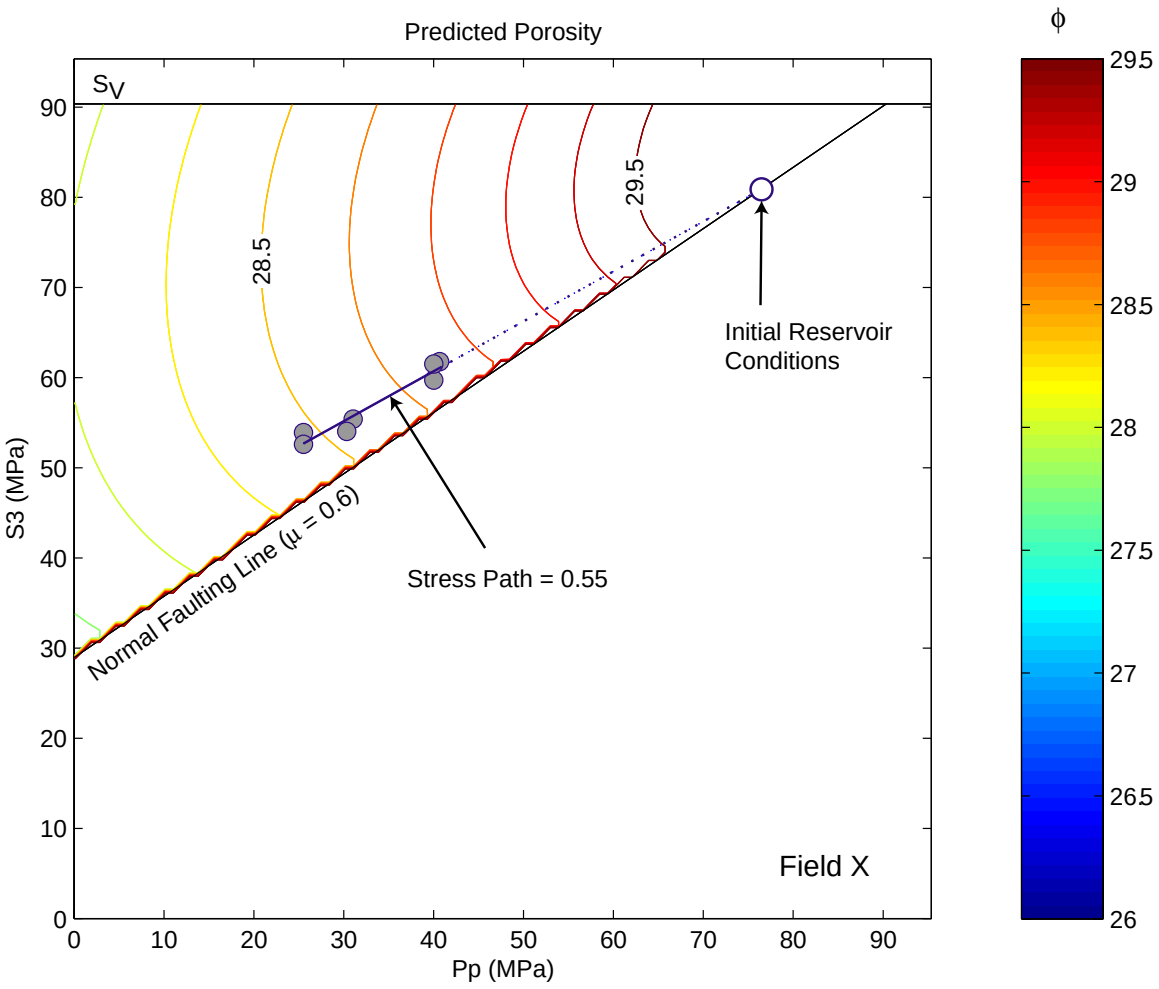

Figure 2.9: The composite diagram of DARS for Field X. The contour represent the porosity reduction based only on the Hagin's elastic compaction curve.

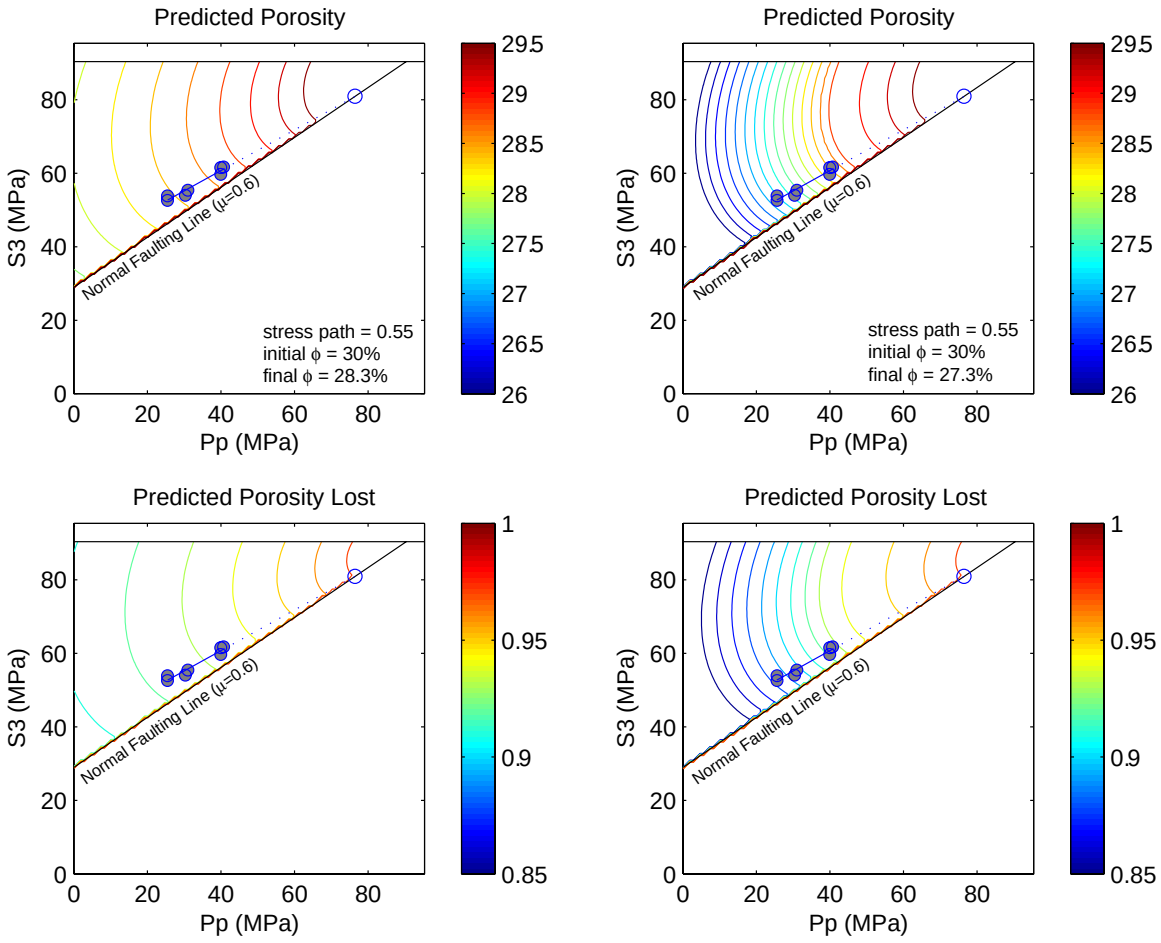

Figure 2.10: Comparing porosity reduction estimation using (a) only the Hagin's elastic compaction curve; and (b) the combined compaction curve. Note that based on initial conditions, DARS predicted a difference of 1% p.u. in porosity reductions between the two model.

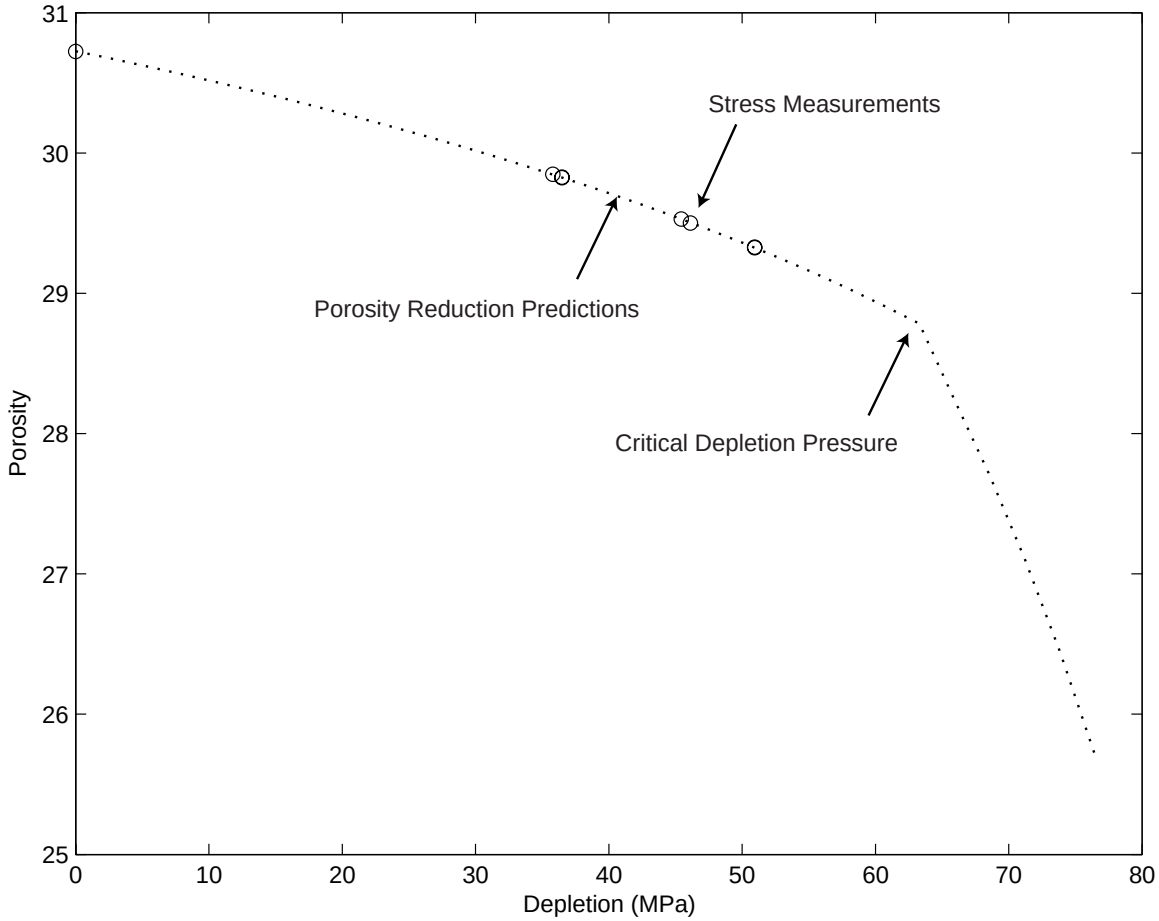

Figure 2.11: Considering S_{Hmax} will decrease in a similar manner as S_{hmin}, the adjusted porosity reduction estimation is smaller than the previous estimate. This is mainly because of the apparent increase in the critical depletion pressure. Given a 30.8% initial porosity as an example, porosity will have decreased to about 29.4% when the last stress measurements made. The apparent increase in the critical depletion pressure allow a larger amount of hydrocarbon withdrawal without significantly compact the formation.

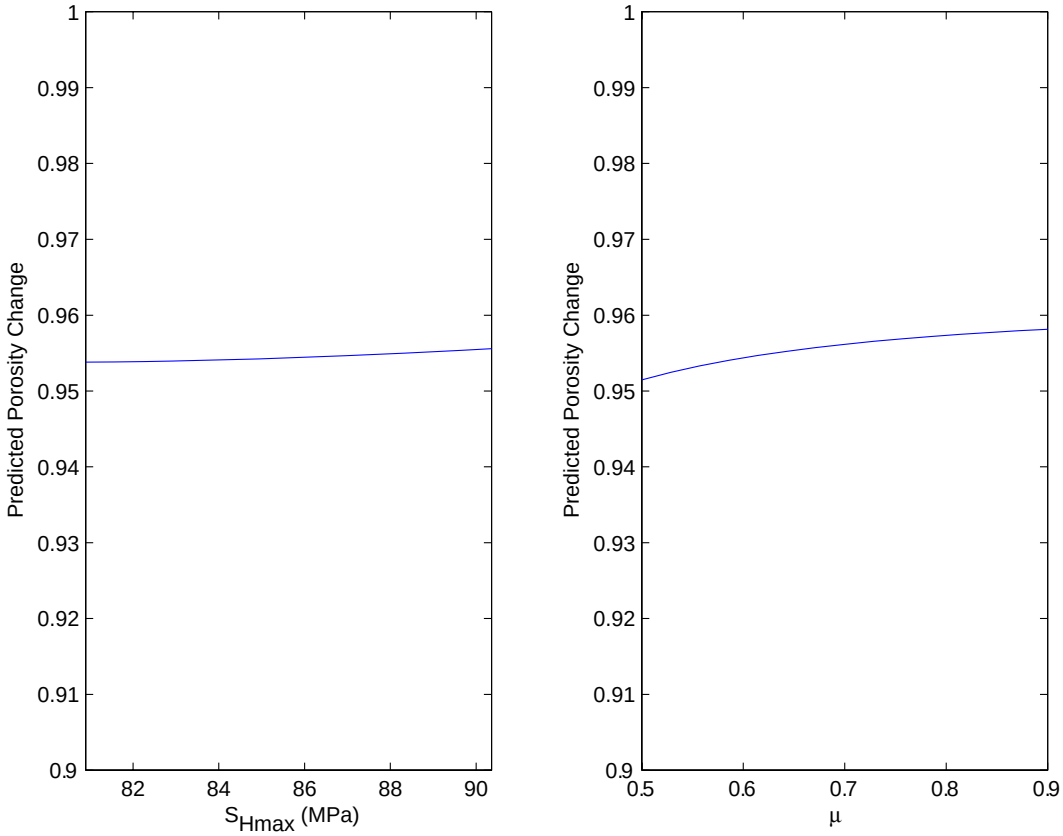

Figure 2.12: The impact of the uncertainties associated with the initial value of S_{Hmax} and μ are insignificant.

CHAPTER 3

Estimating Permeability Changes Associated with Depletion in Weak Sand Reservoirs

3.1 ABSTRACT

Permeability changes associated with depletion in weak sand reservoirs can be estimated by utilizing the formalism of Deformation Analysis in Reservoir Space (DARS) that predicts production-induced porosity changes. Based on laboratory studies on sands from the Gulf of Mexico, empirical upper and lower bounds of permeability reductions corresponding to porosity reductions are derived. These two empirical relationships constrain 95% of the laboratory results. The lower bound of permeability change agrees with the Kozeny-Carman relationship for extremely permeable sands. These empirical relations are then used in conjuncture with DARS to examine the effects of production-induced deformation on permeability reduction in a Gulf of Mexico reservoir, Field Z. DARS predicts a 0.7% change in porosity in Field Z and the corresponding permeability changes derived using the empirical relationships are in good agreement with the measured permeability changes in 3 different wells. While most reservoir simulations assume constant rock properties during depletion, applying both production-induced porosity and permeability changes to a simple simulation model can result in significant variations in the predicted reservoir productivity.

3.2 INTRODUCTION

Depletion-induced porosity loss in a producing formation can have a significant impact on the overall productivity of the reservoir. The reduction of pore volume in the formation may result in the expulsion of oil and can be a potentially important recovery method for weakly consolidated reservoirs. This mechanism is commonly referred to as compaction drive. To assess the significance of compaction drive in the production history of the reservoir, a good knowledge of the formation compressibility is required. However, as pore space is reduced, some of the pathways for fluid migration may be blocked resulting in a permeability reduction. In order to accurately estimate the effect of depletion on reservoir productivity, it is important to understand how permeability will respond to a change in pore volume as a result of depletion-induced reservoir compaction (discussed in Chapter 2).

Numerous laboratory studies document the dependency of permeability on porosity, stress and deformation mechanism. Zhu and Wong (1997) suggest that permeability and porosity changes for most low-porosity sandstones closely track one another in the cataclastic flow regime. Based on experimental data of samples from five different reservoirs and sixteen outcrops, Schutjens *et al.* (2004) illustrate that the change in axial permeability is independent of how the sample is loaded when the applied stress deforms the sample within the elastic domain (i.e., loading within the end cap or within the preconsolidation pressure). However, a drastic change in permeability is triggered by the onset of shear-enhanced compaction once the sample is loaded beyond the elastic domain into the plastic deformation domain in the reservoir stress space (i.e., when the stress state exceeded the preconsolidation pressure causing an expansion of the end cap). The effects of plastic deformation and permeability alteration can be extremely significant in reservoir simulations of a highly compressible formation (Yale, 2002). Using coupled simulations, Yale (2002) shows that the initial stress state and plasticity significantly increases the compressibility of the formation and the compaction drive energy of the reservoir; modeling the changes in permeability with plastic deformation shows an extremely large effect on near wellbore pressure drawdown and deformation over conventional simulations which only elasticity is assumed. Crawford and Yale (2002) use an elastoplastic model (also refer to as critical state model) to study the relationship between deformation and the corresponding permeability loss. They show that an elastoplastic model captures the main characteristics of experimental results for permeability changes as a function of both stress and strain, following a constitutive model similar to that for deformation of weak and unconsolidated sand samples.

Although laboratory experiments on the stress dependency of porosity and permeability are conducted frequently, the stresses used in laboratory tests (mean and shear stress) cannot be measured directly in the reservoir. As presented in Chapter 2, the DARS formalism has been used to transform laboratory studies to the reservoir space such that depletion-induced compaction can be evaluated. In this chapter, the capability of the DARS formalism will be expanded to include the estimation of compaction-induced permeability loss.

Based on several laboratory experiments, I present a plausible relationship between porosity reduction and permeability change during reservoir depletion. To estimate the range of possible permeability changes as a result of depletion, I apply this empirical relationship to the predicted porosity loss estimated from the DARS formalism. A deepwater turbudite sand reservoir, Gulf of Mexico Field Z, is used as an example since *in-situ* permeability measurements are available for validating the applicability of this method to estimate production-induced permeability change. A simple reservoir simulation is also used for demonstrating the impact of porosity change and permeability change on reservoir productivity and recovery.

3.3 LABORATORY EXPERIMENTS ON COMPACTION AND PERMEABILITY LOSS

As reservoir depletion occurs, decreases in pore pressure as a result of production will increase the effective stresses within the reservoir. The increasing effective stresses acting on the formation materials will lead to progressive states of deformation when the material's failure limits (or end caps) are reached. Compaction and grain rearrangement (and eventually grain crushing and pore collapse) are the dominant deformation modes once the formation is loaded beyond the end caps (as discussed in Chapter 2). The reduction in porosity will result in a change in permeability.

Laboratory experiments on samples collected from Gulf of Mexico Field X described in Chapter 2 were used for determining the stress dependency of porosity and permeability. Figure 3.1a and 3.1b are the porosity responses to increasing stress as presented in Chapter 2. The range of confining pressure used in these experiments (0 to 60 MPa) represents the possible range of depletion that might occur in the field (a reduction in pore pressure through depletion will result in an increase in effective stresses acting on the formation). Concurrent permeability measurements are shown in Figure 3.1c which illustrates the variation of permeability as a function of increasing confining pressure. Similar to the porosity experiments, the initial permeability of the samples reflects the initial porosity measurements, varying between 80mD and 1050mD. Contrary to the porosity reduction, Figure 3.1d shows that the change in permeability as a function

of pressure does not follow the simple trend observed for the porosity reduction (Chapter 2). To further examine the relationship between compaction and permeability loss, I re-plot these experimental data to normalized permeability as a function of normalized porosity (Fig. 3.2). The data for Field X, shown in Figure 3.2, seems to follow two different trends: the upper and lower bounds of permeability. It appears the two trends are related to the initial porosity of the samples. The low porosity samples appear to follow the lower bound while the high porosity samples have a more drastic change in permeability as a result of porosity loss. Since no further information about the samples is available, it is unclear if the two empirical trends have a direct relationship with initial porosity. For reference, the permeability change of the samples tested by Hagin (Chapter 2) is shown as the dotted green line on Figure 3.2.

To examine the validity of the two empirical trends, results from published experimental data on 22 deep-water turbidites from different fields within the Gulf of Mexico (Ostermeier, 2000) are used for comparison. Re-plotting Ostermeier's experimental data in terms of normalized permeability vs. normalized porosity and superimposing them on the plot of experimental data from Field X, about 95% of the Ostermeier's data fall within the upper and lower bounds regardless of the initial porosity of the samples, the location and depth at which the samples are collected (noted '+' in Fig. 3.2). In other words, the two empirical trends presented here can be used as a general estimation on how porosity reduction will affect the permeability of the samples for turbidite sands from the Gulf of Mexico. Note that the reduction of permeability can be as high as 70% of the original permeability for a 10% change in porosity. This drastic variation in permeability change as a result of production-induced compaction could greatly affect reservoir simulation if ignored.

3.4 KOZENY-CARMAN RELATIONSHIP

The Kozeny-Carman relationship is used to examine the physical implications of the two empirical permeability trends described in the previous section. This relationship is a widely used method to determine the permeability of a porous formation in terms of generalized parameters such as porosity (Carman, 1961; Mavko *et al*., 1998). To estimate

fluid flow in a porous media, the Kozeny-Carman relationship idealizes the medium as a twisted circular pipe of known dimensions. Applying Darcy's Law for laminar flow through the circular pipe, the Kozeny-Carman relationship states that

$$k = \frac{B\phi^3}{\tau^2 S^2} = B\phi^3 \frac{d^2}{\tau} \quad \text{.....(3.1)}$$

where k is permeability, B is a geometric factor, τ is tortousity and d is the typical grain diameter. The porosity, ϕ, and the specific surface area, S, can be expressed by:

$$\phi = \frac{\pi R^2}{A} \text{ and } S = \frac{2\pi R}{A} \quad \text{.....(3.2)}$$

where R and A are the radius and the cross sectional area of the imaginary pipe.

In general, the Kozeny-Carman relationship implied that permeability is proportional to the porosity cubed. Mavko and Nur (1997) introduce the percolation porosity, ϕ_c, to the Kozeny-Carman relationship. They define the percolation porosity as the limiting porosity at which the existing pores within the formation are disconnected and do not contribute to flow. The modified Kozeny-Carman relationship that includes the percolation porosity becomes:

$$k = B\frac{(\phi - \phi_c)^3}{(1 + \phi_c - \phi)^2} d^2 \quad \text{.....(3.3)}$$

where ϕ_c ranges from 0 to 0.05 in most cases.

To determine the permeability change as a result of porosity change, I use the modified Kozeny- Carman relationship and simplify Equation 3.3 such that both geometric factors are removed (assuming a constant B for simplicity):

$$\frac{k}{k_i} = \left(\frac{\phi - \phi_c}{\phi_i - \phi_c}\right)^3 \left(\frac{1 + \phi_c - \phi_i}{1 + \phi_c - \phi}\right)^2 \quad \text{.....(3.4)}$$

where k_i and ϕ_i are the initial permeability and initial porosity respectively. The theoretical values of compaction-induced permeability changes for ϕ_c between 0 and 0.05% using Equation 3.3 are then superimposed onto the laboratory data from the GOM core samples (Fig. 3.3). The theoretical permeability changes calculated using the

modified Kozeny-Carman relationship are similar to the lower bound estimated from the laboratory data. This similarity might imply that the empirical lower bound represents the lower limit of permeability changes for most GOM sands for which percolation porosity does not exist. In other words, if the producing formation is composed of porous materials in which all pore spaces are well connected, the Kozeny-Carman relationship with $\phi_c = 0$ could be used as a reference for the lower limit of permeability changes as a result of production-induced compaction.

The estimated change in permeability from the normalized Kozeny-Carman relationship (Eq. 3.4) assumes a constant grain size during compaction and cannot fully capture the significantly large permeability loss due to compaction in weak sediments. Several possible explanations for this shortcoming can be caused by grain crushing during compaction (a reduction in average grain size, d), change in tortousity or grain arrangement (resulting in a change in the geometric factor, B). I explore the potential impact of grain-size reduction on permeability estimation based on the modified Kozeny-Carman relationship since changes in tortousity and grain rearrangement are relatively difficult to determine in a laboratory experiment; while changes in average grain size can be estimated or confirmed by examining the thin sections of the sample before and after the experiment. To incorporate the change in average grain size within the modified Kozeny-Carman relationship, Γ is introduced such that:

$$\Gamma = \frac{1 - d/d_i}{1 - \phi/\phi_i} \quad \text{.....(3.5)}$$

where d_i and d are the average grain size prior to and after compaction. $\Gamma=0$ implies the average grain size did not change during porosity reduction. This term is introduced in order to simplify the various responses of grain size reduction as a function of porosity reduction, as illustrated in. Equation 3.5 suggests that a big reduction in porosity is required in order to get a large reduction in average grain size (or a large Γ). Note that $\Gamma>1$ is only possible for a very small range of porosity changes. Introducing the variable Γ, Equation 3.4 becomes:

$$\frac{k}{k_i} = \left(\frac{\phi - \phi_c}{\phi_i - \phi_c}\right)^3 \left(\frac{1 + \phi_c - \phi_i}{1 + \phi_c - \phi}\right)^2 \left[1 - \Gamma\left(1 - \frac{\phi}{\phi_i}\right)\right] \quad \text{.....(3.6)}$$

Figure 3.5 suggests that although grain-size reduction might have some influence on the permeability reduction, a very high grain-size reduction (high Γ) is required to explain the upper bound of permeability loss. As a result, a more complicated model that includes changes in tortousity and the geometric factors might be needed to fully describe the physical mechanism that causes the large drop in permeability represented by the upper bound.

3.5 CASE STUDY: GULF OF MEXICO FIELD Z

Field Z in the Gulf of Mexico is a deepwater Pliocene to Miocene over-pressured reservoir juxtaposed against a large salt dome. Discovered in the late 1980s, Field Z has been in production since the mid 1990s. The formation is mainly turbidite sands with an average porosity of 30%. The succession of several upward-fining sequences resulted in a variation of reservoir quality with depth. The initial horizontal permeability of the sands ranged from 60 to 168mD for a moderate quality sand and 350 to 540mD for a good quality sand interval. Both laboratory experiments on stress-strain relationship and *in-situ* measurements of S_{hmin} are available for this field. In addition to the stress measurements, horizontal permeability measurements are also available for Field Z.

Pore pressure, P_P, measurements from most wells in the field are compiled and corrected to a datum and a continuous decrease in P_P and the least principal stress can be observed. From the pressure data (Fig. 3.6), reservoir pressure in Well A declines along a different path with respect to the other wells in the formation suggesting the existence of sub-compartments within the reservoir. The nature of the compartmentalization (e.g., structural, stratigraphic) that separates Well A from the rest of the reservoir is not clear.

The evolution of S_{hmin} and P_P is presented in Figure 3.7. Similar to Field X reported in Chapter 2, the relatively low stress path in Field Z, $\boldsymbol{A}$ = 0.54, suggests that production-induced normal faulting is unlikely to occur. In other words, the initial stress state was one in which normal faults were active; depletion caused these faults to stabilize. *In-situ* permeability measurements from 3 different wells in Field Z are available (Figure 3.8). Well A is located near the center of the reservoir and wells B and C are located near the edge of the reservoir. Permeability measurements in these wells A and C were collected

immediately after production began and the first permeability measurement in well B was collected after about 10MPa of depletion. Without a measurement of initial permeability in these wells, I use the average value of the reported permeability from Field Z based on the reservoir quality. Well A has a relatively low permeability and is within the range of permeability for a moderate quality sand interval (the initial permeability for well A is assumed to be about 140mD); while the initial permeability for wells B and C is estimated to be 470mD (the average value for good reservoir quality sands).

Laboratory data on rock compressibility is available for GOM Field Z and is used in the DARS study. Unlike the sample from Field X, a marked decrease in porosity is not observed from this Field Z sample. The absence of a drastic porosity change in this sample may be related to the much greater depth, or greater preconsolidation pressure, experienced by the sample. Based on the interpretation of the experimental data, the *in-situ* P_P and S_{hmin} measurements, I conduct a DARS analysis for Field Z (Fig. 3.9) and a 0.7% change in porosity is predicted. The original thickness of the formation is about 20.5m (67ft), the loss in porosity implies a 14cm (or 5.6in) of compaction in Field Z.

Based on the *in-situ* stress and pressure measurements, I predict the change in porosity using DARS. Assuming the reservoir depletion stress path remains unchanged during production, I estimate the theoretical porosity change for Field Z as a function of pore pressure. Utilizing the two empirical porosity-permeability relationships shown in Figure 3.6, the possible range of permeability changes from Field Z is then estimated. Figure 3.10 illustrates the change in permeability associated with depletion for the three wells A, B and C. The *in-situ* permeability data from Figure 3.8 are then superimposed onto the theoretical permeability estimations. The *in-situ* permeability for well A seems to follow the lower-bound of the permeability loss while well B and C appear to agree with the upper-bound of permeability loss. Note that the absence of initial permeability for these wells makes it difficult to determine the accuracy of the prediction. As initial permeability for good quality reservoir sand ranges from 350 to 540 mD, measurements from well B can easily be fitted to the predicted values if the initial permeability used in the analysis is reduced. However, only the average value is used in this case to show that uncertainties associated with *in-situ* measurements can also affect the accuracy of the DARS prediction.

3.6 IMPACT OF POROSITY AND PERMEABILITY LOSS ON RESERVOIR PRODUCTION

As porosity decreases during depletion, compaction can positively affect the reservoir recovery as hydrocarbons are squeezed out of the formation as the pore volume decreases. However, compaction might also affect permeability by decreasing the connectivity of the pore spaces that will lead to a reduction in recovery. The trade off between these two phenomena requires detailed modeling of rock compaction during reservoir simulation since the result might affect the prediction of reservoir recovery, production forecast and well placement decisions.

To illustrate the impact of porosity and permeability loss during depletion on reservoir performance, a simple 2D conceptual single-phase flow model based on Field Z was constructed. Assuming the reservoir is elliptical and has a dimension of 1900m by 960m and a thickness of 21m, a 50 by 50 grid is generated with an average permeability of 350mD and an initial porosity of 30%. Figure 3.11 illustrates the randomized distribution of initial permeability for this conceptual reservoir with the producing well located in the center of the reservoir.

Three scenarios have been investigated using the ECLIPSE simulator to demonstrate the effects of compaction and permeability reduction:

1. Constant Rock Compressibility: A common assumption in most simulation. The rock compressibility is estimated as an average over the expected depletion and can be defined as

$$C_R = \frac{1}{(\phi/\phi_i)} \frac{\partial(\phi/\phi_i)}{\partial P_P} \quad \text{.....(3.7)}$$

2. Compaction Drive: Incorporating the DARS formalism, porosity change as a function of depletion and stress reduction is estimated. The predicted change in porosity is input as varying pore volume multipliers in ECLIPSE. In this scenario, no permeability change will occur during depletion.
3. Compaction Drive with Permeability Loss: By relating the transmissibility multiplier to the pore volume multiplier based on the two empirical bounds of

permeability changes, both permeability and porosity loss will contribute to the estimated cumulative production of the conceptual reservoir.

Several assumptions are made to simplify and to shorten the time required for the simulation. The initial production rate is set to be at 10 MSTB/d (thousand surface tank barrels per day) and no water influx or injection, this single-phase simulator is allowed to run until it reaches one of the following conditions:

1. Minimum bottom hole pressure (BHP) of 1000 psi (~7 MPa);
2. Economic limits: 100 STB/d;
3. Maximum time: 8000 days (~22 years).

Figure 3.12 illustrates the result of the three scenarios. Using constant compressibility throughout the entire production in scenario 1, the conceptual reservoir will yield about 12MMSTB cumulative oil over 2500 days (~7 years). If depletion-induced compaction is considered, the recovery for this reservoir is increased significantly to about 26MMSTB over 7500 days (~20.5 years). In other words, compaction drive enhanced the recovery and extended the production life of this conceptual reservoir. When permeability loss associated with compaction is taken into considerations, the estimated recoveries are reduced. The predicted recoveries ranged from 16 to 25MMSTB over 8000 days (~22 years) depending on which empirical trends are used in the simulator. In the later two cases, the production life for the reservoirs are extended and the total recoveries predicted are still higher than those estimated when only a constant compressibility is used in the simulation. As a result, incorporating both depletion-induced compaction and permeability loss into the simulator can significantly alter the anticipated recovery and the production lifetime of a reservoir. In terms of recovery, production-induced compaction provides an additional driving mechanism that increases the recovery estimate; a small reduction in permeability (lower bound) might not have as much of an impact as a large reduction in permeability (upper bound) on the estimated recovery. The trade off between porosity changes and permeability changes will have significant implications for the determination of the recovery rate and the overall exploitation scheme for the reservoir.

3.7 CONCLUSION

Empirical relationships between production-induced compaction and permeability loss were derived based on several laboratory experiments. The two limiting trends derived in this study describe approximately 95% of the experimental results. While the physical processes controlling the upper bound of the laboratory-derived porosity-permeability relationship remain unknown, the lower bound corresponds well to the Kozeny-Carman relationship for extremely permeable sand. As a result, the use of the Kozeny-Carman relationship to estimate the change in permeability for a depleting reservoir will require caution as it might underestimate the severity of permeability loss. The advantage of using the empirical relationships along with the DARS formalism is that a range of permeability changes the consider changes in *in-situ* stress can be estimated. The case study shows that with adequate information, it is possible to estimate the degree of permeability loss associated with production-induced compaction. A careful and well-planned laboratory study along with *in-situ* stress measurements are the key to reducing the uncertainties associated with the porosity, permeability and compaction prediction from the DARS analysis. The impact of porosity loss and permeability loss as a result of depletion on the overall productivity of the reservoir can be significant. While porosity loss encourages compaction drive that will lead to an increase of productivity, drastic changes in permeability associated with compaction will reduce the reservoir's performance. A detailed simulation that couples porosity change and permeability change is recommended. Since most of the porosity and permeability loss associated with depletion are irreversible, stress management may become critical for reservoirs in which compaction is the dominant mode of reservoir deformation.

3.8 REFERENCE

Carman, P.C., 1961. L'écoulement des Gaz á Travers les Milieux Poreux, Paris: Bibliothéque des Science et Techniques Nucléaires, Press Universitaires de France, 198pp.

Chan, A.W., and Zoback, M.D., 2002, Deformation analysis in reservoir space (DARS): a simple formalism for prediction of reservoir deformation with depletion. SPE 78174.

Crawford, B.R., and Yale, D.P., 2002, Constitutive modeling of deformation and permeability: relationships between critical state and micromechanics. *SPE 78189.*

Mavko, G., Mukerji, T., and Dvorkin, J., 1998, *The Rock Physics Handbook: Tools for Seismic Analysis in Porous Media*. New York: Cambridge University Press, 329pp.

Mavko, G., and Nur, A., 1997. The effect of a percolation threshold in the Kozeny-Carmen relation. *Geophysics*., **62**, 1480-1482.

Ostermeier, R. M. 1993, Deepwater Gulf of Mexico turbidites: compaction effects on porosity and permeability. SPE 26468.

Ostermeier, R. M., 2001, Compaction effects on porosity and permeability: deepwater Gulf of Mexico turbidites. *JPT. Journal of Petroleum Technology,* **Feb. 2001**, p. 68-74.

Schutjens, P.M.T.M., Hanssen, T.H., Hettema, M.H.H., Merour, J., de Bree, P., Coremans, J.W.A. & Helliesen, G., 2004. Compaction-induced porosity/permeability reduction in sandstone reservoirs: data and model for elastic-dominated deformation. *SPE Reservoir Evaluation & Engineering*, **June 2004**, 202-216.

Yale, D.P., 2002, Coupled geomechanics-fluid flow modeling: effects of plasticity and permeability alteration. SPE 78202.

Yale, D.P., Nabor, G.W., and Russell, J.A., 1993, Application of variable formation compressibility for improved reservoir analysis. SPE 26647.

Zhu, W., and Wong, T.F., 1997, The transition from brittle faulting to cataclastic flow: permeability evolution. *Journal of Geophysical Research*, **102**, 3027-3041.

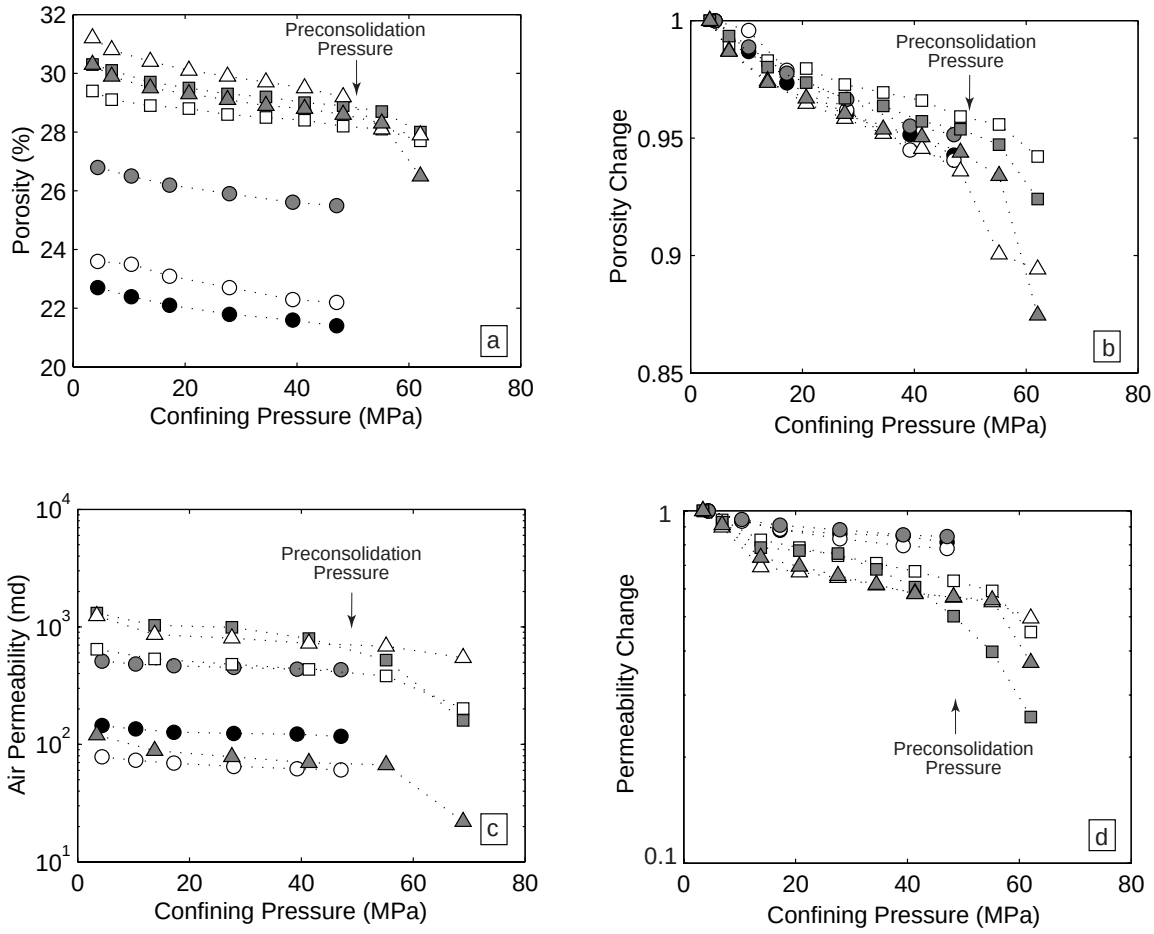

Figure 3.1 Laboratory experiments on samples collected from Gulf of Mexico Field X described in Chapter 2 were used for determining the stress dependency of porosity and permeability. (a) & (b) are the porosity responses to increasing stress as presented in Chapter 2. (c) Concurrent permeability measurements for the same seven samples. The initial permeability of the samples reflects the initial porosity measurements, varying between 80mD and 1050mD. (d) Contrary to the porosity reduction, the change in permeability as a function of pressure does not follow the simple trend observed for the porosity reduction.

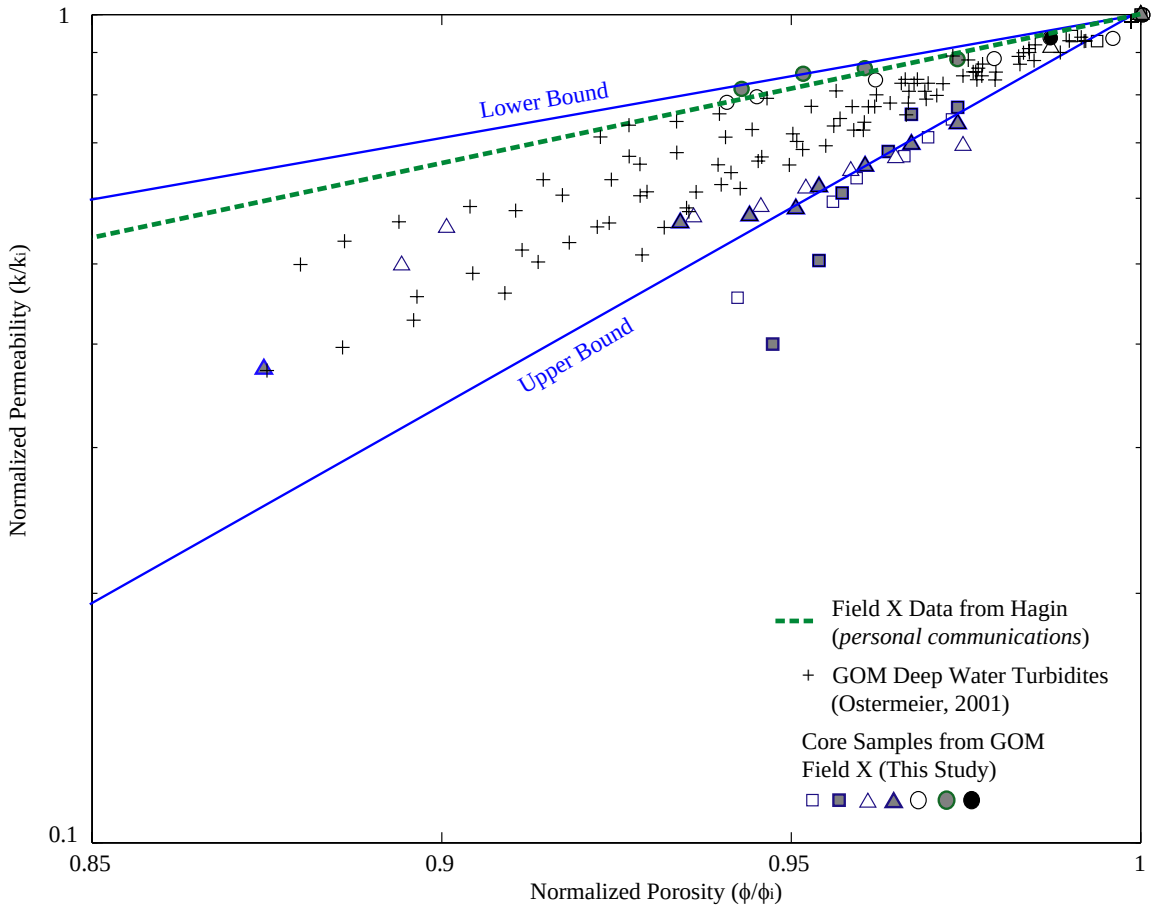

Figure 3.2: Plot of normalized permeability vs. normalized porosity for the laboratory samples. The seven samples seem to follow two different trends (the upper bound and lower bound of permeability loss). The high porosity samples appear to have a more drastic change in permeability when compared to the low porosity samples. The dotted green line represents the permeability response to porosity loss using the data from Hagin (*personal communication*). The '+' signs are data re-plotted based on Ostermeier's 22 deep-water turbudite sands (2001) samples. Note that almost 95% of the data falls between the two empirical trends from Field X.

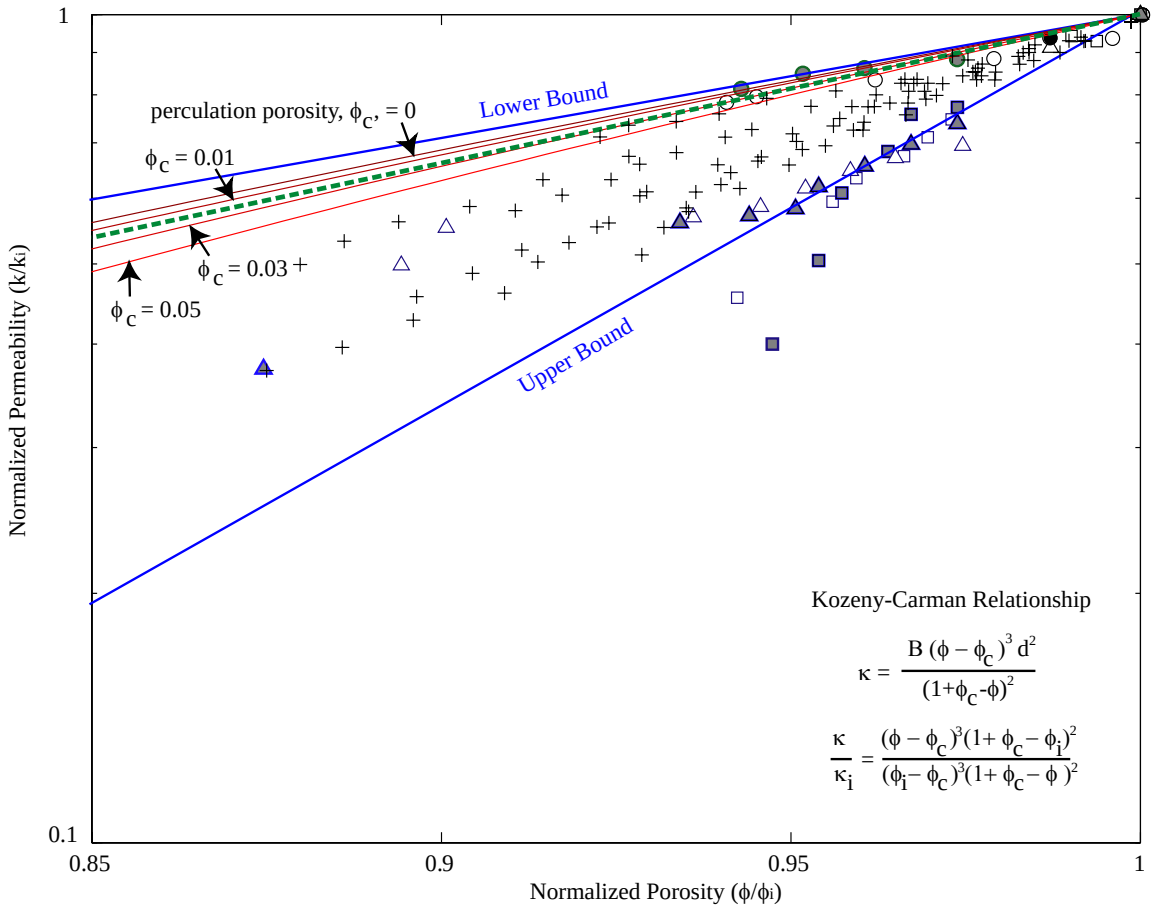

Figure 3.3: Comparing the empirical permeability-porosity relationship derived from several laboratory studies (modified after Chan & Zoback, 2002) with the well-documented Kozeny-Carman relationship. The data points and the two trends are interpretations used in Chan & Zoback's first attempt to study the effect of compaction on permeability. The red lines are derived based on the modified Kozeny-Carman relationship. Note the similarity between the empirical lower bound and the Kozeny-Carman relationship with no percolation porosity. As a result, it is plausible to use the Kozeny-Carman relationship to estimate permeability change as a result of compaction for highly permeable sands. However, the Kozeny-Carman relationship cannot characterize the majority of the data and can therefore only used as a reference for the lower bound of permeability change.

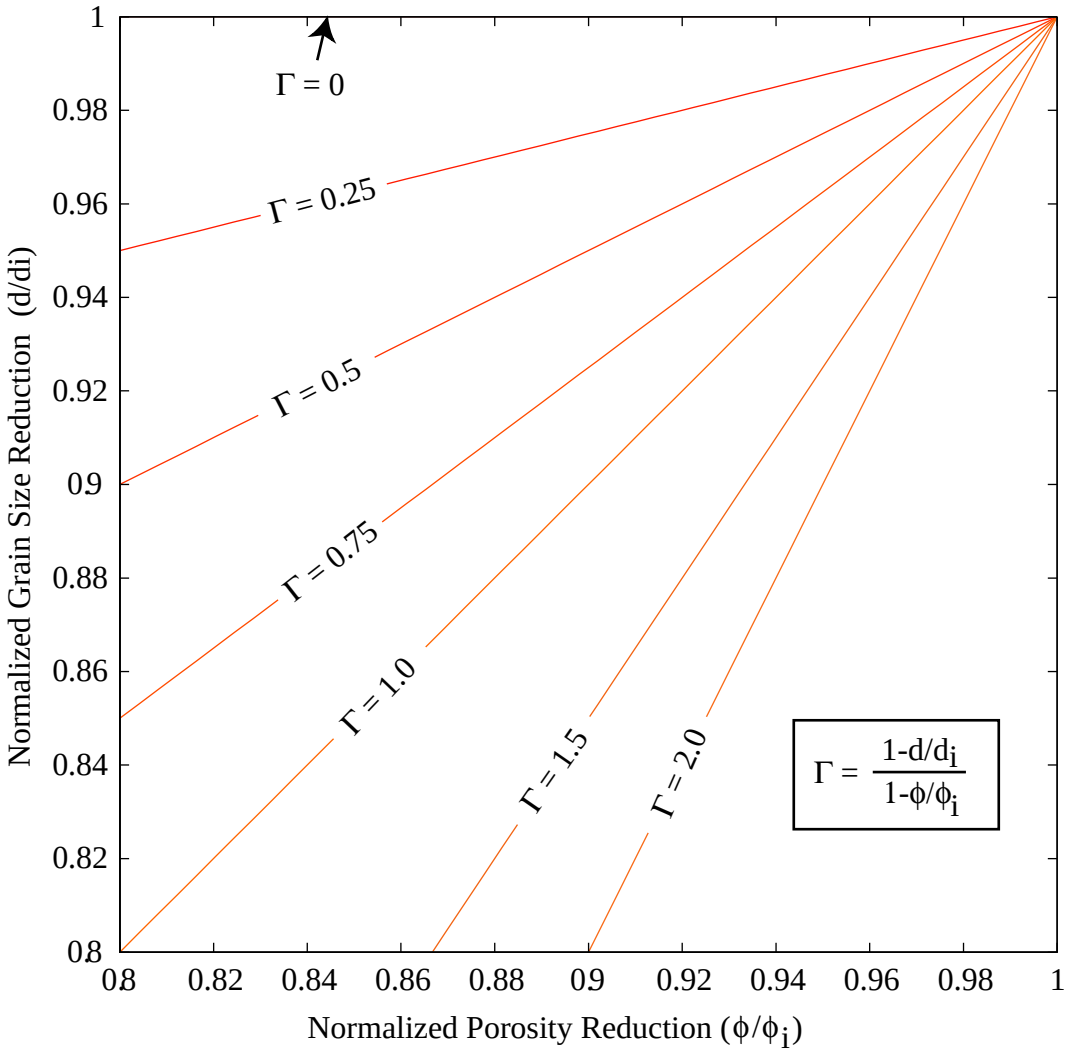

Figure 3.4: The relationship between grain size reduction and porosity loss.

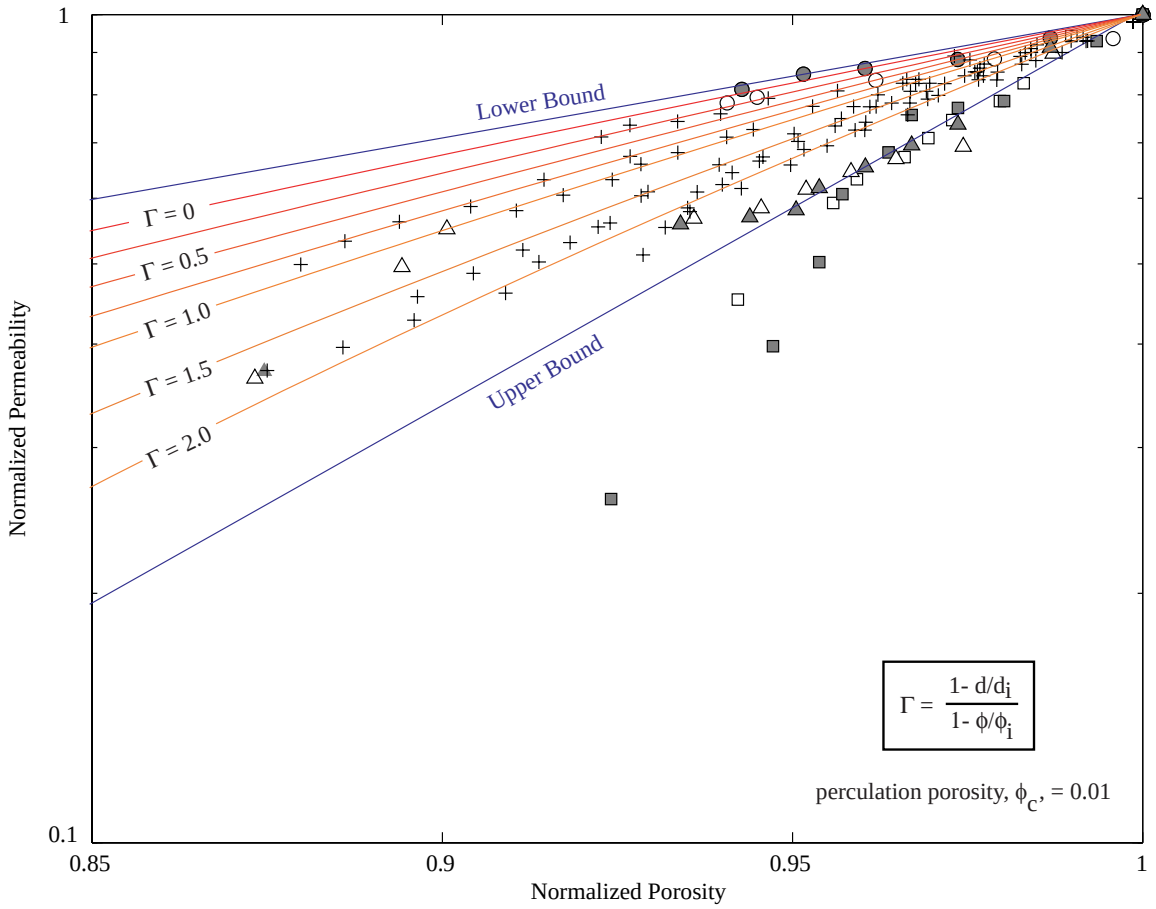

Figure 3.5: The effect of grain size reduction on permeability estimates using the Kozeny-Carman relationship. Using a percolation porosity of 0.01, a drastic decrease in grain size could potentially explain the significant decrease in permeability for some samples. However, grain size reduction is not feasible for a larger porosity change.

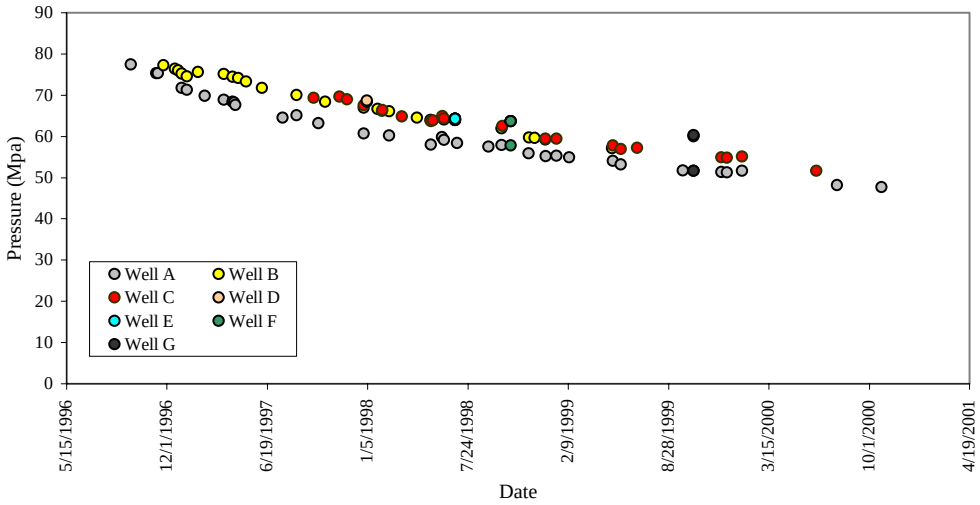

Figure 3.6: Pressure data for Field Z. Two trends are observed suggesting well A penetrated a different sub-compartment to the rest of the wells. Since the reservoir depleted as a single unit in general, stress measurements from most wells can be used to determine the depletion stress path. In addition to the stress measurements, *in-situ* permeability measurements are available from wells A, B and C.

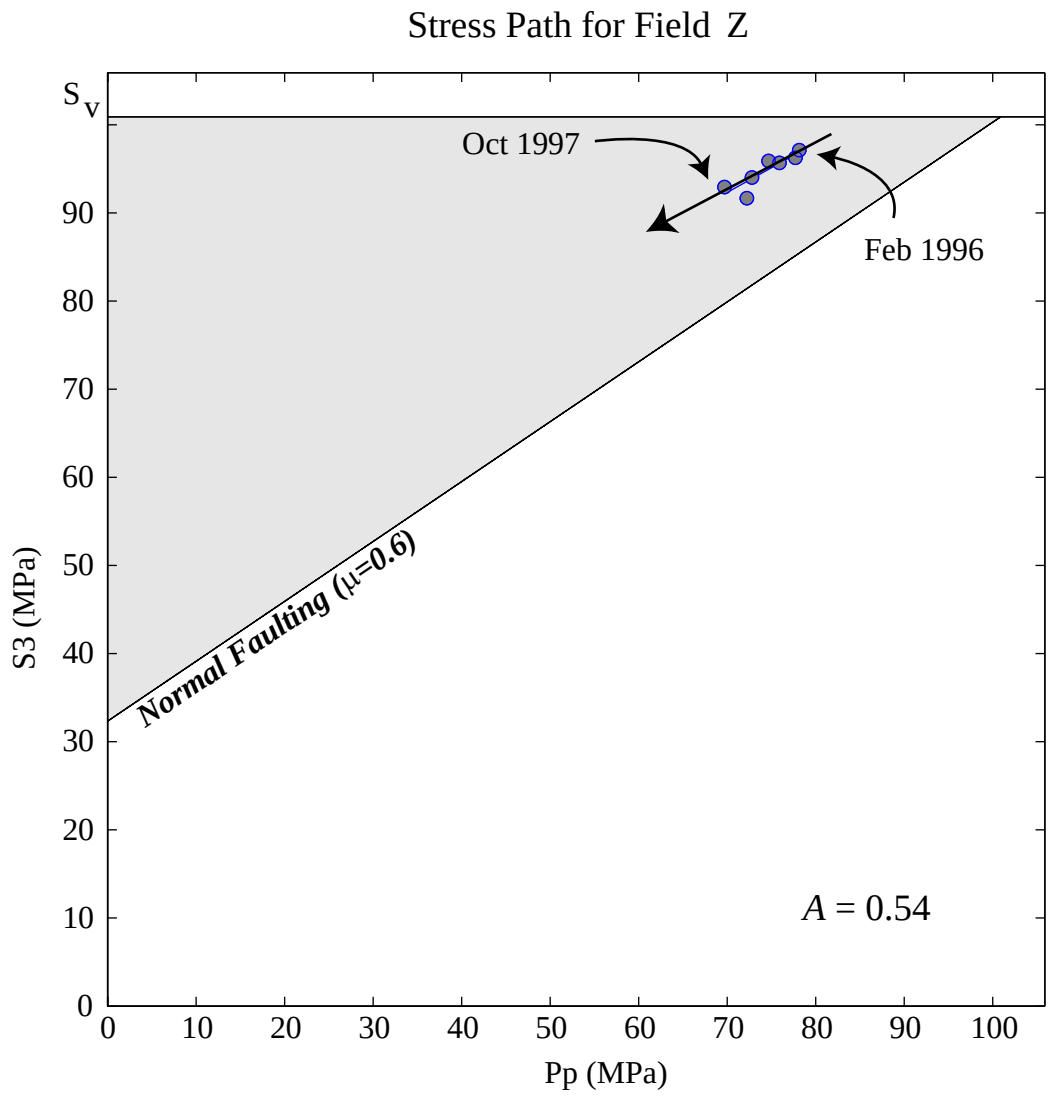

Figure 3.7: Using both pore pressure and *in-situ* stress measurements, the depletion stress path for Field Z is calculated to be about 0.54. In other words, production-induced normal faulting is unlikely to occur in this field.

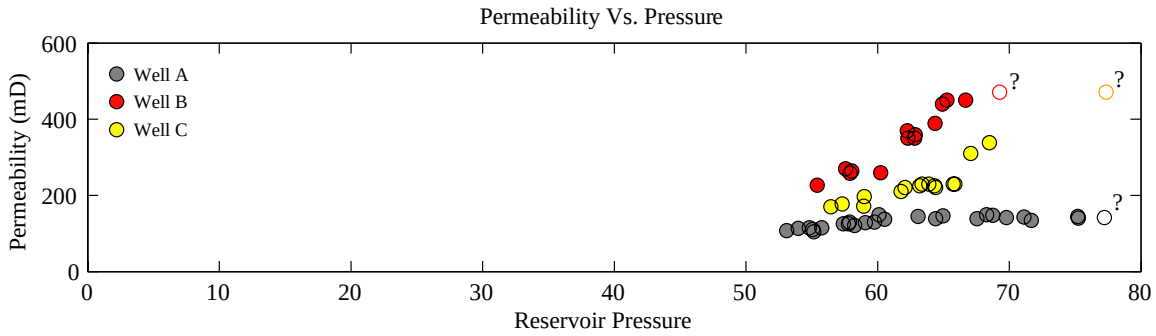

Figure 3.8: Permeability measurements for wells A, B and C. Note that initial permeability for the three wells are missing. Average permeability based on sand quality is used.

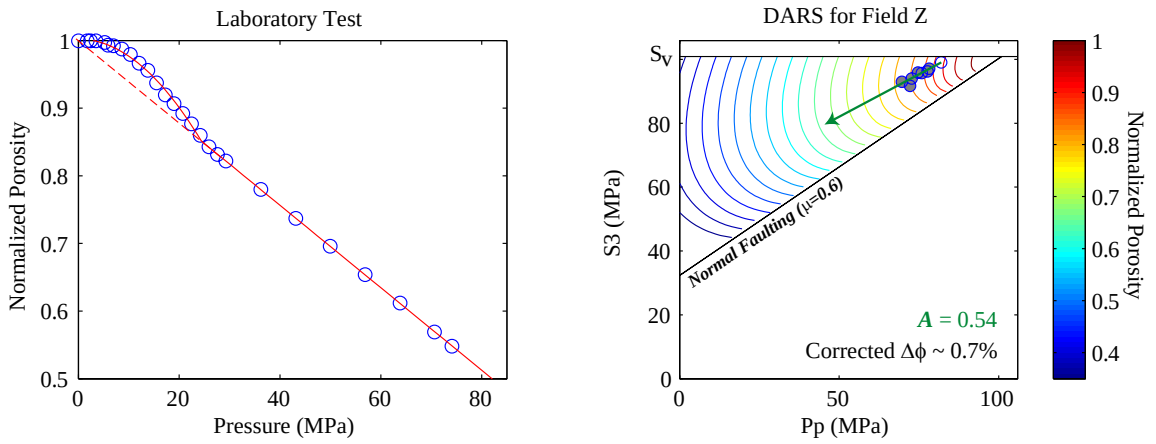

Figure 3.9: DARS for Field Z. The porosity-pressure relationship on the left is derived from the pore volume multiplier used by BP-AMOCO for Field Z based on an internal laboratory report on the samples. The relatively low stress path of 0.54 in Field Z suggests that production-induced normal faulting is unlikely to occur. Using available laboratory experiments, the corrected DARS predicted a 0.7% change in porosity between the two stress measurement points.

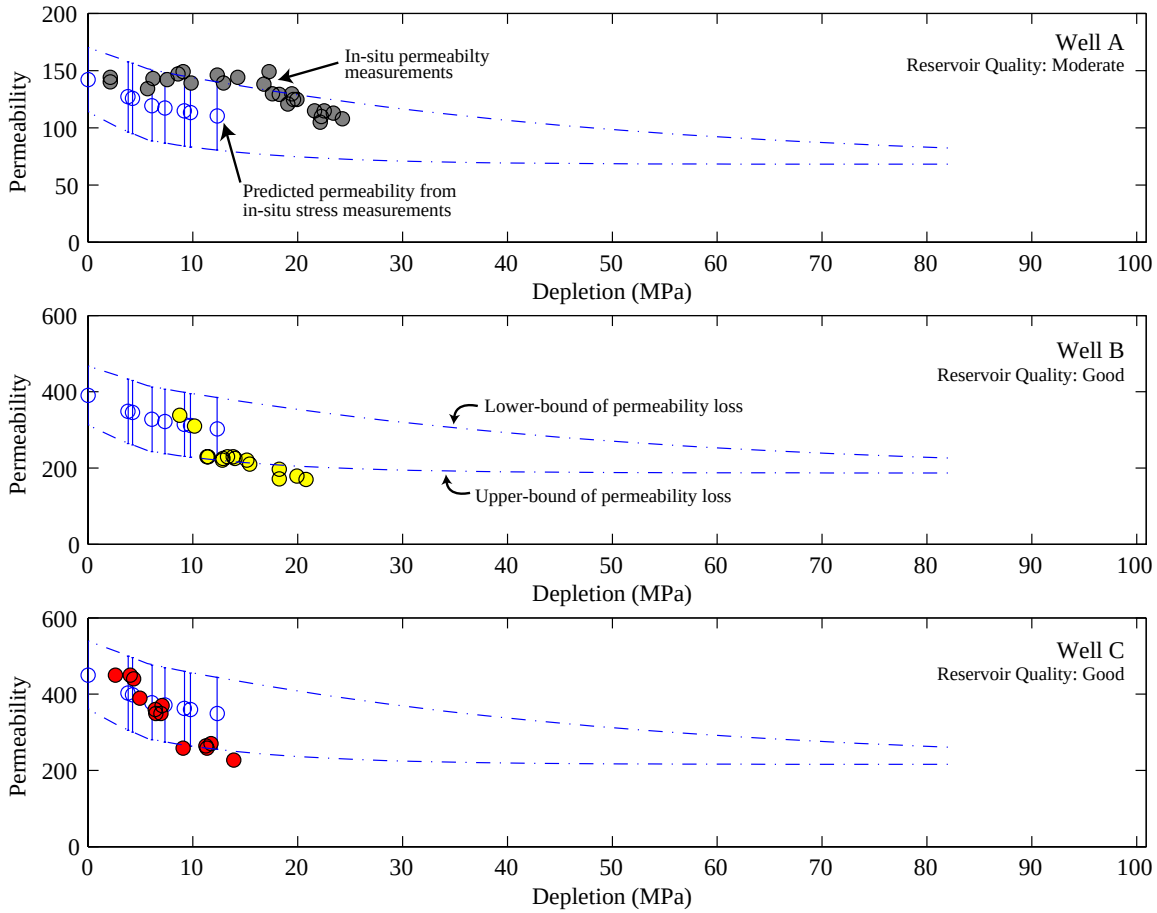

Figure 3.10: Comparison between *in-situ* permeability measurements from well A, B and C with the predicted permeability using DARS and the empirical porosity-permeability relationship. The blue open circles are the predicted average permeability values correspond to the *in-situ* stress measurements. The two blue lines are the lower and upper bound of permeability loss assuming the reservoir will deplete along the same stress path. The color-filled circles are *in-situ* stress measurements from the 3 wells. Initial permeability measurements from these wells are not available. Therefore, estimations based on reservoir properties are used as reference points.

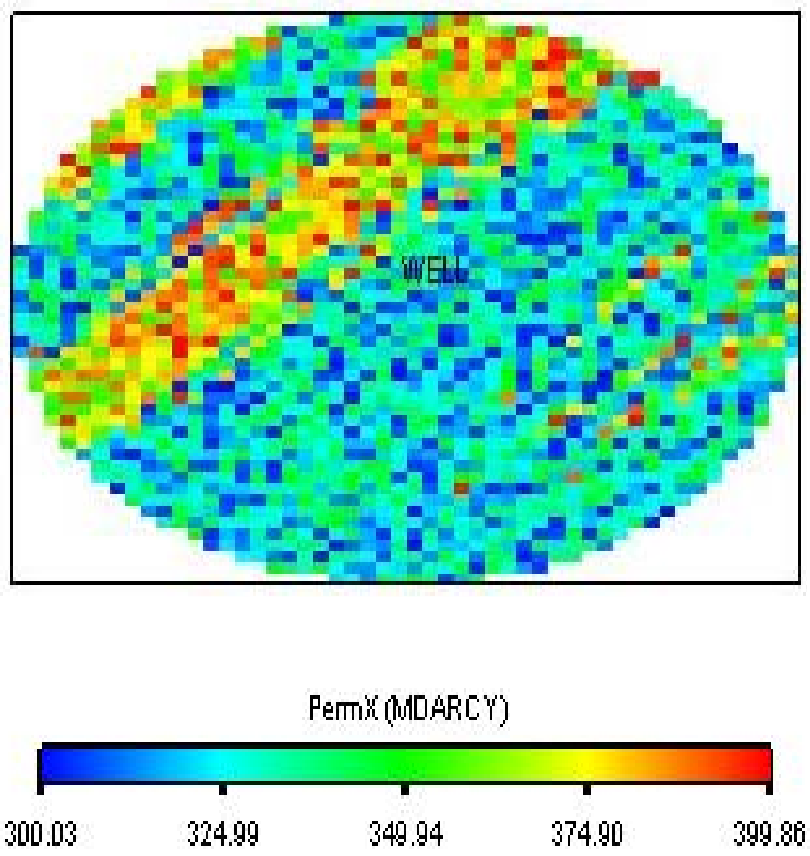

Figure 3.11: The conceptual elliptical reservoir constructed based on *in-situ* stress condition of Field Z. Color code represent a randomized distribution of initial permeability for the reservoir.

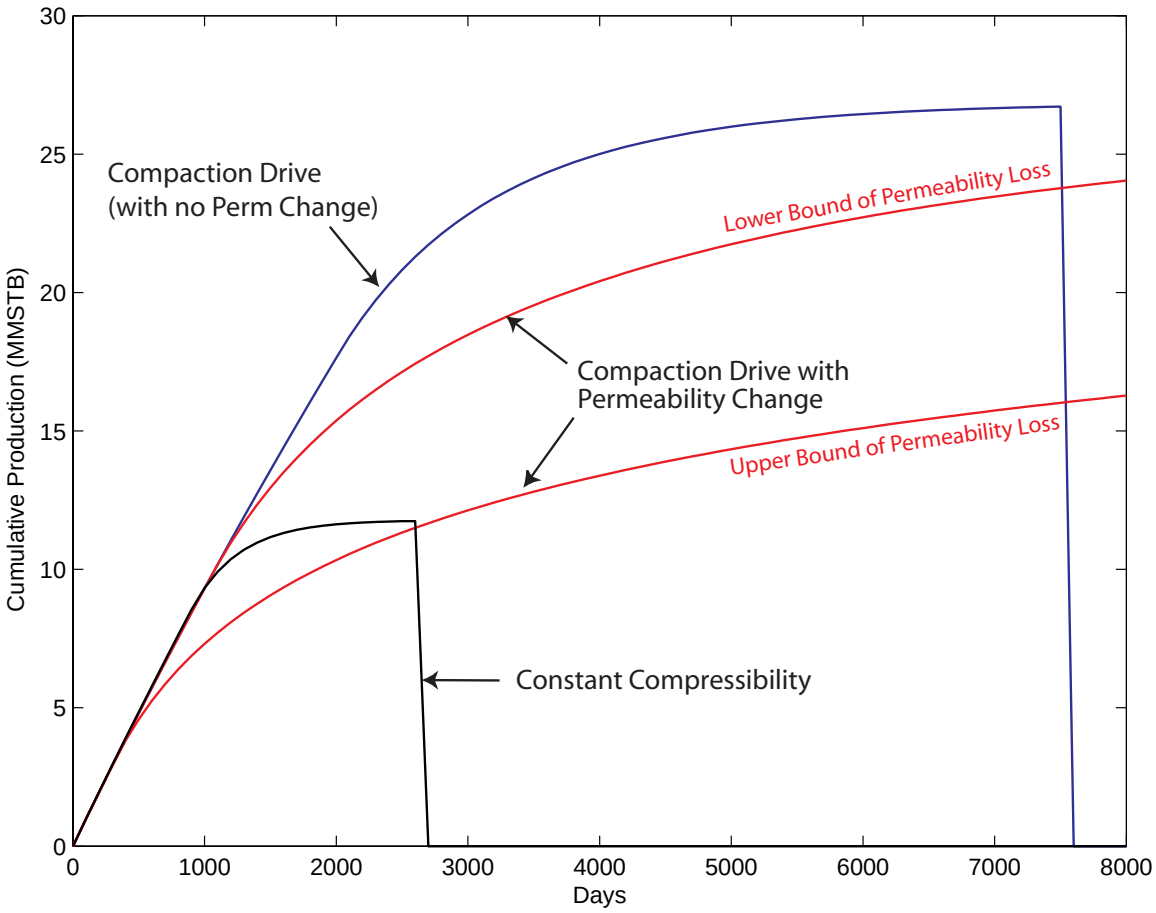

Figure 3.12: Cumulative production estimated from the simulation of a conceptual reservoir. The black line represents the traditional models using constant compressibility throughout production. When porosity loss due to depletion is considered, the cumulative production and production life of this reservoir is increased significantly (blue line). However, the loss in permeability associated with a loss in porosity reduces the reservoir productivity to some degree depending on the severity of compaction-induced permeability loss.

CHAPTER 4

Time-Dependent Elastic-Viscoplasticity (EVP) and the Dynamic DARS

4.1 ABSTRACT

Utilizing a modified Cam Clay cap model, laboratory measurements of the stress-dependency of unconsolidated deformation have been transformed to the reservoir domain such that changes in both stress and strain can be assessed as a function of depletion. In previous chapters, the transformation I termed Deformation Analysis in Reservoir Space (DARS) is built upon a static model to describe the elastic-plastic transformation. Although the static approach yields a reasonable first order approximation of total deformation, it fails to capture the impact of production rate and the time-dependent viscous behaviors that are commonly observed in weak formations associated with depletion. To address time-dependent deformation (e.g., creep strain and viscous deformation), I generalized elastic-viscoplastic strain and strain rate as a function of production rate and time by incorporating Perzyna viscoplastic theory into the modified Cam Clay cap model. Two samples from the Gulf of Mexico Field X have been examined to determine the Perzyna elastic-viscoplastic parameters. The results suggest that viscoplastic effects are minimal until the stress conditions in the reservoir reach the preconsolidation pressure, p*. When the *in situ* stress conditions are larger than p*, the magnitude of viscoplastic strain induced will be a function of the loading rate (or production rate). When production ceases, the induced viscoplastic strain rate decays exponentially through time and independent of pressure. The strain rate decay experienced by the reservoir is equivalent to creep strain experiments conducted in the laboratory. Sensitivity analyses suggest that uncertainties associated with the determination of the Perzyna parameters may have some impact on the estimated cumulative strain. As strain rate can also be expressed as a function of production rate, the static DARS can now be extended into a pressure- and time-dependent dynamic formalism. Applying the elastic-viscoplastic rheology to Field X, I demonstrate that under the current *in situ* stress state, deformation of the producing reservoir is still within the elastic domain. However, if production continues, Field X will reach the preconsolidation pressure and viscoplastic deformation is forecasted to occur and can be significant depending on the future production rate.

4.2 INTRODUCTION

Inelastic deformation associated with hydrocarbon production can lead to irrecoverable porosity and permeability loss as discussed in the two previous Chapters. The modified Cam-Clay cap model has been used for describing the elastic-plastic deformation of unconsolidated sands in the Gulf of Mexico (Chapter 2). Utilizing this model along with *in situ* stress measurements, a pressure-dependent but time-independent static formalism known as the Deformation Analysis in Reservoir Space (DARS) is introduced to estimate how a reservoir responds to depletion. However, this model ignores the time-dependent viscous behavior that can be observed in some weak formations such as Ekofisk chalk (e.g., Tueful & Rhett, 1992) and Wilmington sands, Hagin (e.g., 2004a, b). A time-dependent cap model is required in order to capture such behavior. Perzyna (1966) introduced the elastic-viscoplasticity theory that combined the pressure-dependent elastic/plastic rheology with time-dependent viscous behavior. He suggested that when an elastic-viscoplastic material is subjected to stress that exceeds the material's preconsolidation pressure, p*, the resulting deformation will be a function of strain and strain rate. Lerouiel *et al.* (1985) concluded experimentally that elastic-viscoplastic deformation is dependent on stress, strain and strain-rate but not stress-rate, consistent with the elastic-viscoplastic theory of Perzyna. Adachi and Oka (1982) incorporated the Perzyna viscoplasticity theory to the original Cam-Clay cap model to describe deformation associated with clays and soils. Following Adachi and Oka's procedure, Hagin (2003) successfully demonstrated that the rate-dependent Perzyna viscoplastic parameters can be scaled to the static end cap surfaces described in the modified Cam-Clay cap model through p*. As a result, it is possible to extend the pressure-dependent but time-independent static DARS into a pressure- and time-dependent dynamic DARS formalism because the static DARS is based on the modified Cam-Clay cap model.

In this Chapter, I extend the elastic-viscoplastic model used by Hagin (2003) from laboratory boundary conditions to incorporate a successive loading history such that the cumulative elastic-viscoplastic strain at any given time can be estimated. Following Hagin's experimental procedure (Hagin, 2003), two new samples from the Gulf of Mexico Field X are examined to determine their elastic-viscoplastic behavior and the

necessary Perzyna viscoplastic fitting parameters. Using these Perzyna viscoplastic parameters, I demonstrate how the samples will behave under different loading strategies. The sensitivity of the laboratory-derived constants on the total strain estimation based on these parameters is also examined. I then apply the elastic-viscoplastic rheological model to a dynamic DARS formalism and re-visit the porosity loss in the Gulf of Mexico Field X. A forecast of the impacts of future production rates on porosity loss is also made for Field X.

4.3 TIME-DEPENDENT ELASTIC-VISCOPLASTICITY (EVP)

Although the elastic-plastic Cam-Clay cap model can successfully predict the changes in porosity associated with depletion in most cases, the model may breakdown when attempting to model the deformation of some weak unconsolidated materials. Viscoelasticity and viscoplasticity theory are often used for describing deformation associated with the loading of unconsolidated sands. Both theories add time-dependent viscous behavior to the pressure dependent static deformation that a loaded sample may experience. The main difference between the two theories is the nature of the static deformation: viscoelasticity assumes a recoverable pressure-dependent static deformation while such deformation is irrecoverable for a viscoplastic material (Figure 4.1). Theoretically, both viscoelasticity and viscoplasticity describe the behavior of the sample during loading cycles; however, the assumption of recoverable static deformation for viscoelasticity is unrealistic for rocks in practice because rocks fail under tension as a result of their low tensile strength (Vernik & Zoback, 1990; Vernik *et al*., 1993). The assumption of recoverable static deformation from viscoelasticity becomes unrealistic. Therefore, viscoplasticity is selected to model the time-dependent viscous behavior of weak unconsolidated sands.

4.3.1 Estimating Elastic-Viscoplastic Strain from Production History

Based on the Perzyna viscoplasticity theory, total strain rate is equivalent to the sum of elastic strain rate, $\dot{\varepsilon}_e$, and viscoplastic strain rate, $\dot{\varepsilon}_{VP}$ (see Hagin, 2003 for a more detailed discussion) such that:

$$\dot{\varepsilon}_{Total} = \dot{\varepsilon}_e + \dot{\varepsilon}_{VP} \quad \text{.....(4.1)}$$

As proposed by Hagin (2003), the elastic behavior of weak unconsolidated sands is best described by a power law relationship:

$$\varepsilon_e(t_0) = Gp(t_0)^H \quad \text{.....(4.2)}$$

where G and H are laboratory constants and $p(t_0)$ is the pressure applied on the material at time t_0. Note that time in all the Equations are in terms of seconds. The corresponding elastic strain rate, $\dot{\varepsilon}_e$, is the time derivative of (4.2),

$$\dot{\varepsilon}_e = GHp(t_0)^{H-1}\,\dot{p}(t_0) \quad \text{.....(4.3)}$$

where $\dot{p}(t_0)$ is the loading rate at time t_0.

The viscoplastic strain rate resulting from the same applied pressure is defined as:

$$\dot{\varepsilon}_{VP}(t_0) = Ap(t_0)^D \quad \text{.....(4.4)}$$

where A and D are parameters determined through laboratory experiments. This viscoplastic strain rate will decay through time if no extra pressure is applied onto the material such that:

$$\dot{\varepsilon}_{VP}(t > t_0) = B(t_k + t)^E\,\dot{\varepsilon}_{VP}(t_0) \quad \text{.....(4.5)}$$

with B being another laboratory parameter and t_k is a time constant to satisfy the initial condition of the viscoplastic strain rate and is defined as $t_k = B^{-1/E}$ with $t_0 = 0$. As a result, the viscoplastic strain rate for a given pressure at time t can be described as:

$$\dot{\varepsilon}_{VP}(t) = Cp(t_0)^D(t_k + t)^E \quad \text{.....(4.6)}$$

where C is the product of A and B. To calculate the cumulative viscoplastic strain at time t, Equation (4.6) needs to be summed up from time t_0 to t such that:

$$\varepsilon_{VP}(t) = \sum_{n=0}^{t} Cp(t_0)^D (t_k + t_n)^E \quad \text{.....(4.7)}$$

Assuming $t_0 = 0$, Equation (4.7) can be solved analytically such that:

$$\varepsilon_{VP}(t) = \int_0^t Cp(0)^D (t_k + n)^E dn$$

$$= \frac{Cp(0)^D}{E+1}\left[(t_k + t)^{E+1} + {t_k}^{E+1}\right] \quad \text{.....(4.7a)}$$

As the loading pressure changes through time, a new viscoplastic strain will be introduced. In order to calculate the cumulative viscoplastic strain through time with a changing pressure, contributions from the viscoplastic strains induced at each time step have to be included (Figure 4.2). Mathematically, the cumulative viscoplastic strain at time t_i is:

$$\varepsilon_{VP}(t_i) = C\Big\{p(t_0)^D\left[(t_k + t_0)^E + (t_k + t_1)^E + \ldots + (t_k + t_i)^E\right]$$
$$+ p(t_1)^D\left[(t_k + t_0)^E + (t_k + t_1)^E + \ldots + (t_k + t_{i-1})^E\right] + \ldots$$
$$+ p(t_i)^D (t_k + t_0)^E\Big\} \quad \text{.....(4.8)}$$

Equation (4.8) can be simplified as:

$$\varepsilon_{VP}(t_T) = \sum_{m=0}^{T}\sum_{n=0}^{T-m} Cp(t_m)^D (t_k + t_n)^E \quad \text{.....(4.9)}$$

Equation (4.9) can also be expressed in terms of integrals such that:

$$\varepsilon_{VP}(T) = \int_0^T \int_0^{T-m} Cp(m)^D (t_k + n)^E dndm \quad \text{.....(4.10)}$$

The cumulative viscoplastic strain at time T can now be estimated by solving (4.10):

$$\varepsilon_{VP}(T) = \frac{C}{E+1}\int_0^T p(m)^D\left[(t_k + T - m)^{E+1} - {t_k}^{E+1}\right]dm \quad \text{.....(4.11)}$$

Because t_k is independent from *m*, the second part of the integral can be solved easily:

$$\varepsilon_{VP}(T) = \frac{C}{E+1}\int_0^T p(m)^D (t_k + T - m)^{E+1} dm$$

$$- \frac{Ct_k}{(D+1)(E+1)}\left[p(T)^{D+1} - p(0)^{D+1}\right] \quad (4.12)$$

While the remaining integral in Equation (4.12) can be solved using integration by parts and Taylor Expansion such that:

$$\int_0^T p(m)^D (t_k + T - m)^{E+1} dm = -\frac{p(m)^D}{E+2}(t_k + T - m)^{E+2}\Big|_0^T$$

$$- \int_0^T \frac{-Dp(m)^{D-1}\dot{p}(m)}{E+2}(t_k + T - m)^{E+2} \quad (4.13)$$

The integral in Equation (4.13) can be considered as a higher order term and is assumed to have minimal impact on the solution. Substituting (4.13) back to (4.12) will yield:

$$\varepsilon_{VP}(T) = \frac{C}{(E+1)(E+2)}\left[p(0)^D (t_k + T)^{E+2} - p(T)^D t_k{}^{E+2}\right]$$

$$- \frac{Ct_k}{(D+1)(E+1)}\left[p(T)^{D+1} - p(0)^{D+1}\right] \quad (4.14)$$

To estimate the total strain at time T as a result of both elastic and viscoplastic strain can be determined by combining (4.2) and (4.14) such that:

$$\varepsilon_{Total}(T) = Gp(T)^H + \frac{C}{(E+1)(E+2)}\left[p(0)^D (t_k + T)^{E+2} - p(T)^D t_k{}^{E+2}\right]$$

$$- \frac{Ct_k}{(D+1)(E+1)}\left[p(T)^{D+1} - p(0)^{D+1}\right] \quad (4.15)$$

And the total strain rate at time T is:

$$\dot{\varepsilon}_{Total}(T) = GHp(T)^{H-1}\dot{p}(T) + Cp(T)^D (t_k + T)^E \quad (4.16)$$

4.3.2 Elastic-Viscoplastic Parameters of Samples from the Gulf of Mexico Field X

Following the experimental procedures proposed by Hagin (2003), two samples from GOM Field X have been tested (Hagin, *personal communication*). The results for these two samples are presented in Figure 4.3. The two p* on Figure 4.3 indicate the effective pressures at which the transition from pure elastic deformation to elastic-viscoplastic deformation occur for the two applied strain rates. Note that when the applied effective stress is smaller than p*, the elastic strains experienced by the two samples are very similar. Porosity reduction becomes more drastic when the samples are loaded beyond p* at which viscoplastic strain becomes more significant. Experimental results show that the preconsolidation pressures vary as strain rate changes. Another important characteristic from these two samples is the rate of change in porosity as a result of increasing pressure. Porosity reduction appears to happen faster for a higher strain rate in the elastic-viscoplastic domain. A creep test (where pressure is being held constant) is performed for one of the samples to estimate the time-delay response of porosity. The elastic strain estimated from Figure 4.3 is:

$$\varepsilon_e = 0.01 p^{0.51} \quad \text{.....(4.17)}$$

The Perzyna equation is estimated by comparing p* and strain rate (Fig. 4.4) such that:

$$\dot{\varepsilon}_{VP} = 4.32 \times 10^{-55} p^{28.7} \quad \text{.....(4.18)}$$

To estimate how the strain rate will decay, the decay function for the viscoplastic strain rate is determined based on the creep test performed (Fig. 4.5). Note that this decay function is constant for all p* such that:

$$\dot{\varepsilon}_{VP}(p_0, t) = 4.06 \times 10^{-5} t^{-0.58} \dot{\varepsilon}_{VP}(p_0) \quad \text{.....(4.19)}$$

As discussed in Chapter 3, production-induced porosity change can have a big impact on permeability. Figure 4.6 displays the change in permeability measured during the experiment. Only the initial permeability for the two samples are measured based on the steady state Darcy's Law type inversion due to time constraints. An alternate permeability inversion that required less time was used following the methods proposed by Boitnott (1997). Boitnott (1997) suggested that permeability could be inverted from

observing the transmission of a transient pore pressure pulse across the sample. Using this method, permeability along with strain can be measured simultaneously. In Figure 4.6, it is apparent that permeability of the samples can be estimated fairly closely by the simple Kozeny-Carman relationship introduced in Chapter 2. However, as plastic deformation begins, permeability reduction is more drastic than the Kozeny-Carman relationship predicts.

The total strain and strain rate for Field X estimated from these laboratory experiments based on Equation (4.15) and (4.16) are:

$$\varepsilon_{Total}(T) = 2.94\times10^{-59}\left[p(0)^{28.7}\left(2.68\times10^{-8}+T\right)^{1.42} - 1.77x10^{-11}\,p(T)^{28.7}\right] - 3.77\times10^{-68}\left[p(T)^{29.7} - p(0)^{29.7}\right] + 0.01p(T)^{0.51} \quad \text{.....(4.20)}$$

$$\dot{\varepsilon}_{Total}(T) = 0.0051p(T)^{-0.49}\,\dot{p}(T) + 1.75\times10^{-59}\,p(T)^{28.7}\left(2.68\times10^{-8}+T\right)^{-0.58} \quad \text{.....(4.21)}$$

Figure 4.7 shows the impact of viscoplastic strain on the total strain estimated from Equation (4.20) and (4.21). Assuming there is no change in horizontal stress during pressure reduction for simplicity, i.e., only a change in effective vertical stress acting on the sample, Figure 4.7 demonstrates that loading rates have a big impact on the cumulative viscoplastic strain. The initial effective stress at t = 0 is set at 40 MPa in Figure 4.7, five loading durations are used: 0.5, 1, 3, 10 and 20 years. A 20 MPa change in effective stress is used in Figure 4.7A. The five black lines represent loading from 40 MPa to 60 MPa over the five specific loading durations. Once the effective stress of 60 MPa is reached, loading is abandoned for the remaining time. Note that despite changes in loading durations, the impacts of loading rates on total strain accumulated by year 20 are minimal as a result of the predominantly elastic deformation during the loading. Similarly, Figure 4.7B, C and D are set up as in Figure 4.7A except the final pressures are set at 65, 70 and 75 MPa. As expected, the viscoplastic strain induced during loading is proportional to the applied stress on the samples but inversely proportional to loading rates. Figure 4.7D further suggests that the loading time will have the most significant

impact on the total strain if the change in stress is significantly large (effective stress changes from 40 MPa to 75 MPa).

To illustrate the sensitivity of the Perzyna viscoplastic parameters on the predicted strains, I have conducted a sensitivity analysis assuming the formation is loaded from 40 MPa to 65 MPa for a duration ranging from 0.5 years to 20 years. Figure 4.8A- 4.8D show the sensitivity of the four Perzyna parameters on the estimated viscoplastic strains. The vertical axes for these figures are the production duration, the horizontal axes are potential uncertainties associated with the four parameters. The contour lines represent the estimated viscoplastic strains based on the varying loading rates and the corresponding Perzyna parameter assuming the rest of the parameters determined are accurate. Two of the parameters, A and B, have minimal impact on the viscoplastic strain if the production rates (or duration of loading) are determined. While the estimated viscoplastic strains are less sensitive to production rates, uncertainties in determining parameter D and E can have a significant impact on the estimated strains.

4.4 FROM STATIC DARS TO DYNAMIC DARS

The DARS formalism introduced in Chapter 2 is a pressure-dependent but time-independent analysis since it is based on pressure-dependent experiments and the modified Cam-Clay cap model. For weak sand reservoirs in which viscous deformation could be significant, experiments that capture this phenomenon should be used. By incorporating the elastic-viscoplasticity theory to describe the rheology of the formation, the pressure-dependent time-independent static DARS formalism can now be extended to a pressure- and time-dependent dynamic DARS formalism.

Unlike laboratory conditions in which the sample is loaded through increasing confining pressure (or axial stress), the reservoir formation is loaded as a result of decreasing pore pressure that leads to increasing effective stress acting on the rock. Along with the reduction of horizontal stress in response to depletion, the pressure terms and p(T) in Equation (4.12) and (4.13) should be replaced by the corresponding p* calculated from Equation (2.11). This substitution allows a more accurate estimation of porosity change as a result of depletion and the corresponding depletion-induced stress drop.

Including time and pressure changes when estimating strain represents another extension of DARS for estimating the time-delayed reservoir compaction after production ceases (Chapter 5).

In the following sections, I will re-examine the porosity and permeability reduction in the Gulf of Mexico Field X using the dynamic DARS analysis and forecast the potential impact of varying production rates on reservoir compaction.

Figure 4.9 re-plots the measured stress and pressure from Field X in the p:q space. Note that all the *in situ* measurements are located within the end cap that marks the boundary between the elastic domain and the viscoplastic domain. The end cap in Figure 4.9 is based on the preconsolidation pressure measured based on the 10^{-5}/s strain rate. By transforming the measured changes in stress and pressure into effective p*, porosity reduction is then estimated (Fig. 4.10). The thick black dotted line marks the year when the last stress measurements were recorded. A depletion of 52 MPa has occurred in Field X during this time. Assuming another 15 MPa of pressure reduction will occur in the following 10 years, I estimated the potential impact of production rate at Field X on the changes in porosity. Figure 4.11 shows a close-up view of the predicted porosity reduction that may happen from year 15 to year 25 in Figure 4.10. Four depletion periods have been used for the 15 MPa pressure reduction by changing the production durations from 1, 3, 5 and 10 years. Once the 15 MPa pressure reduction is reached, the pore pressure will be kept constant to simulate reservoir abandonment. The four black lines are the expected change in porosity corresponding to the depletion strategies assuming Field X deformed elastically. Note that in these cases, reservoir abandonment will not cause any further porosity reduction after depletion ceases. However, using the Elastic-viscoplastic rheology derived in this Chapter (red lines) demonstrates that the predicted changes in porosity associated with varying production duration can be significant. It is apparent that the cumulative porosity lost at the time when production ceases increases significantly when the depletion duration is short. In other words, a high production rate (or strain rate) will force the reservoir to hit the preconsolidation pressure sooner than a slower production rate. Once p* is reached, viscoplastic deformation will become the dominant deformation mode and the instantaneous viscoplastic strain associated with the increasing pressure will follow the Perzyna viscoplastic relationship. As demonstrated in

both Figure 4.4 and Equation 4.18, viscoplastic strain rate is highly sensitive to p*. In contrast, if the production rate is reasonably slow, the reservoir will reach the preconsolidation pressure at a much later time and the slow changes in pressure also implies a slower change in the instantaneous viscoplastic strain rate resulting in a significantly smaller porosity reduction. Once production ceases, the deformation occurring in the reservoir will be equivalent to a laboratory creep experiment (as presented in Fig. 4.5 and Equation 4.19 where viscoplastic strain rate decay is independent from applied pressure). As a result, if Field X is to be depleted at a fast rate in the near future, a large porosity reduction should be expected.

4.5 CONCLUSION

By incorporating Perzyna elastic-viscoplasticity, the pressure dependent but time-independent static DARS formalism has been expanded into a dynamic formalism that is both time and pressure dependent. Following experimental procedures proposed by Hagin (2003), two Gulf of Mexico samples from Field X are examined. Constitutive laws for these samples are derived for estimating strain associated with the magnitude and rate of pressure reduction. Since the power-law relationship has been used for describing the viscoplastic strain and the decay function, the uncertainties associated with the determination of coefficient D and E (the power index) can have a significant impact on the estimated strain. In contrast, the uncertainties of A and B have a much smaller impact to the estimated strain compared with production rates.

From the *in situ* stress measurements, depletion at Field X is currently occurring within the elastic domain. However, I have shown that if production is to continue at Field X, viscoplastic deformation will become more significant in the near future. Depending on the rate of production planned, the viscoplastic strain will be significantly larger than the elastic strain if Field X is to be depleted at a high rate. This could be an advantage for the reservoir productivity as a large porosity reduction in a short time might enhance compaction drive and lead to a more productive field (Fig 3.12). Unfortunately, the large porosity loss might also lead to severe reservoir compaction that may damage the well bore or lead to sea floor subsidence. A more detailed finite element

model or simulation is required in order to determine the advantage and disadvantage of a high production rate at Field X in the near future.

4.6 REFERENCES

Adachi, T. & Oka, F., 1982. Constitutive equations for normally consolidated clays based on elasto-viscoplasticity. *Soils and Foundations*, **22** (4), 57-70.

Boitnott, G.N., 1997. Use of complex pore pressure transients to measure permeability of rocks. SPE38717.

Leroueil, S., Kabbaj, M., Tavenas, F., & Bouchard, R., 1985. Stress-strain-strain rate relation for the compressibility of sensitive natural clays. *Geotechnique*, **2**, 159-180.

Hagin, P.N., 2003. *Application of Viscoelastic, Viscoplastic, and Rate-and-State Friction Constitutive Laws to the Deformation of Unconsolidated Sands*. Unpublished Ph.D. Thesis, Stanford University, 126pp.

Hagin, P.N. & Zoback, M.D., 2004a. Viscous deformation of unconsolidated reservoir sands (Part 1): Time-dependent deformation, frequency dispersion and attenuation, *Geophysics*, **69**, 731-741.

Hagin, P.N. & Zoback, M.D., 2004b.Viscous deformation of unconsolidated reservoir sands (Part 2): Linear viscoelastic models, *Geophysics*, **69**, 742-751.

Perzyna, P., 1966. Fundamental problems in viscoplasticity. *Advances in Applied Mechanics*, **9**, 243-377.

Teufel, L.W., & Rhett, D.W., 1992. Failure of chalk during water-flooding of the Ekofisk field. SPE24911.

Vernik, L., Bruno, M., & Bovberg, C., 1993. Empirical relations between compressive strength and porosity of siliclastic rocks. *International Journal Rock Mechanics and Mining Sciences*, **30** (7), 677-680.

Vernik, L., & Zoback, M.D., 1990. Strength anisotropy in crystalline rock: implications for assessment of in situ stresses from wellbore breakouts, in *Rock Mechanics Contributions and Challenges: Proceedings of the 31st U.S. Symposium*, edited by W.A. Hustrulid and G.A. Johnson, 841-848.

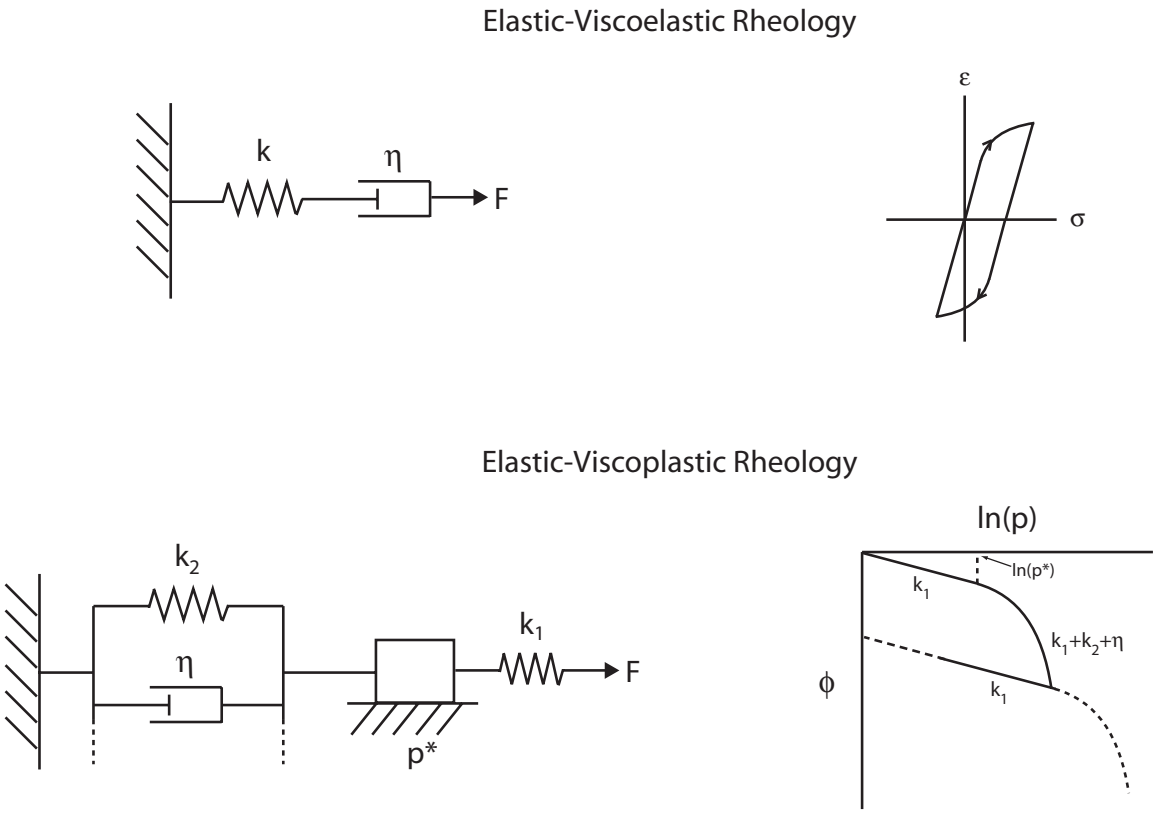

Figure 4.1: Schematic diagrams comparing the elastic-viscoelastic and the elastic-viscoplastic rheology. For an elastic-viscoelastic material, it behaves similarly to a pair of spring and dashboard connected in series. The corresponding stress-strain relationship shown suggests that all the strain induced from pulling the system can be fully recovered. For an elastic-viscoplastic material, some of the strains (or porosity loss in terms of rock property) are irrecoverable. Note that in order to fully recover the strain for the elastic-viscoelastic material, a negative stress is required. In terms of rock mechanics, such negative force (or tension) is restricted to a very small value since tensile strength for most rocks are very small. As a result, elastic-viscoelastic rheology may be able to describe the time-dependent behavior of rock; it does not truly describe the nature of the rock since it is almost impossible to put rocks in tension without causing failure.

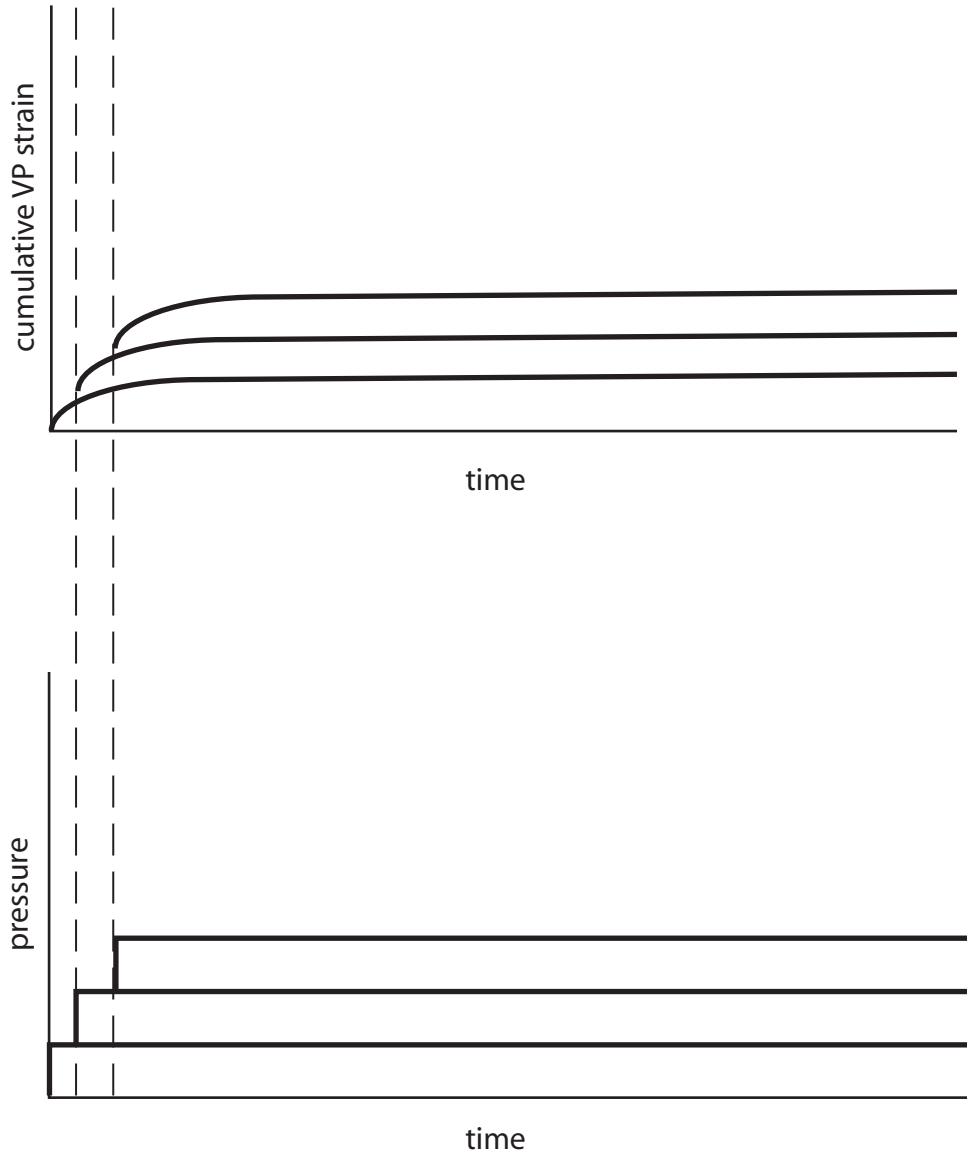

Figure 4.2: Cumulative elastic-viscoplastic strain through a series of loading steps.

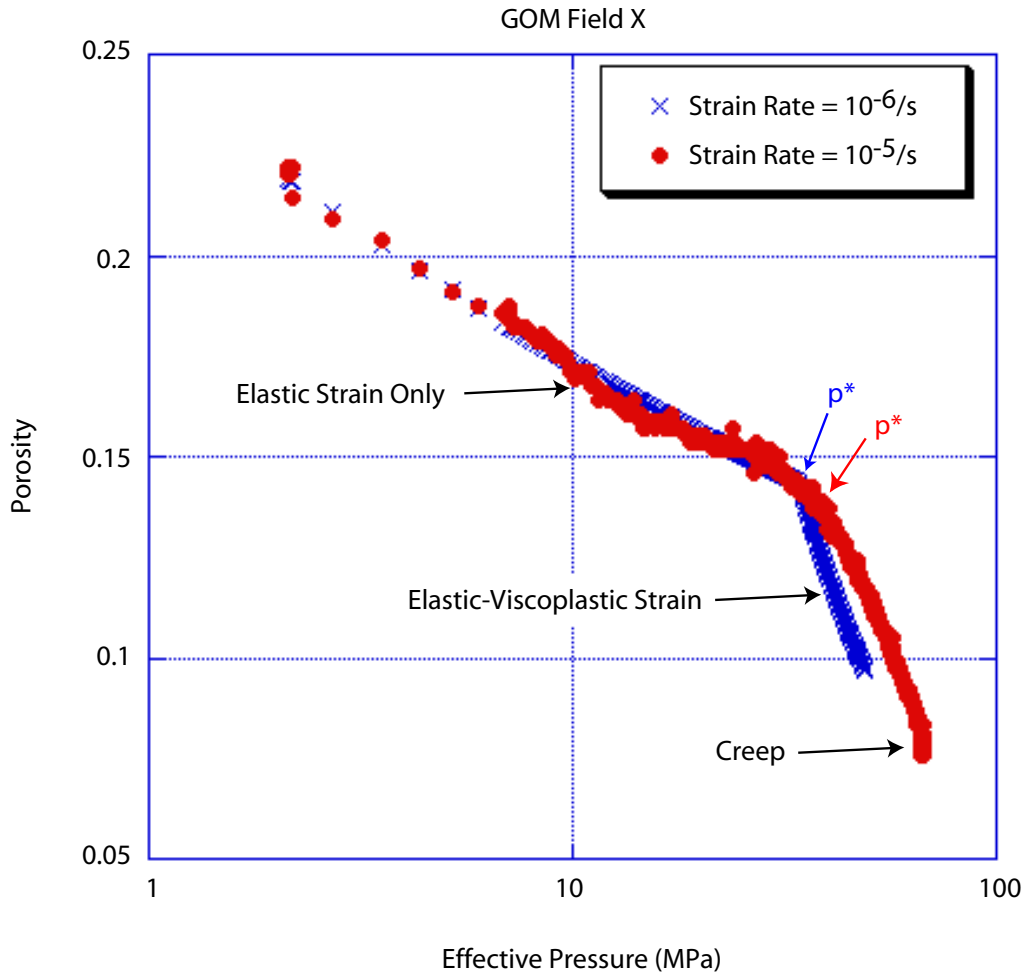

Figure 4.3: Experimental data of the two samples from Gulf of Mexico Field X (Hagin, *personal communication*). The samples are subjected to different strain rates. Significant drops in porosity can be observed in both samples when loaded beyond p* that represents the boundary between the elastic domain from the viscoplastic domain. Porosity reduction for both samples is relatively similar in the elastic domain but show a slight difference in the rate of porosity loss in the viscoplastic domain. It is apparent that higher strain rate will result in a faster porosity reduction than a slower strain rate. A creep test is performed at the end of the experiment for one of the samples to determine the decay of strain through time of the sample.

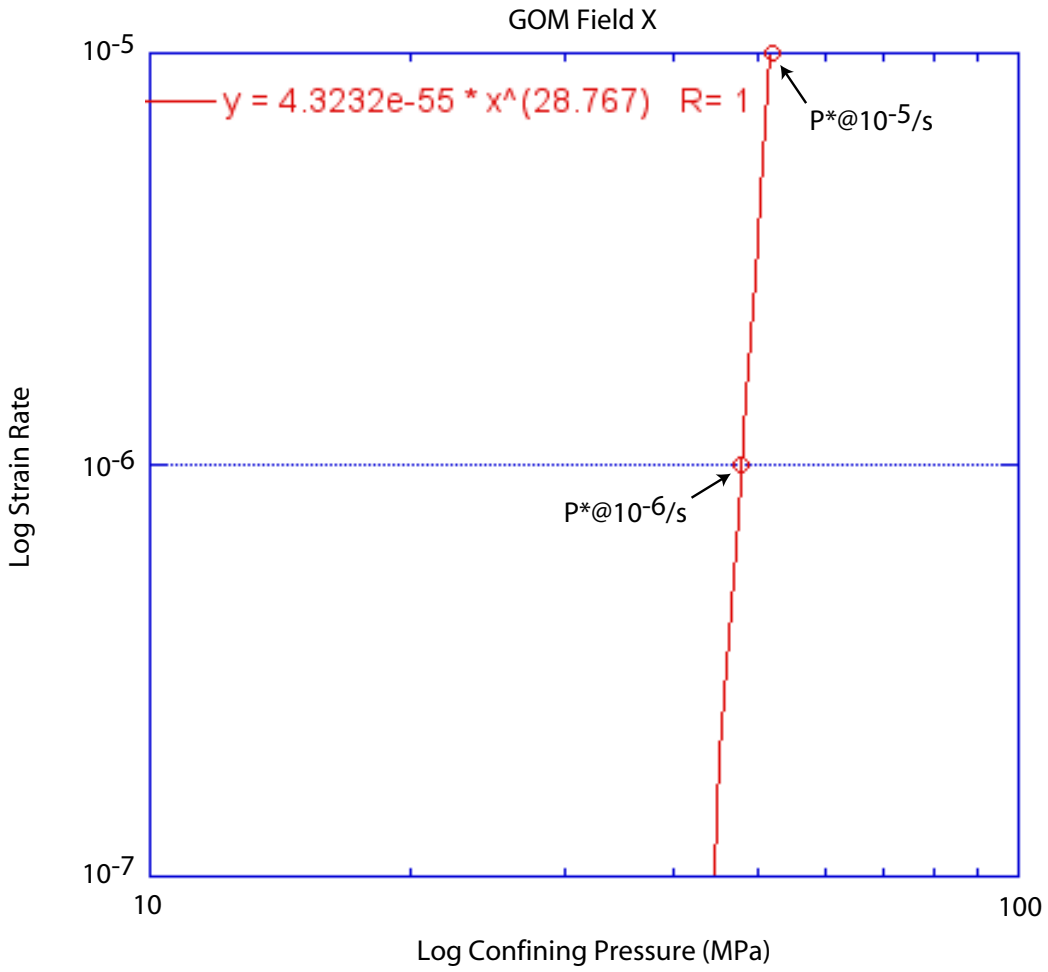

Figure 4.4: Determination of the Perzyna viscoplastic parameters (after Hagin, *personal communication*). The two points are the p* determined in Figure 4.3.

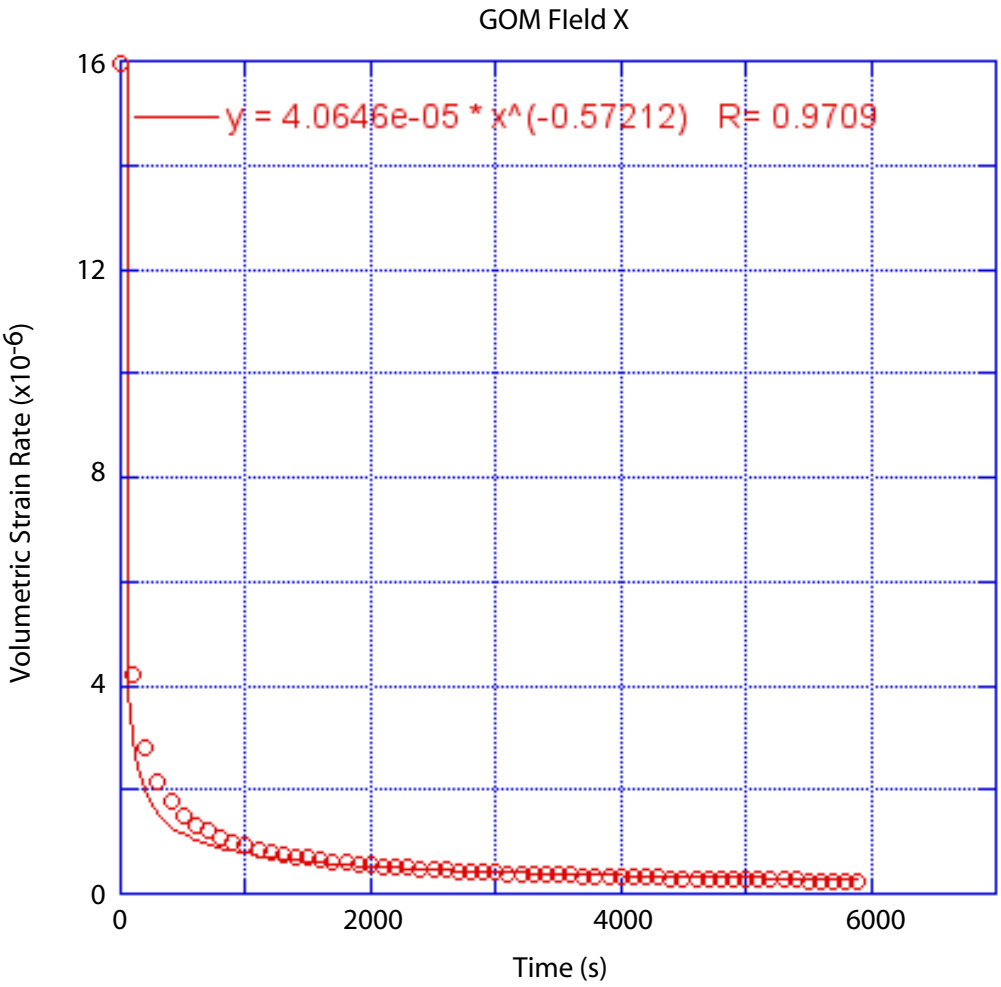

Figure 4.5: Determination of the creep state of the Field X samples (after Hagin, *personal communication*). The open red circles are the actual measurements from the experiment (see Fig. 4.3) while the red line is the best-fit curve. Note that this strain rate decay is independent from pressure and most of the decay occurs in a relatively short duration.

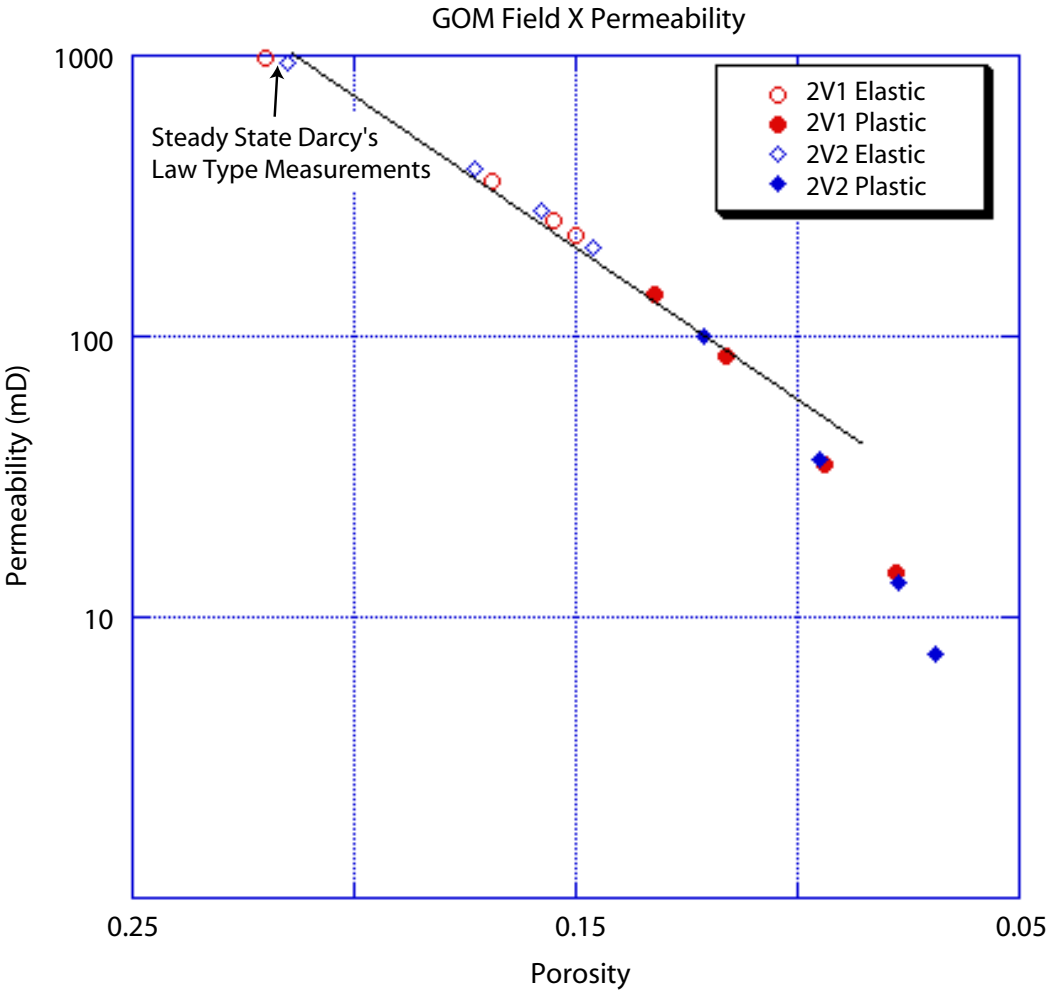

Figure 4.6: Changes in permeability in response to porosity reduction for the Gulf of Mexico Field X samples (modified after Hagin, *personal communication*). The initial permeability is inverted based on the steady state Darcy's Law type measurements. However, this process is relatively time consuming and is replaced by the inversion method by Boitnott (1997). Permeability is inverted based on impulse response of the transient pressure at the top and the bottom of the sample during the experiment. These inversions allow simultaneous measurement of porosity and permeability reduction of the sample. When the samples are deforming within the elastic domain, permeability changes seem to correspond reasonably well with the predicted value based on the Kozeny-Carman relationship. However, once the deformation occurs in the viscoplastic domain, the Kozeny-Carman relationship cannot fully capture the dramatic drop in permeability during compaction.

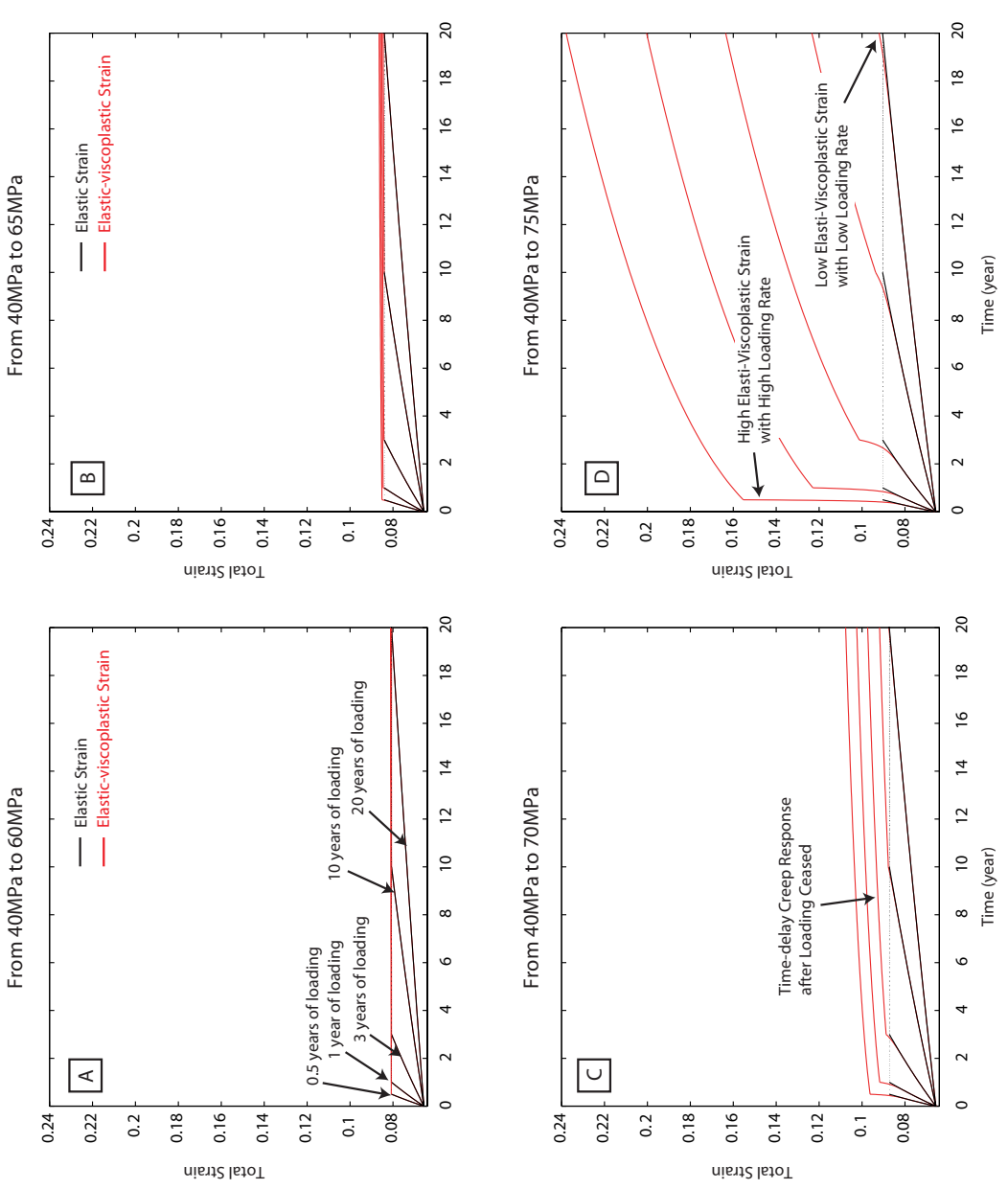

Figure 4.7: The impacts of magnitude and duration of production on estimated total strain. When the loading is small (e.g. 40 MPa to 60 MPa), the effects of viscoplastic strain are minimal and could be ignored. However, as the magnitude of the load increases, the significance of viscoplastic strain increases. If the amount of loading is sufficiently large, the loading duration will have a big impact on the cumulated viscoplastic strain (see Fig. 4.7 D).

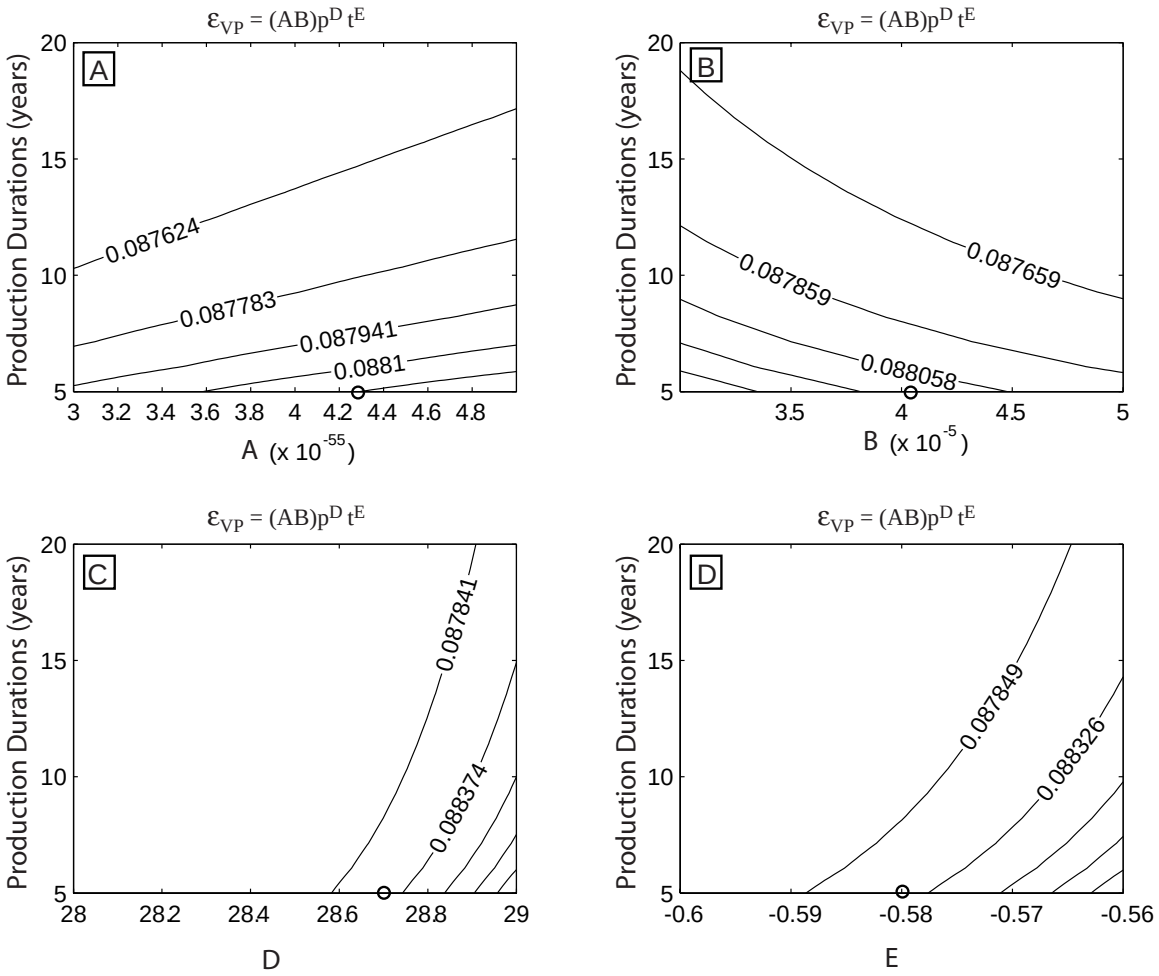

Figure 4.8: Sensitivity analysis for the four Perzyna parameters. Uncertainties associated with parameters A and B seem to have minimal effects on the estimated strain. While errors in determining D and E may have a bigger impact on estimated strain. In other words, improving the accuracy on determining D and E will significantly minimize the errors on strain estimation.

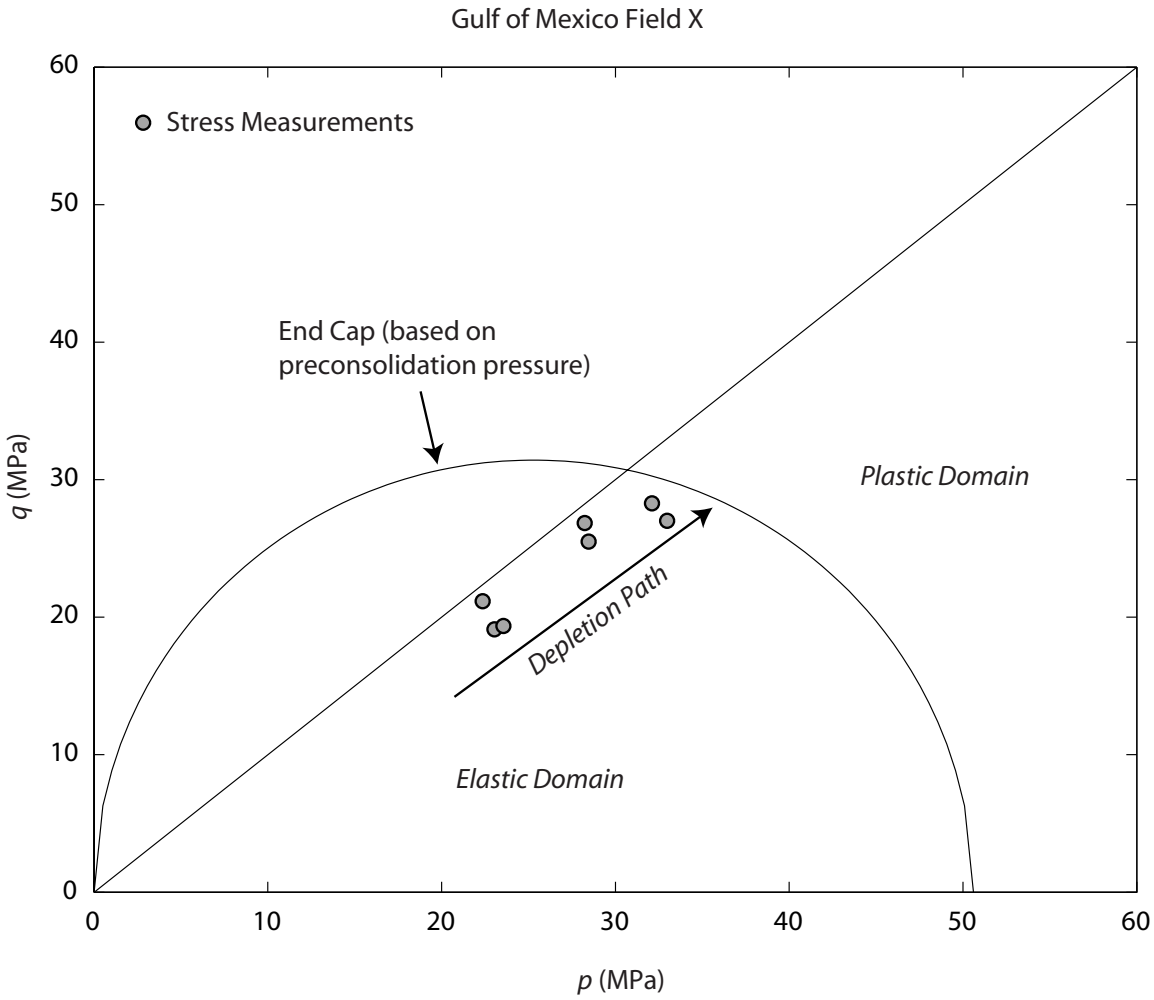

Figure 4.9: Stress measurements from Field X are re-plotted onto p:q space (Laboratory space). The end cap drawn is based on the preconsolidation pressure for the formation. Note that when the *in situ* stresses are plotted in p:q space, they all lie within the end cap, implying that all the deformation associated with depletion occurs in the elastic domain. In other words, deformation is following the reloading path of Field X.

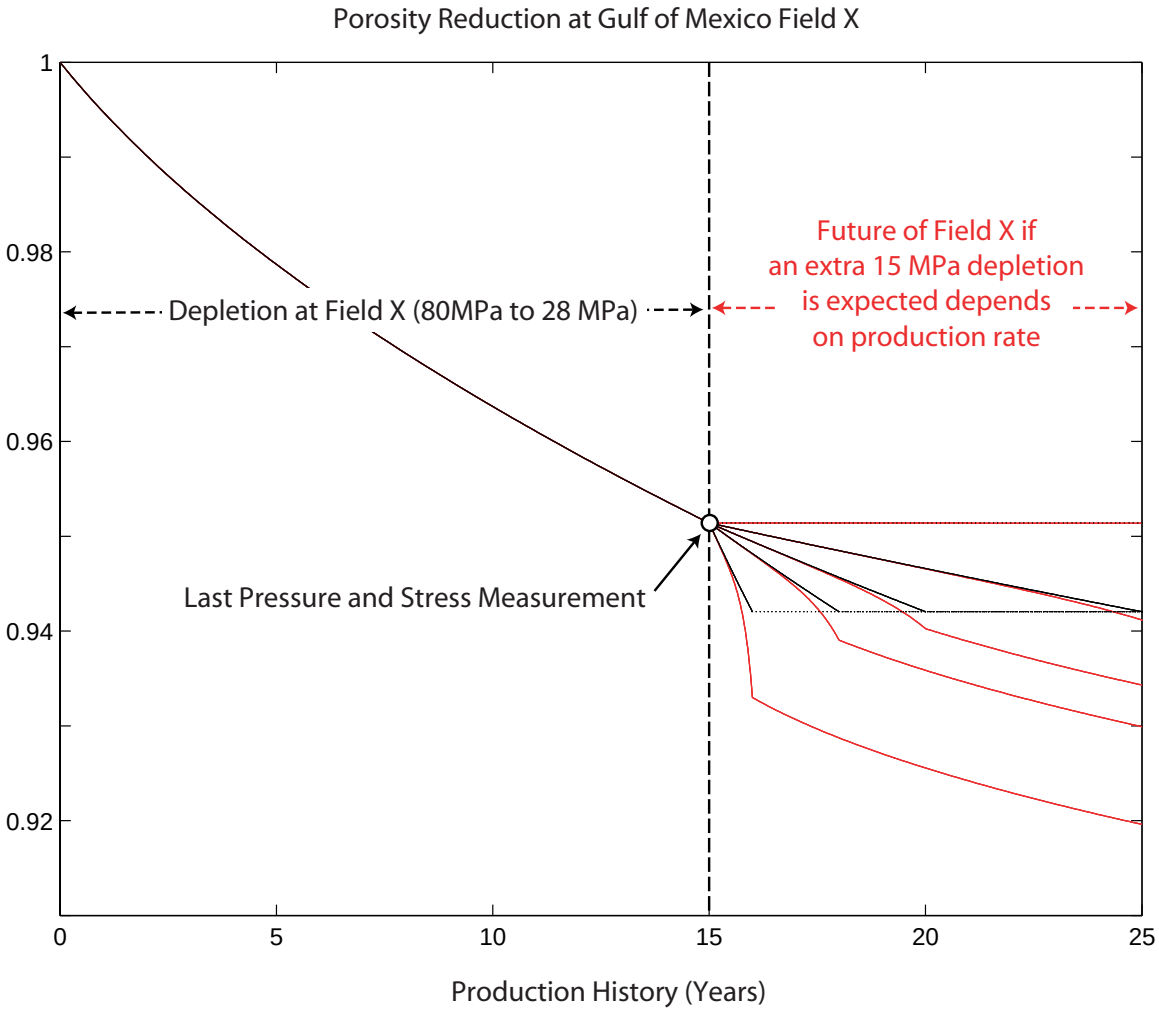

Figure 4.10: Porosity reduction estimated based on the *in situ* stress measurements from Field X. Deformation associated with depletion at Field X occur in the elastic domain hence viscoplastic deformation is negligible.

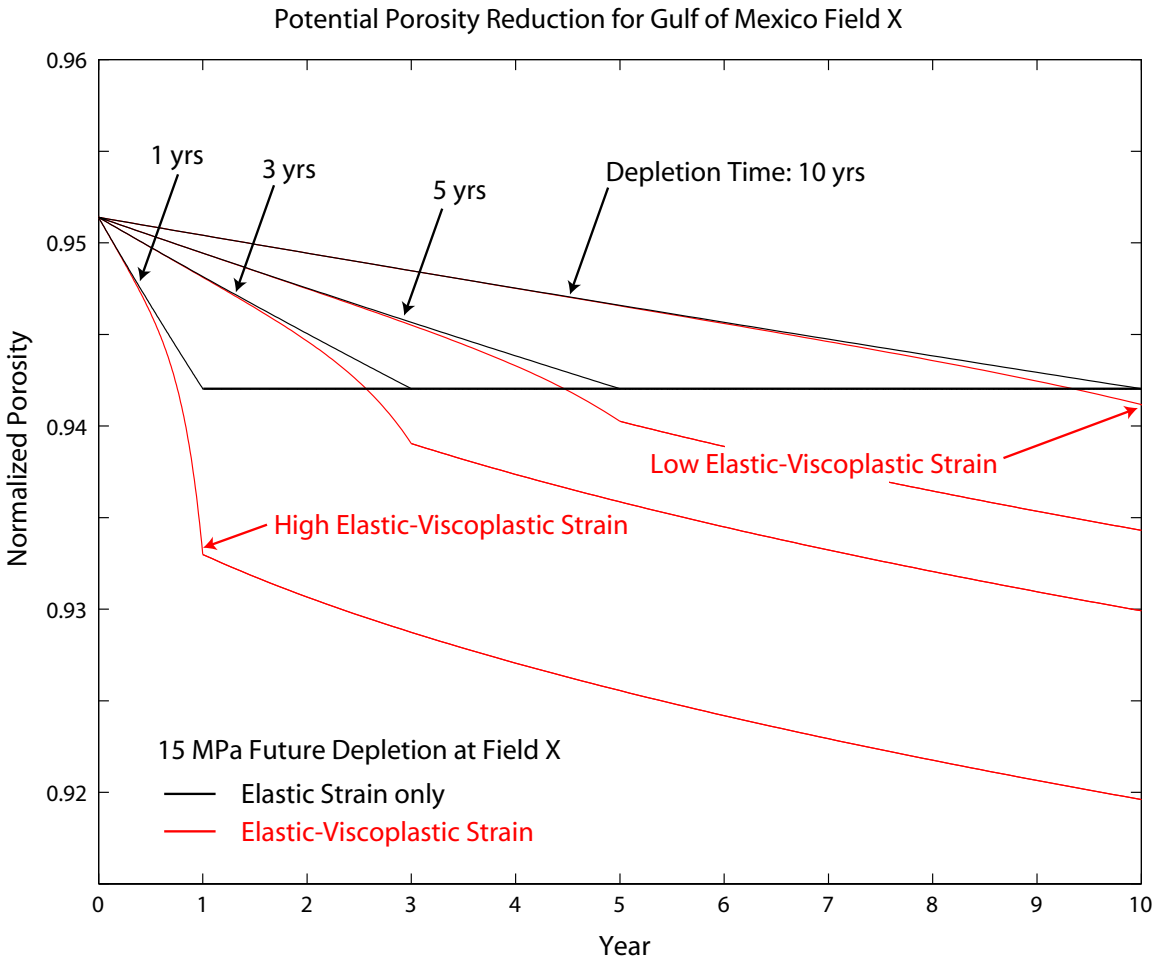

Figure 4.11: The future of Field X. If an extra 15 MPa is to be depleted at Field X, the *in situ* stress state will exceed the preconsolidation pressure and viscoplastic strain can be significant. Four different depletion durations are used to demonstrate the impact of production rate on porosity reduction. Note that when 15 MPa of depletion is reached, production ceases allowing the overstress to relax (similar to a creep experiment in the laboratory). Note that if the production rate is high, the cumulated viscoplastic strain can be quite significant. If Field X is to deplete slowly, the impact of viscoplastic strain becomes negligible.

CHAPTER 5

Louisiana Coastal Wetland Loss: The Role of Hydrocarbon Production

5.1 ABSTRACT

Pore pressure reductions and the associated stress changes due to subsurface hydrocarbon production can lead to reservoir compaction and fault reactivation. These deformations may result in a significant vertical elevation drop on the land surface. When elevation change occurs in a sensitive environment, such as a coastal wetland, the impact of hydrocarbon production cannot be ignored. While coastal wetland loss is caused by complicated interaction between natural processes and human activities, the proximity of some local wetland loss hotspots and active hydrocarbon producing reservoirs had lead to hypothesis of a potential connection between the two by several authors (e.g., Morton *et al.*, 2002). Using a simple analytical solution known as the Geertsma method and a numerical model built upon the Poly3D software, the impact of reservoir compaction and fault slip on surface subsidence is investigated. The Lapeyrouse field in southern Louisiana is chosen as the study site due to its relatively complete pressure data and structural maps. A releveling survey that shows elevation changes over a 30 years time period transecting the field is used for quantitative comparison between the model predictions and actual subsidence. Unlike most offshore oil fields, stress measurements and rock mechanics data for the producing units are not available. Several assumptions were made based on information gathered from the offshore oil fields to demonstrate the procedures for determining the impact of reservoir compaction on land subsidence and fault slip. Despite using data from offshore oil fields, the degree and extent of subsidence estimated from the Geertsma method agrees with the order of magnitude of elevation drop measured from the releveling survey in general. Using different constitutive rheological laws to describe the producing sand formation, the predicted magnitude of subsidence changes accordingly as expected. Numerical models created by Poly3D were used for investigating the impact of compaction-induced slip along the Golden Meadow Fault, located north of the Lapeyrouse field, on surface subsidence. When incorporating the Golden Meadow Fault, the subsidence pattern changes when the fault is allowed to slip freely as a response to deformation associated with reservoir compaction. The magnitude and location of slip along the Golden Meadow Fault are estimated. Subsidence predicted through analytical and numerical methods do not take into account

contributions of natural subsidence and other human activities, however, the magnitude of induced subsidence and fault slip suggest that hydrocarbon production can potentially have some impact on coastal subsidence in a local scale. Coastal wetland loss is a result of complicated interactions between natural processes and human activities; it is difficult to isolate the impact of one specific mechanism from another. The study presented in this chapter suggests that production-induced land subsidence is one of the many mechanisms that should not be ignored when evaluating wetland loss in the Louisiana Coastal Zone.

5.2 INTRODUCTION

Coastal wetland loss is caused by complicated interactions between natural and human activities. Britsch and Dunbar (1993) suggested that wetland loss should be defined as vegetated wetlands that change into (i) uplands or drained areas, (ii) nonvegetated wetlands (e.g., mudflats) and (iii) submerged habitats. For coastal wetland to survive in a rapid submerging region, accumulation of both organic and inorganic soils has to keep pace (Britsch & Dunbar, 1993). Extensive areas of salt, brackish and locally fresh marshes along the coast of northern Gulf of Mexico have been converted to areas of open water and flats as interior wetlands were submerged in the last 50 years (e.g., Britsch & Dunbar, 1993; Penland *et al*., 2000). With 40% of the United State's coastal wetland located in Louisiana, the Louisiana Coastal Wetlands Conservation and Restoration Task Force and the Wetlands Conservation and Restoration Authority (refer as COAST 2050 hereafter) reported in 1998 that land loss in the Louisiana Coastal Zone since the 1930s has accounted for 80% of the total coastal land loss in the United States. The loss of wetlands in Louisiana has significant social, economic and ecological impacts. The coastal zone hosts a large portion of the nation's coastal fisheries and migratory waterfowl population; it also acts as a buffer zone for in-land human population from hurricanes and storms (e.g., Farber, 1987). With over 2 million residents living in the coastal zone (~46% of the state's population), the severe land loss in the next 50 years will cost Louisiana more than $37B (COAST 2050). While up to 16% of coastal land loss is related to canal construction (Boesch *et al*., 1994), more than half of the land loss along the Louisiana coast between 1932 and 1990 was related to land subsidence

(Penland *et al*., 2000). Using color and infrared aerial photographs, Britsch and Dunbar (1993) show that the 36 km^2/yr wetland loss rate in Louisiana between the 1930s to the 1950s was dominated by shoreline erosion. The statewide land loss rate increased dramatically (>100 km^2/yr) from the 1960-1980, the majority of the land loss during this time occurred in the interior with local hotspots that began as small pockets of open water and progressively expanded into large open water with small vegetated islands. The land loss rate declined back to about 65 km^2/yr in the 1990s. The peak of land loss rate in the 1970s seems to coincide with the heavy oil and gas activities in the region (e.g., Morton *et al*., 2002). In this Chapter, I will examine the impacts of oil and gas production in southern Louisiana on land subsidence and fault reactivations in an attempt to characterize the elevation change experienced in some of the hotspots in the Louisiana Coastal Zone.

The process of wetland loss is a combination of land subsidence along with eustatic sea level rise, sediment accumulation, erosion, filling and drainage (Boesch, *et al*., 1994). However, the extent of wetland loss is not a good indicator of the severity of land subsidence due to the complicated interactions between natural and human activities in both the surface and the subsurface. Therefore, I focus on the degree of elevation change as a quantitative indicator of land subsidence because it can be measured through leveling survey, coring, Global Positioning System (GPS) and Interferometry Synthetic Aperture Radar (InSAR). There are several mechanisms involved in coastal Louisiana that can lead to the submergence of wetlands in a regional scale:

(1) On-going compaction of Holocene sediments of the Mississippi River delta. This mechanism results in a spatially variable but temporally constant subsidence pattern (e.g., Suhayda *et al*., 1993); similar studies on compaction of deltaic sands and shales in other parts of the world, such as the coastal area of the Netherlands, suggest that Holocene sediment compaction may have a first order effect on land subsidence (Kooi, 1997, 2000; Kooi & de Vries, 1998) and contribute to a subsidence rate between 0.1 mm/yr and about 1 mm/yr (Kooi & de Vries, 1998);

(2) Regional subsidence as a result of lithospheric flexure response to sediment loadings (e.g., Scardina, *et al.*, 1981) and/or subsidence of Pleistocene and

older sediments (e.g., Paine, 1993). Paine (1993) suggests that the geological subsidence rate for Pleistocene strata along the Texas coast is consistently at 0.05 mm/yr (relatively small compared to the dramatic rate of subsidence experienced along the Gulf coast in the past 50 years);

(3) Relative sea-level change results in a temporally variable but spatially constant subsidence pattern across the entire coastal zone (e.g., Penland *et al*., 1988; Penland & Ramsey, 1990; Roberts *et al*., 1994; Suhayda, 1987). Based on the tide gauge measurement located at some nearby area where tectonic activities are minimal such as Pensacola, Florida, Penland *et al*. (1988) concluded that the rate of relative sea-level change is about 2.29 mm/yr;

(4) Natural movement on growth faults along the coast and the continental shelf of the Gulf (e.g., Gagliano *et al*., 2003). Since most of the wetland losses identified through aerial photographs are located along the downthrown side of known growth faults, these studies proposed that the massive land loss in coastal Louisiana is a result of the episodic movement along the east-west trending growth faults along the entire coast. However, the rates of vertical movement estimated through these studies are the combined effects of all mechanisms; it is impossible to isolate the slip rate and magnitude along these growth faults from other secondary effects;

(5) Hydrocarbon production-induced fault reactivation (e.g., White & Morton, 1997; Morton *et al*., 2001; Morton *et al*., 2002; Morton *et al*., 2003) and reservoir compaction (e.g., Sharp & Hill, 1995). Studies in other parts of the world have demonstrated that reservoir compaction can have a significant impact on surface subsidence For instance, up to 10 m of subsidence was observed at Long Beach, CA, over the Wilmington oilfield between 1926 to 1967 (e.g., Colazas & Strehle, 1995) and more than 3 m of subsidence at the Ekofisk field in the North Sea during the first 20 years of production (e.g., Sulak, 1991).

While the first four mechanisms suggested a maximum subsidence rate of about 3 mm/yr, the historical subsidence rate in some part of Louisiana recorded ranged from 9 mm/yr to as high as 23 mm/yr locally in the past few decades (Morton *et al*., 2002). It is

also critical to note the initial elevation of the wetland may affect the amount of wetland loss. In other words, a slight change in elevation at land close to sea level will have a bigger impact on wetlands than a larger elevation change in the higher ground. It is apparent that natural processes alone are inadequate to explain the high local historical subsidence rate in coastal Louisiana. Production-induced surface subsidence as a result of reservoir compaction and fault reactivation appears to have some significant impact locally in a short duration. As a result, the Lapeyrouse field located in Southern Louisiana has been chosen as a study site in this Chapter to determine the role of hydrocarbon productions on land surface subsidence.

With no rock mechanics experiments for the producing sands in Lapeyrouse, I apply the constitutive rheological relationship derived from Field X (Chapter 4) to estimate the possible compaction experienced by the producing sand in Lapeyrouse. Although using constitutive law from a different field is not an ideal solution, the procedures I present in this chapter can be applied easily to other future sites when all the relevant information is available.

Figure 5.1 illustrates the workflow from raw data to the determination of the degree of production-induced land subsidence. In general, *in situ* stress and pore pressure measurements along with the constitutive laws will be input into the DARS formalism to estimate the change in porosity (or volumetric strain) as a result of production (see Chapter 2 and Chapter 4 for more detailed discussion on the DARS formalism). Depending on the rheological law chosen, it is possible to estimate strain with or without the time effect (i.e., static DARS versus dynamic DARS). The geometry of the reservoirs and the reservoir bounding faults are digitized using GOCAD based on actual structural maps. Combining the estimated strains and the geometry of the reservoirs (in this case, thickness of the sands), the amount of reservoir compactions can be determined. I then use both analytical and numerical methods to analyze the impact of compaction on surface subsidence. Using a simple analytical method proposed by Geertsma (1973), I estimate the magnitude of surface subsidence based solely on reservoir compaction. While by solving the problem numerically using Poly3D, the location and magnitude of fault slip along with its potential contribution to surface subsidence are estimated. These

results are then compared with the actual releveling data. In the following sections, I will discuss the workflow in greater detail.

5.3 PRODUCTION-INDUCED LAND SURFACE SUBSIDENCE

Human-induced land subsidences along coastal Gulf of Mexico due to subsurface fluid withdrawal were first reported along the Texas coast and have since been studied extensively (e.g., Pratt & Johnson, 1926; Swanson & Thurlow, 1973; Neighbors, 1981). The rates of compactional subsidence and eustatic sea-level change range up to 13 mm/yr along the upper Texas coast (Swanson & Thurlow, 1973). However, the rate of subsidence due to human activities greatly exceeded the natural phenomena at about 120 mm/yr from 1964 to 1973 (Gabrysch & Bonnet, 1975). The major cause of human-induced subsidence is the withdrawal of underground fluids including water, oil and gas. In the Houston-Galveston area, land subsidence induced by large-scale groundwater withdrawal since 1906 has been up to 3 m (Gabrysch & Coplin, 1990) while the 'subsidence bowl' formed in the Houston area encompasses more than 10,000 km^2. The implication of elevation changes in coastal wetlands can have dramatic impact on the wetland ecosystem as Reed and Cahoon (1993) suggest that a slight decrease in elevation can lead to frequent flooding that can deteriorate, and eventually destroy, vegetation. Erosions followed by the loss of vegetation will further accelerate the loss of wetlands in these areas. White and Tremblay (1995) reported that wetland loss along the upper Texas coastal area including the Bolivar Peninsula in East Galveston Bay, the Neches River Valley at the head of Sabine Lake and the interfluvial area between the Sabine Lake and the Galveston bay were likely results of hydrocarbon production-induced faulting and subsidence. Although rates of wetland loss doubled locally in the 1950s to 1970s compared to the 1930s to 1950s, White and Tremblay (1995) reported that the rate of wetland loss has declined in some areas since the 1980s. These reductions in the Galveston Bay system may be related to the dramatic reduction in the rate of groundwater production-induced subsidence as a result of curtailment of groundwater pumpage after the 1970s.

Unlike coastal Texas, the link between subsurface fluid withdrawal and wetland loss in coastal Louisiana is more difficult to establish because wetland loss is ubiquitous and caused by many processes and conditions (e.g. Coleman & Roberts, 1989; Williams *et al*., 1994). The relationship between hydrocarbon production and Louisiana coastal wetland loss is poorly understood. Only a few authors have investigated the potential impact of oil and gas production on subsidence in this region (e.g., Suhayda, 1987; Coleman & Roberts, 1989; Boesch *et al*., 1994; Morton *et al*, 2001). Most of the authors prior to Morton *et al.* (2001) concluded that subsidence caused by hydrocarbon production in coastal Louisiana is negligible due to the depth of the reservoirs or that the subsidence affect only the immediate area and do not affect the wetland on a regional scale. However, as Morton *et al*. (2001) pointed out, these conclusions regarding minimal impacts of hydrocarbon production were based neither on subsurface data from the producing fields nor any numerical or analytical models that incorporate the physical changes of the formations associated with depletion and the corresponding stress changes. Using core samples and releveling data, Morton *et al*. (2002) demonstrated that the changes in the historical surface subsidence rates in certain part of coastal Louisiana appear to correspond with the hydrocarbon production rates in those areas (Figure 5.2). The appearance of some surface fault traces after the 1970s also led them to propose the potential of fault reactivation as a contributor of surface subsidence. To investigate the validity of Morton *et al.*'s proposal, I will use both analytical and numerical models to examine and demonstrate the implications of reservoir depletion on surface subsidence in the Louisiana Coastal Zone.

Analytical and numerical models have been proposed since the 1970s in an attempt to relate surface subsidence with oil and gas production. Based on a simple nucleus-of-strain concept from thermoelastic theory, Geertsma (1973) estimated the surface subsidence as a response to the production-induced compaction of oil and gas reservoir (see Appendix 5.A). Assuming the reservoirs are disc-shaped, Geertsma estimated the surface response to reservoir compaction at depth. However, Geertsma assumed a constant formation compressibility and linear stress-strain relationship throughout the entire half-space that might not be representative of weak sand reservoirs in the Gulf of Mexico that show some elastic-viscoplastic deformation during depletion (Chapter 4).

Nonetheless, van Hasselt (1992) studied the Groningen gas field in the Netherlands using a few two-dimensional models and successfully demonstrated that the Geertsma solution can be used for estimating production-induced land surface subsidence. He also validated the predicted subsidence by field observations and showed that the results were comparable to those from a more complicated finite element method.

The Geertsma solutions stated that the magnitude of surface subsidence, U_Z, is a function of pressure change, ΔP_P in the reservoir, the compressibility, C_m, and Poisson's Ratio, ν, of the material, such that:

$$u_z(r,0) = -2c_m(1-\nu)\Delta P_P HA(\rho,\eta) \quad \text{.....(5.1)}$$

where ρ and η are dimensionless parameters and can be defined as ρ = r/R and η = D/R. D, H and R are the depth, thickness and the radius of the reservoir. The solution for *A* is a linear combination of the elliptic integrals of the first, second and third kind (see Appendix A). To incorporate a more complicated rheology to the Geertsma solution, I replaced $-2c_m(1-\nu)\Delta P_P H$ in Equation (5.1) with reservoir compaction, ΔH, estimated from the DARS analysis such that:

$$u_z(r,0) = \Delta HA(\rho,\eta) \quad \text{.....(5.2)}$$

This modification allows the use of the static DARS or the dynamic DARS analysis to estimate the amount of compaction that may occur in each individual reservoir and translate the results to surface subsidence as a function of pressure and/or time by super-positioning the effects from all reservoirs.

Without considering the impact of background regional subsidence, the purpose of using a simple model is to investigate if the Geertsma solution can generate a local subsidence profile of the same order of magnitude as the observed elevation changes. Since the physical properties of the reservoirs are heterogeneous and cannot be fully modeled by circular discs with uniform thickness, I do not expect to capture characteristics of the observed elevation changes to the finest detail. However, if the Geertsma solution yields a reasonable estimate, the impact of production on surface subsidence should not be ignored.

5.4 PRODUCTION-INDUCED FAULT REACTIVIATION

Extensive studies on induced-seismicity as a result of subsurface fluid injection and withdrawal have been conducted since the 1960s (e.g. Evans, 1966; Raleigh *et al*., 1976; Segall, 1985; Mereu *et al*., 1986; Pennington *et al.*, 1986; Segall, 1989, 1992; Grasso & Wittlinger, 1990; Doser *et al.*, 1991; McGarr, 1991; Grasso, 1992; Davis *et al*., 1995; Baranova, 1999). Most of these studies demonstrated that the number of seismic events in the proximity of producing oil or gas field increases significantly after production or injection began. It is well documented that mechanical instability induced by fluid injection is related to the increase of pore pressure which allows slip on pre-existing faults by lowering the effective normal stress (e.g. Evans, 1966; Raleigh *et al*., 1976). Based on this argument, the reduction of pore pressure as a result of production should inhibit faulting. However, observations and studies of seismic events around different oil and gas fields around the world suggested that depletion will result in a change in stress around the reservoir that may encourage slip on faults outside of the reservoir (e.g. Segall, 1985; Mereu *et al*., 1986; Pennington *et al.*, 1986; Segall, 1989, 1992; Grasso & Wittlinger, 1990; Doser *et al.*, 1991; McGarr, 1991; Davis *et al*., 1995; Baranova, 1999). Using poroelastic theory with an assumption of an ellipsoidal reservoir embedded in an elastic medium, Segall (1985, 1989, and 1992) calculated stress changes surrounding a hydrocarbon reservoir induced by reduction of pore pressure inside the reservoir (Fig. 5.3). The stress changes can result in fault reactivation in the proximity of the reservoir (Fig. 5.4). The only significant difference between the Geertsma solution and the Segall solution is their applications: while Geertsma considered the surface displacements due to uniform pressure reduction from a thin circular disc-shaped reservoir; Segall expanded the solution to include stress changes in the elastic medium surrounding the reservoir where no pore pressure change has occurred and their relationship with induced seismicity in the vicinity of the hydrocarbon reservoirs.

While the Segall solution analytically calculates stress changes and the potential of fault reactivation in the vicinity of the depleting reservoir, the impact of the compaction of an irregular shaped reservoir on a non-planar fault surface is best estimated using numerical modeling. Therefore, I use the Poly3D software developed by Andy Thompson (1993) to examine the impact of hydrocarbon production on a fault located outside of the

depleting reservoir. Poly3D uses a boundary element method to calculate the quasi-static displacement, strain and stress fields in a linear elastic, homogeneous and isotropic medium (Thomas, 1993). Instead of coupling pore pressure history with surface subsidence and fault slip as in the analytical solutions, I apply compactions determined from the DARS analysis for each individual reservoir as the boundary conditions. Driven by reservoir compaction, Poly3D can determine the location and magnitude of slip along the fault surface. I model the compacting reservoir as a planar discontinuity surface embedded in an elastic medium. With my interest mainly focused on deformations above the reservoir, I only consider the top surface of the structure and displace the surface downward uniformly to simulate compaction based on the calculated values from the DARS formalism. In other words, compaction in Poly3D is simulated by negative displacement of the planar surface along the z-axis. Assuming the fault surface is free of traction and is able to slip in any direction within the fault plane (i.e., no opening or closing of the fault), the magnitude and location of slip induced by reservoir compaction can be estimated. Although in reality fault surfaces may not be traction-free, it is a reasonable assumption since growth faults in the coastal area are active and constantly slipping (Kuecher *et al*., 2001). As a result, the estimate from Poly3D is the maximum slip that can occur on the fault plane due to reservoir deformation. If the background geological slip rate along the growth fault is known, it is possible to estimate the total slip along the fault due to natural and production-induced fault movement. Alternatively, as most observed surface elevation changes are the combined effects of several regional and local mechanisms, surface deformation associated with compaction-induced fault movement estimated from Poly3D can be used for filtering out elevation changes due to hydrocarbon production.

5.5 CASE STUDY: LAPEYROUSE FIELD, LOUISIANA

The Miocene aged Lapeyrouse field is located west of Madison Bay in the Terrebonne Parish in Southern Louisiana (Fig. 5.5). Both geological and historical subsidence rates have been published in this region. Carbon dating of sediment cores in the Madison Bay area suggest that the Holocene sediments had an average subsidence

rate of 1.4 mm/yr for the last 500 years (Frazier, 1967); Roberts *et al*. (1994) reported that the average rate of subsidence in the region was about 2.7 mm/yr for the last 5000 years. These results are comparable to the tide gauge measurements at Houma prior to 1962 when the measured subsidence rate averaged about 0.7 mm/yr (Penland *et al*., 1988). However, the historical subsidence rate in the Madison Bay area was increased significantly since 1962. Penland *et al*. (1988) reported 19.4 mm/yr of subsidence at the Houma tide gauge between 1962 and 1982. While subsidence rates estimated from surface elevation table (SET) measurements (Cahoon *et al*., 1999) and recent sediment cores (Morton *et al*., 2003) are about 23 mm/yr. Two regional leveling lines (Fig. 5.5) are available in this area with the Bayou Petit Calliou Relevel Line transecting the Lapeyrouse field (Morton *et al*., 2002). Based on the Bayou Petit Calliou relevel line, Morton *et al*. (2002) reported that within the Madison Bay wetland loss hotspot the highest local subsidence rate of 9.3 mm/yr coincides spatially with the nearby Lapeyrouse field. While the cause of the different estimates from the core and releveling data remain unclear, the observed subsidence at Madison Bay is significantly higher than subsidence estimated from relative sea-level change and/or natural sediment compactions in the region. Morton *et al*. (2003) proposed that the occurrence of the Madison Bay hotspot might be related to hydrocarbon production at the Lapeyrouse field and the potential movement of the Golden Meadow Fault Zone located north of Madison Bay. Figure 5.6 shows the general locations of all the gas wells drilled within the Lapeyrouse area. The yellow boxes are the station locations for the 1993 Bayou Petit Calliou relevel line. Morton *et al.* (2002) observe 41-254 mm of subsidence over the Lapeyrouse field between 1966 and 1993 (Fig. 5.7). Station M to Station S marked on Figure 5.7 correspond to the station locations marked on Figure 5.6. Morton *et al.* (2002) also suggested that the dramatic elevation change near station M might be related to movement of the Golden Meadow Fault. Note that the leveling survey published by Morton *et al*. (2002) represents the relative vertical elevation changes with respect to the first bench mark of the Bayou Petit Calliou relevel line. If the first benchmark is not located in a stable region but is also subsiding, the result from this relevel survey will under-estimate the actual magnitude of vertical elevation changes. Thus, background regional subsidence will not be captured in the relative elevation changes. However, since

the primary focus of this study is to examine the local effect of hydrocarbon production on subsidence, the releveling data is adequate to demonstrate the relative elevation changes induced by fluid withdrawal in the subsurface. To evaluate the impact of hydrocarbon production on subsidence, I predict elevation changes relative to Station U south of the field. Ignoring the influences of other background mechanisms that may cause elevation change in this area, I demonstrate the order of magnitude of production-induced subsidence.

Production at the Lapeyrouse field began in the 1950s and accelerated in the 1960s with a peak of production of about 1.6 million barrels per year (MBBLS/yr) in the 1970s (Fig. 5.2) (Morton *et al*., 2002). Cumulative gas production at the Lapeyrouse field is about 624 billion cubic feet (BCF) while cumulative oil production is about 18 MMBBL. Four sand formations, the Exposito, Bourg, Pelican and Duval, are examined in this study. All of these sands are primarily gas producers and the formations are generally clean, fine-grained sand with excellent initial porosity and permeability (Sticker, 1979). There is no known salt diaper near the field and most of the producing sands are stacked anticlinal structures bounded by the Golden Meadow Fault Zone in the north. I have selected this site because of the heavy gas production in the 1970s (Fig. 5.2) that might have lead to a significant amount of wetland loss in the area through reservoir compaction and possibly enhanced the potential of fault movement in the Golden Meadow Fault Zone. The Bayou Petit Calliou Relevel Line will be used as a quantitative control on the amount of elevation change in the area (Fig 5.7) and will be compared to the predictions of the analytical and numerical models.

Pore pressures measured from all the wells located near the Lapeyrouse field have been filtered based on the completeness of the records and were first published by Morton *et al*. (2001). I further filtered the pressure data to remove sidetrack wells and wells located outside of the main structure transected by the Bayou Petit Calliou Releveling line. The remaining pore pressure histories for the selected sands are re-evaluated. Figure 5.8 shows the bottom-hole pressures (BHP) of all wells for the four sands corrected to their corresponding datum based on the average depth of the individual producing sand units. A few of the pore pressure changes for these wells in the selected sands (Fig. 5.8) are quite large (up to 50 MPa reduction in pore pressure) which lead to a

significant increase in effective vertical stress acting on the producing unit during depletion. In some wells the measured pore pressure has been reduced almost to 0 MPa, such as the Bourg B well. From these pressure history plots, it is possible to identify potential subcompartments or barriers between wells (if the wells are located within the same compartment, the pressure history should be on the same trend as pressure declined as a whole unit between the wells). In other words, when the pore pressure reduction trends between two wells do not fit onto one trend after datum correction, the two wells are likely located in two hydrological units separated by some barrier. The best example of compartmentalization is in the Pelican sand where three distinct pressure reduction trends are observed.

In order to determine if such compartmentalization has any relationship to the physical structure of the reservoir, I superimpose the well locations along with the structural contour map onto the aerial photographs (Fig. 5.9, 5.10, 5.11 & 5.12). The simplified contour maps in the four composite diagrams are modified based on a number of documented structural maps filed at the Department of Natural Resource, Louisiana, in Baton Rouge. Compartments inferred from the pore-pressure histories are indicated on the composite diagrams.

The composite diagram along with the pore pressure history from the Exposito sand is presented in Figure 5.9. As shown in the pore pressure history plot, the Exposito sand seems to be highly compartmentalized. At least three hydrological compartments can be identified and they correlate well with the compartments (or fault blocks) separated by the subsurface faults as shown in the structural map. Fault block I (wells C, D and E) and Fault Block V (wells I and L) are the best-defined compartments from the pressure history plot. Sticker (1979) had identified four separate reservoirs based on his structural maps and these reservoirs agree with the fault blocks identified through the pressure history plot. The agreement of compartments recognized from both structural map and pressure history suggests that the faults act as barriers to lateral fluid flow preventing the fault blocks from being hydrologically communicative.

For Bourg Sand (Figure 5.10), pressure histories of wells B, C and D follow a similar trend suggesting that these three wells are within the same unit (Fault Block I). Fault Block IV (Well J) identified from Figure 5.8 is located outside of the structural map and

will not be considered in this study. Note the dramatic pressure reduction from about 40 MPa to about 2 MPa within a few years at well H. It is uncertain if such decrease is totally a result of gas production or if gas leakage has occurred. As in the case of well J, depletion at well H will not be considered since it located on the up-thrown side of the fault outside of the main structure.

Compartmentalization for the Pelican sand is the most obvious among the four sands examined. Three separate pressure reduction trends can be clearly identified from the pressure history plot (Fig. 5.11). Combining the well locations, hydrological compartments and the actual structural map of the Pelican sand, it is obvious that the faults that separating the sand units prevent fluid from migrating laterally between the blocks. The compartments identified from the pressure history plot correspond extremely well with the fault blocks identified from the structural map: Fault Block I consists of wells B and C, wells E and F are located within fault block II and well A seems to be located in a separate fault block from the rest of the wells.

Although no obvious compartment is identified from the pore pressure history plot for Duval sand, the structural map suggested that well D, E, F, G and H lie within the same block (Fig. 5.12). Subcompartments may exist within this fault block that lead to difference in pore pressure trends among these wells.

5.5.1 Reservoir Compaction and Land Surface Subsidence

To estimate the impact of oil and gas production in the four producing sands at Lapeyrouse on surface subsidence, it is essential to estimate the amount of reservoir compaction in the formations. Unlike offshore fields, several problems related to the estimation of reservoir compaction for the Lapeyrouse field exist and several assumptions are made in order to demonstrate the magnitude of production-induced subsidence above the Lapeyrouse field:

(1) Lack of Stress Measurements: As most of the wells were drilled in the 1960s and 1970s, there are no stress measurements available prior to or during production. Leak-Off-Test (LOT) or Mini-Fractures results were not available in the public data base in Baton Rouge since the operators are not required to report such information and in most cases, only the BHP are reported. As a result, I have to assume the original *in situ* stress

state prior to production in all these reservoirs was at frictional equilibrium. In other words, any increase in stress in the crust will lead to slip on some well-oriented pre-existed faults. This assumption is reasonable since gas leakages had been reported in some nearby fields prior to their productions (e.g. Lirette Field, Morton *et al*., 2002). The occurrence of gas leakage implies the reservoir-bounding fault is active and slip on this reservoir-bounding fault can create a conduit for fluid to migrate upward. Another issue concerning the stress measurement is that no stress path can be determined in the Lapeyrouse Field since no such measurements are reported or made after production began. The stress path is defined as the change in horizontal stress as a result of change in pore pressure that can affect the nature of reservoir deformation induced by depletion (see Chapter 2 for a more detailed discussion of stress path). To effectively study the stress changes due to production, I use a general stress path that is known for the Gulf of Mexico offshore fields. Nearly all the offshore Gulf of Mexico reservoirs used in the previous chapters follow a depletion stress path of about 0.54 regardless of whether they are located at the continental shelf or in deepwater (e.g., Field X and Field Z in Chapter 2 and 3; Field Y located on the continental shelf near southeastern Texas also recorded a depletion stress path of about 0.54). As a result, I assume Lapeyrouse field will follow a similar stress path ($\boldsymbol{A} = 0.54$) over its production lifetime.

(2) Lack of Rock Mechanics Studies: Since Lapeyrouse is an onshore gas field and most of the wells are drilled in the 1960s. Reports on rock mechanics studies are not required for field development. Without proper rock mechanics experiments, I can only assume the producing sands at Lapeyrouse behave similarly to those offshore sands in the Gulf of Mexico as described in the previous Chapters. I make this assumption based on the age of the formation and that both are located in the same deltaic basin. Although applying laboratory data from a different field is not ideal for the geomechanical modeling, I use these rheologies to demonstrate how the analysis can be done with adequate rock mechanics data. As a result, predictions presented here need to be used with caution. However, the procedures and techniques performed can be applied universally regardless of the material properties of the producing sand.

To understand the magnitude and extent of subsidence induced by reservoir compaction, I use the modified Geertsma method assuming no faulting will be triggered

as a result of depletion. The existence of subcompartments in the producing sands suggests that it is possible to treat the individual fault blocks separately. Since the thickness of the reservoirs in Lapeyrouse is relatively small compare to the depth of the sands, the variation in thickness of these sands should only have minimal impact on surface deformation. As a result, I create a number of circular discs with uniform thickness at different depths to represent the individual reservoirs of interest (Fig. 5.13). The color code represents the different formation while the size of the disc is set to encompass all the wells that are identified as in the same hydrological compartment or fault block from the pressure history data. In other words, the maximum size of the disc will be restricted to the size of the fault block. As all of these reservoirs are relatively thin (average thickness of 10m) with respect to their depth (average of 4.5 km in depth), the uncertainties associated with the size of the discs created should have no significant impact on the estimated vertical elevation change locally and only a slight influence on the lateral extent of the surface subsidence bowl (see Appendix 5.A).

Based on the pre-production BHP measurements, the initial values for S_{hmin} of each disc-shaped reservoir, with the assumption of frictional equilibrium prior to production, are estimated. I assume the initial value of S_{Hmax} is very close to but slightly larger than the value of the corresponding S_{hmin}. Using the pressure reduction data, I then estimate the final S_{Hmax} and S_{hmin} at the time of abandonment assuming the reservoir depletion stress path of 0.54 is valid for Lapeyrouse. Using the equations derived in Chapter 2, I calculate the p* corresponding to the pressure and stress data for all the reservoirs. By applying the calculated p* to the constitutive law, the degree of porosity loss that happens in each reservoir as a result of production can be determined. Substituting the amount of compaction into the modified Geertsma solution, a map of surface deformation is produced (Fig. 5.14). The solutions presented in Figure 5.14 are based on compaction estimated from the elastic rheology derived for Field X in Chapter 4. By changing the constitutive law, the degree of reservoir compaction will alter leading to a change in surface subsidence predictions. Figure 5.14A represents the vertical displacement predicted by the Geertsma solution while Figures 5.14B and C are the predicted horizontal displacements. Figure 5.14D represents the predicted subsidence at the station where the relevel measurements were made. The blue line in Figure 5.14D represents the

predicted subsidence at each station, with the southern most station as the reference station since it is farthest from the center of the subsidence bowl in Lapeyrouse and minimal oil and gas related activities were conducted south of Lapeyrouse (note that the elevation change estimated from the relevel survey is based upon the Houma tide gauge located at the northern end of the survey line). The elevation change measured at the reference station is larger than the predicted subsidence from the Geertsma solution. This difference may be related to the regional background subsidence in the area. However, the magnitude of the regional background subsidence should not be estimated from this figure unless the predicted subsidence is estimated using constitutive laws derived from laboratory measurements on the Lapeyrouse field samples directly.

Figure 5.15 compares the predicted subsidence from the modified Geertsma solution using the different rheologies introduced in Chapter 2 and Chapter 4. The magnitudes of the predicted and measured subsidence are corrected to the reference station. This modification suggests that the degree of induced subsidence due to production at Lapeyrouse can be significant depending on the rheology of the formation sands. It is apparent that in general the amount of compaction-induced subsidence is comparable to the elevation drop measured in this area. While the predicted subsidence based on the generalized compaction curve for friable sands (Yale *et al*., 1993; see discussion in Chapter 2) seems to underestimate the severity of the surface subsidence at Lapeyrouse, the generalized compaction curve for unconsolidated sand in the Gulf of Mexico has over-estimated the magnitude of subsidence. The prediction based on the elastic compaction curve for Field X (Chapter 4) appears to capture the order of magnitude in subsidence near the center of the subsidence bowl. The over-estimation by the generalized compaction curves for unconsolidated sands suggests that the four Lapeyrouse sands may have undergone some degree of consolidation. Cementation can alter the compressibility of the formation that can lead to uncertainties in compaction estimation. The heterogeneity of the formation as a result of lateral variations of compressibility and thickness of the formation can also affect the estimated vertical elevation change on the surface. Although the estimated subsidence cannot fully capture the significant subsidence observed near Station M, this simplified analytical solution suggests that production-induced reservoir compaction can have some impact locally on

land subsidence. As a result, the modified Geertsma method can be used as a first-degree estimation on the magnitude of subsidence related to reservoir depletion.

5.5.2 Reservoir Compaction and the Potential of Fault Reactivation

The misfit at Station M in Figure 5.15 and the proximity of the survey station to the approximate location of the surface trace of the Golden Meadow Fault Zone suggest that subsidence measured at Station M may be influenced by the movement along the Golden Meadow Fault. I utilized Poly3D to numerically estimate the impact of reservoir compaction in Lapeyrouse on the Golden Meadow Fault. Sticker (1979) compiled detailed structural maps of the producing sands for the Lapeyrouse field based on all the structural maps filed at the Department of Natural Resources, Louisiana, in Baton Rogue. Along with a seismic study across the Lapeyrouse field (Fig 5.16) by Kuecher *et al*. (2001), I digitize the shape of all the reservoirs and the Golden Meadow Faults using GOCAD so that the digitized surfaces and meshes can be imported into Poly3D (Fig. 5.17). While the producing sands are anticlinal structures and some of the individual reservoir blocks are dipping gently to the southwest, I assumed all the reservoirs are horizontally layered for simplicity.

Similar to the procedures used in the previous section, I calculate the degree of reservoir compaction for all reservoirs based on the DARS formalism. Both the Field X elastic rheology and the generalized compaction curve for unconsolidated sands are used as a demonstration on how rheology impacts compaction-induced fault slip. The predicted compactions are then input into Poly3D as uniform negative displacements along the Z-axis across the reservoir surfaces. To determine the impact of compaction-induced fault slip along the Golden Meadow Fault on surface subsidence, I assume the fault is traction-free. In other words, the Golden Meadow Fault can slip freely along its surface without any restrictions. Figure 5.18 compares the effect of Golden Meadow Faults on surface subsidence based on the Hagin elastic compaction curve. Note that when the fault is locked (i.e., no displacement allowed), surface subsidence is controlled by reservoir compaction and yields a similar result to that of the Geertsma solution (compare to Fig. 5.14A). The slight difference between the subsidence bowls of Figure 5.14 and Figure 5.18 is due to the shape of the reservoirs: all the reservoirs are disc-

shaped in the Geertsma solution while the reservoirs are irregular shaped in the numerical model. The occurrence of fault slip along the Golden Meadow Fault significantly alters the shape of the subsidence bowl especially in the vicinity of the fault. The additional subsidence at the fault is a result of the fault movement induced by reservoir compaction. The subsidence shown in Figure 5.18B is the maximum subsidence that can occur with the influence of slip on the Golden Meadow Fault (since in reality, friction along the Golden Meadow Fault will reduce the amount of slip that can occur along the fault). Thus, Figure 5.18B presents the worst-case scenario for subsidence due to hydrocarbon production in Lapeyrouse assuming the producing sand deforms according to the Field X elastic compaction curve. Slip distribution along the Golden Meadow Fault also varies spatially (Fig. 5.19) due to the location of the reservoirs and the shape of the fault. As expected, the maximum slip occurs near the top of the shallowest reservoir. Since the Golden Meadow Fault is modeled as a discontinuity in the elastic half space, deformation on one side of the fault will not translate to the other side (hence no deformation to the north of the fault), predicted subsidence near the edge is an artifact due to the size of subsurface structural map used for identifying the location of the Golden Meadow Fault. The edge of the surface trace of the Golden Meadow Fault corresponds to the edge of the structural maps used in the study. As a result, subsidence at the edge of the fault trace will disappear in this figure if a larger structural map is used.

Comparing the predicted subsidence with the Geertsma method and the releveling line as in Figure 5.15, it is apparent that the occurrence of compaction-driven fault slip along the Golden Meadow Fault significantly changes the prediction of the vertical elevation change across the Lapeyrouse Field (Fig 5.20). Slip on fault as a result of reservoir compaction provided extra vertical elevation change at Station M in the two cases examined (the Field X elastic rheology and the generalized compaction curve for unconsolidated sands). For the elastic case, compaction-driven slip on fault resulted in an additional 6 cm of elevation change at Station M; an additional 10 cm of elevation change is predicted when the reservoirs are assumed to be unconsolidated. Although the generalized compaction curve for unconsolidated sands provides larger estimated elevation changes at Station M, it also over-estimates the magnitude of subsidence south of the field.

While the slip distribution estimated through Poly3D is driven by compaction and deformation around the reservoir with the assumption of a traction-free fault, it is important to investigate if the stress induced by compaction is large enough to potentially trigger fault slip if the fault is locked. As a result, I alter the boundary conditions for the Golden Meadow Fault in Poly3D such that the fault is displacement-free during reservoir compaction and allow stresses to build up on the fault. Figure 5.21 illustrates the shear and normal tractions accumulated on the fault surface as a result of reservoir compaction (based on the Hagin elastic rheology). The tractions calculated from Poly3D define compressional stress as negative, I have changed the sign of the stress such that compressive stress is positive since *in situ* stresses in the crust are compressional in most parts of the world (e.g., Zoback & Zoback, 1989, 2002). Figure 5.21 shows that the downdip shear traction is more compressional along the fault above the reservoirs (Fig. 5.21A) while shear traction along strike are minimal (Fig. 5.21B). Normal traction (Fig. 5.21C) reduces significantly near the center of all the reservoirs. The Coulomb Failure Stress (CFS) is then calculated to investigate the potential of the stress change to trigger fault slip along the Golden Meadow Fault.

Coulomb Failure Stress is commonly used in earthquake seismology to determine if stress changes as a result of a particular seismic event will trigger fault slip and earthquakes on nearby faults (see review by Harris, 1998). However, earthquakes or slip on faults triggered by induced stress changes are not limited to naturally occurring events, the phenomena can also occur as a result of human activities (e.g., Seeber *et al*., 1998). Based on the Coulomb failure assumption (Jaeger & Cook, 1969), the Coulomb Failure Stress (CFS) can be defined as:

$$CFS = |\vec{\tau}| + \mu(\sigma - p) - S \quad \text{.....(5.3)}$$

where τ and σ are the shear and normal stress acting on the fault while μ is the coefficient of friction, S is the cohesion and p is the fluid pressure. Assuming S and μ remain constant through time, a change in CFS can now be defined as:

$$\Delta CFS = \Delta|\vec{\tau}| + \mu(\Delta\sigma - \Delta p) \quad \text{.....(5.4)}$$

In most cases when the change in pore pressure is unknown, an effective coefficient of friction is often used such that:

$$\Delta CFS = \Delta|\vec{\tau}| + \mu'\Delta\sigma \quad \text{.....(5.5)}$$

where μ' is often between 0.4 and 0.5.

From earthquake seismology, several authors have reported that stress change of as low as 0.01 MPa can have an impact on the location and occurrence of aftershocks (e.g., Reasenberg & Simpson, 1992; King *et al*., 1994; Hardebeck *et al*., 1998). Figure 5.22 suggests that the ΔCFS from reservoir compaction is large enough to trigger slip along the Golden Meadow Fault (comparing to the 0.01 MPa reported in seismological studies). The green zone on Figure 5.22 marks the area of the fault where no stress change is expected. The blue zone indicates where slip is unlikely to occur while the red zones are areas of high slip potential on the Golden Meadow Fault. Figure 5.23 shows that the maximum slip on the Golden Meadow Faults estimated from Poly3D coincides with the high slip potential zone from the Coulomb Failure Stress analysis. The calculations are based on Equation 5.5 assuming the μ' is equal to 0.6. If a lower μ' is used, the size of the 'slip unlikely' zone is reduced (Figure 5.24). The dark red area at the bottom of the fault is an artifact as a result of interpolation from MATLAB. Based on the magnitude of the change in Coulomb Failure Stress induced by compaction, the predicted compaction-induced fault slip along Golden Meadow Fault can occur in the crust.

Altering material properties of the surrounding medium, such as the Young's modulus or the Poisson's ratio in Poly3D, has little impact on the estimated compaction-induced slip along the Golden Meadow Fault. Changes in the material properties in the vicinity of the reservoir only affect the magnitude of cumulated stress on a locked Golden Meadow Fault. However, the variation of stress cumulated on the locked Golden Meadow Fault is still at least an order of magnitude larger than the commonly used 0.1 MPa thresholds for stress changes in earthquake seismology. As a result, local production-induced compaction-driven slip on fault is a mechanism that should not be ignored.

5.6 DISCUSSION

Wetland loss is a result of complex interactions between compaction, relative sea-level change, sediment accumulation, fault movement and other human activities from canal constructions to subsurface fluid withdrawal. Using offshore oilfields as an analog, both analytical and numerical models show that production-induced reservoir compaction can lead to substantial surface subsidence. With limited information, the vertical elevation change estimated at Lapeyrouse is comparable to that by the observed releveling survey. The extent of the subsidence bowl is inversely proportional to the depth of the producing reservoir and directly proportional to the amount of compaction occurred in the producing reservoir (Geertsma, 1973). However, it is clear that reservoir compaction is not the only mechanism that causes surface subsidence and thus wetland loss in the Louisiana Coastal Zone. While pore pressure reduction in the reservoir leads to compaction, stress changes as a result of reservoir deformation may encourage and trigger fault slip along regional growth faults located in the vicinity of the reservoirs.

The impact of movement along regional growth faults is often ignored in wetland loss studies, Penland *et al*. (2002) report that 54% of wetland loss in coastal Louisiana is related to land subsidence and attributed ~1% of land loss to faulting which corresponds to one location: the Empire Fault in the Balize Delta (Penland *et al*., 2000). However, Gagliano *et al*. (2003) argue that Penland *et al.* (2002) have mistakenly attributed most of the wetland loss to faulting-induced secondary phenomena such as altered hydrology, natural waterlogging and alteration associated with water impoundment. Gagliano *et al*. (2003) suggested that wetland loss was primarily the result of slip along regional growth faults that are linked to the Oligocene-Miocene detachment surface at depth of over 6 km. They also proposed that the massive land loss in the Terrebonne Trough was a result of movement along the regional faults as a result of the subsurface salt migration towards the Gulf of Mexico creating an onshore extensional zone. Using aerial photographs, they identified more than one hundred surface fault traces and concluded that most of these fault traces are related to subsurface faults. Since most of the wetland loss located near the surface trace of these major faults, Gagliano *et al.* (2003) concluded that fault movements along these growth faults have been occurring throughout the Quaternary and the sudden loss of wetland in the 1960s is just a result of sediment deprivation from the

Mississippi River that accentuates surface signatures. They also suggested that fault movement along these active growth faults are episodic and are not uniform across the fault regionally. Based on surface elevation changes, they concluded that the rate of vertical movement along active faults ranged from 1.5 mm/yr to 12.2 mm/yr. Unfortunately, these rates of movement are estimated without separating effects from any other potential contributors to fault movements, as a result, the fault movement rates proposed by Gagliano *et al*. (2003) cannot be used as the background slip rate for the regional growth faults since they include the combined effects of natural and human-induced fault movement plus other mechanisms mentioned in previous sections.

If the regional growth faults located in the coastal Louisiana are active and have natural episodic movements, it is fair to assume that these faults behave similarly to some plate boundary faults that are subjected to constant loading. Failure (or fault movement) occurs when the stress acting on the fault surface reaches a threshold stress. After the fault slips, the accumulated stress is released and the fault is locked again until stress builds up to the threshold stress again. The perturbations of ΔCFS can bring the pre-stressed fault closer to (or further from) failure that lead to the fault to slip sooner (or later) than the normal slip schedule (e.g., Harris & Simpson, 1992; King *et al*., 1994) by an amount of Δt (Fig. 5.25). Since most growth faults in coastal Louisiana are active, the relatively large ΔCFS induced by reservoir compaction due to hydrocarbon production may have an impact on the frequency of slip along these growth faults.

A few modifications can be preformed in the future to improve the accuracy of the model predictions presented in this Chapter:

(1) Better rock mechanics experiments based on cores collected from on-shore fields. This will provide important insights on how these reservoirs will compact during depletion and possibly after abandonment. As shown in Figure 5.15, estimated subsidence is highly dependent on the chosen rheology used in the model.

(2) Recent developments at the Lapeyrouse field have not been taken into consideration. Gas production at Lapeyrouse is still under way but in different sand units. The presented models only focus on the four sands where peak production appears to coincide with the peak wetland loss in the Madison Bay

hotspot. However, as production continues in other sand units after the abandonment of the four sands examined, their corresponding contributions to surface subsidence have been ignored. These contributions might be enough to explain some of the misfit observed between the model predictions and the measured elevation change.

(3) There are additional producing hydrocarbon reservoirs north of the Golden Meadow Fault, the models presented in this Chapter have not taken into account the deformation which occurred in these reservoirs. If the offset in vertical elevation changes near the Golden Meadow Fault is removed from Figure 5.7, the remaining subsidence pattern might potentially be explained by the cumulative subsidence induced by compaction of all producing reservoirs in the region. Stress changes induced by reservoir compaction north of the Golden Meadow Fault may also affect the magnitude and location of slip along the fault. These changes may alter the predicted subsidence in this region.

(4) A more complete numerical model should be able to estimate the potential interaction among the subsurface faults. Note that only the Golden Meadow Fault is considered in this study, the effects of compaction on other subsurface faults in Lapeyrouse are ignored. With a more detailed finite element or Poly3D model, a better understanding of how faults in and around the Lapeyrouse field interact and their potential impacts on movement along the Golden Meadow Fault can be determined.

(5) Incorporation of potential lateral heterogeneity on compressibility and thickness along with heterogeneous pressure decline within the fault block will lead to a better control on reservoir compaction modeling and understanding of the reservoir bounding fault.

(6) Micro-seismicity experiments should be preformed to monitor the behavior of the reservoir-bounding fault as a result of fluid withdrawal or injection. These experiments can also yield a more precise subsurface mapping of the location of the faults.

(7) Although the relevel line should yield a relatively accurate result on vertical elevation changes, disagreements on the actual elevation changes measured by the releveling line exist (Morton, *personal communications*). As a result, uncertainties associated with the releveling survey should be examined in greater detail.

5.7 CONCLUSIONS

Utilizing an analytical method known as the Geertsma solution and a numerical model derived from Poly3D, the relationship between subsurface hydrocarbon production, land surface subsidence and fault reactivation has been investigated in the Louisiana Coastal Zone. The Lapeyrouse field located in the Terrebonne Parish is chosen as the study site due to its proximity to the Madison Bay land loss hotspot and because it is bounded by a major regional growth fault in the north. The magnitudes of reservoir compaction are estimated based on changes in pressure and stress along with several constitutive rheological relationships derived from samples of other offshore oilfields in the Gulf of Mexico. Although there are some uncertainties associated with the severity of reservoir compaction due to massive fluid withdrawal in Lapeyrouse, the predicted subsidence based on the Geertsma solution yields a comparable result to the measured elevation change from releveling surveys. The similarity between the simple Geertsma solution and surface elevation measurements suggests that subsurface hydrocarbon production has some influence on surface deformation. However, compaction-induced subsidence cannot fully capture the subsidence profile near the Golden Meadow Fault. Using a more complicated numerical model using Poly3D, I have demonstrated how reservoir compaction may have encouraged slip along the Golden Meadow Fault. The change in stress acting on the fault induced by reservoir compaction may have advanced (or in some areas reduced) the slip schedule of this active growth fault. The estimated elevation change as a result of compaction-induced fault slip only contributes about 35% of the actual measured elevation change. It is uncertain if this misfit is caused by the uncertainties associated with the modeling (such as rock properties, reservoir geometries and interaction among faults) or other natural processes. Regardless, using both simple

analytical and numerical models with limited information, I have demonstrated that hydrocarbon production can introduce surface subsidence (and to some extent fault slip) in the order of the observed surface elevation change locally. With a more sophisticated model, it should be possible to filter out the contribution of hydrocarbon production induced subsidence from local surface subsidence signals once relevant information becomes available.

Coastal wetland loss is a result of complicated interactions between natural processes and human activities; it is difficult to isolate the impact of one specific mechanism from another. The study presented in this chapter suggests that production-induced land subsidence is one of the many mechanisms that should not be ignored when evaluating wetland loss in the Louisiana Coastal Zone. Detailed studies and modeling incorporating other mechanisms are required in order to accurately assess the interaction between these mechanism and their cumulative contributions to surface subsidence. While wetland loss is ubiquitous in southern Louisiana, it is fair to assume that extensive hydrocarbon production may have accelerated or encouraged deformation in the vicinity of the reservoir that led to surface subsidence in a local scale. An understanding on the impact of fluid withdrawal could help determine if pressure maintenance during production, such as fluid injection, could slow down or eliminate subsidence due to reservoir compaction in sensitive wetland areas.

5.8 REFERENCE

Baranova, V., Mustaqeem, A., & Bell, S., 1999. A model for induced seismicity caused by hydrocarbon production in the Western Canada sedimentary basin. *Canadian Journal of Earth Sciences*, **36**, 47-64.

Barras, J.A., Bourgeois, P.E., & Handley, L.R., 1994. Land loss in coastal Louisiana: 1956-1990. National Wetlands Research Center Open File Report 94-01

Boesch, D.F., Josselyn, M.N., Mehta, A.J., Morris, J.T., Nuttle, W.K., Simenstad, C.A., & Swift, D.J.P., 1994. *Scientific Assessment of Coastal Wetland Loss, Restoration & Management in Louisiana. Journal of Coastal Research Special Issue* **20**. 103pp.

Britsch, L.D., & Dunbar, J.B., 1993. Land loss rates: Louisiana Coastal plain. *Journal of Coastal Research*, **9**, 324-338.

Byrd, P.F., & Friedman, M.D., 1971. *Handbook of Elliptic Integrals for Engineers and Scientists, 2nd Edition.* Springer-Verlag: New York, 358pp.

Cahoon, D.R., Day, J.W., Jr, Reed, D.J., 1999. The influence of surface and shallow subsurface soil processes on wetland elevation; a synthesis. *Current Topics in Wetland Biogeochemistry*, **3**, 72-88.

Colazas, X.C., & Strehle, R.W., 1995. Subsidence in the Wilmington oilfield, Long Beach, California, USA. *In: Chilingarian, G.V. eds., Subsidence due to Fluid Withdrawal*. Elsevire Science, 285-336.

Coleman, J.M., & Roberts, H.H., 1989. Deltaic coastal wetlands. *Geologie en Mijnbouw*, **68**, 1-24.

Davis, S.D., Nyffenegger, P.A., & Frohlich, C., 1995. The 9 April 1993 earthquake in south-central Texas: was it induced by fluid withdrawal? *Bulletin of Seismological Society of America*, **85**(6), 1888-1895.

Doser, D.I., Baker, M.R., & Mason, D.B., 1991. Seismicity in the War-wink gas field, Delaware Basin, West Texas, and its relationship to petroleum production. *Bulletin of the Seismological Society of America*, **81**(3), 971-986.

Eason, G., Noble, B., & Sneddon, I.N., 1954. On certain integrals of Lipschitz-Hankel type involving products of Bessel functions. *Philosophical Transaction, Royal Society of London*, **A247**, 529-551.

Evans, D.M., 1966. The Denver area earthquakes and the Rocky Mountain Arsenal Disposal Well. *Mountain Geologist*, **3**, 23-36.

Farber, S., 1987. The value of coastal wetlands for protection of property against hurricane wind damage. *Journal of Environmental Economics and Management,* **14**(2), 143-151.

Gabrysch, R.K. and Bonnet, C.W., 1975. Land-surface subsidence in Houston-Galveston region, Texas. *Texas Water Development Board Report 188*, Austin: Texas, 19p.

Gabrysch, R.K. and Coplin, L.S., 1990. Land-surface subsidence resulting from ground-water withdrawals in the Houston-Galveston region, Texas, through 1987. *U.S. Geological Survey Report of Investigations No. 90-01*, Washington, D.C., 53p.

Gagliano, S.M., Kemp, E.B., III, Wicker, K.M., Wiltenmuth, K.S., & Sabate, R.W., 2003. Neo-tectonic framework of southeast Louisiana and applications to coastal restoration. *Transactions of the 53rd Annual Convention of the Gulf Coast Association of Geological Societies and the Gulf Coast Section SEPM 2003, Baton Rogue, Louisiana, October 22-24, 2003*, **LIII**, 262-272.

Geertsma, J., 1973. Land subsidence above compacting oil and gas reservoirs. *Journal of Petroleum Technology*, **June 1973**, 734-744.

Grasso, J. R. 1992. Mechanics of seismic instabilities induced by the recovery of hydrocarbons, *Pure and Applied Geophysics* **139**, 507-533.

Grasso, J.R., & Wittlinger, G., 1990. Ten years of seismic monitoring over a gas field. *Bulletin of the Seismological Society of America*, **80**(2) 450-473.

Harris, R.A., 1998. Introduction to special section: stress triggers, stress shadows and implications for seismic hazard. *Journal of Geophysical Research*, **103** (B10), 24,347-24,358.

Harris, R.A., & Simpson, R.W., 1992. Changes in static stress in southern California faults after the 1992 Lander earthquake. *Nature*, **360**, 251-254.

Hardebeck, J.L., Nazareth, J.J., & Hauksson, E., 1998. The static stress change triggering model: constraints from two southern California aftershock sequences. *Journal of Geophysical Research*, **103** (B10), 24,427-24,438.

Jaeger, J.C. & Cook, N.G.W. 1969, *Fundamentals of Rock Mechanics*. Methuen and Co. Ltd.: London, 515p.

King, G.C.P., Stein, R.S., & Lin, J., 1994. Static stress changes and the triggering of earthquakes. *Bulletin of the Seismological Society of America*, **84**, 935-953.

Kuecher, G.J., Roberts, H.H., Thompson, M.D., & Matthews, I., 2001. Evidence for active growth faulting in the Terrebonne Delta Plain, South Louisiana: implications for wetland loss and the vertical migration of petroleum. *Environmental Geosciences*, **8** (2) 77-94.

Kooi, H., 1997. Insufficiency of compaction disequilibrium as the sole cause of high pore fluid pressure in pre-Cenozoic sediments. *Basin Research*, **9**, 227-241.

Kooi, H., 2000. Land subsidence due to compaction in the coastal area of The Netherlands: the role of lateral fluid flow and constraints from well-log data. *Global and Planetary Change*, **27**, 207-222.

Kooi, H., & de Vries, J.J., 1998. Land Subsidence and hydrodynamic compaction of sedimentary basins. *Hydrological Earth System Science*, **2**, 159-171.

Louisiana Coastal Wetlands Conservation and Restoration Task Force and the Wetlands Conservation and Restoration Authority, 1998. *Coast 2050: Toward a Sustainable Coastal Louisiana.* Louisiana Department of Natural Resources: Baton Rouge, LA. 161 p.

Marshall, G. A., R. S. Stein, and W. Thatcher, 1991. Faulting geometry and slip from co-seismic elevation changes: The 18 October 1989, Loma Prieta, California, earthquake, *Bulletin of the Seismological Society of America*, **81**, 1660-1693.

McGarr, A., 1991. On a possible connection between three major earthquakes in California and oil production. *Bulletin of the Seismological Society of America*, **81**(3), 948-970.

Mereu, R.F., Brunet, J., Morrissey, K., Price, B., & Yapp, Y., 1986. A study of the microearthquakes of the Gobles oil field area of Southwestern Ontario. *Bulletin of the Seismological Society of America*, **76**(5), 1215-1223.

Morton, R.A., Buster, N.A., & Krohn, M.D., 2002. Subsurface controls on historical subsidence rates and associated wetland loss in south central Louisiana. *Gulf Coast Association of Geological Societies Transactions*, **52**, 767-778.

Morton, R.A., Purcell, N.A., & Peterson, R., 2001. Field evidence of subsidence and faulting induced by hydrocarbon production in Coastal Southeast Texas. *Gulf Coast Association of Geological Societies Transactions*, **51**, 239-248.

Morton, R.A., Tiling, G., Ferina, N., 2003. Primary causes of wetland loss at Madison Bay, Terrebonne Parish, Louisiana. *USGS Open File Report* **03-60**.

Neighbors, R.J., 1981. Subsidence in Harris and Galveston counties, Texas, in: *A.I. Johnson, ed., Legal, Socio-Economic and Environmental Significance of Land Subsidence in the United States*. *American Society of Civil Engineering Journal of the Irrigation and Drainage Division,* **107** (IR2), 161-174.

Paine, J.G., 1993. Subsidence of the Texas coast: inferences from historical and late Pleistocene sea levels. *Tectonophysics*, **222**, 445-458.

Penland, S., & Ramsey, K.E., 1990. Relative sea-level rise in Louisiana and the Gulf of Mexico: 1908-1988. *Journal of Coastal Research*, **6**, 323-342.

Penland, S., Ramsey, K.E., McBride, R.A., Moslow, T.F., & Westphal, K.A., 1988. *Relative Sea Level Rise and Subsidence in Louisiana and the Gulf of Mexico*: Louisiana Geological Survey, Baton Rouge, Louisiana. 65p.

Penland, S., Wayne, L., Britsch, L.D. Williams, S.J., Beall, A.D. and Butterworth, V.C., 2000. Process classification of coastal land loss between 1932 and 1990 in the Mississippi river delta plain, Southeastern Louisiana. *USGS Open File* **00-418**.

Penland, S., Williams, S.J., Britsch, L.D., & Beall, A.D., 2002. Geologic classification of coastal land loss between 1932 and 1990 in the Mississippi River Delta Plain, southeastern Louisiana. *Transactions of the Gulf Coast Association of Geological Societies*, **52**, 799-807.

Pennington, W.D., Davis, S.D., Carlson, S.M., DuPree, J.D., & Ewing, T.E., 1986. The evolution of seismic barriers and asperities caused by the depressuring of fault planes in oil and gas fields of south Texas. Bulletin *of the Seismological Society of America*, **76**, 939-948.

Raleigh, C.B., Healy, J.H., & Bredehoeft, J.D., 1976. An experiment in earthquake control at Rangely, Colorado. *Science*, **191**, 1230-1237.

Reasenberg, P.A., & Simpson, R.W., 1992. Response of regional seismicity to the static stress change produced by the Loma Prieta earthquake, *Science*, **244**, 1687-1690.

Reed, D.J. and Cahoon, D.R., 1993. Marsh submergence vs. marsh accretion: interpreting accretion deficit data in coastal Louisiana. *In Magoon, O.T., Wilson, W.S. Converse, H. and Tobin, L.T. (eds.), Coastal Zone '93, Proceedings of the Eighth Symposium on Coastal and Ocean Management.* New York: American Society of Civil Engineers, 243-257.

Roberts, H.H., Bailey, A., & Kuecher, G.J., 1994. Subsidence in the Mississippi River delta; important influences of valley filling by cyclic deposition, primary consolidation phenomena, and early diagenesis. *Forty-fourth annual convention of the Gulf Coast Association of Geological Societies, American Association of Petroleum Geologists*

and the Forty-first annual convention of the Gulf Coast Section of the Society of Economic Paleontologists and Mineralogists, **44**, 619-629.

Scardina, A.D., Nunn, J.A., & Pilger, R.H., Jr., 1981. Subsidence and flexure of the lithosphere in the North Louisiana salt basin. *EOS, Transactions*, American Geophysical Union, **62**(17), 391.

Seeber, L., Armbruster, J.G., Kim, W.Y., & Barstow, N., 1998. The 1994 Cacoosing Valley earthquakes near Reading, Pennsylvania: a shallow rupture triggered by quarry unloading. *Journal of Geophysical Research*, **103** (B10) 24,505-24,521.

Segall, P. 1985. Stress and subsidence resulting from subsurface fluid withdrawal in the epicentral region of the 1983 Coalinga earthquake. *Journal of Geophysical Research* **90**, 6801-6816.

Segall, P., 1989. Earthquakes triggered by fluid extraction. *Geology*, **17**, 942-946.

Segall, P. 1992. Induced stresses due to fluid extraction from axisymmetric reservoirs. *Pure and Applied Geophysics* 139: 535.

Segall, P., & Fitzgerald, S.D., 1998. A note on induced stress changes in hydrocarbon and geothermal reservoirs. *Tectonophysics* **289**, 117-128.

Segall, P., Grasso, J.R., Mossop, A., 1994. Poroelastic stressing and induced seismicity near the Lacq gas field, southwestern France. *Journal of Geophysical Research* **99** (B8) 15423-15438.

Sharp, J.M., Jr., & Hill, D.W., 1995. Land subsidence along the northeastern Texas Gulf coast: effects of deep hydrocarbon production. *Environmental Geology*, **25**, 181-191.

Stein, R.S., Whalen, C.T., Holdahl., S.R., & Strange, W.E., 1986. Saugus-Palmdale, California, field test for refraction error in historical leveling surveys. *Journal of Geophysical Research*, **91**, 9031-9044.

Sticker, E.E., 1979. *Geology and Reservoir Analysis of the Lapeyrouse Field, Terrebonne Parish, Louisiana.* Unpublished M.S. Thesis. University of New Orleans, New Orleans, Louisiana: 68pp.

Suhayda, J.N., 1987. Subsidence and sea level. *In*: *Turner, R.E., & Cahoon, D.R., (eds.), Causes of Wetland Loss in the Coastal Central Gulf of Mexico, Volume II: Technical Narrative.* OCS Study/MMS 87-0120. New Orleans: Louisiana: Minerals Management Service. 187-202.

Suhayda, J.N., Bailey, A., Roberts, H.H., Penland, S., & Kuecher, G., 1993. Subsidence properties of Holocene sediments: South Louisiana. *Coastal Zone '93 New York*, New York: American Society of Civil Engineering, 1215-1229.

Sulak, R.M., 1991. Ekofisk: the first 20 years. *Journal of Petroleum Technology*, **43**(10), 1265-1271.

Swanson, R.L. and Thurlow, C.I., 1973. Recent subsidence rates along the Texas and Louisiana coasts as determined from tide measurements. *Journal of Geophysical Research*, **78**, 2665-2671.

Thompson, A.L., 1993. *Poly3D: A Three-Dimensional, Polygonal Element, Displacement Discontinuity Boundary Element Computer Program with Applications to Fractures, Faults and Cavities in the Earth's Crust*. Unpublished M.S. Thesis, Stanford University, Stanford, California.

van Hasselt, J.Ph., 1992. Reservoir compaction and surface subsidence resulting from oil and gas production: A review of theoretical and experimental research approaches. *Geologie en Mijnbouw*, **71**, 107-118.

White, W.A. and Morton, R.A., 1997. Wetland losses related to fault movement and hydrocarbon production, Southeastern Texas coast. *Journal of Coastal Research*, **13**, 1305-1320.

White, W.A. and Tremblay, T.A., 1995. Submergence of wetlands as a result of human-induced subsidence and faulting along the upper Texas Gulf coast. *Journal of Coastal Research*, **11**, 788-807.

Yale, D.P., Nabor, G.W., Russell, J.A., Pham, H.D., & Yousef, Mohamed, 1993. Application of variable formation compressibility for improved reservoir analysis. SPE 26647.

Zoback, M.D., & Zoback, M.L., 1989. Tectonic stress field of the conterminous United States. *Geological Society of America Memoir*, **172**, 523-539.

Zoback, M.D., & Zoback, M.L., 2002. Stress in the Earth's lithosphere. *In: Encyclopedia of Physical Sciences and Technology, Third Edition*, **16**, 143-154.

APPENDICE 5.A: THE GEERTSMA METHOD

For a disc-shaped reservoir of thickness *H* and radius *R* at depth *D*, Geertsma (1973) estimated the effect of production on surface subsidence based on a nucleus-of-strain concept. The reservoir is modeled as an "isolated volume of reduced pore pressure in a porous or non-porous but elastically deforming half-space with traction free surface" (Geertsma, 1973). Based on poroelastic theory, subsidence due to a uniform pore pressure reduction, ΔP_P, can be treated as the displacement perpendicular to the free surface as a result of the nucleus of strain for a small but finite volume, V, such that:

$$u_z(r,0) = -\frac{1}{\pi} c_m (1-\nu) \frac{D}{\left(r^2 + D^2\right)^{3/2}} \Delta P_P V \quad \text{.....(5.A.1)}$$

$$u_r(r,0) = +\frac{1}{\pi} c_m (1-\nu) \frac{r}{\left(r^2 + D^2\right)^{3/2}} \Delta P_P V \quad \text{.....(5.A.2)}$$

Where c_m is defined as the formation compaction per unit change in pore-pressure reduction, and Poisson's Ratio, ν. Assuming both c_m and ν are constant throughout the entire half space, the amount of subsidence caused by a producing disc-shaped reservoir at depth can then be estimated by integrating the nucleus-of-strain solution over the reservoir volume:

$$u_z(r,0) = -2c_m (1-\nu) \Delta P_P HR \int_0^\infty J_1(R\alpha) J_0(r\alpha) e^{-D\alpha} d\alpha \quad \text{.....(5.A.3)}$$

$$u_r(r,0) = +2c_m (1-\nu) \Delta P_P HR \int_0^\infty J_1(R\alpha) J_1(r\alpha) e^{-D\alpha} d\alpha \quad \text{.....(5.A.4)}$$

J_0 and J_1 are Bessel function of the zero and first order respectively. Eason *et al.* (1954) evaluate integrals involving products of Bessel functions. The general form of such integrals is noted as:

$$I(\mu,\nu;\lambda) = \int_0^\infty J_\mu(at) J_\nu(bt) e^{-ct} t^\lambda dt \quad \text{.....(5.A.5)}$$

Introducing the dimensionless parameters ρ = r / R and η = D / R, Equation (5.A.3) and (5.A.4) can be simplified as

$$u_z(r,0) = -2c_m (1-\nu) \Delta P_P HA(\rho,\eta) \quad \text{.....(5.A.6)}$$

$$u_r(r,0) = 2c_m(1-\nu)\Delta P_p HB(\rho,\eta) \quad \text{.....(5.A.7)}$$

Where $A = RI(1,0;0)$ and $B = RI(1,1;0)$. The solutions for A and B are linear combinations of the elliptic integrals of the first, second and third kind (Eason *et al.*, 1954).

$$A = I(1,0;0) = \begin{cases} -\dfrac{k\eta}{4\sqrt{\rho}}F_0(m) - \dfrac{1}{2}\Lambda_0(p,k) + 1 & (\rho < 1) \\ -\dfrac{k\eta}{4}F_0(m) + \dfrac{1}{2} & (\rho = 1) \\ -\dfrac{k\eta}{4\sqrt{\rho}}F_0(m) + \dfrac{1}{2}\Lambda_0(p,k) & (\rho > 1) \end{cases} \quad \text{.....(5.A.8)}$$

$$B = I(1,1;0) = \frac{1}{k\sqrt{\rho}}\left[\left(1-\tfrac{1}{2}k^2\right)F_0(m) - E_0(m)\right] \quad \text{.....(5.A.9)}$$

where $m = k^2 = \dfrac{\rho}{(1-\rho)^2+\eta^2}$ and $p = \dfrac{k^2\left\{(1-\rho)^2+\eta^2\right\}}{(1-\rho)^2+k^2}$. F_0, E_0 and Λ_0 are the completed elliptic integrals of the first, second kind and the Heuman's Lambda function respectively (see Appendix 5.B).

Figure 5.26 and 5.27 demonstrate the sensitivity of the estimated subsidence due to uncertainties associated with R, D, c_m and ν. Figure 5.26a shows that a 10% change in the radius of the disc-shaped reservoir could yield a 20% uncertainty in the estimated subsidence for a shallow reservoir (i.e, $D \approx R$). A 10% change in D could results in a 10% change in the estimated subsidence (Fig. 5.26b). Uncertainty related to Poisson's Ratio is relatively insignificant, but the estimated surface subsidence appears to be directly proportional to the uncertainty associated with compressibility (Fig. 5.26c & 5.27c). However, if the reservoir is significantly deeper (i.e., $D > 10R$), the impact of the size of the disc on surface subsidence is less than 2% (Fig. 5.27a).

As Geertsma noted, rate and degree of pore pressure reduction in any gas reservoir depends on the permeability distribution within the reservoir, locations of the wells and the production rate. The analytical solution presented by Geertsma is limited to a disc-shaped reservoir. However, the Geertsma method could still be used for an irregular-shaped reservoir by replacing integration to summation of the effect of nucluei of strain over the reservoir volume.

APPENDIX 5.B: THE LEGENDRE'S ELLIPTIC INTEGRALS

An integral with the form of $\int R\left(t,\sqrt{a_0t^4+a_1t^3+a_2t^2+a_3t+a_4}\right)dt$ is called the elliptic integral if the equation $a_0t^4+a_1t^3+a_2t^2+a_3t+a_4=0$ has no multiple roots and if R is a rational function of t and of the square root $\sqrt{a_0t^4+a_1t^3+a_2t^2+a_3t+a_4}$. The integral $\int R\left(t,\sqrt{a_0t^4+a_1t^3+a_2t^2+a_3t+a_4}\right)dt$ can be expressed linearly in terms of the three fundamental integrals (Byrd & Friedman, 1971):

a. The Legendre's normal elliptic integral of the first kind:

$$F(\varphi,k)\equiv\int_0^{\varphi}\frac{d\zeta}{\sqrt{1-k^2\sin^2\zeta}} \quad \text{.....(5.B.1)}$$

b. The Legendre's normal elliptic integral of the second kind:

$$E(\varphi,k)\equiv\int_0^{\varphi}\sqrt{1-k^2\sin^2\zeta}\,d\zeta \quad \text{.....(5.B.2)}$$

c. The Legendre's normal elliptic integral of the third kind:

$$\Pi\left(\varphi,\gamma^2,k\right)\equiv\int_0^{\varphi}\frac{d\zeta}{\left(1-\gamma^2\sin^2\zeta\right)\sqrt{1-k^2\sin^2\zeta}} \quad \text{.....(5.B.3)}$$

d. The Heuman's Lambda Function:

$$\Lambda(\varphi,p,k)=\sqrt{(1-p)\left(1-\frac{k^2}{p}\right)}\Pi(\varphi,p,k) \quad \text{.....(5.B.4)}$$

Where k is known as the modulus that could be any real or imaginary value, but most transformation used $0 < k < 1$; φ is known as the argument and could be either real or complex but usually limited to $0 < \varphi \le \pi/2$. When $\varphi = \pi/2$, the integrals (5.B.1) to (5.B.4) are said to be completed and the corresponding completed integrals are noted as:

$$\begin{aligned} &F_0(k)=\frac{2}{\pi}F\left(\frac{\pi}{2},k\right);E_0(k)=\frac{2}{\pi}E\left(\frac{\pi}{2},k\right);\\ &\Pi_0\left(\gamma^2,k\right)=\frac{2}{\pi}\Pi\left(\frac{\pi}{2},\gamma^2,k\right);\Lambda_0(p,k)=\frac{2}{\pi}\Lambda\left(\frac{\pi}{2},p,k\right)\end{aligned} \quad \text{.....(5.B.5)}$$

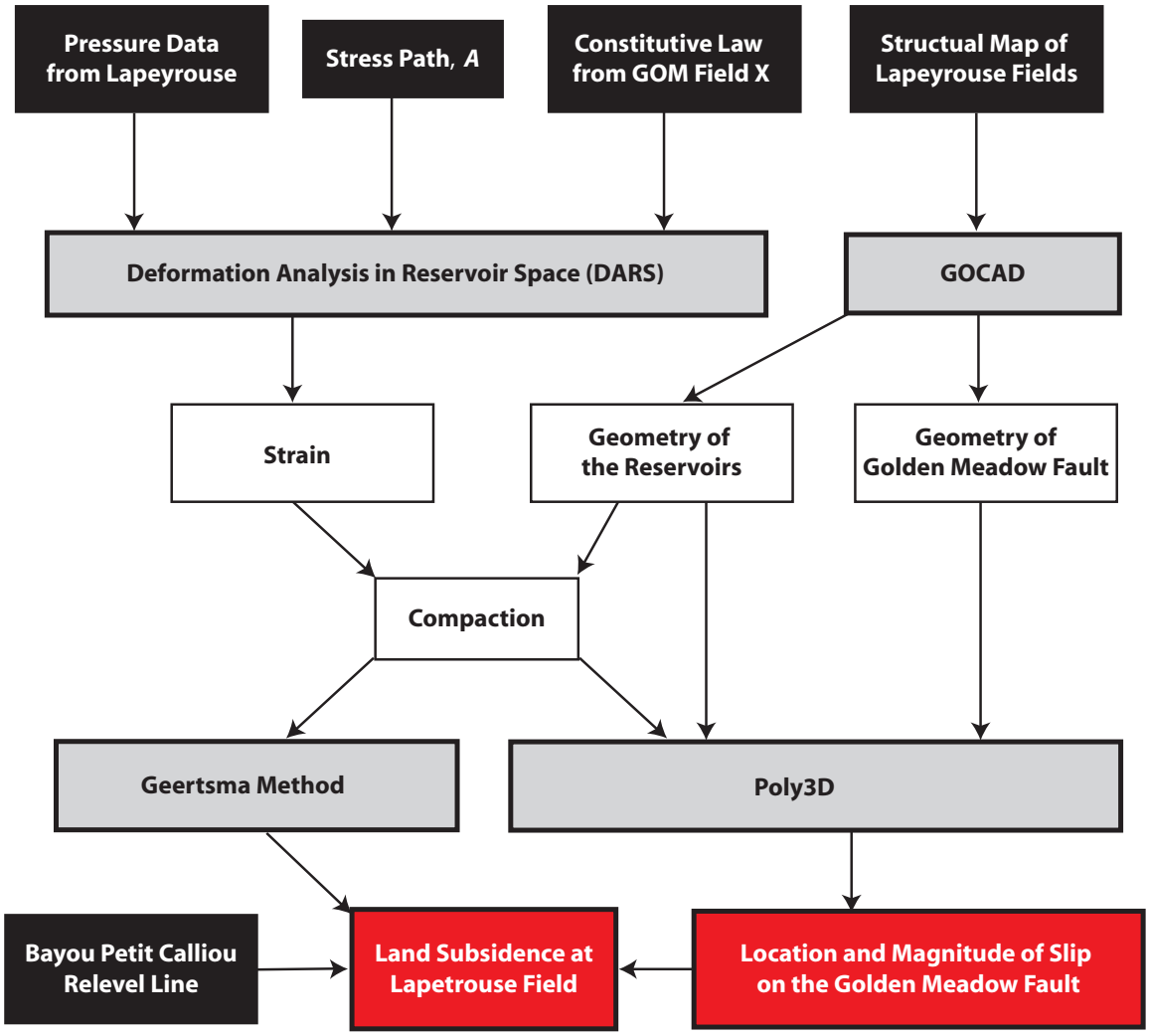

Figure 5.1: Workflow from raw data to the determination of the degree of production-induced subsidence. The black boxes represent data input from different sources; the gray boxes are the methodology used while the red boxes are the outcomes of the analysis.

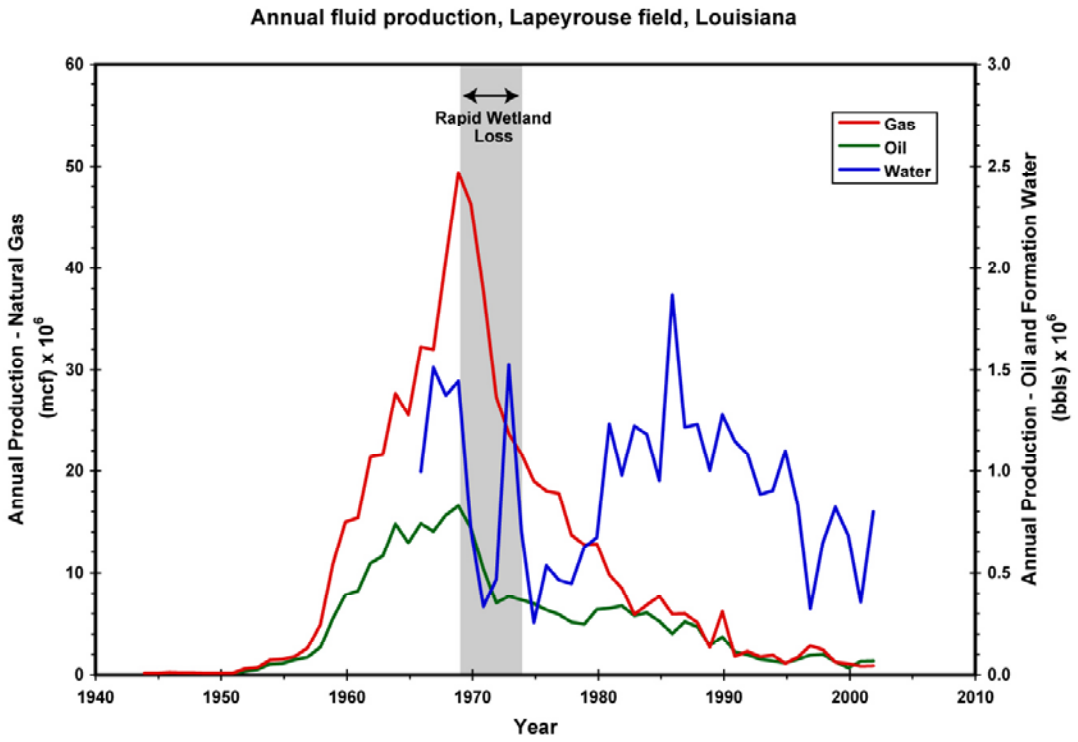

Figure 5.2: Cumulative annual production data for Lapeyrouse Field (modified after Morton *et al*., 2002). Rapid wetland loss occurs after the peak production period of the 1960s.

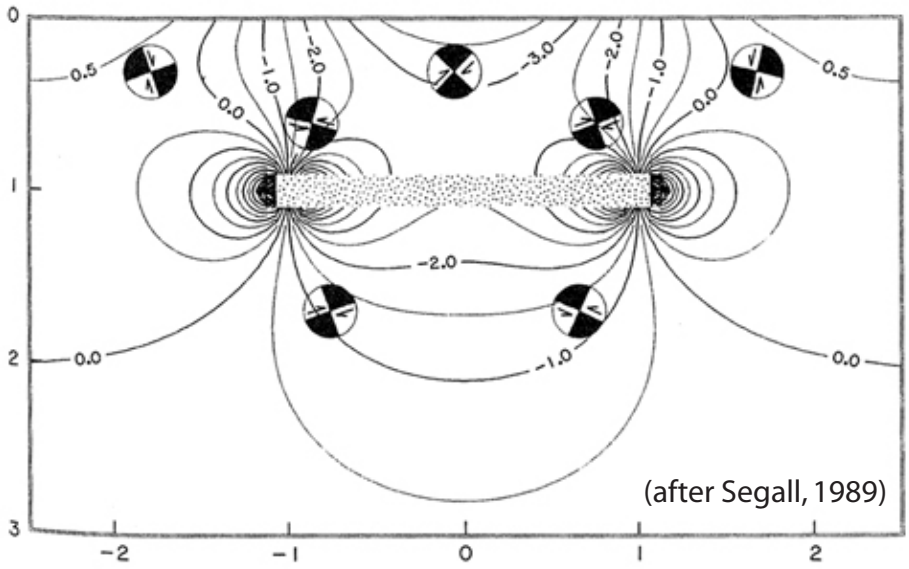

Figure 5.3: Segall (1989) calculated change in horizontal stress associated to depletion for a poroelastic reservoir embedded in an elastic medium (tension positive). The beach balls are the expected focal mechanisms for the induced earthquakes. Both axes in this diagram are normalized to the depth of the reservoir (after Segall. 1989).

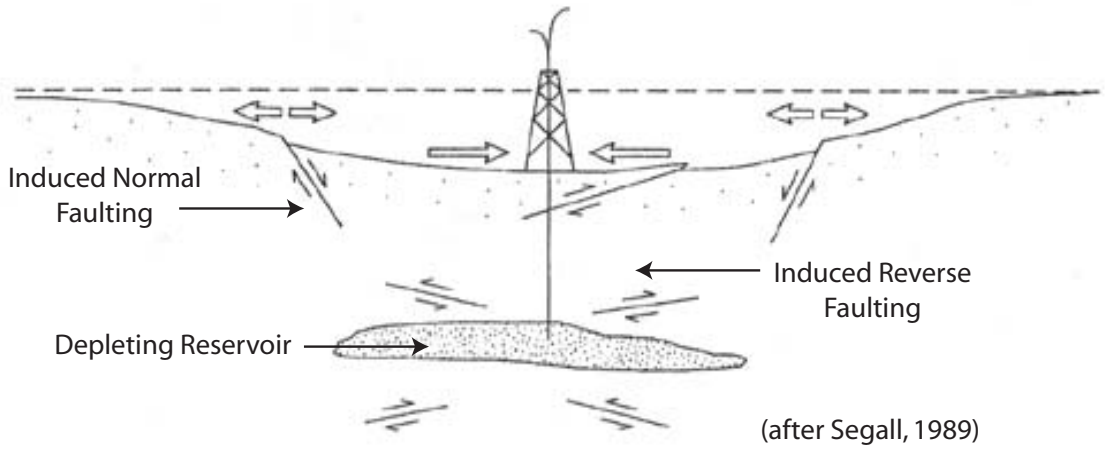

Figure 5.4: Schematic cross section of deformation surrounding a depleting reservoir (after Segall, 1989). Open arrows represent horizontal strain at the surface. Normal faulting will be induced in the extensional area near the flank while reverse faulting will developed in the more compressive environment.

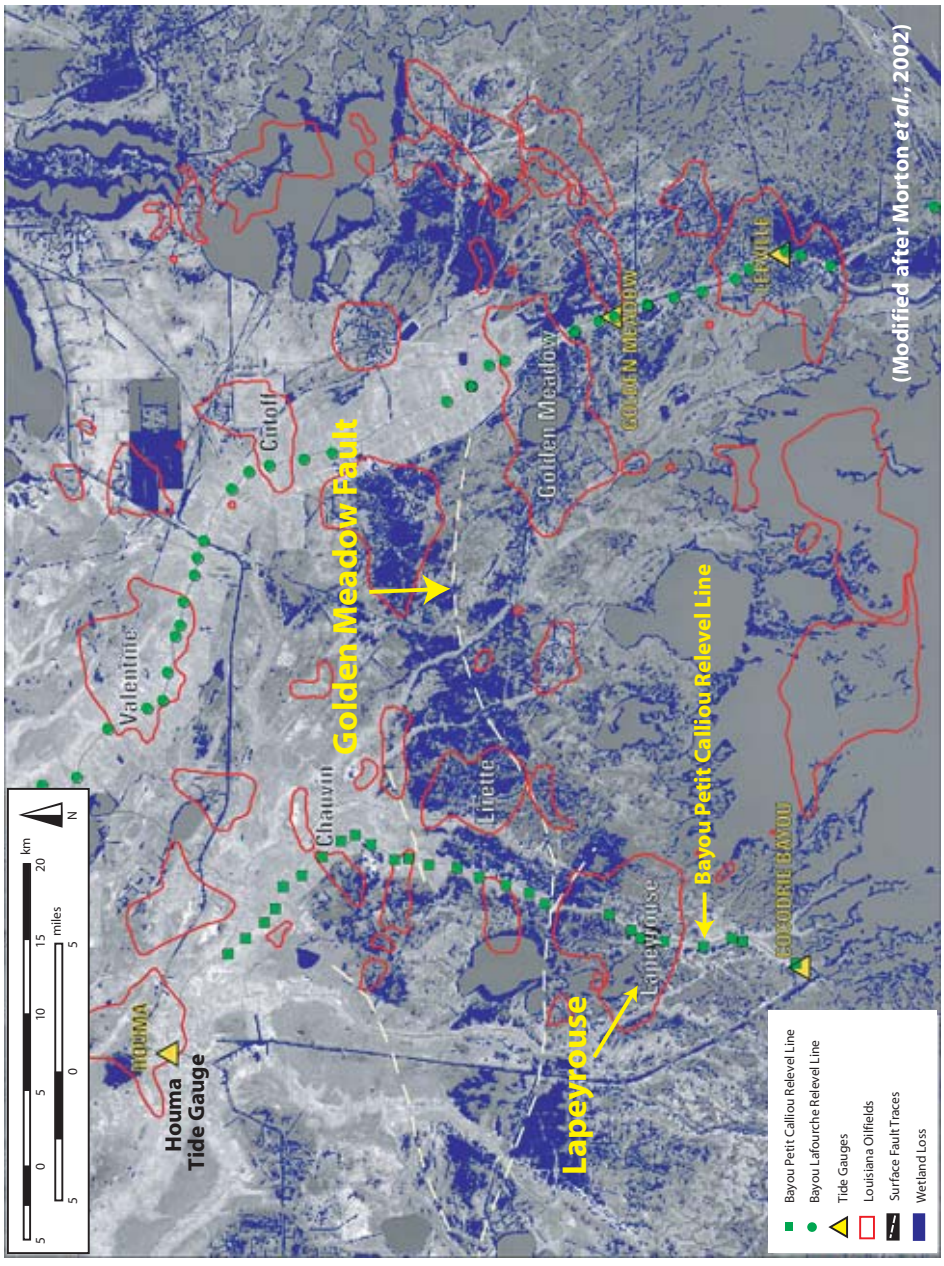

Figure 5.5: Regional aerial photograph of the study area (after Morton *et al.*, 2002). The Lapeyrouse field is located near the southern end of the Bayou Petit Calliou Releveling line (green squares). The Golden Meadow Fault is a regional growth fault and the surface trace has been mapped just north of the Lapeyrouse field. The dark blue zones are the wetland loss identified from aerial photographs.

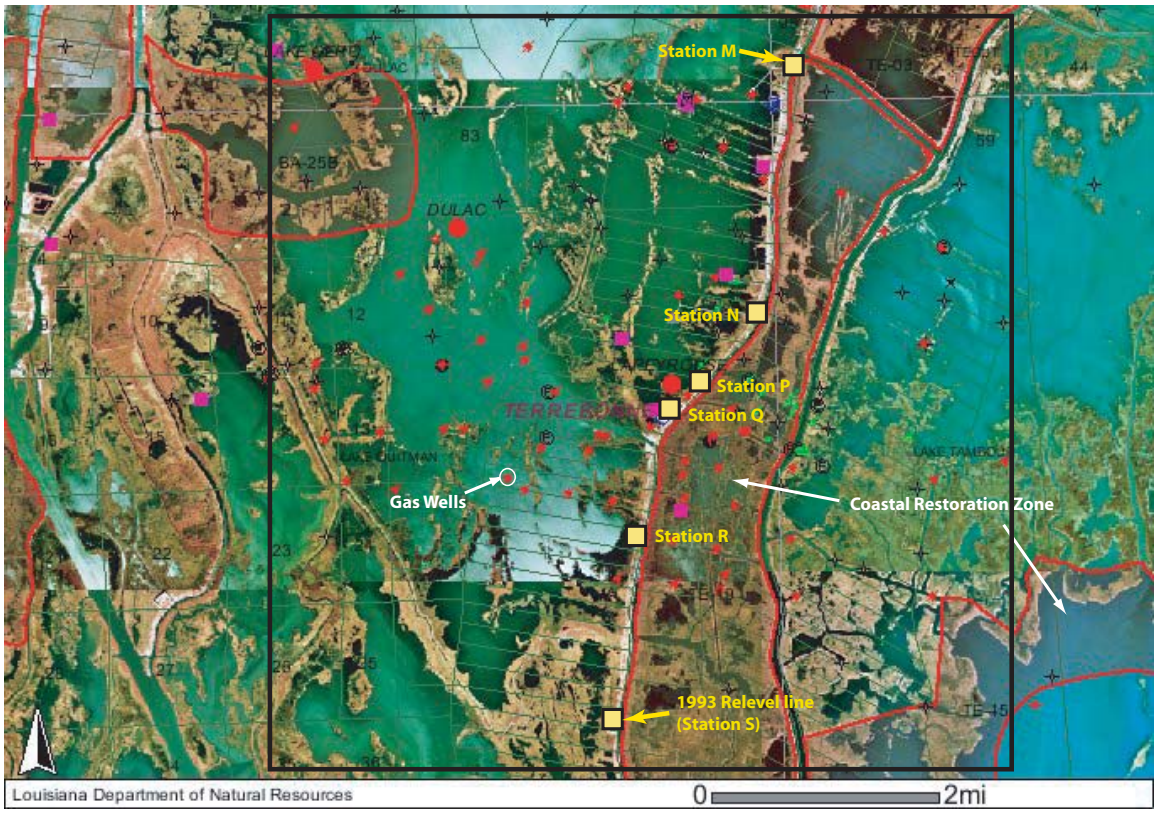

Figure 5.6: A close up aerial photograph of the Lapeyrouse Field (aerial photograph and location of wells are retrieved from the Louisiana Department of Natural Resources). This map shows the general location of the wells for the Lapeyrouse field (red dots). The yellow squares are the locations of the survey stations of the 1993 Bayou Petit Calliou Releveling study that transects the Lapeyrouse field.

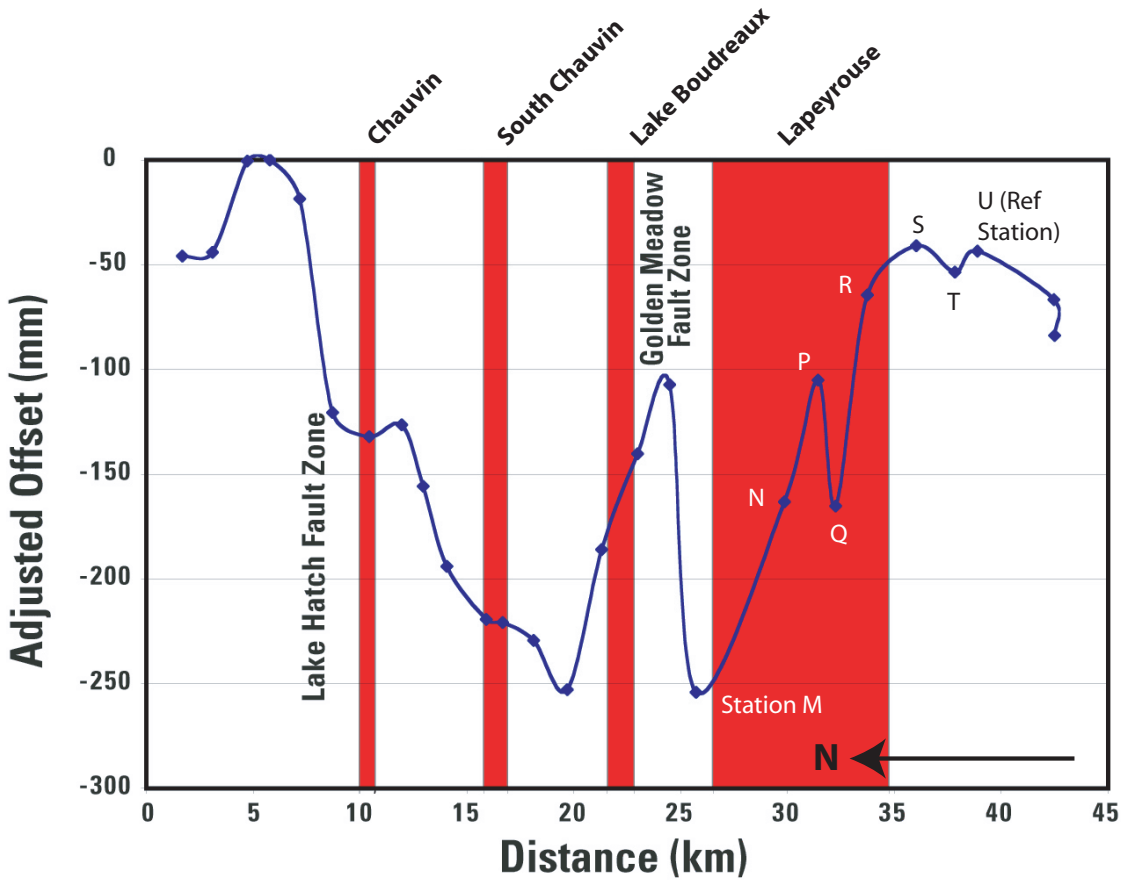

Figure 5.7: Relevel line along the Bayou Petit Calliou showing elevation changes between 1966 and 1993 (After Morton *et al.*, 2002).

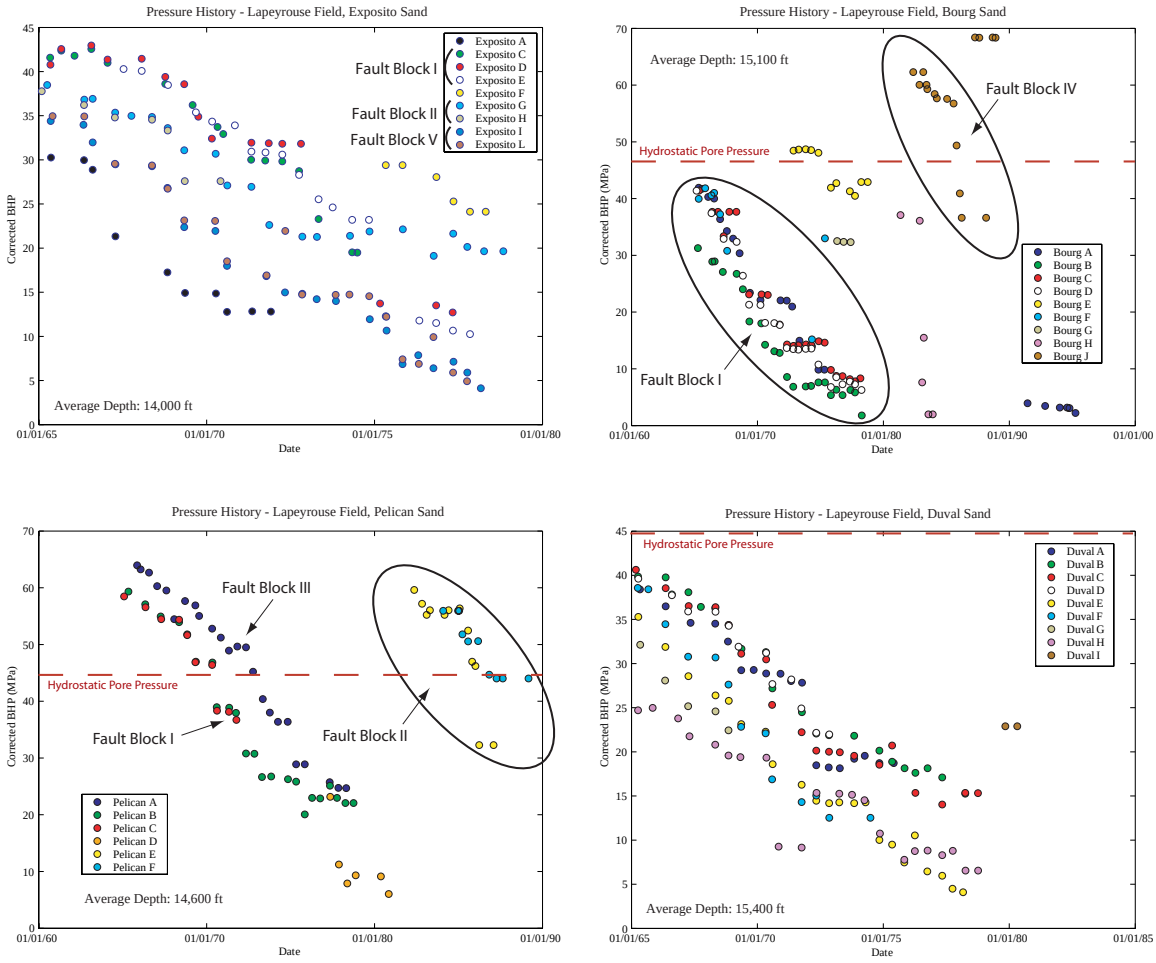

Figure 5.8: Pressure history plot for all the available wells in the Lapeyrouse field (after Morton *et al*., 2001). These pressure data are corrected to their corresponding datum based on the average depth of the producing sand units. If two wells are located in the same hydrological unit, the pressure reduction recorded should follow the same general trend (e.g., Pelican E and Pelican F). However, when the pressure reductions between different wells follow separate trends, this implies the wells are located in units separated by some barrier. Fault blocks are identified based on this concept without the assistant of the actual structural map of the formation.

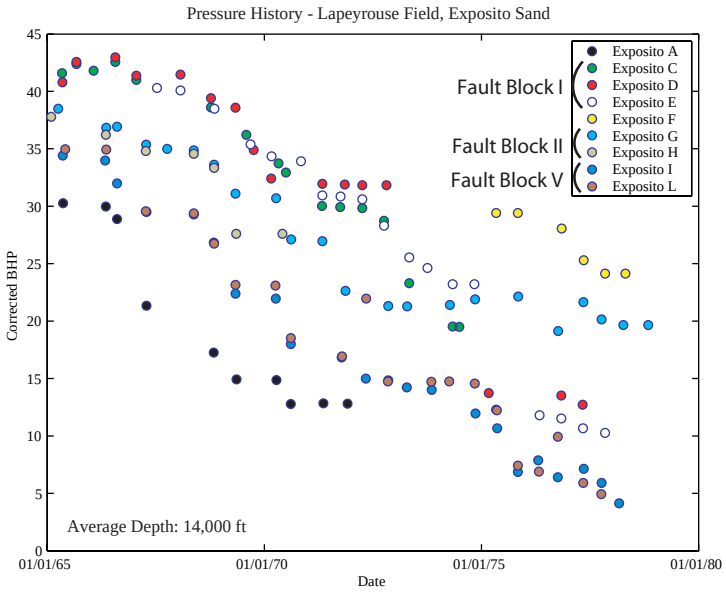

Figure 5.9: Composite diagram (above) showing the structural map for Exposito Sand along with the wells overlaying the aerial photographs. 3 compartments are identified based on the pore pressure history from Figure 5.8 (left). Notice that these compartments seem to correspond with the location of subsurface faults. In other words, the fault might have acted as a barrier within the sand. The structural contour maps are collected from the Department of Natural Resources of Louisiana in Baton Rouge.

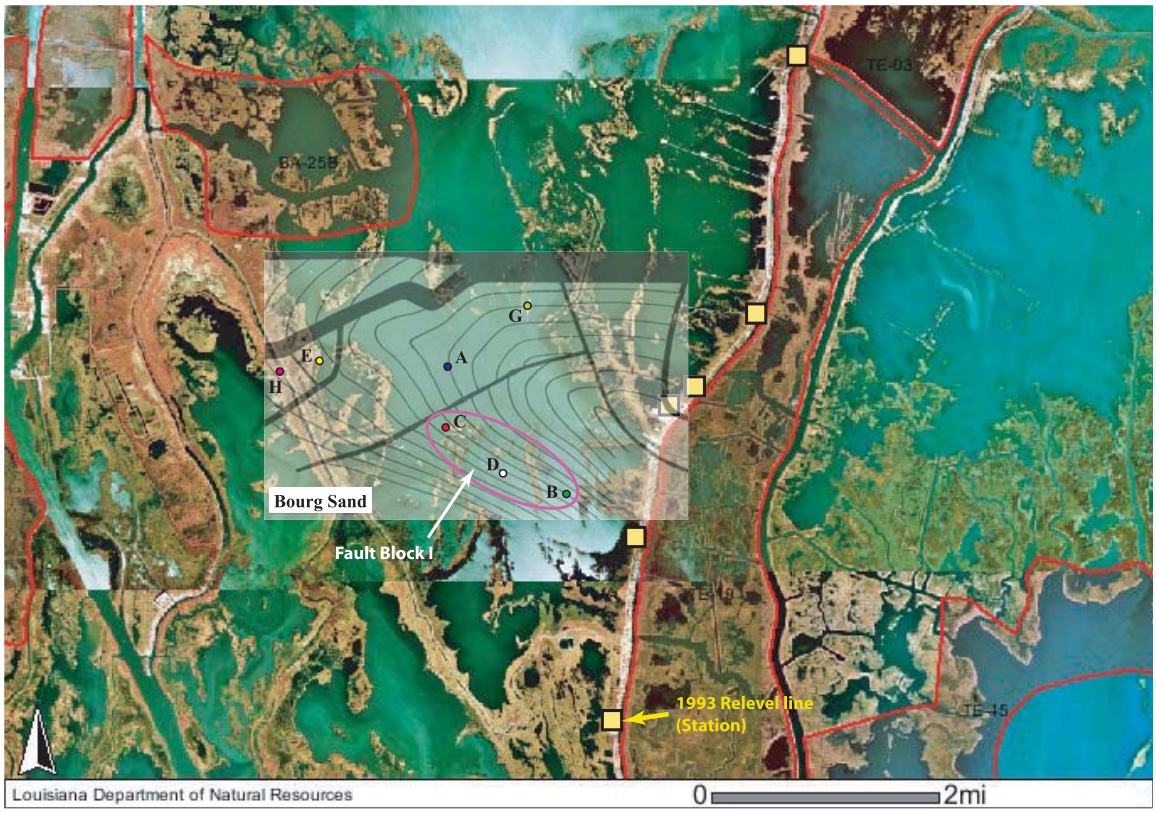

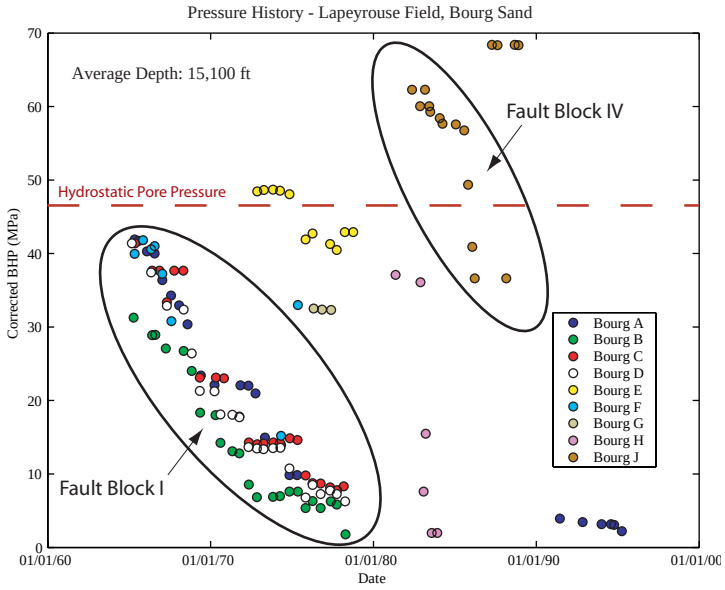

Figure 5.10: Composite diagram for Bourg sand (above). Compartment 1 is identified from the pore pressure history (left). Fault Block IV (or well J in Figure 5.8, left) is located outside of this structural map and will not be considered in this study.

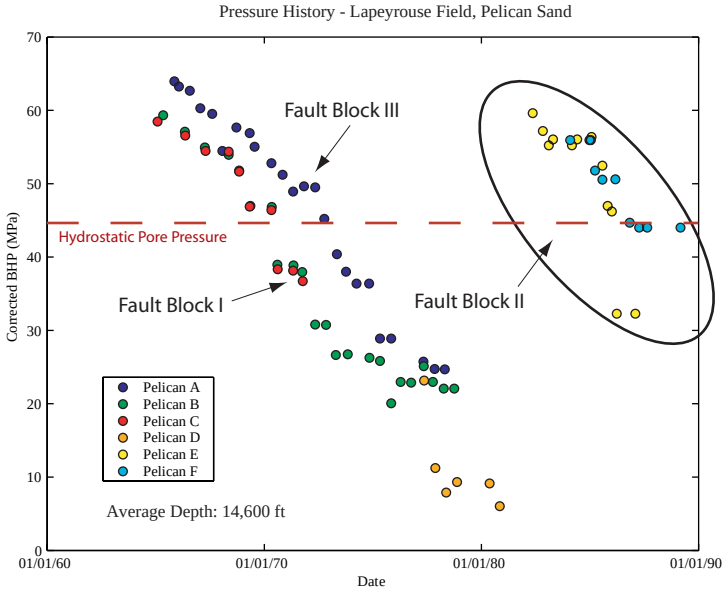

Figure 5.11: Composite diagram (above) showing the structural map for Pelican Sand along with the wells overlaying the aerial photographs. The 3 compartments are identified based on the pore pressure history from Figure 5.8 (left). Fault blocks identified from the pressure history plot and structural map corresponds extremely well suggesting that the faults that separate these compartments are good barrier for lateral fluid movements.

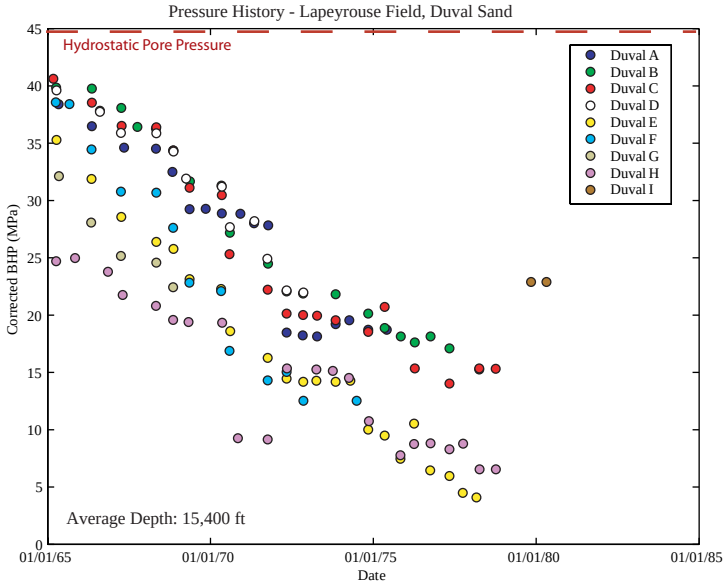

Figure 5.12: Composite diagram for Duval Sand similar to Figure 5.9. Well D, E, F, G and H are drilled within Fault Block I but the pore pressure history suggests the possibility of subcompartments within this block.

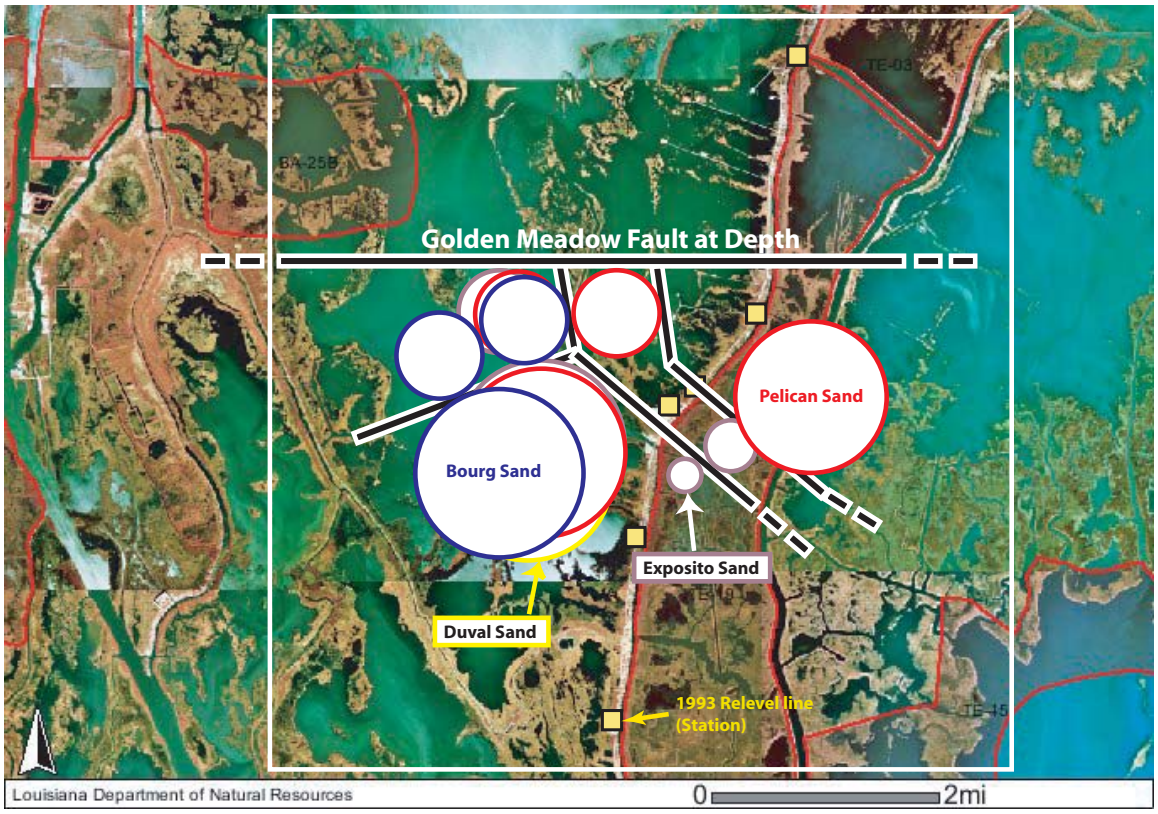

Figure 5.13: Map view of the circular-disc reservoirs used in the Geertsma solution for estimating the impact of reservoir compaction on surface subsidence. The black lines are the approximate locations of the fault at depth but will not be used in the calculation. The white box is the boundary of the examined area. The size of the reservoirs corresponds to the compartments identified in Figure 5.9 to Figure 5.12 that encompass all the wells from that specific compartment. The size of the disc is also restricted such that they will not cross the faults.

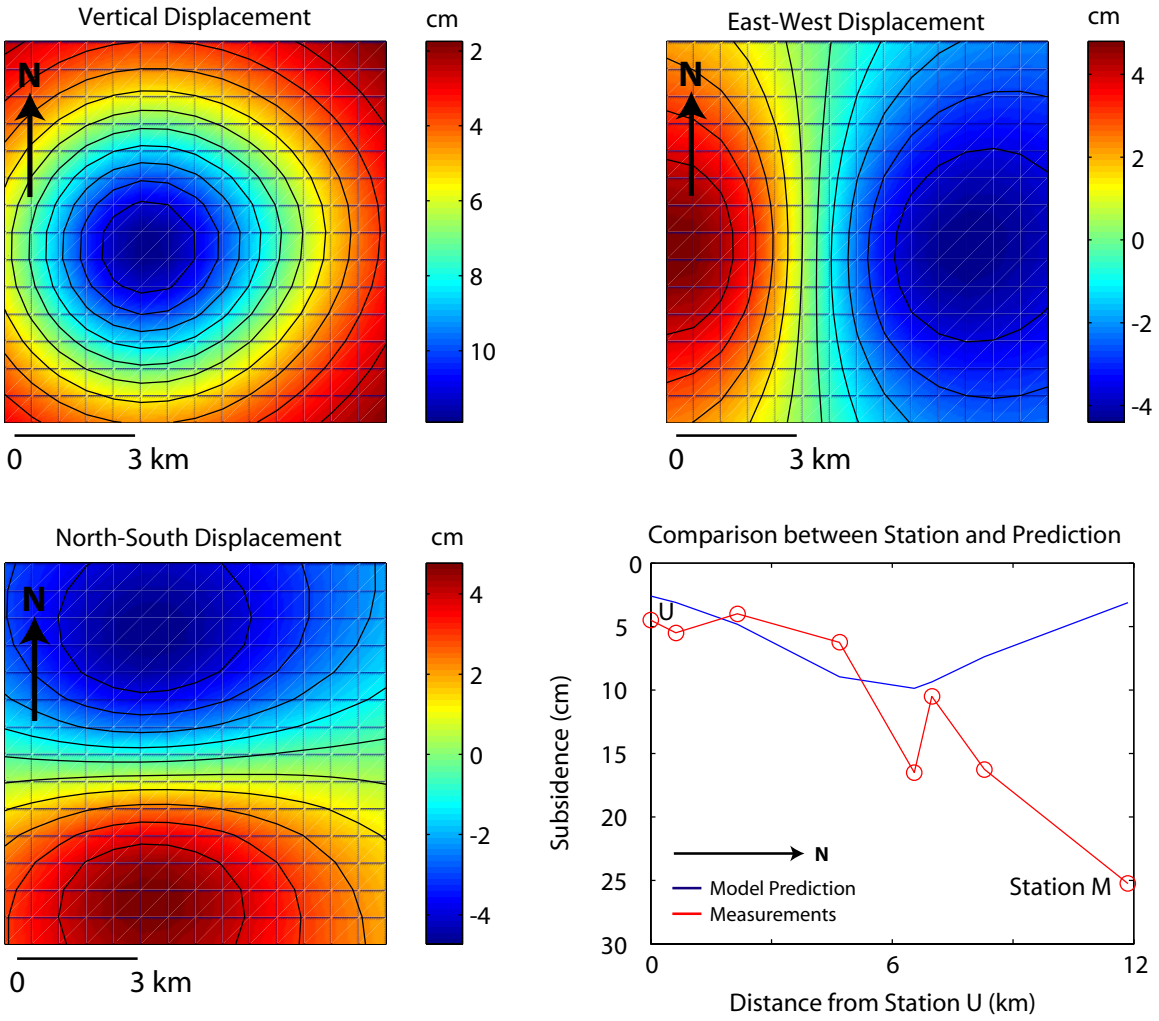

Figure 5.14: Results from the Geertsma solution based on the Hagin elastic-viscoplastic rheology. The predicted displacement U_X, U_Y and U_Z are measured in mm. The predicted subsidence from the Geertsma solution based on the elastic-viscoplastic rheology (blue line) is comparable to the measured elevation change from the relevel survey (red line).

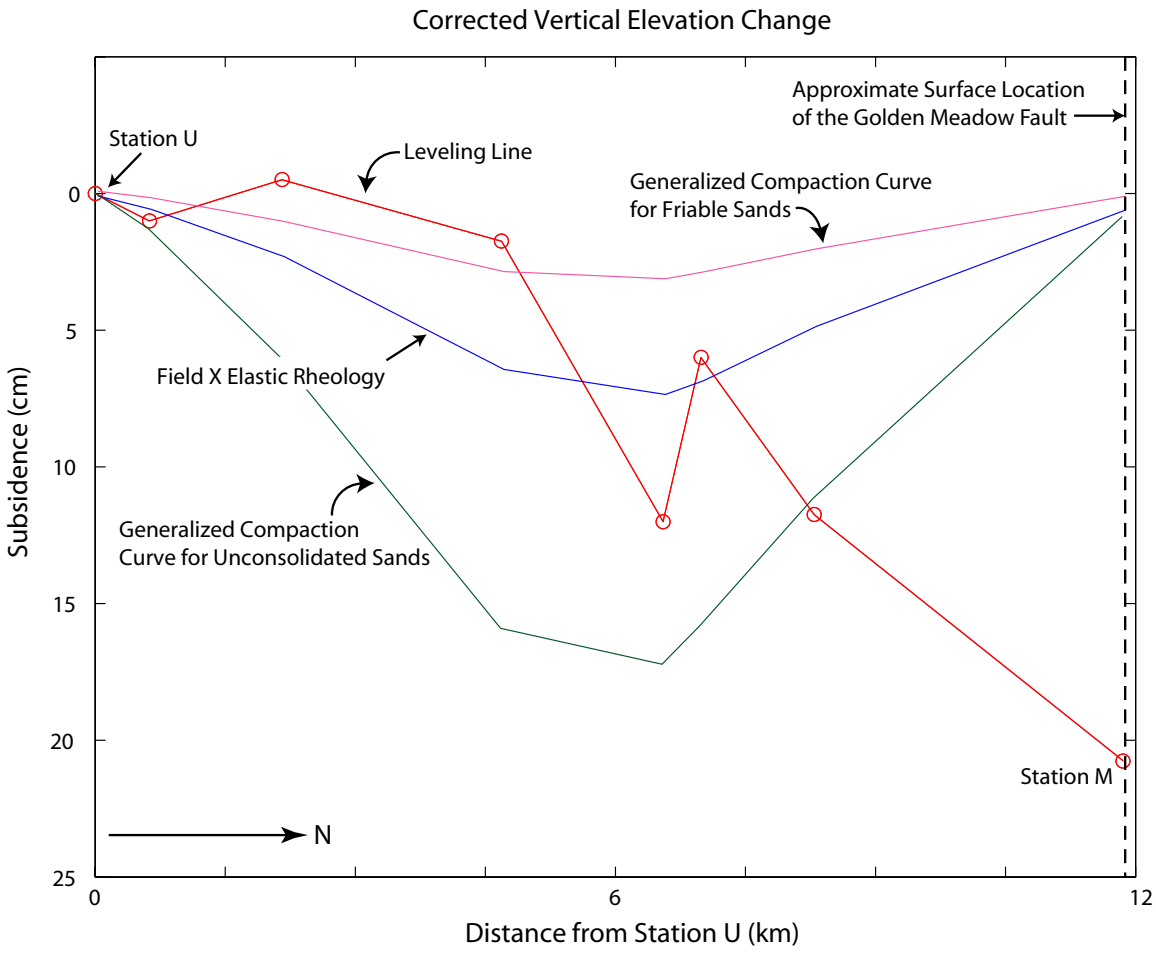

Figure 5.15: By changing the rheology of the producing sand, the magnitude of the predicted subsidence varies. The predicted subsidence using the Yale's compaction curve for friable sands (Chapter 2) appears to under-estimate the actual subsidence occurred in this region. While the Yale's compaction curve for unconsolidated sands seems to over-estimate the magnitude of subsidence, prediction based on the Hagin elastic curve seems to re-create the measured magnitude of elevation change. However, all of the subsidence profiles cannot describe the drastic change in vertical elevation measured by the station near the north end of this section of the releveling line. This drastic drop in elevation may be related to the fault movement along the Golden Meadow Fault just north of this station.

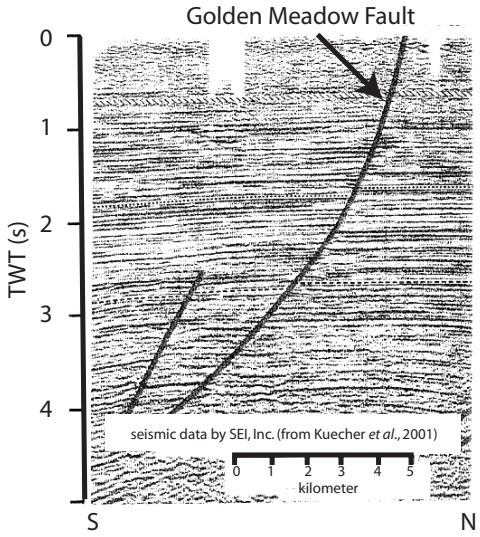

Figure 5.16: Seismic profile across the Golden Meadow Fault near the Lapeyrouse field shows that the fault is dipping towards the Gulf of Mexico. The dip estimated from this profile will be used for projecting the Golden Meadow Fault from subsurface structural map to the land surface (seismic profile after Kuecher *et al.*, 2001)

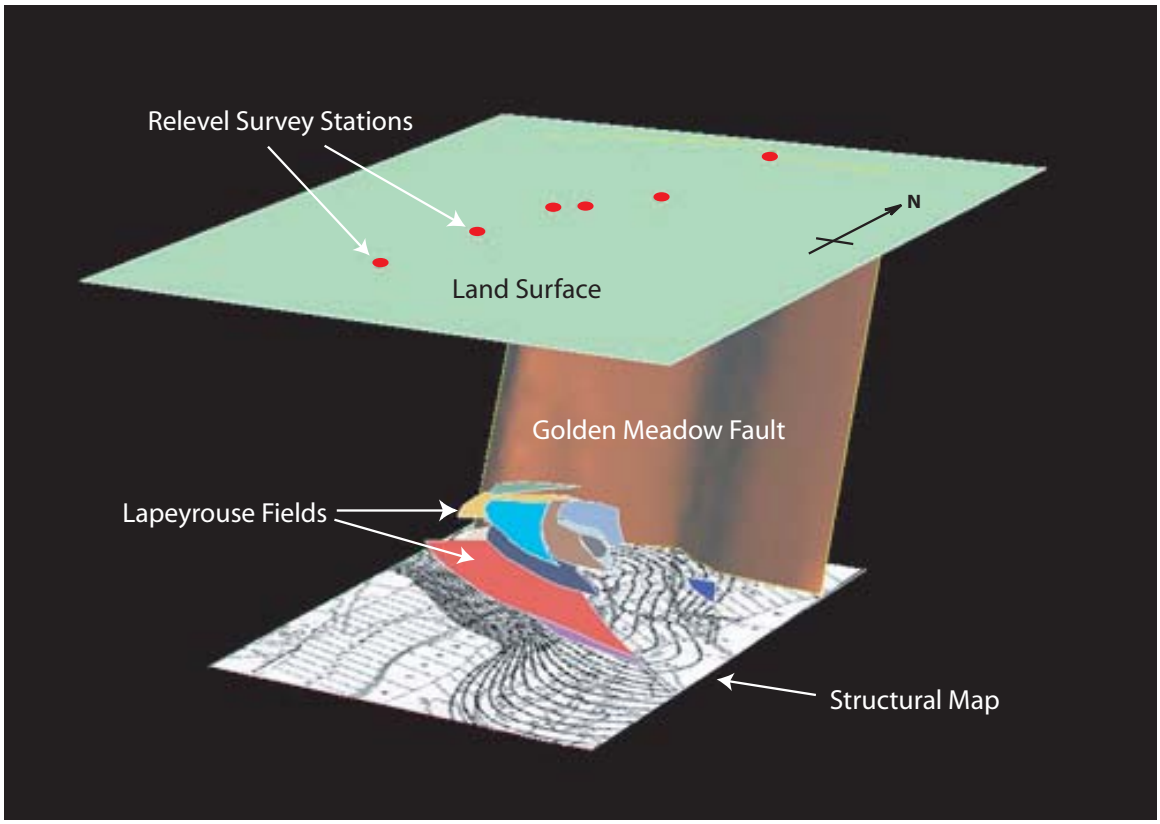

Figure 5.17: A perspective view of the simplified Lapeyrouse field and the Golden Meadow Fault created based on actual structural map in GOCAD. The digitized reservoirs are assumed to be flat and only the top surfaces of the producing sands are used. All these surfaces are exported directly to Poly3D to calculate the impact of reservoir compaction on fault slip and its contribution to surface subsidence.

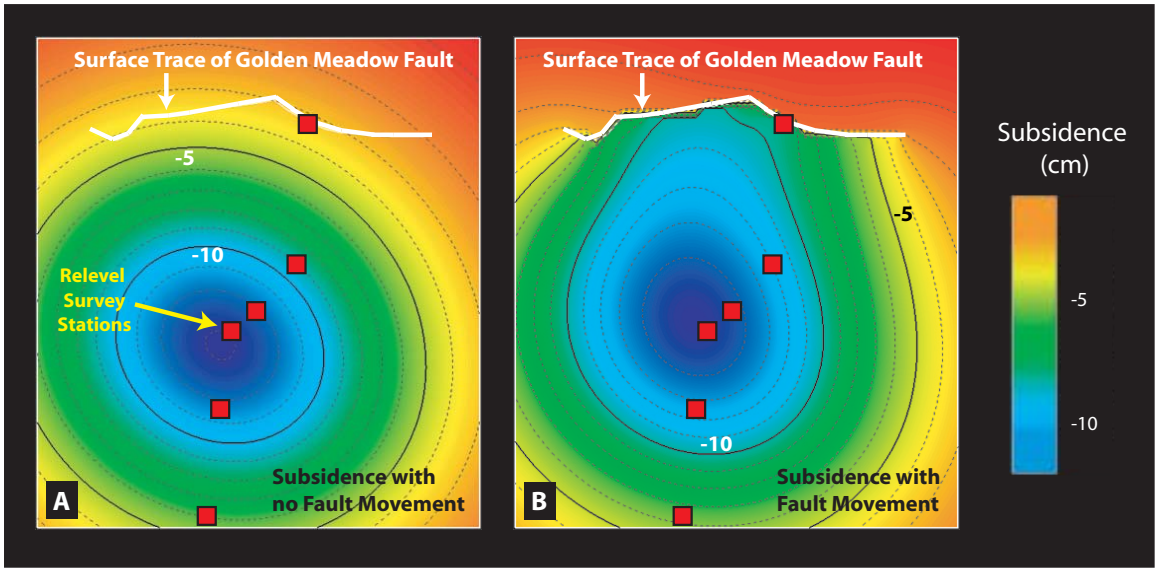

Figure 5.18: Surface subsidence estimated from Poly3D. When the fault is locked, the shape of the subsidence bowl is extremely similar to the result estimated from the Geertsma solution. The shape of the subsidence bowl altered significantly if the fault is allowed to move freely (rheology: Hagin's elastic constitutive law).

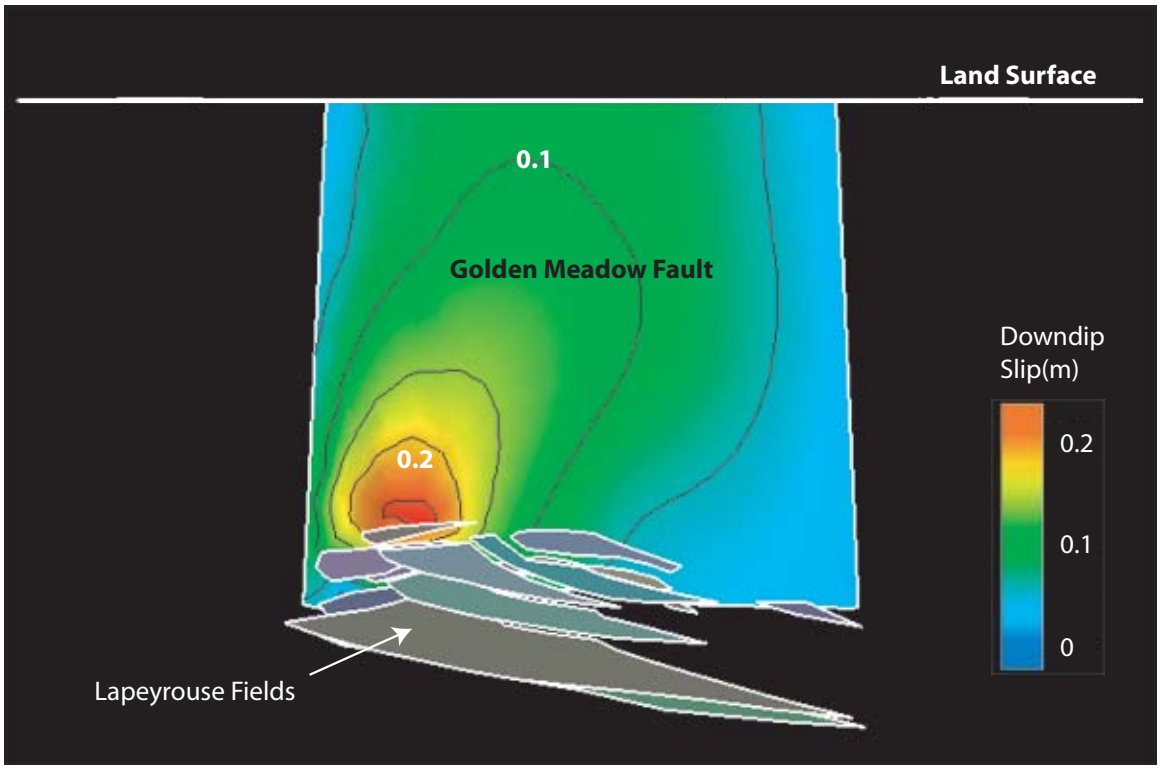

Figure 5.19: When the Golden Meadow Fault is allowed to slip, the highest downdip slip recorded on the fault is above the top surface of the shallowest reservoir (looking North).

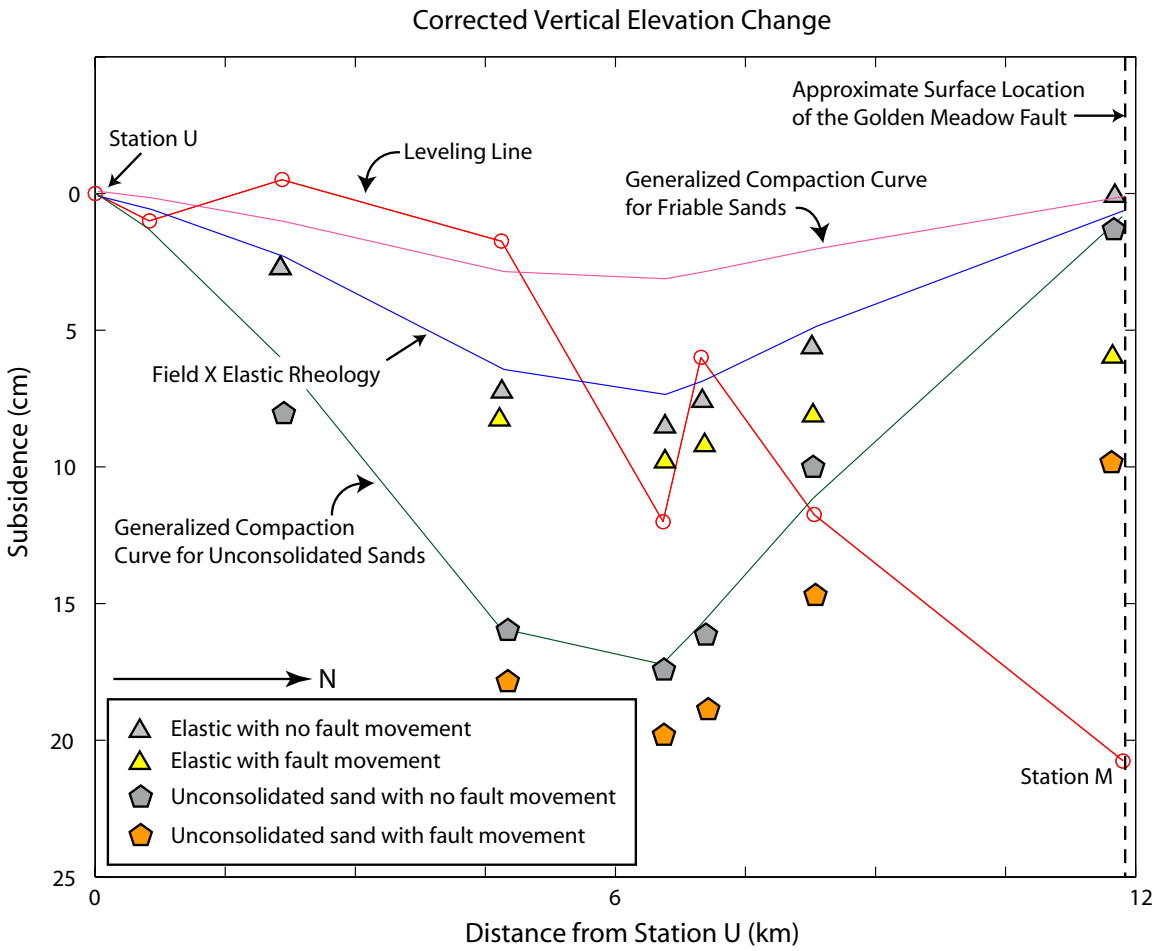

Figure 5.20: Comparison of the predicted subsidence from the Geertsma methods and Poly3D with the observed subsidence measured by releveling. Note that in both Poly3D models, the influence of the slip on Golden Meadow Fault can be observed. However, slip induced by reservoir compaction from the four Lapeyrouse sands examined alone still cannot totally capture the slip at Station M along the Golden Meadow Fault. The predicted slip only account for about 35% of the elevation change observed at Station M. While the compaction curve for unconsolidated sands yield an additional 9 cm of vertical elevation changes at Station M, the rheology tends to over-estimated the magnitude of subsidence in general.

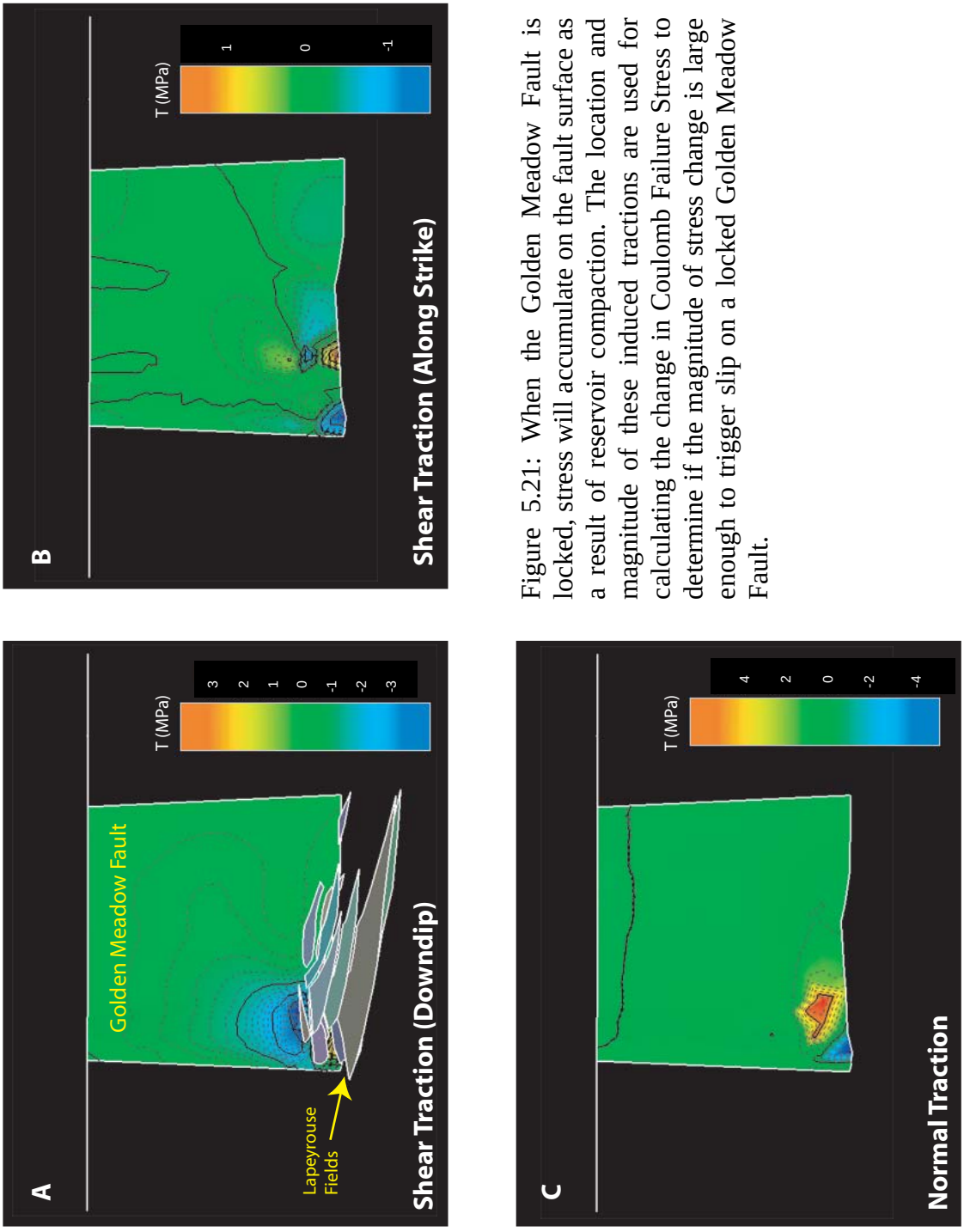

Figure 5.21: When the Golden Meadow Fault is locked, stress will accumulate on the fault surface as a result of reservoir compaction. The location and magnitude of these induced tractions are used for calculating the change in Coulomb Failure Stress to determine if the magnitude of stress change is large enough to trigger slip on a locked Golden Meadow Fault.

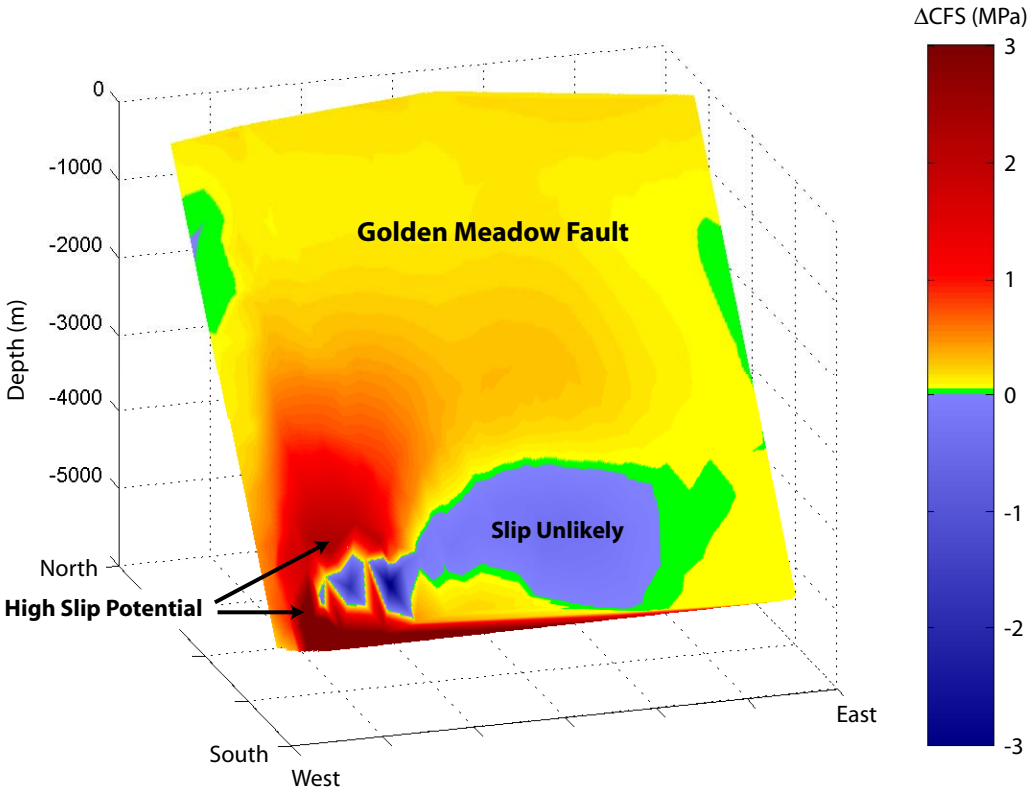

Figure 5.22: Distribution of the change in Coulomb Failure Stress on the Golden Meadow Fault based on the estimated tractions from Figure 5.21 using the Hagin's elastic rheology. Looking northeast, the blue zone represents patches of the fault where stress are relaxed as a result of reservoir compaction such that slip on that part of the fault is highly unlikely. The red and yellow zones represent patches of the Golden Meadow Fault that experience an increase in the Coulomb Failure Stress. High slip potential along this part of the Golden Meadow Fault is expected. The red zone at near the bottom of the fault surface is an artifact from data interpolation.

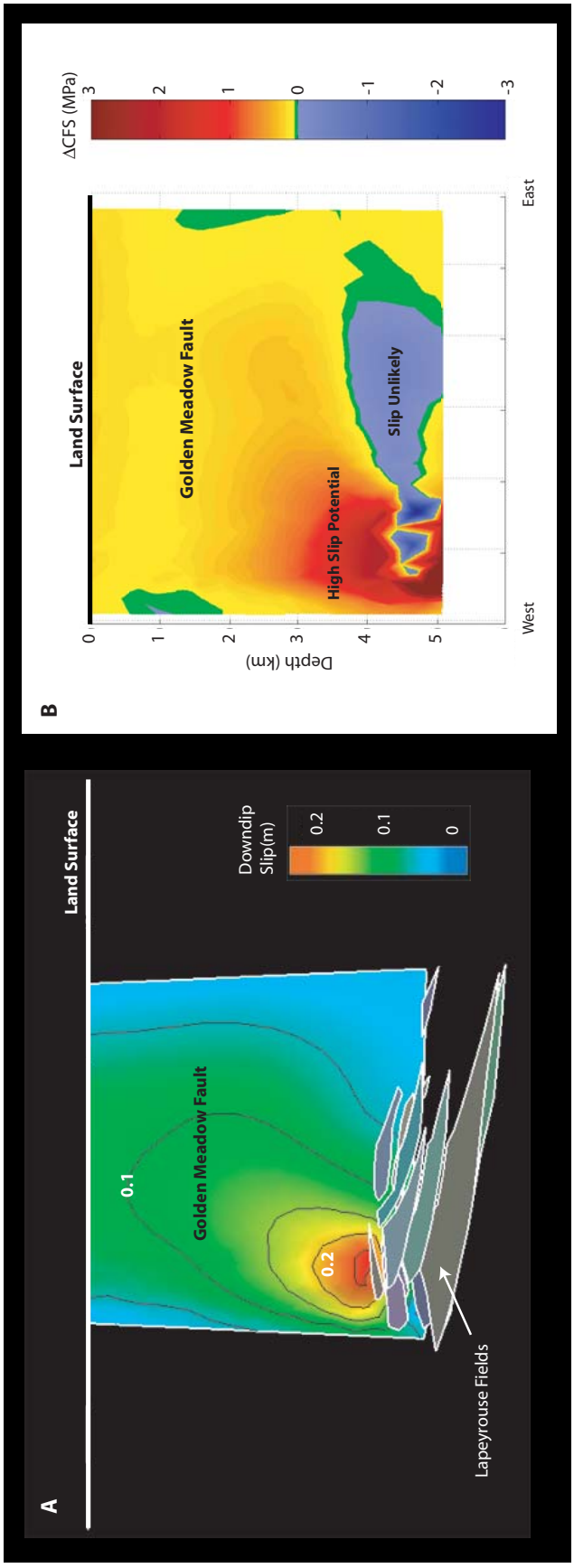

Figure 5.23: A comparison between the predicted slip and the slip potential based on Coulomb Failure Stress. The zone of 'High Slip Potential' corresponds well to the high displacement estimated from Poly3D when the fault is allowed to slip freely.

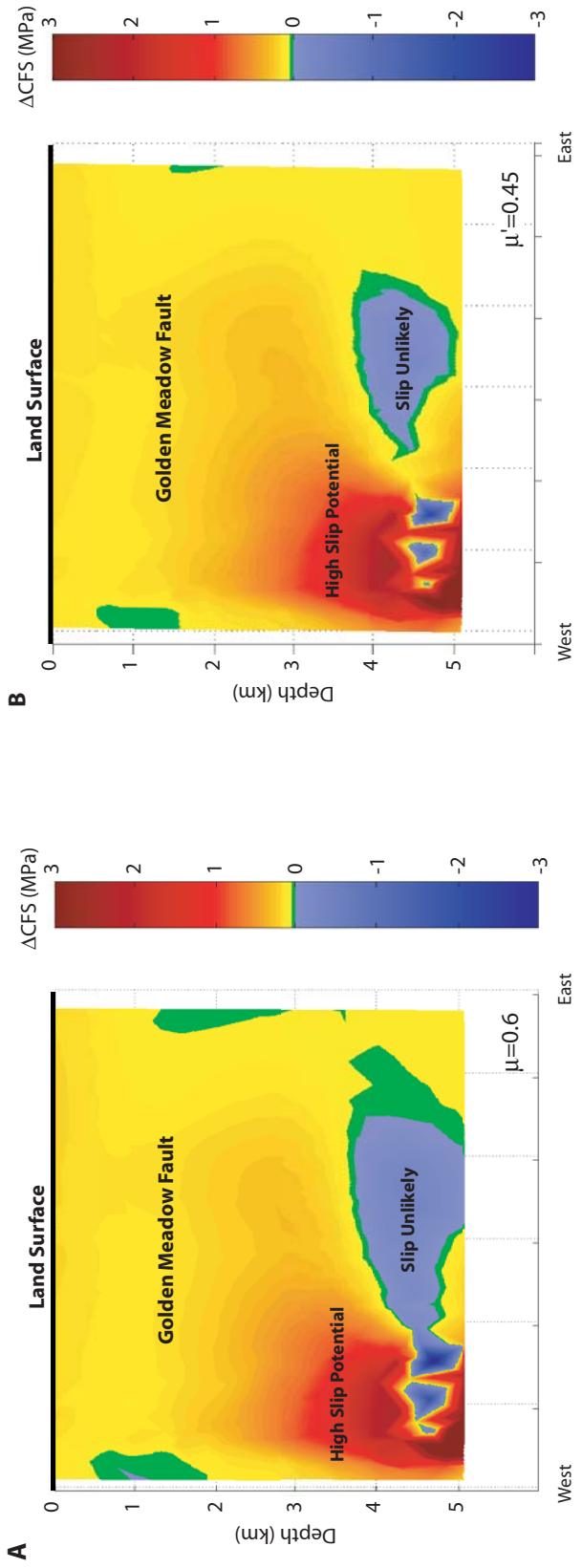

Figure 5.24: A comparison of slip potential estimated from the Coulomb Failure Stress with the use of different μ'. Note that the decreases in μ' has minimal effect on the area of high slip potential but significantly reduce the size of the slip unlikely zone.

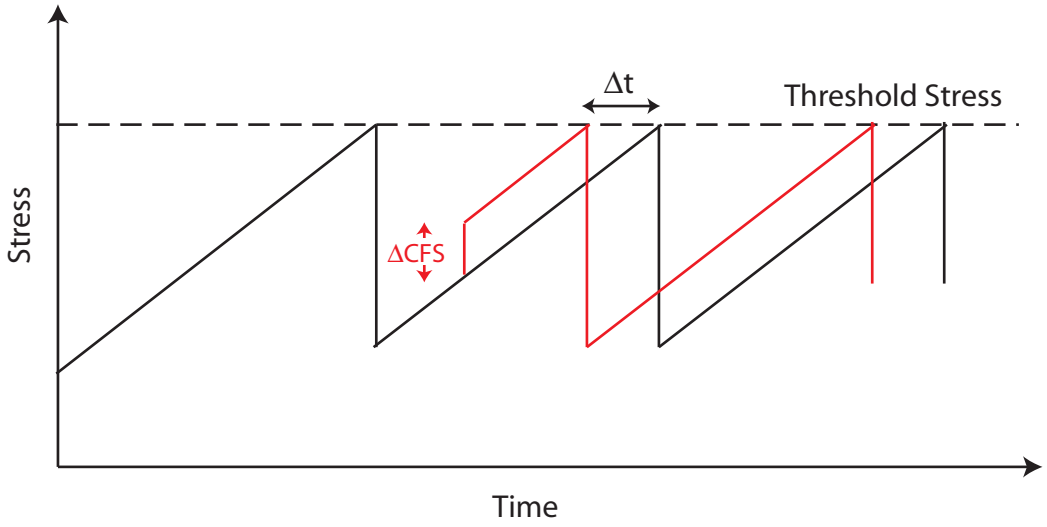

Figure 5.25: If a fault is under constant loading as in the case of the Golden Meadow Fault, a change in Coulomb Failure Stress may advance the next slip event scheduled to occur on the fault. On other words, production induced stress change along the Golden Meadow Fault may have some impact on the frequency of slip along this active growth fault.

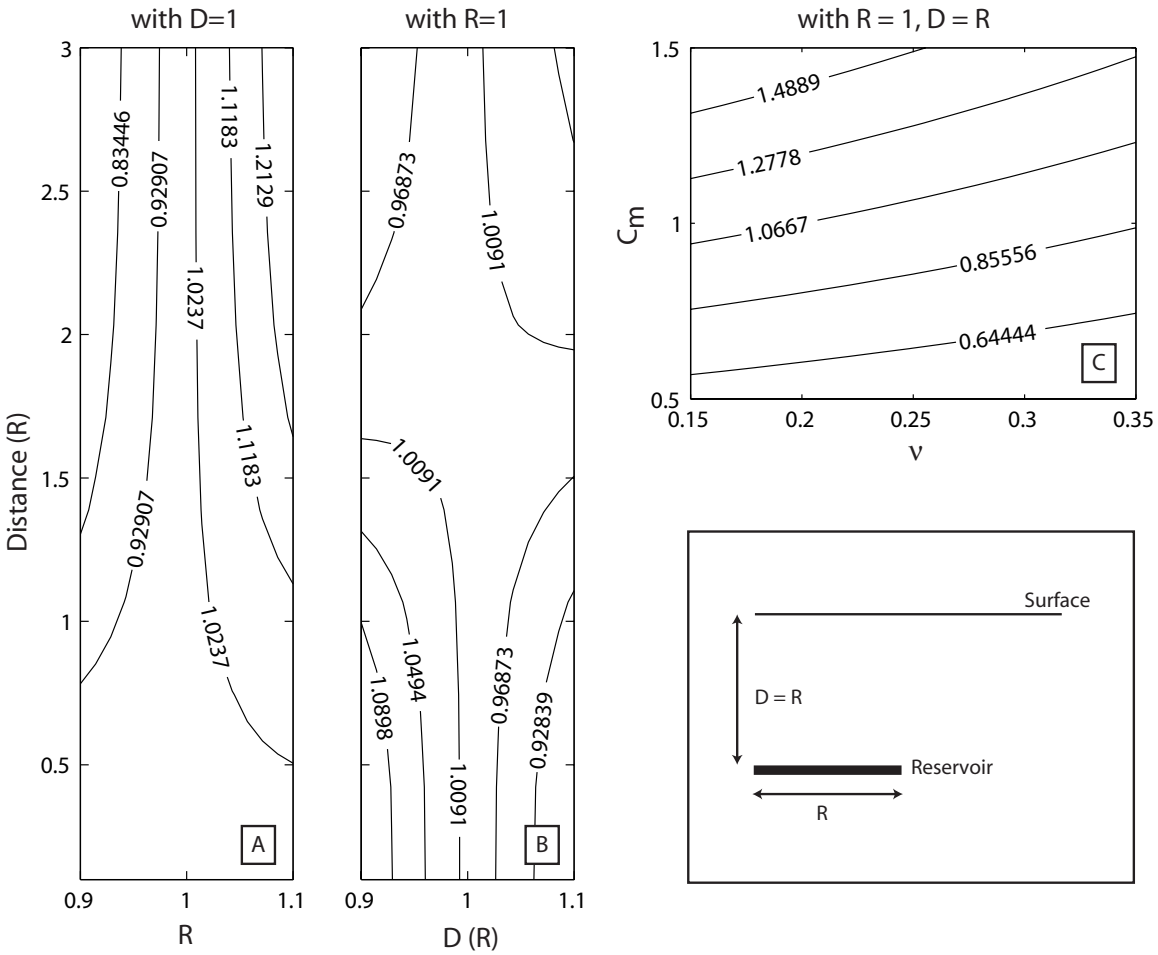

Figure 5.26: Sensitivity of the estimated subsidence due to uncertainties associated with different parameters. For a shallow reservoir (i.e., D = R), a 10% change in the radius of the circular disc could yield a 20% change in the estimated subsidence. Uncertainty related to the Poisson's Ratio is insignificant, but the estimated surface subsidence appears to be directly proportional to the uncertainty associated with compressibility.

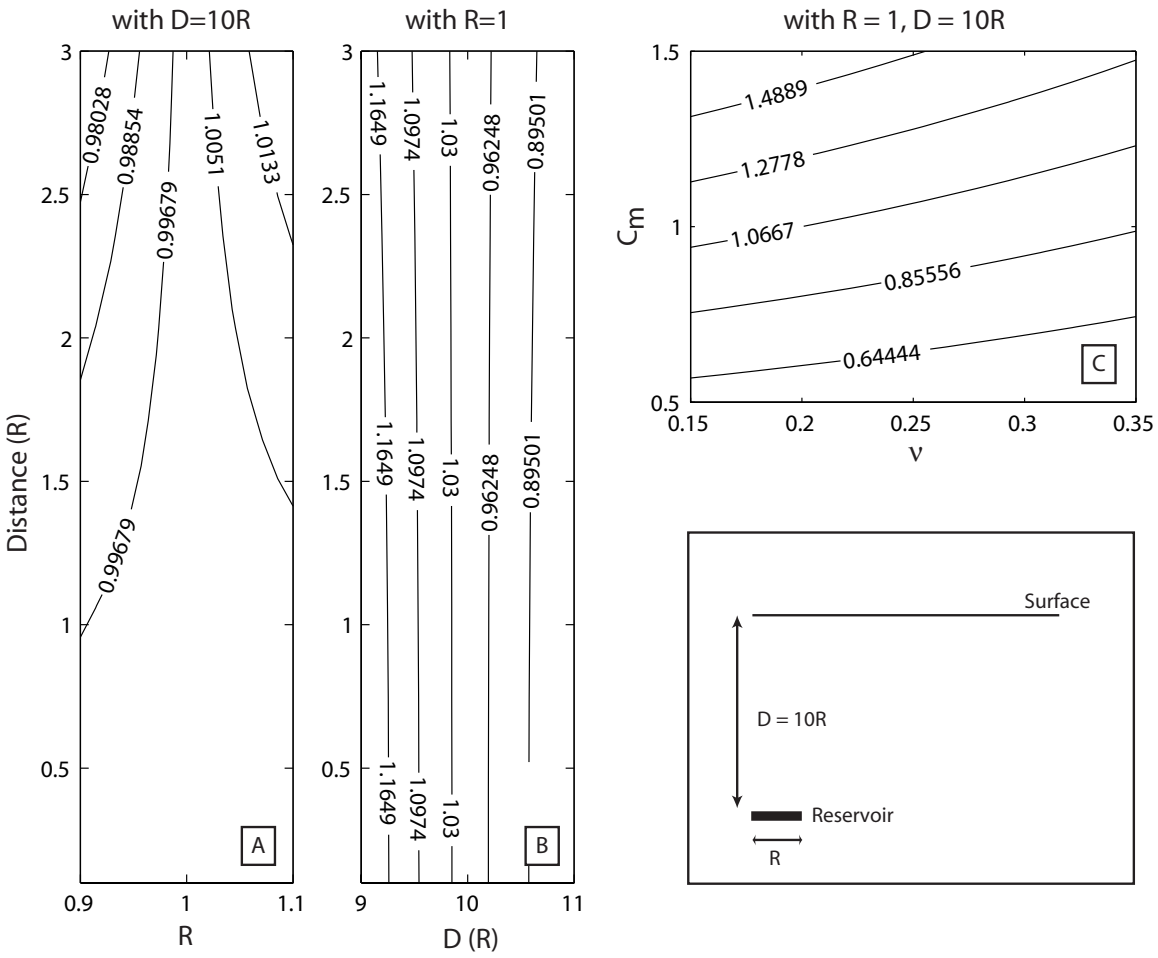

Figure 5.27: Sensitivity of the estimated subsidence due to uncertainties associated with different parameters. For a deep reservoir (i.e., D > 10R), a 10% change in the radius of the circular disc will only result in a 2% change in the estimated subsidence. Similar to shallow reservoir, uncertainty related to the Poisson's Ratio is insignificant, but the estimated surface subsidence appears to be directly proportional to the uncertainty associated with compressibility.

CHAPTER 6

Variation of Velocity and Anisotropy around a Vertical Borehole and its Potential Application for Stress Estimation from Sonic Logs

6.1 ABSTRACT

Stress estimation is extremely important to geomechanical modeling. While hydrofractures, minifractures and leak-off tests can provide accurate estimates of *in situ* stress, these tests can result in significant damage to the formation. An alternative stress estimation method based on acoustic velocity dispersion data gathered from Dipole Sonic Imager logs has been proposed by Schlumberger. I construct a forward model based on the Kirsch equation to examine the sensitivity and applicability of this method for stress estimation around a vertical borehole. Using nonlinear elasticity theory, a small stress perturbation induced from drilling will alter the stiffness tensor of the formation resulting in a change in velocity. The nonlinearity is introduced to the stiffness tensor through some third-order elastic parameters (T.O.E.). The forward model presented in this Chapter demonstrates that the predicted velocity fields are highly dependent on the accuracy of the T.O.E. determination.

6.2 INTRODUCTION

Determining the magnitude of the *in situ* stresses is one of the important factors required for an accurate geomechanical model. Uncertainties associated with stress estimation can have significant impacts on reservoir simulation that may affect the process of decision-making related to reservoir exploitation scheme. Stress changes associated with production-induced reservoir compaction may also affect fracture gradient developments, borehole stability and sand production, 4-D seismics, compaction drive and reservoir performance; and induced seismicity. As discussed in Chapter 2, estimating stress changes as a result of depletion (or depletion stress path where $\boldsymbol{A}=\Delta S/\Delta Pp$) are often based on analytical models such as the poroelastic theory. However, Zoback *et al.* (2001) showed that while poroelastic theory can be used in a few reservoirs, the range of reported stress paths is so wide that they recommended mapping the stress evolution empirically throughout the time scale of production is essential (see discussion in Chapter 2). While most of the stress measurements are collected empirically through leak-off tests, hydrofractures, minifractures or borehole imagers, these tests are not

always readily available and can cause damages in the formation. Schlumberger recently proposed a new approach using acoustic shear wave anisotropy from the Dipole Sonic Imaging (DSI) tool to determine both the orientation and the magnitude of stress (e.g., Brie *et al*., 1998; Sinha, 1998; Plona *et al*., 2002; Sinha, 2002; Sinha *et al*., 2002). In this chapter, I will focus on determining the sensitivity and applicability of this new Schlumberger method. Through forward modeling, I will estimate the theoretical acoustic wave a vertical velocity based on stress distribution around borehole and sets of elastic moduli from the literature.

Instead of estimating stress from velocity dispersion curves as described by Sinha (2002), I construct a forward model from measured geomechanical data to estimate how the existence of a borehole affects the stress concentration, elastic property and velocity field in the surrounding medium (Fig. 6.1). Since most existing 3-D anisotropic finite difference codes for seismic modeling are based on rectangular grid and are not readily applicable for borehole modeling, I attempt to examine the concept of drilling-induced stress changes and the resulting velocity anisotropy around the borehole into a format that can be incorporated into these codes (i.e., I estimate velocities at all nodes surrounding the borehole in a fixed rectangular grid setting). With this modification, it is possible to conduct numerical seismic modeling prior and after drilling. I also investigate the sensitivity of the nonlinear elastic stiffness tensor on the estimated velocity field around the borehole.

Figure 6.2 demonstrates the workflow of the modeling. The two input fields, *in situ* stress and the unperturbed elastic tensor of rock, are based on actual field data collected in the Gulf of Mexico Field S. Two different types of outputs are generated: the velocity field surrounding the borehole and the effective stiffness matrices in X-Y global Cartesian coordinates that can be inputted into existing seismic modeling codes. In the following section, I will discuss the processes described in the workflow in greater detail.

6.3 NONLINEAR ELASTICITY

Linear elastic theory is frequently used for describing the stress-strain relationship of most materials. For a linear elastic solid, Hooke's Law states that the stress σ_{ij} is linearly proportional to the strain ε_{kl} such that:

$$\sigma_{ij} = C_{ijkl}\varepsilon_{kl} \quad \text{.....(6.1)}$$

where C_{ijkl} is known as the elastic stiffness tensor with 81 components of which 21 are independent. The fourth-order tensor C is often reduced into a 6-by-6 second-order tensor using the Voigt contraction based on the symmetry of stress and strain (e.g., Mavko *et al*., 1998). The number of independent constants required to construct the elastic stiffness tensor can be reduced to two for an isotropic solid (e.g., Mavko *et al*., 1998). Similarly, five independent constants are required to construct the stiffness tensor (see Appendix C for the stiffness matrix construction) for a transversely isotropic solid (i.e., isotropic on a single plane such as a layered medium). The stiffness tensor is often used for modeling in conjunction with seismic or sonic wave propagation. While linear elasticity assumes that the stiffness tensor is independent from stress perturbation, experimental studies have demonstrated that the elastic stiffness tensor is also a function of the applied static stress (e.g., Johnson & Rasolofosaon, 1996; Winkler & Liu, 1996; Bakulin *et al*., 2000; Sarkar et al., 2003). As a result, nonlinear elasticity is introduced to describe such phenomena (e.g., Thurston & Brugger, 1964; Thurston, 1974).

Nonlinear elasticity relates the stress-induced potential energy as both a quadratic (second-order) function of strain along with a cubic (third-order) terms that account for changes in 'effective' elastic properties with static pre-stress (e.g., Thurston, 1974). The third-order elastic (or T.O.E.) constants are often referred to as the nonlinear component of the stress-strain relationship while the second-order elastic constants describe the linear relationship between stress and strain. In general, an effective stiffness tensor, C^{eff}_{ijkl}, is used for the inclusion of the T.O.E. such that:

$$C^{eff}_{ijkl} = C_{ijkl}\left(1+\Delta\right) \quad \text{.....(6.2)}$$

where Δ is the corresponding perturbation describing stress dependence controlled by third-order elasticity parameters (Sarkar *et al*., 2003a).

To describe the small-amplitude wave propagation through a nonlinear elastic medium, three distinct configurations are required (e.g., Prioul *et al*., 2004): (1) a reference state that describe the medium prior to the stress-perturbation where A_{ijpq} is the stiffness tensor at this stress state (in most laboratory experiment, the reference stress state is set to be equal to zero); (2) an intermediate state that characterizes the deformed state of the medium as a result of the static stress perturbation, τ_{ij}, with a stiffness tensor B_{ijpq}; and (3) the current state that describe the wave propagation in a statically stressed medium with C_{ijpq}^{eff} as the effective stiffness tensor. Thurston (1974) demonstrates that the effective stiffness tensor and the stiffness tensor for the reference state are related such that:

$$C_{ijpq}^{eff} = \delta_{ip}\tau_{jq} + A_{ijpq} + A_{ijpqrs}\varepsilon_{rs} \quad \text{.....(6.3)}$$

where τ_{jq} is the preexisting stress field and ε_{rs} is the static strain tensor for the transformation from the reference state to the intermediate state. Since such a transformation includes finite strains, the six-order tensor A_{ijpqrs} is introduced to describe the nonlinear deformation with δ_{ip} as the Kronecker delta. As described above, the fourth-order tensor A_{ijpq} can be contracted into a second-order tensor A_{ij}, and similarly the sixth-order tensor can be reduced into a third-order tensor A_{ijk} (hence the term third-order elastic parameters). In the most general case, the third-order tensor has 56 independent elements. However, most experimental studies concluded that the third-order elastic tensor is isotropic implying that only three independent constants are required, i.e., A_{111}, A_{112} and A_{123} (e.g. Prioul *et al*., 2003). Similar to the second-order tensor, if the third-order tensor has a different symmetry other than isotropic, more independent constants are required to construct the tensor (Hearmon, 1953). While the changes of stress and strain associated with the transformation from the reference state are significantly larger than the changes induced by wave propagation, nonlinear elasticity theory uses the higher-order terms to describe the stress-induced finite deformation while keeping the wave perturbations linear (e.g., Thurston, 1974).

Based on the nonlinear elasticity theory, a few laboratory experimental results on the determination of third order elastic parameters are published (e.g., Sarkar *et al*., 2003a, b; Prioul *et al*., 2004). Most of these experiments use an isotropic stress state as the reference state. For instance, Sarkar *et al*. (2003a) collect multi-azimuth acquisition of PP and PS reflection data on top of a block of unstressed Berea sandstone to construct the elastic stiffness tensor (Appendix C). They then apply stresses onto the sandstone block to determine the difference in velocity before and after loading. The changes in velocity are used for the construction of the effective stiffness tensor, C^{eff}, at each stress state. This data allowed determination of the T.O.E. constants for the Berea sandstone. They also present the weak anisotropy approximation that links the measured Thomsen coefficients describing velocity anisotropy to the principal stresses acting on the sample.

Thomsen parameters (ϵ, γ, δ) are often used in exploration geophysics to characterize wave propagation through vertical transverse isotropic (VTI) medium. They are related to the elastic stiffness tensor as follows (Thomsen, 1986):

$$\begin{aligned} \epsilon &\equiv \frac{C_{11}-C_{33}}{2C_{33}} \\ \gamma &\equiv \frac{C_{66}-C_{44}}{2C_{44}} \\ \delta &\equiv \frac{\left(C_{13}+C_{44}\right)^2-\left(C_{33}-C_{44}\right)^2}{2C_{33}\left(C_{33}-C_{44}\right)} \end{aligned} \qquad \text{.....(6.4)}$$

while the vertical P and S acoustic wave velocities are defined as:

$$\begin{aligned} V_p &= \sqrt{C_{33}/\rho} \\ V_s &= \sqrt{C_{44}/\rho} \end{aligned} \qquad \text{.....(6.5)}$$

where ρ is the density of the medium. Since Thomsen parameters are often readily available from surface seismic data, it is logical to use these parameters to construct the *in situ* stiffness tensor for the formation prior to drilling.

Winkler & Liu (1996) examine T.O.E. constants along with porosity, density, velocity and uniaxial strength for nine rocks. They conclude that T.O.E. provides an accurate description of the velocity variation over a small stress deviation about a reference state even though the nonlinear parameters show no significant correlation with

other rock physics parameters. However, as noted from the experimental data by Prioul *et al.* (2004), the T.O.E. parameters are valid only for a limited stress range. In other words, if the stress perturbations are too large, a different set of T.O.E. parameters is required. Therefore, the determination of the reference state is critical.

6.4 DRILLING-INDUCED STRESS REDISTRIBUTION

For a vertical borehole drilled in a stressed linear elastic material, the redistribution of stress around the borehole can be estimated under the assumption of plane strain. With the global and principal stress axes aligned, the drilling-induced stress around the borehole can be estimated analytically in cylindrical coordinate such that:

$$\sigma_{rr} = \left(\frac{\sigma_H + \sigma_h}{2}\right)\left(1 - \frac{R^2}{r^2}\right) + \left(\frac{\sigma_H - \sigma_h}{2}\right)\left(1 + \frac{3R^4}{r^4} - \frac{R^2}{r^2}\right)\cos 2\theta + \Delta P\left(\frac{R^2}{r^2}\right) \quad ...(6.6a)$$

$$\sigma_{\theta\theta} = \left(\frac{\sigma_H + \sigma_h}{2}\right)\left(1 - \frac{R^2}{r^2}\right) - \left(\frac{\sigma_H - \sigma_h}{2}\right)\left(1 + \frac{3R^4}{r^4}\right)\cos 2\theta - \Delta P\left(\frac{R^2}{r^2}\right) \quad .....(6.6b)$$

$$\sigma_{zz} = \sigma_V - \nu\left[2(\sigma_H - \sigma_h)\frac{R^2}{r^2}\cos 2\theta\right] \quad .....(6.6c)$$

where σ_V, σ_H and σ_h are the three *in situ* effective stresses and σ_{rr}, $\sigma_{\theta\theta}$ and σ_{zz} are the drilling-induced radial, tangential and vertical stresses. ΔP is the difference between the pore pressure in the formation and the mud pressure in the borehole. *R* is the radius of the borehole and *r* is the distance away from the center of the borehole and θ and ν are the azimuth from the principal stress axes and the Poisson's ratio of the formation. It is well documented that when the two horizontal stresses are different, the tangential stress (or hoop stress) become more compressive in the direction of the minimum horizontal stresses and more tensile in the direction of the maximum horizontal stress (Fig 6.3). When the drilling-induced stress around the borehole exceeds the compressive strength or the tensile strength of the formation, breakouts and tensile fractures may occur. The occurrence of these mechanical failures around the borehole have been used extensively

as tools for determining the direction of the in situ maximum and minimum horizontal stresses (e.g., Bell & Goughm 1981; Zoback *et al.,* 1985).

To rotate the induced stresses from cylindrical coordinates back to the Cartesian coordinates such that it could be used in seismic modeling, a simple matrix rotation is required. Figure 6.4 demonstrates the effect of the borehole on stress redistribution in the surrounding medium in Cartesian coordinates. The *in situ* stress and pressure used in Figure 6.4 are based on actual measurements from an offshore Gulf of Mexico Field S. The top panels are the stress around a borehole in Cartesian coordinate assuming the far-field horizontal stresses are equal. Note that only the top right quadrant is presented as a result of symmetry such that calculation time can be minimized. The middle row represents the resulting stress of an applied uniaxial stress along the x-axis with zero far-field stress. The near-borehole region on the along the y-axis experienced a significant increase in compressive stress while the tangential stress along the x-axis in the near-borehole region becomes more tensile as expected. The bottom row in Figure 6.4 represents the combine effect of the presence of a borehole in the formation in which the two principle horizontal stresses are not equal.

6.5 THE DETERMINATION OF STRESS FROM DIPOLE SONIC IMAGER (DSI) LOGS

Based on the nonlinear elastic model for acoustic waves in a stressed medium, several authors (e.g., Sinha & Kostek, 1996; Sinha, 1998; Winkler *et al*., 1998; Plona *et al.* 2002; Sinha, 2002) have proposed that drilling-induced stress perturbation around boreholes can affect the velocity fields and create characteristic velocity dispersion curves. By examining the velocity dispersion for both stresses and unstressed media, Sinha and Kostek (1996) suggest that the existence of stress concentration around a vertical borehole introduce characteristic frequency dependencies of flexural wave velocities as a function of the azimuth. Since low frequency flexural waves penetrate deeper into the formation than the higher frequency flexural waves, stress anisotropy can be measured and estimated by studying the fast and slow dipole dispersion curves obtained through cross-dipole logging tool at a range of frequencies (e.g., Sinha, 1998; Plona *et al.*, 2002).

In the case of isotropic medium with isotropic stress state, the dipole dispersion curve should be the same in all direction. For intrinsic anisotropic materials, the dipole dispersion curves reflect the preferred orientation (fast/slow) axis of the material without the curves crossing over. The fast and slow dipole dispersion curves will intersect each other in the frequency domain only when stress anisotropy exists (e.g., Winkler *et al*., 1998; Sinha, 2002). The azimuth dependent dispersion curves show a characteristic cross over when the two horizontal stresses are not equal. Hence, by realizing the existence of the dispersion curves crossover could be used as a tool to determine the magnitude of the two principal horizontal stresses (e.g., Sinha and Kostek, 1996; Plona *et al*., 2002). Winkler *et al*. (1998) also provide the theoretical and experimental framework for estimating dipole-dispersion curves in stressed and unstressed borehole. As a result, Sinha (2002) propose that it is possible to estimate the magnitude of the two principal horizontal stresses by inverting the dispersion curves from the DSI logs.

6.6 FORWARD MODELLING: FROM STRESS TO VELOCITY

To determine the impact of the existence of a borehole on velocity dispersion, Winkler *et al*. (1998) define their reference state stiffness tensor by creating an open borehole in a block of unstressed Berea sandstone. They then applied a uniaxial stress to create stress perturbation around the borehole and construct the effective stiffness tensor by measuring ultrasonic wave velocities in a variety of directions. However, since a borehole is drilled into a stressed medium in the real world, I construct two reference states for the forward model: an isotropic stress state and an anisotropic stress state. The drilling-induced stress perturbation around the borehole will then be used as the intermediate state (Fig. 6.5). The isotropic stress state is picked assuming both horizontal principal stresses acting on the formation are equal to the average of the *in situ* maximum and minimum horizontal stresses. The stiffness tensor for such a stress state can easily be determined with the assumption of a vertical transversely isotropic (VTI) medium (Appendix 6.A). Adjusting the two principal stresses to the actual estimation of the *in situ* stress magnitude sets the second reference state. In other words, the second reference

state can be viewed as the intermediate state, similar to laboratory experiment by applying differential stress on the formation (similar to the experiment conducted by Sarkar *et al*., 2003a). This second reference state is used for determining the P and S wave velocities prior to drilling; Therefore, I do not refer this stage as the intermediate state but as a second reference state. The intermediate state in this model refers to the stress state after a borehole is introduced in the second reference state. Although mathematically, the second reference state is not necessary, the purpose of using this second reference state is to demonstrate the impact of the borehole on the velocity fields in the formation before and after drilling. In other words, I compare the velocity field after drilling to the *in situ* stress condition rather than an isotropic stress condition. The *in situ* stress prior to drilling for Field S is generated by proprietary Shell geomechanical modeling software (Schutjens, *personal communications*).

However, since the stresses acting on the formation in the second reference state are anisotropic, the formation no longer maintains its vertical transversely isotropic symmetry but become orthorhombic. In other words, the stiffness tensors at any given point in the formation become azimuthally dependent. To solve this complex issue, I use the first reference state (VTI symmetry) to construct the stiffness tensor. Mathematically, I can apply both the anisotropic stresses and the drilling-induced stress simultaneously. Using Equation (6.6a) to (6.6c), I estimate the new effective stiffness tensors at every grid node in the Cartesian coordinate system. Note that the stress perturbation from the borehole is calculated in polar coordinates, so the estimated effective stiffness tensors as a result are also aligned with the local principal stress axis. In other words, the effective stiffness tensors are not always aligned with the global Cartesian axes. If the formation has VTI symmetry, aligning the effective stiffness tensors with the global coordinates is relatively straightforward (since VTI formation implies stiffness matrices are azimuthally independent). Unfortunately, the differential far-field stresses experienced by the formation imply an orthorhombic symmetry in which the stiffness tensors are azimuthally dependent. In other words, to align the effective stiffness tensors at every grid point with the global Cartesian coordinate, a Bond transformation is required to rotate the tensors (see Appendix 6.B). The alignment between the local stiffness tensors and the global Cartesian coordinate is extremely important because it will affect wave propagation in

such medium. Since the study focus on DSI logs, only the vertical P wave velocity, V_{ZZ}, and the vertical shear wave velocities, V_{YZ} and $V_{XZ,}$ are considered.

While most of the published T.O.E. parameters are based on laboratory experiments, only a few *in situ* T.O.E. parameters are reported (e.g., Sinha *et al*., 2002). The T.O.E. parameters from Field S are not available for this study; I have adopted the T.O.E. parameters from Sinha *et al*. (2002) to demonstrate the impact of drilling-induced stress perturbation might have on the formation in Field S. Since the parameters are inverted from DSI logs acquired in an Indonesian well, the accuracy of the model will depend on how these parameters translate from one well to another. As a result, I generate a range of T.O.E. parameters based on these reported value to investigate their sensitivity on the predicted velocity (see following section).

Using the reported value of the T.O.E. parameters from Sinha *et al*. (2002), along with the in situ stress model from Schutjens (*personal comminucations*), Figure 6.6 illustrate the impact of the borehole to the background velocities. The top panels are the estimated velocities based on the rotated effective stiffness tensors. When comparing these velocities with the background velocities (the background velocities are defined based on the second reference state prior to drilling), the variations in velocities are less than 10%. Figure 6.7 shows the degree of shear-wave anisotropy estimated from the effective stiffness tensors while the arrows represent the fast shear wave direction. The shear-wave anisotropy is defined by Thomsen (1974) as:

$$\gamma^{(s)} \equiv \frac{C_{44} - C_{55}}{2C_{55}} \approx \frac{V_{sf} - V_{ss}}{V_{ss}} \quad \text{.....(6.7)}$$

where V_{sf} and V_{ss} are the fast and slow shear wave velocities. Figure 6.8 shows the magnitude and the direction of the fast and slow shear waves predicted by the forward model.

6.6 THE SENSITIVITY OF T.O.E. ON VELOCITY FIELD

The effective stiffness tensors constructed in the previous section are based on the T.O.E. parameters from a different basin; I examine how uncertainties associated with the

determination of T.O.E. parameters may affect the resulting velocity field. Assuming the T.O.E. parameters are valid for Gulf of Mexico Field S, I create ranges of the three T.O.E. parameters based on the reported values from Sinha *et al*. (2002). By varying the T.O.E. parameters one at a time, their corresponding impacts on anisotropy can be examined. Figure 6.9 to 6.11 represent the changes in $V_{ZZ,}$ V_{YZ} and V_{XZ} parallel to the two principal stresses. The top panels are the estimated velocities in the direction of the maximum horizontal stress, while the bottom panels represent the velocity variation along the direction of the minimum horizontal stress. The maximum horizontal stress is set to be parallel to the X-axis, as a result, V_{YZ} and V_{XZ} represent the polarized shear wave velocities that are parallel to the minimum and maximum horizontal stresses respectively. The vertical-axis for the panel corresponds to the distance away from the borehole (in terms of borehole radius). The horizontal axis corresponds to the range of the T.O.E. parameters assuming the other two parameters remain constant. The three panels correspond to the three T.O.E. parameters. For the compressional P-wave $V_{ZZ,}$ uncertainties associated with the determination of the three T.O.E. parameters have minimal effect (< 1%) in both directions (Fig. 6.9). However, the shear-wave velocities are more sensitive with respect to variations in the T.O.E. parameters. Figure 6.10 shows that A_{112} and A_{123} have some significant effects (~ 5%) on V_{YZ} along the minimum horizontal stress direction especially in the immediate surroundings around the borehole; while the impact of these two parameters along the maximum horizontal stress direction is slightly smaller (< 5%). Figure 6.10 also shows that V_{YZ} is relatively insensitive to variations of A_{111}. For the shear-waves polarized in the direction of the maximum horizontal stress V_{XZ}, a variation of A_{111} seems to have minimal impact on the velocity. While variations of A_{112} and A_{123} have some effects (~ 3%) on the near field V_{XZ} along the minimum horizontal stress axis.

The impacts of the variations of the three T.O.E. parameters on the shear-wave velocity can also be demonstrated using shear-wave anisotropy (Fig. 6.12). Figure 6.12 illustrates the impacts of these uncertainties on the degree of shear-wave splitting. The center panel corresponds to the shear-wave anisotropy using the reported value of the three T.O.E. parameters (same as Fig. 6.7). Assuming the reported value of A_{112} and A_{123} are equal to the reported (or average) values, the top row in Figure 6.12 represents the

effect of uncertainties associated with A_{111} may have on the estimation of shear-wave anisotropy. If the average value of A_{111} is used, the anisotropy will be the same as the center panel (hence the omission of the top-centre panel). Similarly, the middle and bottom rows represent the predicted anisotropy with a varying A_{112} and A_{123}. From the seven panels in Figure 6.12, it is apparent that under-estimation of A_{111} and A_{123} or over-estimation of A_{112} might minimize the resulting anisotropy. However, over-estimation of A_{111} and A_{123} or under-estimation of A_{112} can result in an anisotropy for up to 10%.

6.7 CONCLUSIONS

Nonlinear elasticity describes velocity variations as a function of drilling-induced stress perturbations around a borehole and the required assumptions result in several limitations on the applicability of using DSI logs for stress determination. The drilling-induced stress perturbation model used by most authors (e.g., Winkler & Liu, 1996; Winkler *et al*., 2002; Sinha, 2002) and in this study, is based upon a perfectly shaped borehole drilled vertically in a linear elastic medium. In reality, such perfectly shaped borehole rarely exists. Mechanical damages such as breakouts and drilling induced tensile failures are often observed (e.g., Bell & Gough, 1981; Zoback *et al*., 1985). The fundamental assumption of using DSI logs to determine stress magnitude is that stiffness of the formation increase resulting an increase in velocity as a function of increasing stress. Using multi-frequency flexural waves, it has been proposed that the magnitude of in situ stress can be estimated through the dispersion curves. However, if the stress concentration around the borehole exceeds the rock strength, breakouts will occur and lead to a reduction in stiffness at the high stress area. When such mechanical damage exists, the velocity field and the dispersion curve will be affected such that the simple stress-stiffness-velocity relationship presented in the previous sections will not be adequate. Another assumption that can result in large uncertainties in determining stress from DSI logs is the isotropic nature and the stress-independency of the Third-Order Elastic parameters. Prioul *et al*. (2004) shows that the T.O.E. parameters they determined from laboratory studies are limited to a small stress anisotropy. In other words, the T.O.E. parameters are valid only in a specific range of stress perturbation. As a result, the

determination of the reference state is extremely important. The simple forward model presented in this chapter also demonstrates that the predicted velocity fields are highly dependent on the accuracy of the T.O.E. determination. Future works are required to determine how the variation in velocity fields might have affected the dispersion curve by simulating seismic wave propagations through the medium.

6.8 REFERENCES

Brie, A.,Takeshi, E., Hoyle, D., Codazzi, D., Esmersoy, C., Hsu, K., Denoo, S., Mueller, M., Plona, T., Shenoy, R., & Sinha, B., 1998. New directions in sonic logging. *Oilfield Review*, **Spring 1998**, 40-55.

Gough, D.I., Bell, J.S., 1981. Stress orientations from oil well fractures in Alberta and Texas. *Canadian Journal of Earth Sciences*, **18**, 638-645.

Hearman, R.F.S., 1953. Third-order elastic coefficients. *Acta Crystallography*, **6**, 331-340.

Johnson, P.A., & Rasolofosaon, P.N.J., 1996. Nonlinear elasticity and stress-induced anisotropy in rock. *Journal of Geophysical Research*, **101**, 3113-3124.

Mavko, G., Mukerji, T., & Dvorkin, J., 1998. *The Rock Physics Handbook: Tools for Seismic Analysis in Porosu Media*. NY: Cambridge University Press, 329 pp.

Plona, T.J., Kane, M.R., Sinha, B., & Walsh, J., 2002. Evaluating stress-induced anisotropy and mechanical damage from cross-dipole sonic data using dispersion analysis. **SPE/ISRM 78233**.

Prioul, R., Bakulin, A., & Bakulin, V., 2004. Nonlinear rock physics model for estimation of 3-D subsurface stress in anisotropic formations: theory and laboratory verification. *Geophysics*, **69**, 415-425.

Sarkar, D., Bakulin, A., & Kranz, R.L., 2003a. Anisotropic inversion of seismic data for stressed media: theory and a physical modeling study on Berea sandstone. *Geophysics*, **68**, 690-704.

Sarkar, D., Bakulin, A., & Kranz, R.L., 2003b. Errata to: "Anisotropic inversion of seismic data for stressed media: theory and a physical modeling study on Berea sandstone. Geophysics, 68(2), 690-704" *Geophysics*, **68**, 1103-1103.

Sinha, B.K., Kane, M.R., & Borland, W.H., 2002. Analyses of sonic data in an Indonesian well for formation damage, stresses and bedding. **SPE/ISRM 78232**.

Sinha, B.K., & Kostek, S., 1996. Stress-induced azimuthal anisotropy in borehole flexure waves. *Geophysics*, **61**, 1899-1907.

Sinha, B.K., 2002. Determining stress parameters of formations from multi-mode velocity data. *US Patent* 6351991.

Thomsen, L., 1986. Weak elastic anisotropy, *Geophysics*, **51**, 1954-1966.

Thurston, R.N., & Brugger, K., 1964. Third-order elastic constants and the velocity of small amplitude elastic waves in homogeneously stressed media. *Physical Review*. **133**(6A), A1604-A1610.

Toupin, R.A., & Bernstein, B., 1961. Sound waves in deformed perfectly elastic materials. Acousoelastic effect. *Journal of the Acoustical Society of America*, **33**(2) 216- 225.

Winkler, K.W., & Liu, X., 1996. Measurements of third-order elastic constants in rocks. *Journal of Acoustic Society of America*, **100**(3) 1392-1398.

Winkler, K.W., Sinha, B.K. & Plona, T.J., 1998. Effects of borehole stress concentrations on dipole anisotropy measurements. *Geophysics*, **63**(1), 11-17.

Winterstein, D.F., 1990. Velocity anisotropy terminology for geophysicists. *Geophysics*, **55** (8), 1070-1088.

Zoback, M.D., Chan, A.W. & Zinke, J., Production-induced normal faulting. *Proceedings of the 38th US Rock Mechanics Symposium, DC Rocks 2001*, Washington D.C., 7-10 July 2001, 157-163.

Zoback, M.D., Moos, D., Mastin, L., & Anderson, R.N., 1985. Wellbore breakouts and in situ stress. *Journal of Geophysical Research*, **90**, 5523-5530.

APPENDIX 6.A: EFFECTIVE ELASTIC STIFFNESS TENSOR

For a vertical transversely isotropic (VTI) solid, the stiffness tensor can be defined by 5 independent parameters such that (e.g., Thurston, 1974):

$$C = \begin{pmatrix} c_{11} & c_{12} & c_{13} & 0 & 0 & 0 \\ c_{12} & c_{11} & c_{13} & 0 & 0 & 0 \\ c_{13} & c_{13} & c_{33} & 0 & 0 & 0 \\ 0 & 0 & 0 & c_{44} & 0 & 0 \\ 0 & 0 & 0 & 0 & c_{44} & 0 \\ 0 & 0 & 0 & 0 & 0 & c_{66} \end{pmatrix} \quad \text{.....(6.A.1)}$$

The coefficients of the stiffness tensor of the VTI media can be determined from velocities such that (e.g., Prioul *et al*., 2004):

$$c_{11} = c_{22} = \rho V_{11}^2 = \rho V_{22}^2 \quad (6.A.2)$$

$$c_{33} = \rho V_{33}^2 \quad (6.A.3)$$

$$c_{44} = c_{55} = \rho V_{23}^2 = \rho V_{32}^2 = \rho V_{13}^2 = \rho V_{31}^2 \quad (6.A.4)$$

$$c_{66} = \rho V_{12}^2 = \rho V_{21}^2 \quad (6.A.5)$$

$$c_{13} = c_{31} = c_{23} = c_{32} = -c_{44} + \sqrt{\left(c_{11} + c_{44} - 2\rho V_{45^\circ}^2\right)\left(c_{33} + c_{44} - 2\rho V_{45^\circ}^2\right)} \quad (6.A.6)$$

where V_{45° is the velocity measured at 45° relative to the axis.

Prioul et al. (2004) demonstrate the transformation of the stiffness matrix of this VTI solid to an orthorhombic solid such that:

$$\begin{cases} c_{11} \approx c_{11}^0 + c_{111}E_{11} + c_{112}\left(E_{22} + E_{33}\right) \\ c_{22} \approx c_{11}^0 + c_{111}E_{22} + c_{112}\left(E_{11} + E_{33}\right) \\ c_{33} \approx c_{33}^0 + c_{111}E_{33} + c_{112}\left(E_{11} + E_{22}\right) \\ c_{44} \approx c_{44}^0 + c_{144}E_{11} + c_{155}\left(E_{22} + E_{33}\right) \\ c_{55} \approx c_{44}^0 + c_{144}E_{22} + c_{155}\left(E_{11} + E_{33}\right) \\ c_{66} \approx c_{66}^0 + c_{144}E_{33} + c_{155}\left(E_{11} + E_{22}\right) \\ c_{12} \approx c_{12}^0 + c_{112}\left(E_{11} + E_{22}\right) + c_{123}E_{33} \\ c_{13} \approx c_{13}^0 + c_{112}\left(E_{11} + E_{33}\right) + c_{123}E_{22} \\ c_{23} \approx c_{23}^0 + c_{112}\left(E_{22} + E_{33}\right) + c_{123}E_{11} \end{cases} \quad (6.A.7)$$

where c_{ij} are the effective stiffness tensor and c_{ij}^0 is the five independent second-order elastic parameters defined for a VTI solid. C_{111}, C_{112} and C_{123} are the three independent T.O.E. parameters and their combinations such that $c_{144} = \left(c_{112} - c_{123}\right)/2$ and $c_{155} = \left(c_{111} - c_{112}\right)/4$ (Thurston, 1974).

APPENDIX 6.B: BOND TRANSFORMATION

The Bond transformation is often used for rotating the stiffness and compliance matrix without using tensor notation (see discussion by Winterstein, 1990). The transformation is done through matrix multiplication using the Bond transformation matrix, $\underline{\underline{M}}$. This transformation is required since stiffness matrices are contracted from fourth-order tensors to second-order tensors. If $\underline{\underline{C}}$ is the original stiffness matrix, the rotated stiffness matrix, $\underline{\underline{C}}'$, can be obtained by:

$$\underline{\underline{C}}' = \underline{\underline{M}}\,\underline{\underline{C}}\,\underline{\underline{M}}^T \quad \text{.....(6.B.1)}$$

where $\underline{\underline{M}}^T$ is the transpose of $\underline{\underline{M}}$. The Bond transformation matrix is defined as:

$$\underline{\underline{M}} = \begin{bmatrix} a_{11}^2 & a_{12}^2 & a_{13}^2 & 2a_{12}a_{13} & 2a_{13}a_{11} & 2a_{11}a_{12} \\ a_{21}^2 & a_{22}^2 & a_{23}^2 & 2a_{22}a_{23} & 2a_{23}a_{21} & 2a_{21}a_{22} \\ a_{31}^2 & a_{32}^2 & a_{33}^2 & 2a_{32}a_{33} & 2a_{33}a_{31} & 2a_{31}a_{32} \\ a_{21}a_{31} & a_{22}a_{32} & a_{23}a_{33} & a_{22}a_{33}+a_{23}a_{32} & a_{21}a_{33}+a_{23}a_{31} & a_{22}a_{31}+a_{21}a_{32} \\ a_{31}a_{11} & a_{32}a_{12} & a_{33}a_{13} & a_{12}a_{22}+a_{13}a_{32} & a_{13}a_{31}+a_{11}a_{33} & a_{11}a_{32}+a_{12}a_{31} \\ a_{11}a_{21} & a_{12}a_{22} & a_{13}a_{23} & a_{12}a_{23}+a_{13}a_{22} & a_{13}a_{21}+a_{11}a_{23} & a_{11}a_{22}+a_{12}a_{21} \end{bmatrix} \text{. (6.B.2)}$$

where $\{a_{ij} | i, j = 1...3\}$ are the elements of the rotational matrix. With a rotational angle of φ along the z-axis, the rotational matrix is defined as:

$$\underline{\underline{a}} = \begin{bmatrix} \cos\varphi & \sin\varphi & 0 \\ \sin\varphi & \cos\varphi & 0 \\ 0 & 0 & 1 \end{bmatrix} \quad \text{.....(6.B.3)}$$

Similarly, to rotate the second-order compliance matrix, the Bond transformation matrix $\underline{\underline{N}}$ can be used such that,

$$\underline{\underline{S}}' = \underline{\underline{N}}\,\underline{\underline{S}}\,\underline{\underline{N}}^T \quad \text{.....(6.B.4)}$$

where $\underline{\underline{S}}$ and $\underline{\underline{S}}^T$ are the compliance matrix and its transpose. $\underline{\underline{N}}$ is defined as

$$\underline{\underline{N}} = \begin{bmatrix} a_{11}^2 & a_{12}^2 & a_{13}^2 & a_{12}a_{13} & a_{13}a_{11} & a_{11}a_{12} \\ a_{21}^2 & a_{22}^2 & a_{23}^2 & a_{22}a_{23} & a_{23}a_{21} & a_{21}a_{22} \\ a_{31}^2 & a_{32}^2 & a_{33}^2 & a_{32}a_{33} & a_{33}a_{31} & a_{31}a_{32} \\ 2a_{21}a_{31} & 2a_{22}a_{32} & 2a_{23}a_{33} & a_{22}a_{33}+a_{23}a_{32} & a_{21}a_{33}+a_{23}a_{31} & a_{22}a_{31}+a_{21}a_{32} \\ 2a_{31}a_{11} & 2a_{32}a_{12} & 2a_{33}a_{13} & a_{12}a_{22}+a_{13}a_{32} & a_{13}a_{31}+a_{11}a_{33} & a_{11}a_{32}+a_{12}a_{31} \\ 2a_{11}a_{21} & 2a_{12}a_{22} & 2a_{13}a_{23} & a_{12}a_{23}+a_{13}a_{22} & a_{13}a_{21}+a_{11}a_{23} & a_{11}a_{22}+a_{12}a_{21} \end{bmatrix} \quad (6.B.5)$$

The Bond transformation can also be used for stress and strain transformation by similar matrix multiplication such that $\underline{\underline{\sigma}}' = \underline{\underline{M}}\,\underline{\underline{\sigma}}$ and $\underline{\underline{\varepsilon}}' = \underline{\underline{N}}\,\underline{\underline{\varepsilon}}$. One of the advantages of using the Bond transformation is its simplicity, matrix multiplication through Bond transformation allows a more efficient algorithm when compared to the more complicated full tensor transformation of the fourth order stiffness and compliance matrices (e.g. Auld, 1973; Winterstein, 1990).

When anisotropic stress is applied onto a solid, the stiffness matrix become orthorhombic. In other words, nine independent constants are required to define the stiffness matrix. For instance, if the axes of the solid are aligned with the applied stress, the stiffness matrix may looks like

$$\begin{bmatrix} 26.1 & 10.4 & 10.4 & 0 & 0 & 0 \\ 10.4 & 25.8 & 11.0 & 0 & 0 & 0 \\ 10.4 & 11.0 & 21.4 & 0 & 0 & 0 \\ 0 & 0 & 0 & 5.77 & 0 & 0 \\ 0 & 0 & 0 & 0 & 6.15 & 0 \\ 0 & 0 & 0 & 0 & 0 & 7.76 \end{bmatrix} \text{(in GPa)} \quad (6.B.6)$$

If this solid is to be rotated by 45° about the z-axis, the new stiffness matrix will become:

$$\begin{bmatrix} 25.9 & 10.4 & 10.7 & 0 & 0 & -0.08 \\ 10.4 & 25.9 & 10.7 & 0 & 0 & -0.08 \\ 10.7 & 10.7 & 21.4 & 0 & 0 & 0 \\ 0 & 0 & 0 & 5.96 & -0.19 & 0 \\ 0 & 0 & 0 & -0.19 & 5.96 & 0 \\ -0.08 & -0.08 & 0 & 0 & 0 & 7.76 \end{bmatrix} \text{(in GPa)} \quad (6.B.7)$$

The existence of the off-diagonal terms when the axes of the solid is not aligned with the principle stresses suggest that estimating velocity from the stiffness matrix will require a

more tedious algebraic operation than a simple vertical transversely isotropic (VTI) solid which stiffness matrix is independent from the horizontal azimuth.

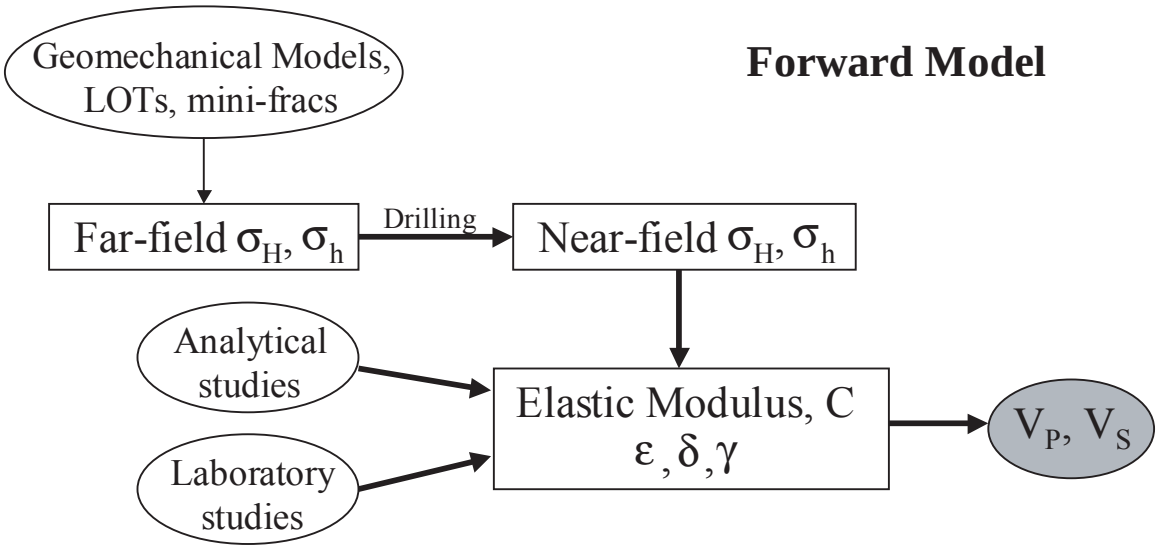

Figure 6.1: Forward model from measured geomechanical data to estimate how the existence of a borehole affects the stress concentration, elastic property and velocity in the surrounding medium.

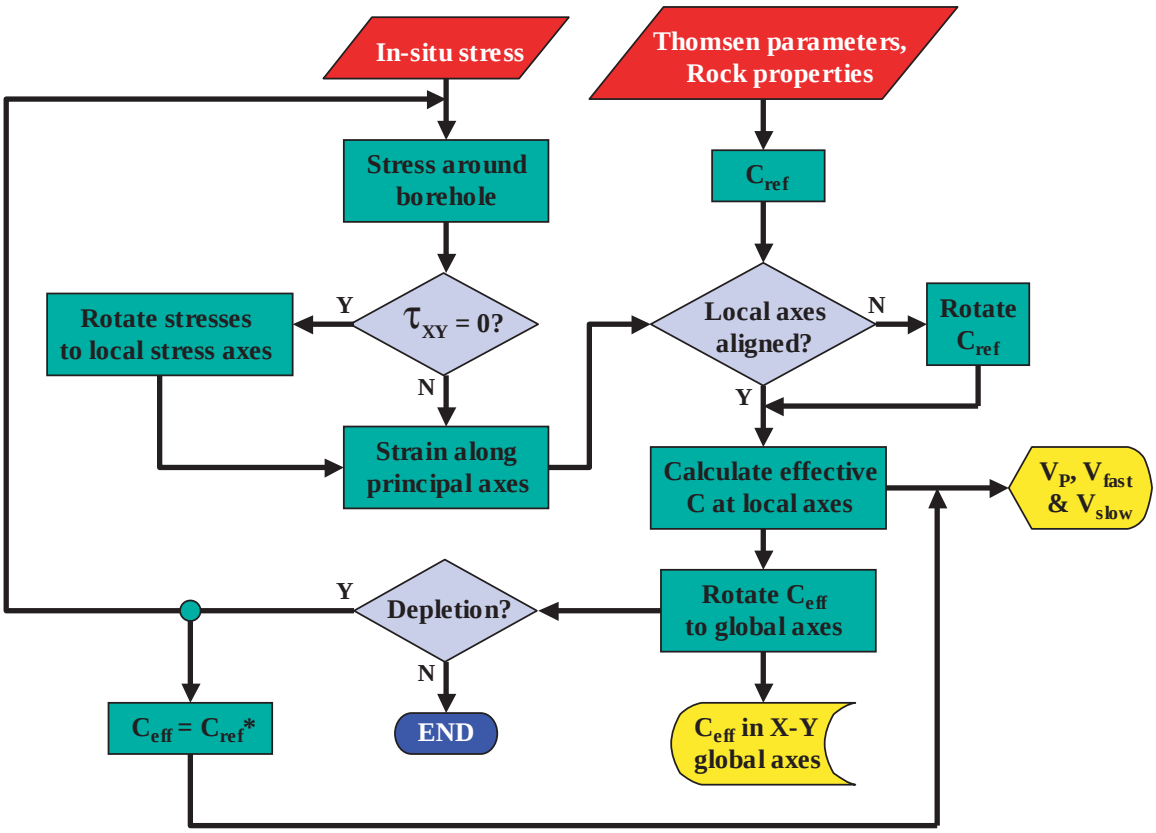

Figure 6.2: The workflow of the modeling. The two red boxes represent the input data from field and laboratory measurements. The two outputs are generated to demonstrate how drilling induced stress perturbation may impact the stiffness tensor and velocities.

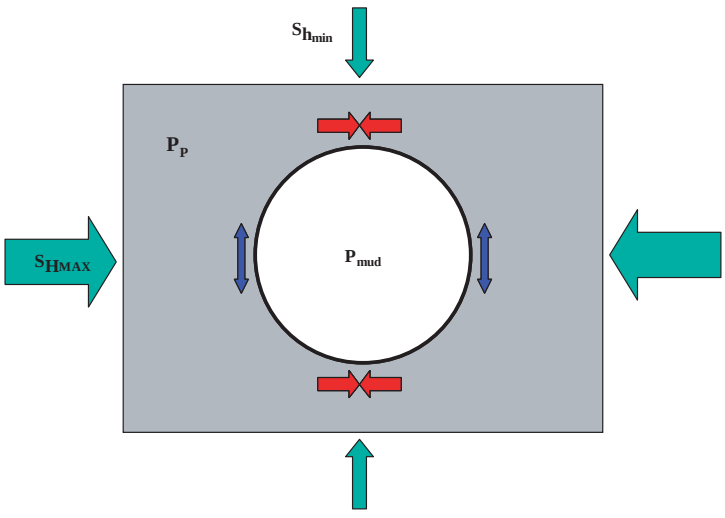

Figure 6.3: When a borehole is drilled in a stressed medium, the existence of the borehole will redistribute the stress around the borehole resulting an increase of compressive stress in the direction of the minimum horizontal stress and an increase in tensile stress along the maximum horizontal stress axis.

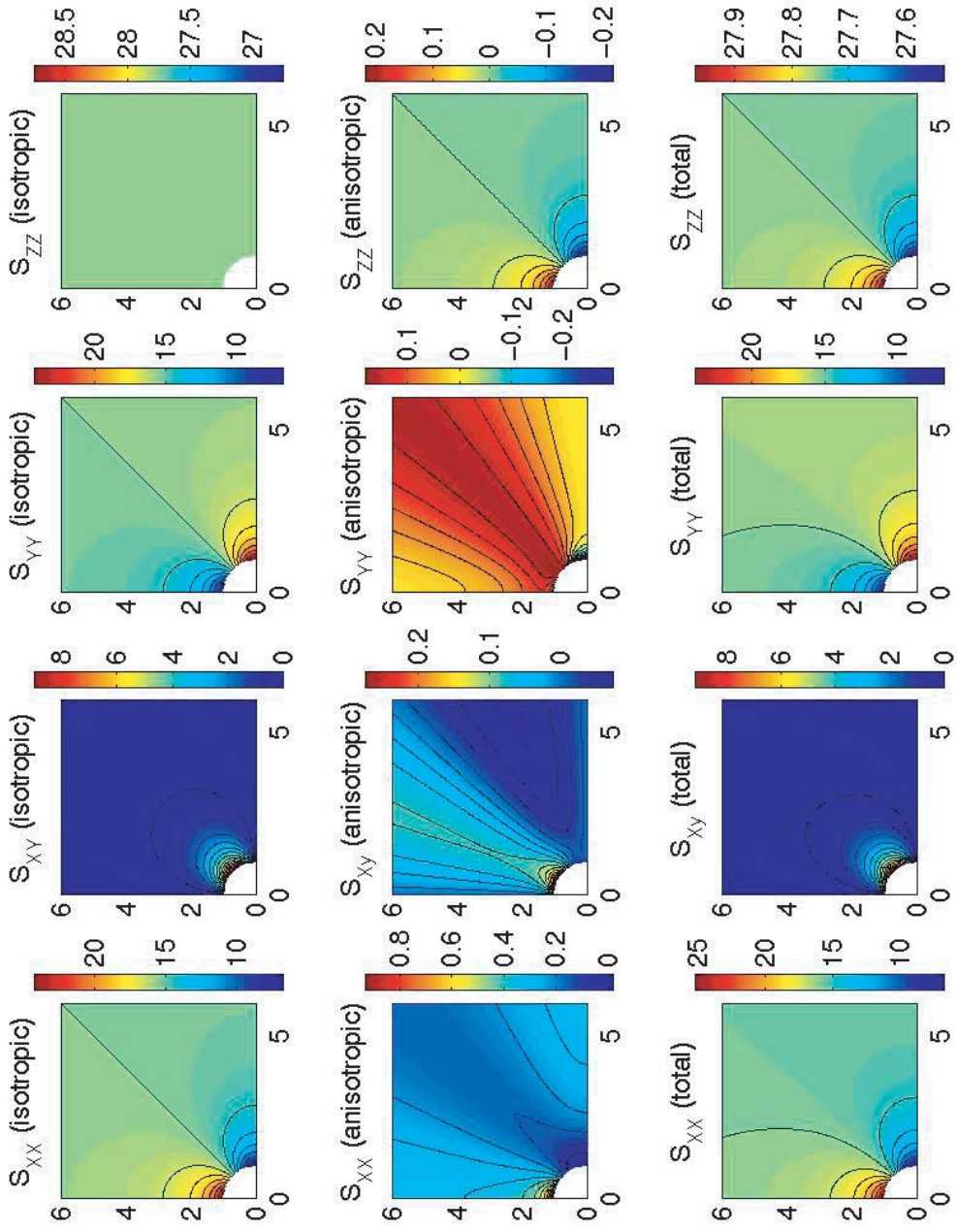

Figure 6.4: The effect of the borehole on stress redistribution in the surrounding medium in Cartesian coordinates. The top panels are the stress around a borehole in Cartesian coordinate assuming the far-field stresses are equal. The middle row represents the resulting stress of an applied uniaxial stress along the x-axis with no far-field stresses. The bottom row is the combine effect of the presence of a borehole in the formation in which the two principal horizontal stresses are not equal.

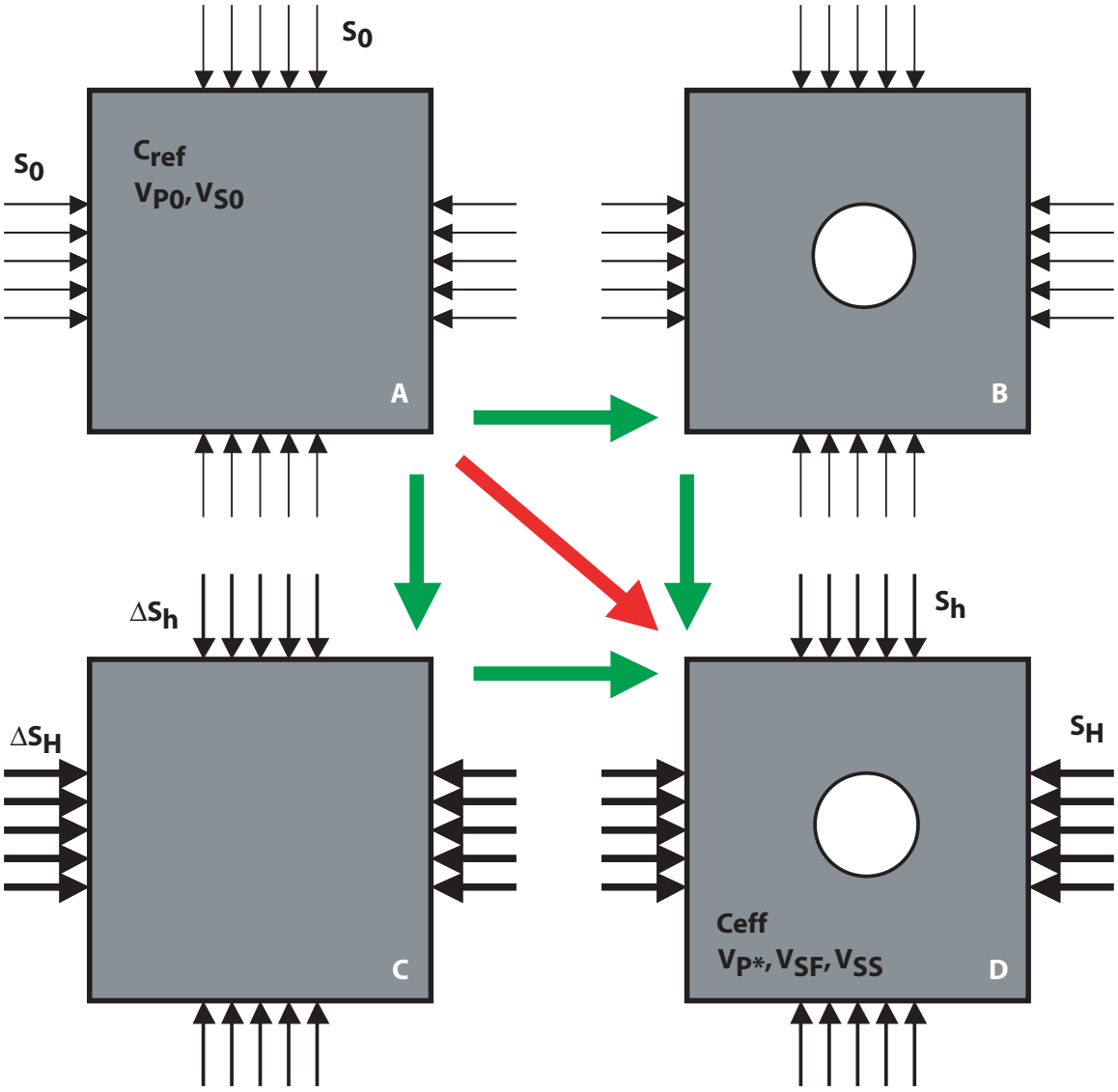

Figure 6.5: Drilling-induced stress perturbation around a borehole. The upper left block represents a formation under isotropic stress. The stiffness tensor for this block is equivalent to a vertical transversely isotropic (VTI) medium. For most authors (e.g., Winkler *et al*., 1998), an open hole drilled in an isotropic stressed block is picked as the reference state (upper right) and uniaxial stress is then applied to the block to calculate the effective stiffness tensor using nonlinear elasticity (lower right). However, in reality, the borehole is drilled into a stressed medium (lower left). As a result, I use the lower left block as the second reference state (i.e., velocities estimated from the final state are compared to this pre-drilling reference state). Mathematically, it is possible to use the upper left block as the reference state and calculate the effective stiffness tensor directly by applying anisotropic stress and a borehole to the isotropic medium (the red arrow).

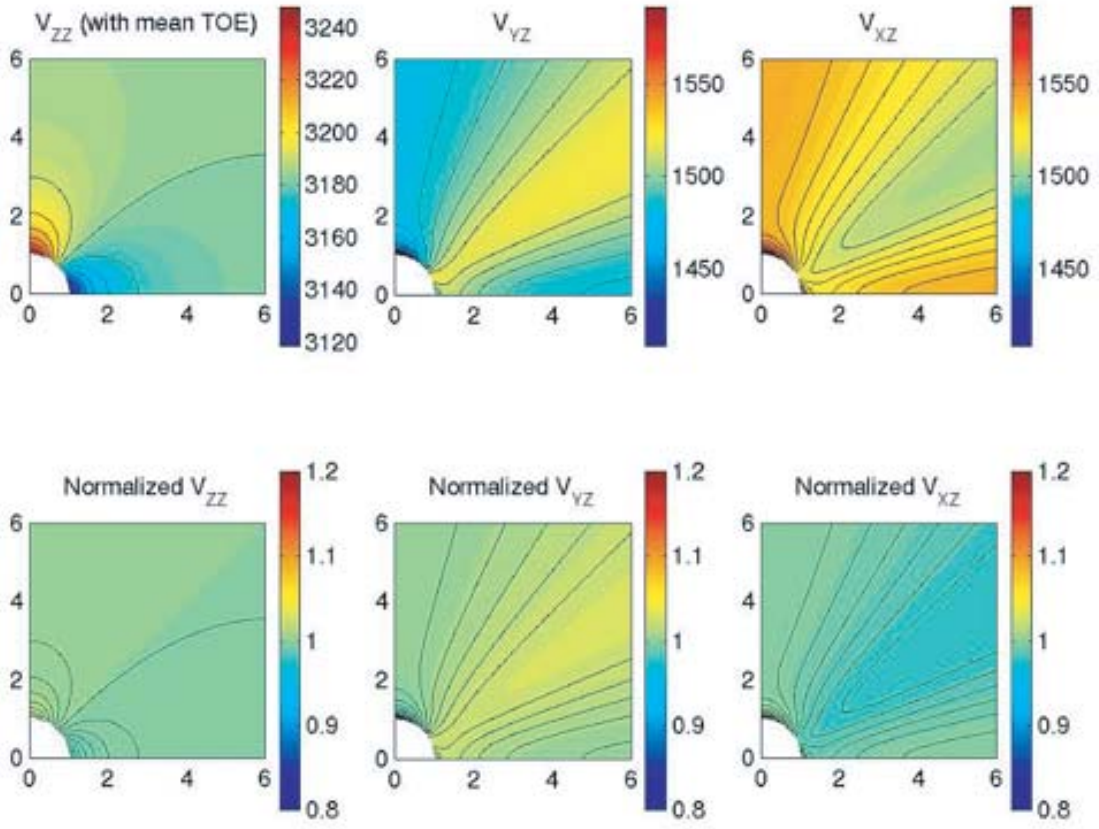

Figure 6.6: Impact of drilling-induced stress redistribution on velocities. The top panels are the P and S waves velocity. The bottom panels are velocities compared to the pre-drilled stressed state. Note that the existence of a borehole does not make a significant impact on the velocity field in this case.

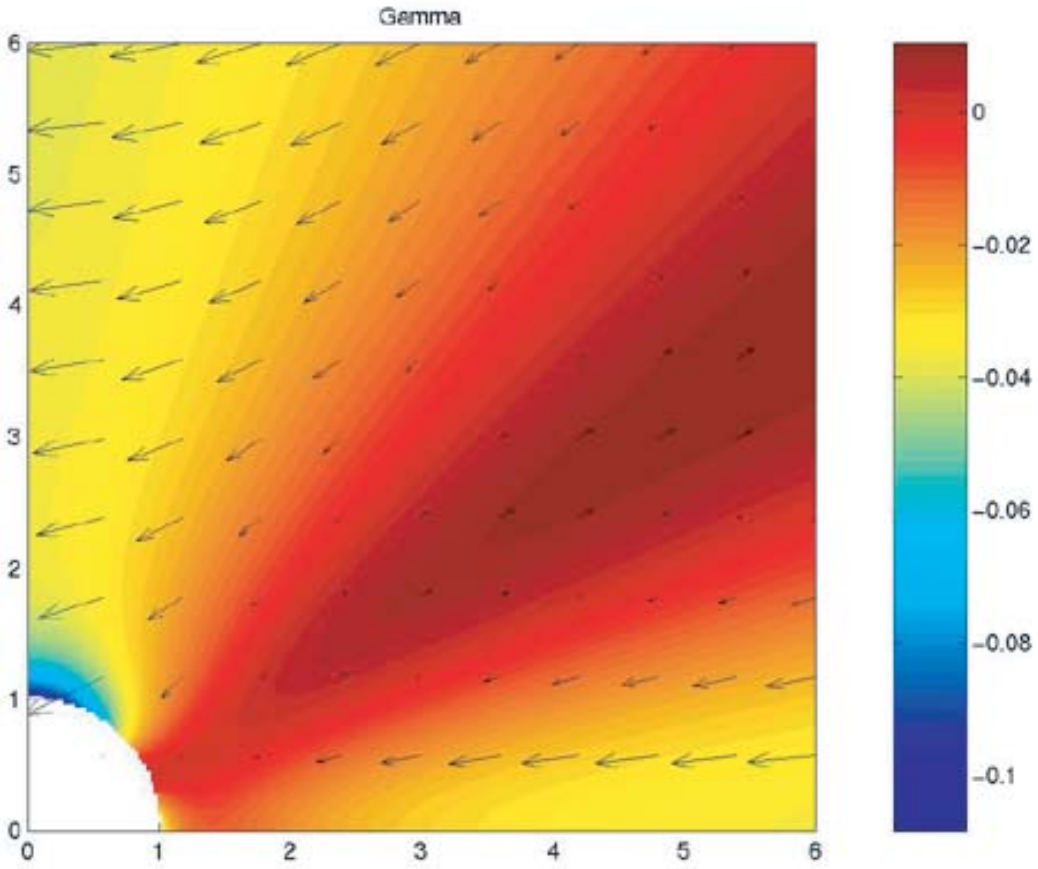

Figure 6.7: Shear-wave splitting due to the existence of a borehole in a stressed medium.

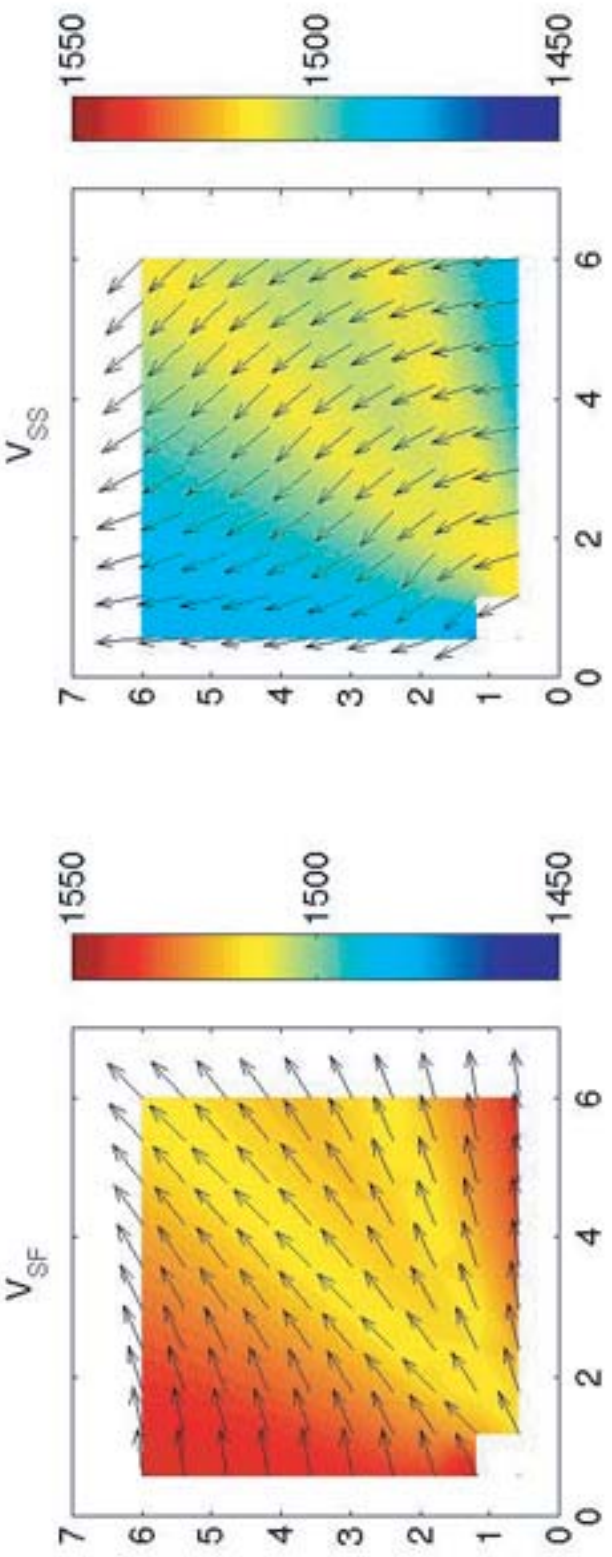

Figure 6.8: The magnitude and direction of the fast and slow shear waves.

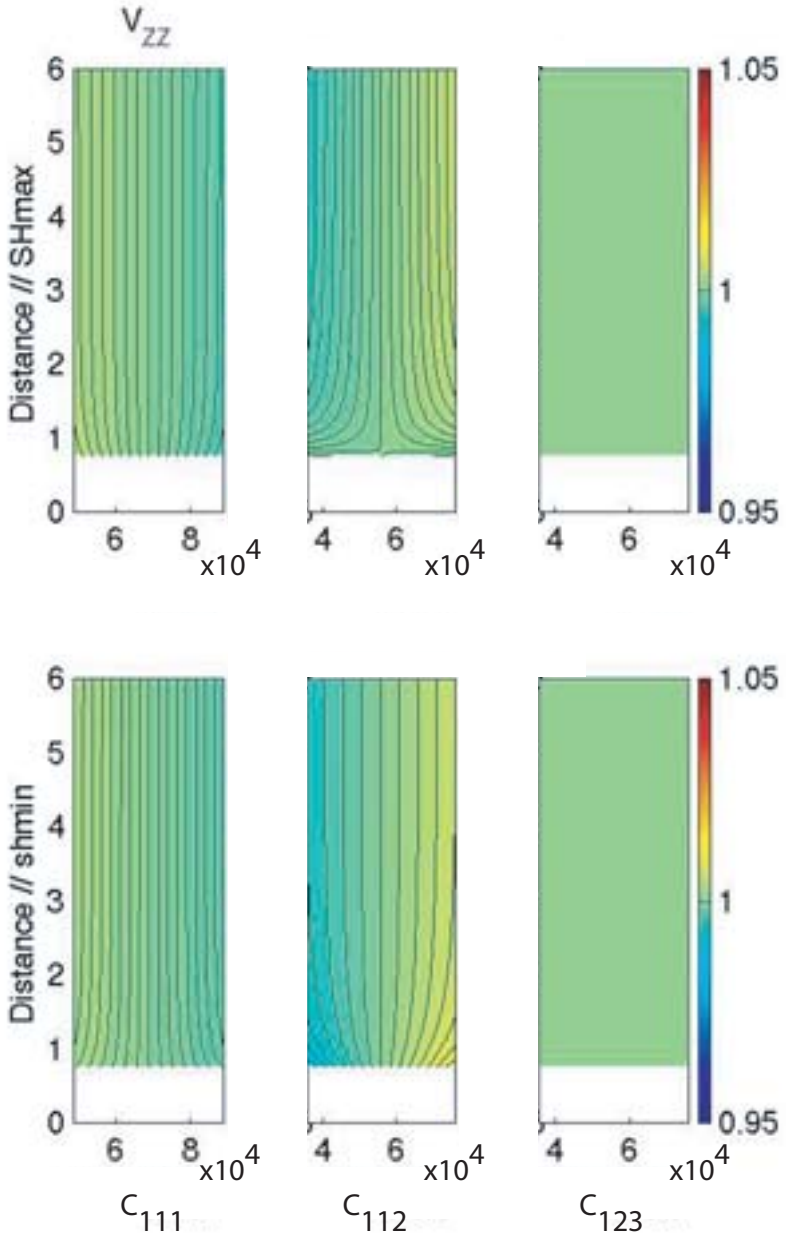

Figure 6.9: The sensitivity of the T.O.E. parameters on P-wave velocity. The vertical axis is the distance away from the borehole normalized to the borehole radius. The three columns correspond to the three T.O.E. parameters. The horizontal axes represent the possible uncertainties of the parameters. Note that the uncertainties associated with C_{123} have minimal impact on P-wave velocity along both principal stresses directions. Only minimal effects can be observed from the existence of the borehole on velocity.

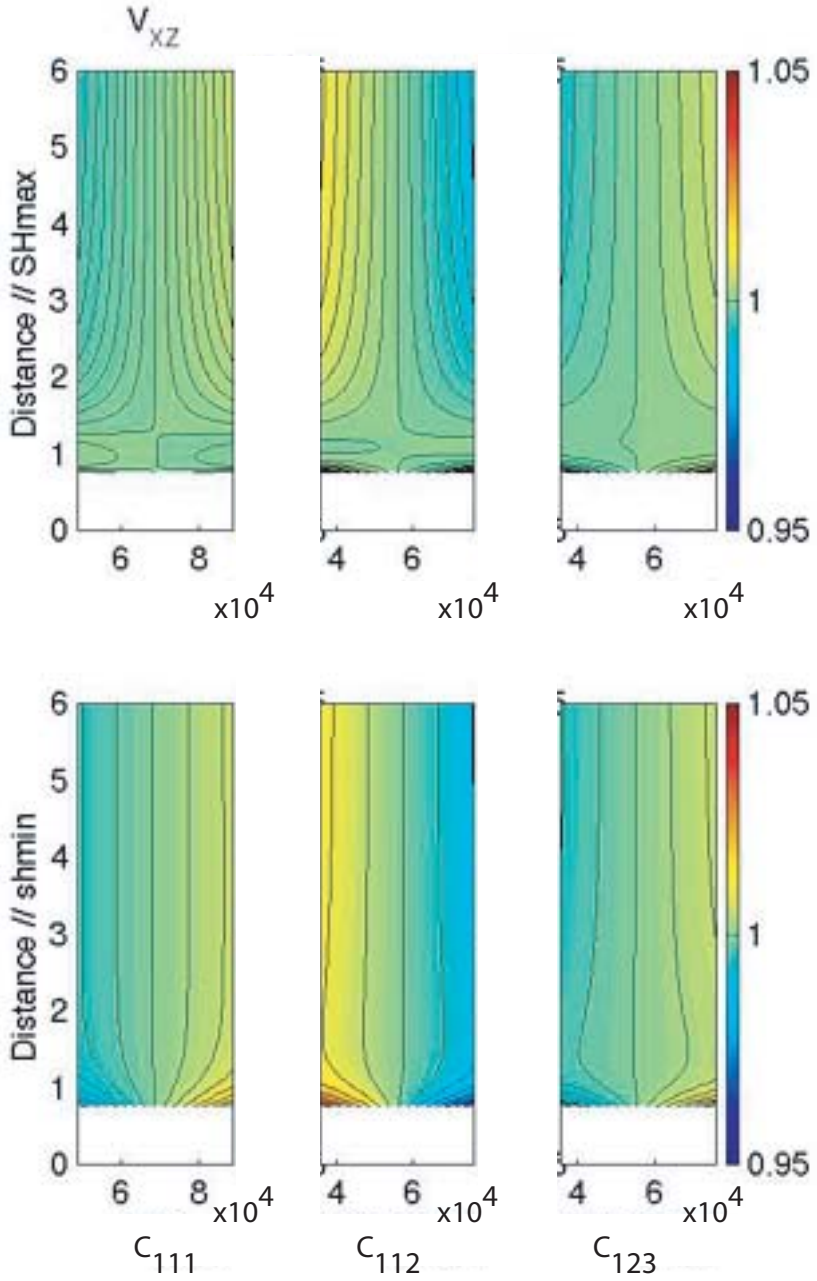

Figure 6.10: The sensitivity of the T.O.E. parameters on S-wave velocity (polarized parallel to the global x-axis).

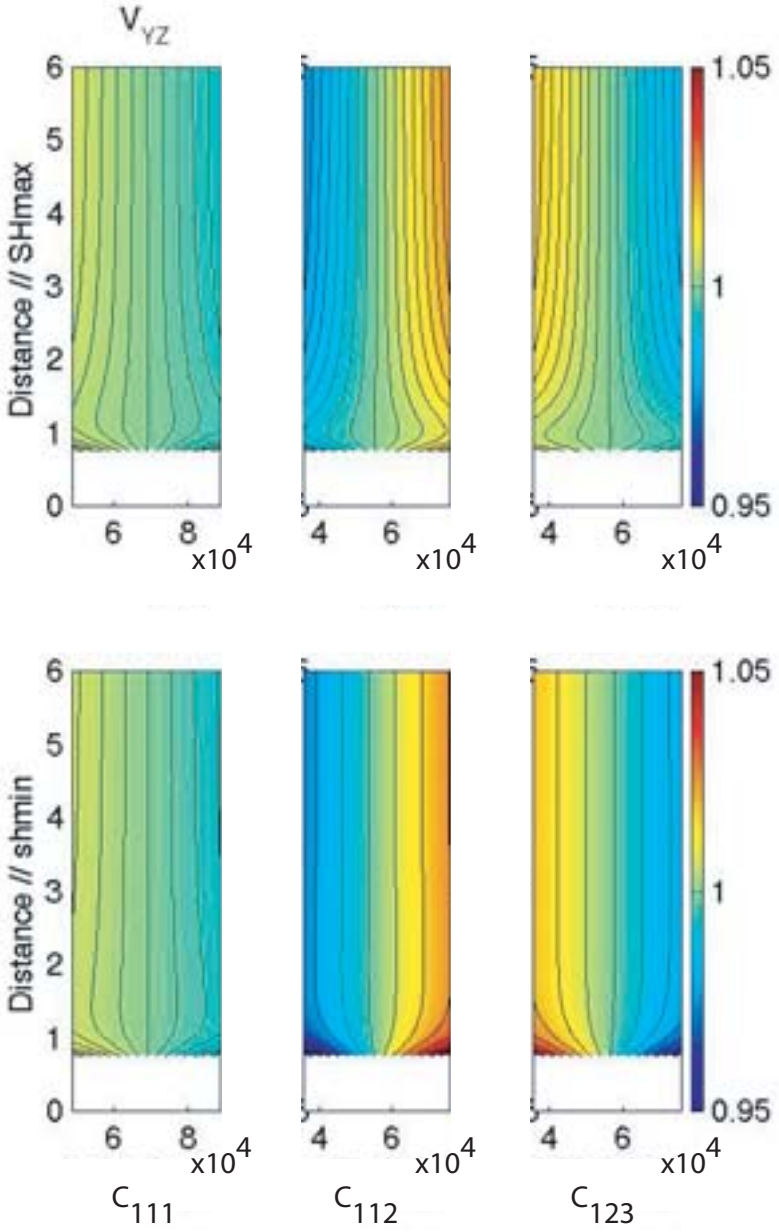

Figure 6.11: The sensitivity of the T.O.E. parameters on S-wave velocity (polarized parallel to the global y-axis).

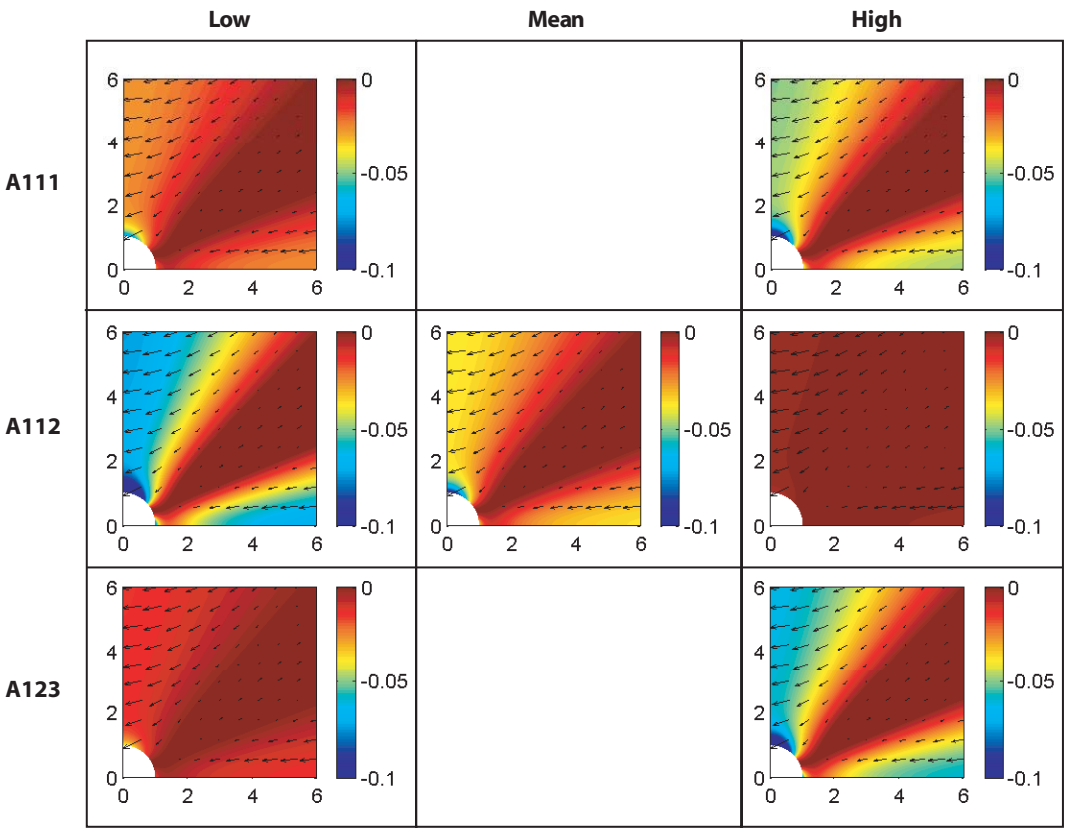

Figure 6.12: Sensitivity of the T.O.E. parameters on the magnitude of shear wave splitting. The central panel corresponds to the gamma estimated from average values of the three T.O.E. parameters. By altering the value of the T.O.E. one at a time, their respective impacts on gamma are shown.